GLOBAL WARMING IMPACTS OF LANDSCAPE MOSAIC IN SOUTHWESTERN MICHIGAN: A CROSS-SCALE ASSESSMENT OF THE CLIMATE BENEFIT POTENTIALS OF ALBEDO AND NET ECOSYSTEM EXCHANGE

By

Pietro Sciusco

A DISSERTATION

Submitted to
Michigan State University
in partial fulfillment of the requirements
for the degree of

Geography—Doctor of Philosophy

2023

ABSTRACT

What are the contributions of landscape composition, weather, and seasonality to the overall variation in surface albedo and the albedo-induced warming or cooling climate benefit potentials across multiple spatiotemporal scales? What are the main key influences to growing season net ecosystem exchange fluxes at major bioenergy crops under different land use history and management? These are the main questions of this dissertation, addressed through three complementary studies focused on climate benefit potentials (i.e., cooling and mitigation effects) of biogeophysical and biogeochemical mechanisms in the context of global warming research, across managed agricultural landscapes in southwestern Michigan, USA. Chapter 1 provides an introduction of the overall research work by introducing the two mechanisms examined, as well as the knowledge gaps and future research needs. Chapters 2 and 3 focus on the climate benefit potentials of the biogeophysical mechanisms, hence the cooling and mitigation effects induced by changes in surface albedo. In particular, Chapter 2 provides a proof of concept to quantify the ecosystem and landscape contribution to local and global climate through the analysis of spatiotemporal changes of surface albedo across five equal area landscapes, each within an individual ecoregion, in southwestern Michigan, USA, and during different weather conditions. Results showed that ecoregions, land mosaic, and seasonality contributed to the variation of surface albedo. Different was the response to changes in weather conditions in changes of surface albedo at forest- and cropland-dominated landscapes. The five ecoregions were characterized by cooling effects, with higher magnitudes in forest-dominated landscapes (i.e., higher difference between forest and cropland albedos). Chapter 3 extends the analysis in Chapter 2 to a broader landscape (i.e., watershed level) and over a period of 19 years, by looking at the contribution of major cover types, compared to original land uses, during both growing season and non-growing

season (i.e., the effects of snow *vs* snow-free surface albedo). The 19-year analysis showed that land mosaic (with respect to the original forest cover type) exhibited net cooling effects, varying by cover types and ecoregions considered. Croplands contributed the most to cooling the local climate, with seasonal and monthly offsets of 18% and 83%, respectively, of the annual greenhouse gas emission of maize fields in the same area. On the other hand, urban showed both cooling and warming effects. Overall, landscape composition produced different landscape climate benefit potentials. Chapter 4 focuses on the climate benefit potentials of biogeochemical mechanisms, by looking at investigating the main key influences to net ecosystem exchange fluxes of three major bioenergy crops (viz., no-till continuous maize, restored native prairie, and switchgrass) under different land use history and management. The interannual variations of hypothesized main key influences to net carbon (C) fluxes varied by cover types and growing season considered, with maize showing a unique pattern. Net C uptakes were higher within maize, with magnitudes between -9.4 and -22.8 gC m^{-2} d^{-1}. Results also showed that number, importance, and magnitude of main influences to C uptakes varied by cover type, highlighting the different nature of bioenergy crops (annual *vs* perennial; monoculture *vs* polyculture). Lastly, I show that the use of fine-resolution optical and radar remote sensing can improve forecasts of growing season C uptakes at maize cover type, depending on certain remote sensing variables and stage of maize's growth. Recommendations for further research needs are discussed and include coupling my estimates with emissions from other greenhouse gasses (GHGs) and extending the analysis to non-growing season period for a more comprehensive understanding of C uptake dynamics under different land use history. These analyses of biogeophysical and biogeochemical mechanisms fill important gaps in landscape ecology and ecosystem science as well as global warming research.

ACKNOWLEDGEMENTS

I would like to thank my advisor, Dr. Jiquan Chen, for allowing me to grow both academically and professionally. I will never forget his strict and demanding personality, but at the same time a person rich in expertise and knowledge, without which my dissertation would have not been in the present shape today. Dr. Chen represented my main guidance, my academic father, and I am thankful for accepting me in his lab and for showing appreciation and good expectations since the beginning of my journey. I also thank my dissertation committee: Drs. Geoffrey Henebry, Ashton Shortridge, and Phoebe Zarnetske not only for agreeing on serving on my PhD committee, but also for supporting my growth and progress through several advice, inputs, brainstorming, during classes and meetings. In particular, I would like to thank Dr. Henebry (my informal PhD mentor) for being always available for random meetings, during which he would constantly express his professional and human support to any possible complain/fear of mine, as well as for his very picky but constructive comments to my work and way to "do research".

I would also like to thank all the people at the department of Geography, Environment & Spatial Sciences and at the Center for Global Change and Earth Observations (CGCEO) for supporting me during the past 5 years. In particular, a special thanks goes to Jean Lepard, Sharon Ruggles, Joni Burns, Nathan Moore, and Wilson Ndovie, for all the academic, bureaucratic, and technical support, without which I would have had much more hard time navigating through the past years.

A great thanks to all my colleagues/friends (with no specific order) from LEES lab: Gabriela, Cheyenne, Vincenzo, Mike, Maowei, Hogeun, Zutao, Ranjeet, Fei Li, Connor, and Jing; Geography department: Cristina, Shengpan, Donald, Ken, Liz, Herve, BJ, Kyle, Yingyue, Ana, Katie, Mehmet, and Vasily; fieldwork crew: Kaylee, Kaitlyn, Pedro, and Ezequiel; volleyball crew:

Pouyan, Anna, Chauncey, Kevin, Affan, Lauren(s), Liza, Bre, Timur, Max, Arija, and Dice; "Celebrate Life" crew: Alex, Abdullah, Alesssandro, Evan, Jaques, Kaity, Laura, Leo, Nathan, João, and Alice; Prospect St. crew: Yasmina, Valeria (roomie), Cristina (chica), Phil (brother), Abe, Karima (sista), Abeng, Valentino, little Yasmina, Diana, Giacomo, Welore, and all the other housemates I have had the great pleasure to share my daily routine with; and "Mich-Italians" crew: Luisa (boo), Patricia (nocciolina), Luciano (papà), and Alessandro.

Last but not least, I want to thank from the bottom of my heart my lovely family: Mamma, Papà, Luisa, Rossana, Giuliano, and Savio, for being always present and for representing a constant figure that has always been proud of my accomplishments and growth, and for waiting for me, every time I went back to visit, with the same enthusiasm, love, and joy. In particular, I want to express my DEEP THANKS to my parents who gave me the great opportunity to be in love with education, learning, and discovery and who always gave me the complete freedom to "find my path" and my way into my future. I made many sacrifices during the past 5, which led to a lot of progress, personally and professionally, which I dedicate to THEM.

TABLE OF CONTENTS

LIST OF ABBREVIATIONS

α_{SHO}	White-Sky Shortwave (0.3–5.0 μm) Surface Albedo (unitless or %)
AF	Carbon-Dioxide Airborne Fraction (unitless or %)
AGR	Agriculturally Cultivated lands
ANOVA	Analysis of Variance
BDLM	Bayesian Dynamic Linear Model
BRDF	Bidirectional Reflectance Distribution Function
C	Carbon
CDR	Carbon-Dioxide Removal Option
CH_4	Methane
CIg	Green Chlorophyll Index (unitless)
CO_2	Carbon-Dioxide
CONUS	Conterminous United States
Cos(θ)	Cosine Solar Zenith Angle
CROP	Cropland-Dominated Landscapes
CRP	Conservation Reserve Program lands
$\Delta\alpha$	Albedo Changes (unitless or %)
η^2	Eta-Squared
E_a	Actual Vapor Density (kg m^{-3})
e_a	Actual Vapor Pressure (kPa)
EC	Eddy Covariance
EPA	Environmental Protection Agency
E_s	Saturation Vapor Density (kg m^{-3})

e_s	Saturation Vapor Pressure (kPa)
ESA	European Space Agency
EVI/2	Enhanced Vegetation Index/2 (unitless)
FOR	Forest-Dominated Landscapes
GEE	Google Earth Engine
GHG	Greenhouse Gas
GLBRC	Great Lakes Bioenergy Research Center
GLM	Generalized Linear Model
GloVis	Global Visualization Viewer
GRD	Ground Range Detected
GS/gs	Growing Season
$GWI_{\Delta\alpha}$	Albedo-Induced Global Warming Impact ($gCO_{2\text{-}eq}$ or $C_{\text{-}eq}$ m^{-2} yr^{-1})
$GWP_{\Delta\alpha}$	Albedo-Induced Global Warming Potential ($gCO_{2\text{-}eq}$ or $C_{\text{-}eq}$ m^{-2} yr^{-1})
f_a	Two-Way Atmospheric Transmittance Parameter
Ht	Vegetation Height (m)
IPCC	Intergovernmental Panel on Climate Change
IW	Interferometric Wide
KBS	W.K. Kellogg Biological Station
K_T	Clearness Index (%)
LAI	Leaf Area Index (m^2 m^{-2})
LCA	Life Cycle Assessment
LSM	Least Square Means
LTER	Long-Term Ecological Research

LULCC	Land Use and Land Cover Change
MLP	Multi-Layer Perceptron
MO/mo	Months
MODIS	Moderate Resolution Imaging Spectroradiometer
MSI	Multispectral Instrument
N_2O	Nitrous Oxide
NDVI	Normalized Difference Vegetation Index (unitless)
$NDWI_{SWIR}$	Normalized Difference Vegetation Index using SWIR (unitless)
NEE	Net Ecosystem Exchange Fluxes ($gCO_2\ m^{-2}\ d^{-1}$)
NEE_{adj}	Adjusted Net Ecosystem Exchange Fluxes ($gCO_2\ m^{-2}\ d^{-1}$)
NHS	Natural-Human Systems
NIR	Near-Infrared (nm)
NLCD	National Land Cover Database
PAR	Photosynthetic Active Radiation ($\mu mol\ m^{-2}\ d^{-1}$)
PD	Partial-Dependence
PolSAR	Polarimetric SAR
PPT	Precipitation (mm)
PRISM	Parameter-Elevation Regression of Independent Slopes Model Group
R^2	R-Squared Score
RF	Random Forest
rf_{CO2}	Marginal Radiative Forcing of CO_2 ($W\ kg\ CO_2^{-1}$)
$RF_{\Delta\alpha}$	Albedo-Induced Radiative Forcing ($W\ m^{-2}$)
RH	Relative Humidity (%)

RMSE	Root Mean Square Error
RVI	Radar Vegetation Index (unitless)
σ°	Sigma Nought (intensity)
S1/2	Sentinel-1/2
SAR	Synthetic Aperture Radar
SPAD	Soil and Plant Development index (unitless)
S_{po}	Solar Constant (W m^{-2})
SRM	Solar Radiation Modification Option
SWC	Soil Water Content (%)
SW_{in}	Incident Shortwave Radiation at the Surface (W m^{-2})
SWIR	Shortwave Infrared (nm)
SW_{TOA}	Incident Shortwave Radiation at Top-of-Atmosphere (W m^{-2})
θ	Solar Zenith Angle
T_a	Upward Atmospheric Transmittance (unitless or %)
T_{air}	Air Temperature (°C or K)
TH	Time Horizon (year)
TOA	Top-of-Atmosphere
UNFCCC	United Nations Framework Convention on Climate Change
USGS	United States Geological Survey
VI	Vegetation Index
VPD	Vapor Pressure Deficit (kPa)

CHAPTER 1. INTRODUCTION

General introduction

To date, there is strong scientific evidence that atmospheric concentrations of carbon-dioxide (CO_2) are gradually increasing and reaching 1.5 times of those of the pre-industrial era (Wiesner et al., 2022). Anthropogenic activities, such as burning fossil fuels and industrial processes, represent the highest contribution to the total greenhouse gas (GHG) emissions during the last four decades (1970–2010) and are the major driver of climate change (Masson-Delmotte et al., 2021). In turn, current climate change and future climate change scenarios—e.g., warming of the atmosphere and oceans, altered global water cycle, reduction in snow and ice, rising in global mean sea level, etc.—equate to high risks and impacts on all kinds of coupled natural-human (CNH) systems worldwide. Ultimately, current and future climate changes represent a real problem to the sustainable development of a given CNH system, which might be already experiencing the threat of climate change. For instance, increasing in global mean surface temperature above the pre-industrial period (1850–1900) have directly and indirectly affected human communities depending on natural and managed systems for foods, clean water, safe places to live, and livelihoods among many other ecosystems goods and services. Thus, some CNH systems might result more vulnerable to climate changes than others. (Hoegh-Guldberg et al., 2019). Hence, assessing the exposure and vulnerability of CNH system has become a fundamental goal in climate change research (National Research Council, 2010). To that purpose, many complementary adaptation and mitigation options have been proposed to help reduce the risk of climate change impacts. No single option is sufficient by itself, and only through the realization of policies and international cooperation across multiple scales (i.e., international ↔ regional ↔ national ↔ sub-national ↔ local) can we achieve effective implementation of such options.

In order to inform current climate benefit potentials (i.e., adaptation and mitigation efforts), robust Earth System Models and Regional Climate Models are needed to accurately reflect global and regional circulation and feedbacks among land, ocean, and atmosphere. Two different mechanisms are essential to these models: biogeophysical (i.e., surface energy fluxes, with particular interest in surface albedo changes) and biogeochemical (i.e., carbon (C) cycle, with particular interest in the net ecosystem exchange (NEE) fluxes). Moreover, to better inform worldwide initiatives (e.g., REDD+) involved in mitigating the overall (i.e., GHGs and energy fluxes impacts) adverse climate change, feedbacks from biogeophysical mechanisms must be considered in conjunction with those from the biogeochemical ones (Gotangco Castillo et al., 2012). However, several knowledge gaps exist related to how different land use and land cover affect these mechanisms. Filling these knowledge gaps will ultimately advance explanation and prediction about the local climate mitigation potentials—referred here as cooling and mitigation effects—of different land use and land cover types through their biogeophysical and biogeochemical properties, which operate at different spatial and temporal scales. At that purpose, my study investigates the local climate benefit potentials of biogeophysical and biogeochemical mechanisms across intensively managed agricultural landscapes in the Kalamazoo River Watershed in southwestern Michigan, USA, by proposing a cross-scale (i.e., spatial and temporal) approach based on *in-situ* ground measurements and multi-sensor remote sensing imagery.

To be quantitatively comparable, the climate benefit potentials of both biogeophysical and biogeochemical mechanisms are studied in terms of the amount of energy imbalance that they can cause in the Earth's climate system. Such imbalance is referred in terms of radiative forcing (RF; $W\ m^{-2}$)—the change in the net radiative flux at the top-of-atmosphere (TOA) due to the change in atmospheric CO_2 (or any other GHG) concentration—which can be positive or negative,

representing the warming or cooling effects of a given GHG, respectively. Moreover, given the complexity and number of the mechanisms involved in global warming research, the Intergovernmental Panel on Climate Change (IPCC) has introduced pulse emission metrics that facilitate the process of multi-component climate policies by allowing the comparison of different GHGs, along with other climate forcing agents (e.g., albedo), to be expressed in mitigations/emissions equivalent to a reference GHG. Usually, the reference GHG found in the literature is CO_2, and so the mitigations/emissions equivalent to CO_2 (i.e., CO_{2eq}). One example of pulse emission metric is the global warming potential (GWP; $kgCO_{2eq}\ m^{-2}\ yr^{-1}$)—hereinafter, referred to as global warming impact (GWI), to be in line with previous studies (Abraha et al., 2021; Sciusco et al., 2020, 2022). To date, GWI has become the default pulse emission metric among a range of international cooperation parties, such as the United Nations Framework Convention on Climate Change (UNFCCC) and the Kyoto Protocol (Masson-Delmotte, et al., 2021).

It is clear that there is immediate need to reduce emissions to mitigate climate change and ensure we do not exceed 1.5 °C above pre-industrial levels, at which point there is very high risk of severe, extensive, and irreversible impacts worldwide (Masson-Delmotte, et al., 2021). Continuing to reduce emissions, implementing so-called geoengineering or "climate intervention" (National Research Council, 2010) strategies, has been proposed to further reduce global temperature (Lenton & Vaughan, 2009). Climate intervention strategies represent a set of proposed methods and technologies that have the goal of deliberately altering the climate system of Earth by increasing the removal of CO_2 from the atmosphere (i.e., carbon-dioxide removal; CDR, which includes reforestation, and direct air capture and carbon storage technologies), or by reducing the amount of absorbed solar energy that reaches Earth (i.e., solar radiation modification; SRM, which

includes stratospheric aerosol injection and marine cloud brightening; National Research Council, 2015). While the CDR option refers to the climate benefit potentials due to CO_2 uptake/emission in the context of ecosystem C budget, SRM specifically refers to the climate benefits due to increasing surface albedo—the fraction of incoming shortwave solar radiation scattered by a surface back to space—in the context of surface radiation budget.

Although both biogeophysical and biogeochemical mechanisms are essential to accurately model Earth's climate now and into the future and determine potential impacts of different climate adaptation and mitigation scenarios (including with or without climate intervention; Lenton & Vaughan, 2009), there are still many uncertainties and research gaps related to them. First, while research has focused on understanding how landscape degradation affects the C sequestration (Gellie et al., 2018; Matos et al., 2020), little is known about changes in albedo-induced RF ($RF_{\Delta\alpha}$) and GWI ($GWI_{\Delta\alpha}$) in the context of landscape mosaics at broader temporal scales and for multiple anthropogenic land uses. For that reason, the forcing effects of albedo due to land-use land cover change (LULCC) are ranked as medium-low relative to the rich scientific evidence of the forcing effects due to anthropogenic GHGs (Myhre et al., 2014). Second, current climate simulations do not consider surface albedo changes in the context of land composition and mosaic, but rather focus on land use conversion from natural vegetation (e.g.., deforestation; Sciusco et al., 2020, 2022; F. Zhao et al., 2021). Third, there is a need to reduce uncertainty when applying biogeophysical models to study the canopy CO_2 exchange with the atmosphere. As shown by Baldocchi et al. (2002), such models need better accuracy about the structure and the physiology of the canopy (i.e., leaf area index and photosynthetic activity), hence, it is fundamental to investigate direct and indirect effects of environmental factors on CO_2 exchange between vegetation canopy and the atmosphere (Shao et al., 2016). Fourth, to better understand the climate

benefit offsets of biogeophysical and biogeochemical mechanisms, we need to quantify their dependence on external influences (e.g., extreme weather events, land management practices, land use history) that are fundamental to investigate whether the systems maintain their status as C sink or they become C source (Bonan, 2008). To fill these knowledge gaps, my research focuses on the climate benefit potentials of biogeophysical and biogeochemical mechanisms across intensively managed agricultural landscapes in the Kalamazoo River Watershed in southwestern Michigan, USA. This research is based on a cross-scale (i.e., spatial and temporal) approach to achieve my study objectives based on *in-situ* ground measurements and multi-sensor remote sensing imagery at multiple spatial and temporal resolutions. The questions that lay the basis of my research fall within three scientific foci, one per each Chapter: (i) Chapter 2: What are the contributions of landscape composition, weather, and seasonality to the overall variation in surface albedo, and albedo-induced radiative forcing and global warming impact across five contrasting ecoregions of equal area for three different years? (ii) Chapter 3: What are the contributions of land mosaic (i.e., major cover types) to seasonal (growing season) and monthly (non-growing season) surface albedo-induced global warming impacts at landscape level and for a 19-year study period across five contrasting ecoregions in the Kalamazoo River Watershed? (iii) Chapter 4: What are the main key influences to the growing season net ecosystem C fluxes of three major bioenergy cropping systems under different land use history and land management?

Research Context and Background

Anthropogenic activities represent the main driver of local and global climate change (Masson-Delmotte et al., 2021), and the magnitude of such activities has been escalating starting from the pre-industrial era, when the amount of well-mixed GHGs—i.e., CO_2, methane (CH_4), and nitrous oxide (N_2O)— concentration released into the atmosphere started increasing exponentially,

mainly driven by economic and population growth. There is scientific agreement that such increase in atmospheric CO_2 concentration, alone, contributes to a total anthropogenic RF with a warming effect of +2.3 W m^{-2}. To date, we have already witnessed the potential consequences of such changes at both regional and global scales (Zarnetske et al., 2021). For years, the scientific community has researched a range of options to address climate change with the aim of reducing both the GHG emissions through carbon sequestration methods (i.e., mitigation options), and to assess how vulnerable a given CNH system becomes due to changing climate (i.e., adaptation options). Additionally, new approaches to manipulate the climate have been introduced, called climate intervention proposals (Lenton & Vaughan, 2009; National Research Council, 2015). Such proposals include deliberate actions (i.e., CDR and SRM options) to reduce some anthropogenic climate change, hence, there is increasing interest from researchers and policy makers to understand the outcomes of those proposals (National Academies of Sciences, Engineering, and Medicine, 2021; National Research Council, 2015; Williamson et al., 2014). CDR options (e.g., afforestation) have already been applied and tested in different ecosystems, whereas SRM options (e.g., increasing the atmospheric albedo through stratospheric aerosol injections or marine cloud brightening) are still untested and carry with them numerous uncertainties, side effects, and risks for ecological systems (Kvalevåg et al., 2010; Zarnetske et al., 2021). Overall, this gap leaves many pending considerations, such as the environmental, economic, social, and ethical risks, associated to climate intervention proposals. When considering alternative futures with CDR, SRM, and continued anthropogenic climate change, a major knowledge gap is understanding the climate regulations of albedo due to LULCC on warming/cooling the climate.

Surface albedo—the fraction of incoming shortwave solar radiation scattered by a surface back to space—is a physical characteristic of land surface that is strongly affected by both physical

and biophysical land cover properties, such as canopy structure, soil water content, plant phenology, presence of snow, and more. Hence, it is important to consider spatiotemporal variation when quantifying albedo's contribution to off-setting local to global climate warming. Currently, the IPCC (Forster et al., 2021) estimates that RF of well-mixed GHGs has a warming effect equivalent to ~+2.91 W m^{-2}, while that of surface albedo, due to LULCC (i.e., deforestation, agricultural development, and urban expansion), has a cooling effect equivalent to ~-0.20 W m^{-2}. In other words, albedo changes due to LULCC can offset up to ~7% of the RF from anthropogenic GHGs. Such climate benefit may sound small, although it is just a global average estimate and with medium confidence. As a matter of fact, previous studies showed that, while the effects of LULCC-induced biogeophysical mechanisms on climate can be negligible on global scales, it turns to be pronounced when smaller extents are considered (Brovkin et al., 2004; Gotangco Castillo et al., 2012; Matthews et al., 2004; Zhao et al., 2021). Hence, one can expect the benefits might turn into greater magnitudes if reported to regional/local scales and if considered as complementary methods to the CDR options, i.e., overall trade-off of the climate regulations between the two mechanisms.

In this research work, I considered the climate benefit potentials originating from two different mechanisms: biogeophysical and biogeochemical (Figure 1.1). Particularly, this study investigates the biogeophysical mechanisms (Figure 1.1a) at landscape scale, where spatiotemporal variations of climate and management (Δ_{CM}; e.g., wetter *vs* drier, fertilization *vs* non-fertilization, etc.), vegetation phenology (Δ_{VP}; e.g., leaf development, inflorescence, etc.), land use history (Δ_{LUH}; e.g., change of cover type), and land mosaic (Δ_{LM}; e.g., coexistence of multiple land cover types within the same spatial extent) may strongly affect surface albedo (α). On the other hand, the biogeochemical mechanisms (Figure 1.1b) are investigated at parcel scale

(i.e., single field scale), where a variety of key influences (e.g., leaf area index, vegetation height, leaf chlorophyll content, soil water content, etc.) affect the variation of net ecosystem exchange (NEE; net ecosystem C) fluxes at tower scale.

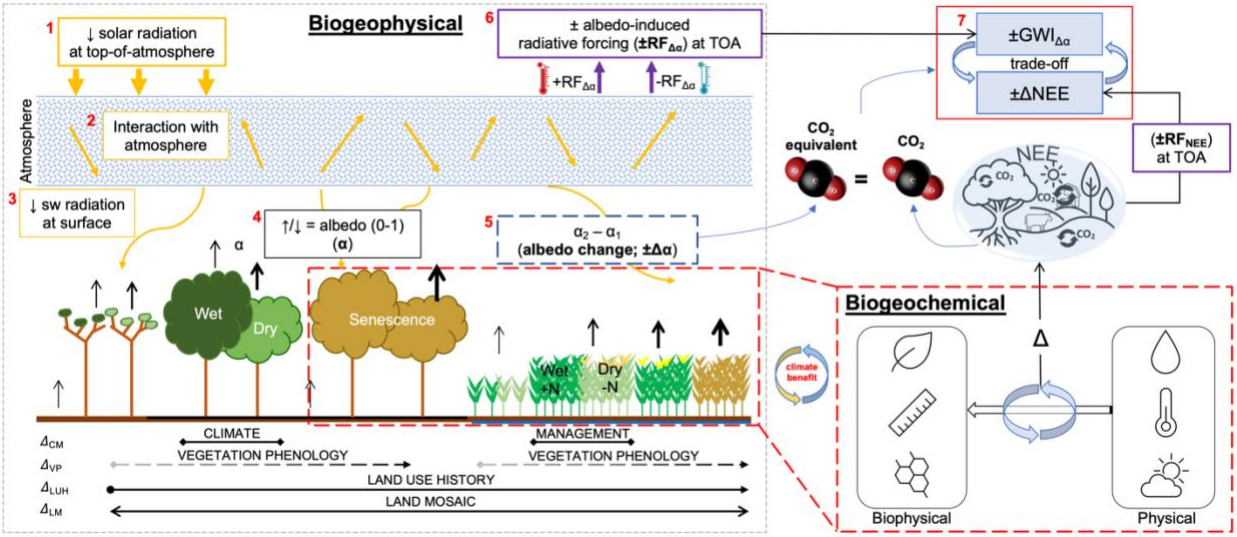

Figure 1.1: Conceptual framework showing the (a) biogeophysical (i.e., surface albedo; α) and (b) biogeochemical (i.e., net ecosystem exchange fluxes; NEE) mechanisms involved in the climate benefit potentials at landscape (a) and parcel (b) levels, within the Kalamazoo River Watershed, southwestern Michigan, USA. Regarding (a), the main hypothesis is that spatiotemporal variations of climate and management (Δ_{CM}; e.g., wetter *vs* drier, fertilization *vs* non-fertilization, etc.), vegetation phenology (Δ_{VP}; e.g., leaf development, inflorescence, etc.), land use history (Δ_{LUH}; e.g., change of cover type), and land mosaic (Δ_{LM}; coexistence of multiple land cover types within the same spatial extent) strongly affect α. Regarding (b), the main hypothesis is that a variety of key influences (e.g., leaf area index, vegetation height, leaf chlorophyll content, soil water content, precipitation, air temperature, etc.) affect the interannual variation NEE fluxes, with regard of cover type considered.

The biogeophysical mechanisms refer to surface energy fluxes, with particular interest in albedo climate benefit potentials, that I defined here as the albedo-induced forcing (warming/cooling) on climate due to LULCC, land mosaic, and weather conditions. The latter mechanisms refer to the C cycle, with particular interest in NEE fluxes climate benefit potentials due to land use history/management and biophysical and physical key influences.

Biogeophysical mechanisms

Even though biogeochemical mechanisms represented the main concern for the climate change mitigation options, recent IPCC reports have shown that biogeophysical mechanisms also play an important role in the climate regulation context (Masson-Delmotte, 2021). There is then the need to review climatic policies (McAlpine et al., 2010). In fact, for years now the main focus of global warming research has been the capability of natural ecosystems to sequester CO_2 from the atmosphere (i.e., carbon-centric view) without considering the effects of LULCC on energy fluxes, water cycle, and atmospheric composition (Zhao & Jackson, 2014). Human activities, worldwide, have strongly reshaped the landscapes over the past 2-3 thousand years, at an escalating rate since the industrial revolution (Forster et al., 2021; Pielke et al., 2011). In turn, Earth's surface reflectivity properties have changed accordingly, resulting in alterations of the Earth's radiation balance, partially responsible for the change in climate. At that purpose, an important physical property by which LULCC can regulate the local climate is surface albedo, which can be either expressed with no units (i.e., 0–1) or as percentage (i.e., 0–100%). Globally, deforestation, agricultural development—including forest and grassland conversion—and urban expansion have been shown to be major sources of albedo change (Pielke et al., 2011; Shao et al., 2014), which in turn can directly affect the Earth's radiation budget. For instance, the albedo of forests is lower (i.e., darker; less incoming shortwave solar radiation is scattered back to space) than that of croplands (i.e., lighter; more incoming shortwave solar radiation is scattered back to space), and so, forests have warming effects because of the higher absorbed solar radiation (Bonan, 2008). In turn, various examples of climate benefit potentials of surface albedo due to changes in LULCC can be found in the literature (Akbari et al., 2009; Carrer et al., 2018; Houspanossian et al., 2017; Lugato et al., 2020; Ouyang et al., 2022). More drastic proposals that aim to alter

planetary albedo (e.g., land and marine clouds albedo, surface albedo, etc.) can be found in the literature (Lenton & Vaughan, 2009), however such proposals are still theory/model-based and difficult to apply to real world's cases—with few exceptions, such as those proposing the use of white roofs/roads as heat mitigation strategy (Akbari et al., 2009; Jandaghian & Akbari, 2018; Wang et al., 2020)—not only because of the lack of needed technology, but also due to the general concern of irreversible changes to ecosystems such proposals might cause (National Academies of Sciences, Engineering, and Medicine, 2021; Zarnetske et al., 2021).

Biogeochemical mechanisms

Understanding the NEE fluxes between terrestrial and aquatic ecosystems and atmosphere is fundamental to investigate many ecological processes. Such processes govern ecosystems and play a primary role in the context of global climate change (Campioli et al., 2016; Peters et al., 2007). Previous studies highlighted that the biogeochemical mechanisms are driven by both anthropogenic activities (i.e., such as burning fossil fuel and LULCC) and by the capacity of terrestrial and aquatic ecosystems to uptake CO_2 from the atmosphere (Hong et al., 2021). For example, clearing forests and natural grasslands for crops and grazing, and vice versa, has been widely investigated, and still, represents the main driver of climate change forcing for both local and global climate scales (Mahmood et al., 2014). In response, previous studies have emphasized the role of afforestation and forest management to offset anthropogenic CO_2 emissions, and they have been recognized as necessary measures to mitigate climate change (Naudts et al., 2016). For example, it has been demonstrated that U.S. regions dominated by evergreen and deciduous forests can uptake up to 0.63 PgC yr^{-1}, and that terrestrial ecosystems can offset up to 40% of the CO_2 emissions (Xiao et al., 2011). Moreover, in terms of forest management, Cannell (2003) showed that growing biomass for energy has the same C offset benefits of growing it for sequestration

purposes. Nevertheless, today's agricultural cropping systems represent a conspicuous percentage of worldwide LULC (FAO, 2007; Smith et al., 2007) and for decades now they have been investigated to provide better scientific understanding of how ecosystems function and what services (i.e., ecosystem services) they provide or hinder (Bommarco et al., 2018), especially in the context of adaptations and mitigations strategies (Barrios et al., 2018). Among the various adaptation and mitigation strategies, one of the more studied deals with well-mixed GHGs emissions of a system, with particular focus on CO_2 emissions. Hence, assessing whether a system behaves as sink or source of C, is of fundamental importance global warming research studies and for policy makers. The IPCC reports that, globally, in 2019, agricultural activities were responsible for emissions equivalent to 13 $GtCO_2$ (aka ~22% of the net anthropogenic GHG emissions; Allan et al., 2022). The sink/source nature of agricultural cropping systems is function of vegetation-related key influences (e.g., physical, biophysical, and phenological) as well as external factors such as land management, land use history, and weather conditions. Hence, there are multiple considerations behind the development of climate policies and mitigation strategies.

Aligning with IPCC standards

To be quantitatively comparable, both mechanisms are studied in terms of the amount of energy imbalance that they can cause in the Earth's climate system. Such imbalance is referred in terms radiative forcing (RF; W m^{-2})—the change in the net radiative flux at the top-of-atmosphere (TOA) due to the change in atmospheric CO_2 concentration—which can be positive or negative, representing the warming or cooling effects of a given GHG, respectively. For example, the increased atmospheric concentration of CO_2 (i.e., up to 410 pmol mol^{-1}), due to anthropogenic emissions in 2019, have had warming effects equivalent to +2.16±0.26 W m^{-2}, with respect to pre-industrial conditions (Forster et al., 2021). Moreover, given the need of comparison between

relative and absolute contributions of different GHGs to climate change, the IPCC has introduced the global warming impact (GWI) pulse emission metric—also referred by the literature to as global warming potential (GWP)—that allows the calculation of the forcing of anthropogenic activities on climate by taking the climate forcing of CO_2 gas as the baseline. In other words, the GWI is expressed in terms forcing effects equivalent to emission (positive GWI) or mitigation (negative GWI) of CO_2 per unit area and per unit of time (i.e., $\pm kgCO_{2eq}\ m^{-2}\ yr^{-1}$). At the same way, the climate benefit potentials of albedo changes are expressed as both albedo-induced RF ($RF_{\Delta\alpha}$) and GWI ($GWI_{\Delta\alpha}$) by applying simple changes to the original RF and GWI equations (Bright & Lund, 2021; Chen et al., 2021). In this way, one can easily report the energy balance induced by albedo in terms of its warming/cooling and emissions/mitigations of CO_{2eq}, respectively. For example, Houspanossian et al. (2017) found that conversion from forests to croplands, forests to pastures, and pastures to croplands in dry subtropical forests of South America offset 12–27 $MgC_{eq}\ ha^{-1}$ during a 12-year period, or 15% to 55% of the total C emissions due to deforestation. Carrer et al. (2018) estimated that variation of albedo of 0.0025 (e.g., 0.25% of solar radiation reflected by Earth's surface) due to the introduction of cover crops in European agricultural systems, can be equivalent to a $RF_{\Delta\alpha}$ of -0.15 W m^{-2} (i.e., cooling effect), and to a $GWI_{\Delta\alpha}$ of -3.16 $MtCO_2$-eq. m^{-2} (i.e., effect equivalent to C mitigation); while Lugato et al. (2020) showed that such mitigation potential due to the inclusion of cover crops could be substantially enhanced by growing high-albedo chlorophyll-deficient cover crops. Furthermore, in urban settings, Akbari et al. (2009), studied that increasing urban albedo by about 0.15–0.25 (i.e., 15–25% of solar radiation reflected by the Earth's surface) can reduce summertime temperatures and associated air-conditioning costs, allowing to save about $1,100 billion. On the other hand,

Ouyang et al. (2022) found that the decrease in albedo due to global urbanization over a 17-year period, resulted in a 100-year average annual albedo-induced global warming of 0.00014 °C.

Dissertation Focus and Organization

The overarching goal of this work is to address questions related the climate benefit potentials (i.e., warming or cooling effects) of biogeophysical (albedo) and biogeochemical (NEE) mechanisms. Chapters 2 through 4 are complementary studies, each of them with unique but interrelated research objectives and hypothesis, as well as study area and methodology.

To achieve this goal, I selected the Kalamazoo River Watershed as overall study area for my investigations (Figure 1.2).

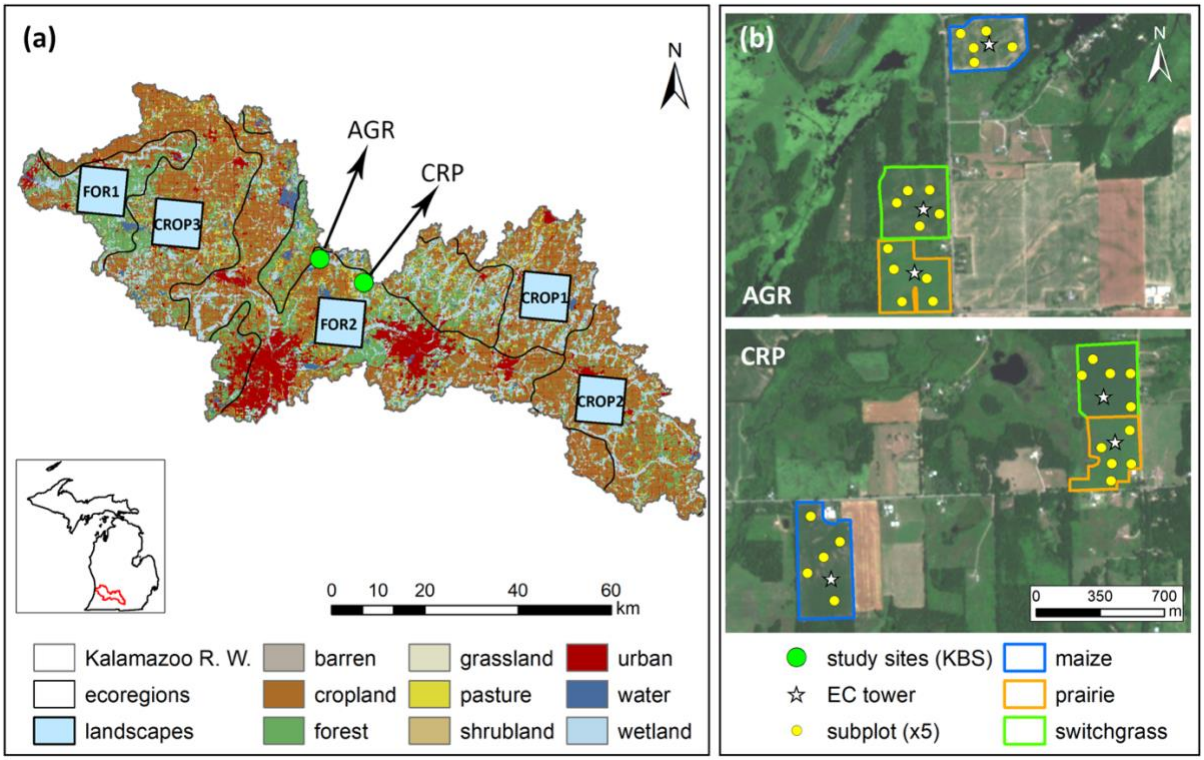

Figure 1.2: The locations of the study areas considered for the chapters 2, 3, and 4. (a) Equal area forest-dominated (FOR_1 and FOR_2) and cropland-dominated ($CROP_1$, $CROP_2$ and $CROP_3$) landscapes within the five United States Environmental Protection Agency (US EPA) Level IV ecoregions (Chapter 2) and the nine National Land Cover Database (NLCD) cover type classes at the five Level IV ecoregions within the Kalamazoo River Watershed (Chapter 3). (b) Agriculturally cultivated (AGR; upper right) and Conservation Reserve Program (CRP; bottom right) sites within the Kellogg Biological Station (KBS), with corresponding Eddy Covariance (EC) flux towers and ground sampling sublots (Chapter 4). Cover types at the KBS sites are continuous maize (*Zea mays*), restored native prairie, and switchgrass (*Panicum virgatum*). NLCD cover type classes (on 2016) and the true color from imagery (accessed on 07-14-2019, summer season) were used for (a) and (b) base-maps, respectively.

The Kalamazoo River Watershed (5621 km^2; Figure 2) is located in southwestern Michigan, USA. It includes portions of 10 counties: Allegan, Barry, Calhoun, Eaton, Hillsdale, Jackson, Kalamazoo, Kent, Ottawa, and Van Buren. Mean annual temperature (1981–2010) is 9.9 °C and average annual precipitation is 900 mm evenly distributed throughout the year (Michigan State Climatologist's Office, 2013). The dominant cover type prior to European settlement in the early 1800s was eastern deciduous forest (Brown et al., 2000), with scattered patches of tallgrass prairie, oak savanna, lakes, and wetlands (Chapman & Brewer, 2008). Today, the dominant land

covers include cultivated crops, successional forest stands, pasture-hay grasslands, and two urban areas (Kalamazoo and Battle Creek). Medium to coarse texture soils and mesic climate allow continuous recharge of groundwater (Schaetzl et al., 2009). Within the watershed, there are several Long-Term Ecological Research (LTER) sites, part of the Great Lakes Bioenergy Research Center (GLBRC) of the Kellogg Biological Station (KBS). Different portions of the watershed were considered as focal areas of each Chapter.

In Chapter 2, the underlying objective was to examine the spatiotemporal variation in surface albedo ($\Delta\alpha$) in contrasting managed agricultural landscapes through the calculation of albedo-induced radiative forcing ($RF_{\Delta\alpha}$) and global warming impact ($GWI_{\Delta\alpha}$), under different precipitation regimes in a 3-year analysis and across equal area heterogeneous landscapes within the Kalamazoo River Watershed. The portion of Kalamazoo River Watershed considered as study area for this Chapter is based within an ecological-based frame system by considering five contrasting ecoregions (Figure 1.2a), which are defined as areas characterized by unique combinations of physiographic, geologic, pedologic, botanic, hydrologic, and climatic characteristics (Omernik & Griffith, 2014). Within the Kalamazoo River Watershed there are five United States Environmental Protection Agency (US EPA) Level IV ecoregions: Battle Creek Outwash Plain; Michigan Lake Plain; Lake Michigan Moraines; Lansing Loamy Plain; and Interlobate Dead Ice Moraines. Within each of the five ecoregions, I selected five equal area (100 km^2) landscapes for proof of concept of my investigations. I hypothesized that both land mosaic and precipitation regimes (i.e., drier *vs* wetter *vs* normal precipitation events) affect the $\Delta\alpha$, $RF_{\Delta\alpha}$, and $GWI_{\Delta\alpha}$ at landscape scale. Depending on the precipitation regime and the landscape composition (i.e., cropland- *vs* forest-dominated landscapes), I expected the five landscapes being characterized by different magnitudes of climate benefit potentials (i.e., warming/cooling and

emission/mitigation equivalent to CO_2) due to Δα. The framework proposed expresses the relationship between Δα and $RF_{\Delta\alpha}$ and $GWI_{\Delta\alpha}$ as follows (Sciusco et al., 2020):

$$[\Delta\alpha_c \times \Delta lm_l \times \Delta w_l] \rightarrow \Delta RF_{\Delta\alpha} \rightarrow \Delta GWI_{\Delta\alpha} \quad (1.1)$$

where $\Delta\alpha_c$ is the surface albedo change at cover type c, Δlm_l is the variation of land mosaic (i.e., forest- *vs* cropland-dominated) for landscape l, Δw_l is the variation of weather conditions (i.e., precipitation regime) for landscape l, $\Delta RF_{\Delta\alpha}$ and $\Delta GWI_{\Delta\alpha}$ are the net landscape albedo-induced radiative forcing and global warming impact, respectively. The reason behind the proposed framework at Eq. 1.1 comes from the fact that, according to previous works, although land surface albedo is significantly affected by LULCC (Bala et al., 2007; Cai et al., 2016), the magnitude of spatiotemporal changes of albedo (and thus $RF_{\Delta\alpha}$ and $GWI_{\Delta\alpha}$) depend on a range of physical and biophysical characteristics such as vegetation type and canopy structure (Bennett et al., 2006; Tian et al., 2018), soil water content and leaf wetness (Wang et al., 2004)—which on their turn, are driven by spatiotemporal distributions of precipitation—plant phenology (Homer et al., 2020), and agricultural practices (Houspanossian et al., 2017). Primary data for Chapter 2 are albedo and land cover classification. In particular, surface albedo data were acquired from the most recent MCD43A3 (V006) MODIS Bidirectional Reflectance Distribution Function (BRDF) product (cf. https://doi.org/10.5067/MODIS/MCD43A3.006), which includes parameters for the computation of both black- and white-sky albedo at 500 m spatial resolution, as a daily product obtained by a 16-day composite centered on the given day. Regarding the land cover classification, it was obtained for the year 2011 from a supervised classification, following the Anderson level I classification scheme that includes seven land cover types (urban, croplands, barrens, forest, water, wetlands, and grasslands) and constructed using the Landsat archives at 30 m spatial resolution obtained from the United States Geological Survey (USGS) Earth Explorer and Global

Visualization Viewer (GloVis) portals. Additionally, secondary data employed are the Level IV ecoregions layer, daily precipitation, normalized difference vegetation index (NDVI), and incident shortwave radiation at the surface (SW_{in}; W m^{-2}). More details are provided in the *Material and Methods* section at Chapter 2.

In Chapter 3, I considered the following three objectives: (i) to quantify the contributions from different seasons and months to the annual total cooling or warming effects by cover type and ecoregion; (ii) to quantify the variations of $GWI_{\Delta\alpha}$ contributions by cover type, ecoregion, and year; and (iii) to estimate the magnitude of cooling or warming effects due to land cover change relative to mature forest cover, the original land cover in all ecoregions. The portion of Kalamazoo River Watershed considered as study area for this Chapter 3 is extended to the entire Watershed (Figure 1.2a), still considering the subdivision provided by the five Level IV ecoregions. The main underlying hypothesis is that the seasonal and monthly variations in surface albedo (i.e., growing season *vs* non-growing season surface albedos) show different contributions (i.e., warming *vs* cooling *vs* neutral) and magnitudes to the total $GWI_{\Delta\alpha}$ across the five ecoregions and the major cover types considered. Overall, I expected the non-growing season months to contribute more than the growing season ones in terms of cooling effects and mitigation equivalent to CO_2, due to the presence of snow. For example, the late planting of dominating croplands (i.e., maize) within the watershed leaves bare soils during the non-growing season months and during the first part of the growing-season months when snowfall occurs, resulting in higher albedo of cropland than forest. As in Chapter 2, primary data for Chapter 3 are the surface albedo (obtained from the MCD43A3 (V006) MODIS BRDF product) over a 19-year period (i.e., 2001–2019) and at both seasonal and monthly (growing season *vs* non-growing season) time steps and the land cover classification, obtained from the National Land Cover Database (NLCD) (cf.

https://www.usgs.gov/centers/eros/science/national-land-cover-database?qt-science_center_objects=0#qt-science_center_objects; Homer et al., 2020) which provides twenty land cover classes—consequently grouped into nine classes: barren, cropland, forest, grassland, pasture, shrubland, urban, water, and wetland—at 30 m spatial resolution and it is available for the years 2001, 2004, 2006, 2008, 2011, 2013, and 2016. Secondary data are the five Level IV ecoregions layers and the enhanced vegetation index (EVI) remote sensing data. More details are provided in the *Material and Methods* section at Chapter 3.

In Chapter 4, I considered two main objectives: (i) to investigate the main key influences (e.g., soil water content, air temperature, leaf area index, vegetation height, etc.) to the interannual variations of net ecosystem exchange (NEE) fluxes, drawing inferences on net growing season climate regulations due to crop type, land use history and management; and (ii) to use multi-sensor remote sensing approach to forecast one year of growing season NEE at continuous maize bioenergy crop. The study area considered for Chapter 4 are two groups of pre-existing LTER sites at KBS: the agriculturally cultivated (AGR) and Conservation Reserve Program (CRP) sites (Figure 1.2b). The main difference between AGR and CRP sites is that AGR ones have been managed for more than 50 years as conventionally tilled maize-soybean rotations whereas, the CRP sites have been managed as grasslands for 22 years. Although, in 2009, all the sites were converted first to no-till soybean (*Glycine max L.*), and then in 2010, they were converted into no-till continuous maize systems and perennial croplands such as restored native prairie, and switchgrass with bioenergy purposes (Abraha et al., 2019). Each site is equipped with an Eddy Covariance (EC) flux tower. The underlying hypothesis is that main key influences to the net climate benefit potentials of bioenergy crops depend on the crop considered (e.g., annual *vs* perennial; monoculture *vs* polyculture) as well as on the land use history and land

management. Among the data employed in this Chapter, the AGR and CRP sites are equipped with EC flux towers that take continuous instantaneous measurements of NEE fluxes and other ancillary biometric data (i.e., air and soil temperature, photosynthetically active radiation, etc.). In addition, other *in-situ* measurements are considered, as result of four years (2018–2021) summer fieldwork campaigns conducted roughly during May–August. In particular, the measurements collected during the summer fieldwork campaigns include leaf area index (LAI, m^2 m^{-2}), Soil and Plant Analysis Development index (SPAD index, which is a leaf-level index of leaf chlorophyll content; Hlavinka et al., 2013), vegetation height (Ht, m), and soil water content (SWC, %) within the first 10 cm of soil. These field measurements were collected at subplot level (five subplots at each site; Figure 1.2b) at a time step of ~14 days. Regarding the fine-resolution remote sensing imagery, I employed Sentinel-2 (i.e., optical) and Sentinel-1 (i.e., radar) at 20 m spatial resolution. The images were downloaded from the European Space Agency (ESA) online catalog Copernicus Open Access Hub (cf. https://scihub.copernicus.eu/dhus/#/home). Further details are provided in the *Material and Methods* section at Chapter 4.

REFERENCES

Abraha, M., Chen, J., Hamilton, S. K., Sciusco, P., Lei, C., Shirkey, G., Yuan, J., & Robertson, G. P. (2021). Albedo-induced global warming impact of Conservation Reserve Program grasslands converted to annual and perennial bioenergy crops. *Environmental Research Letters*, *16*(8), 084059. https://doi.org/10.1088/1748-9326/ac1815

Abraha, M., Gelfand, I., Hamilton, S. K., Chen, J., & Robertson, G. P. (2019). Carbon debt of field-scale conservation reserve program grasslands converted to annual and perennial bioenergy crops. *Environmental Research Letters*, *14*(2), 024019. https://doi.org/10.1088/1748-9326/aafc10

Akbari, H., Menon, S., & Rosenfeld, A. (2009). Global cooling: Increasing world-wide urban albedos to offset CO_2. *Climatic Change*, *94*(3–4), 275–286. https://doi.org/10.1007/s10584-008-9515-9

Allan, R. P., Cassou, C., Chen, D., Cherchi, A., Connors, L., Doblas-Reyes, F. J., Douville, H., Driouech, F., Edwards, T. L., Fischer, E., Flato, G. M., Forster, P., AchutaRao, K. M., Adhikary, B., Aldrian, E., & Armour, K. (2022). IPCC, 2021: Summary for Policymakers. In *Climate Change 2021: The Physical Science Basis. Contribution of Working Group I to the Sixth Assessment Report of the Intergovernmental Panel on Climate Change* (p. 3−32). Cambridge University Press, Cambridge, United Kingdom and New York, NY, USA.

Bala, G., Caldeira, K., Wickett, M., Phillips, T. J., Lobell, D. B., Delire, C., & Mirin, A. (2007). Combined climate and carbon-cycle effects of large-scale deforestation. *Proceedings of the National Academy of Sciences*, *104*(16), 6550–6555. https://doi.org/10.1073/pnas.0608998104

Baldocchi, D. D., Wilson, K. B., & Gu, L. (2002). How the environment, canopy structure and canopy physiological functioning influence carbon, water and energy fluxes of a temperate broad-leaved deciduous forest—An assessment with the biophysical model CANOAK. *Tree Physiology*, *22*(15–16), 1065–1077. https://doi.org/10.1093/treephys/22.15-16.1065

Barrios, E., Valencia, V., Jonsson, M., Brauman, A., Hairiah, K., Mortimer, P. E., & Okubo, S. (2018). Contribution of trees to the conservation of biodiversity and ecosystem services in agricultural landscapes. *International Journal of Biodiversity Science, Ecosystem Services & Management*, *14*(1), 1–16. https://doi.org/10.1080/21513732.2017.1399167

Bennett, A. F., Radford, J. Q., & Haslem, A. (2006). Properties of land mosaics: Implications for nature conservation in agricultural environments. *Biological Conservation*, *133*(2), 250–264. https://doi.org/10.1016/j.biocon.2006.06.008

Bommarco, R., Vico, G., & Hallin, S. (2018). Exploiting ecosystem services in agriculture for increased food security. *Global Food Security*, *17*, 57–63. https://doi.org/10.1016/j.gfs.2018.04.001

Bonan, G. B. (2008). Forests and climate change: Forcings, feedbacks, and the climate benefits of forests. *Science*, *320*(5882), 1444–1449. https://doi.org/10.1126/science.1155121

Bright, R. M., & Lund, M. T. (2021). CO_2-equivalence metrics for surface albedo change based on the radiative forcing concept: A critical review. *Atmospheric Chemistry and Physics*, *21*(12), 9887–9907. https://doi.org/10.5194/acp-21-9887-2021

Brovkin, V., Sitch, S., Von Bloh, W., Claussen, M., Bauer, E., & Cramer, W. (2004). Role of land cover changes for atmospheric CO_2 increase and climate change during the last 150 years. *Global Change Biology*, *10*(8), 1253–1266. https://doi.org/10.1111/j.1365-2486.2004.00812.x

Brown, D. G., Pijanowski, B. C., & Duh, J. D. (2000). Modeling the relationships between land use and land cover on private lands in the Upper Midwest, USA. *Journal of Environmental Management*, *59*(4), 247–263. https://doi.org/10.1006/jema.2000.0369

Cai, H., Wang, J., Feng, Y., Wang, M., Qin, Z., & B. Dunn, J. (2016). Consideration of land use change-induced surface albedo effects in life-cycle analysis of biofuels. *Energy & Environmental Science*, *9*(9), 2855–2867. https://doi.org/10.1039/C6EE01728B

Campioli, M., Malhi, Y., Vicca, S., Luyssaert, S., Papale, D., Peñuelas, J., Reichstein, M., Migliavacca, M., Arain, M. A., & Janssens, I. A. (2016). Evaluating the convergence between eddy-covariance and biometric methods for assessing carbon budgets of forests. *Nature Communications*, *7*(1), Article 1. https://doi.org/10.1038/ncomms13717

Cannell, M. G. R. (2003). Carbon sequestration and biomass energy offset: Theoretical, potential and achievable capacities globally, in Europe and the UK. *Biomass and Bioenergy*, *24*(2), 97–116. https://doi.org/10.1016/S0961-9534(02)00103-4

Carrer, D., Pique, G., Ferlicoq, M., Ceamanos, X., & Ceschia, E. (2018). What is the potential of cropland albedo management in the fight against global warming? A case study based on the use of cover crops. *Environmental Research Letters*, *13*(4), 044030. https://doi.org/10.1088/1748-9326/aab650

Chapman, K. A., & Brewer, R. (2008). Prairie and savanna in southern lower Michigan: History, Classification, ecology. Michigan Botanic Club, 47, 48

Chen, J., Brosofske, K. D., Noormets, A., Crow, T. R., Bresee, M. K., Le Moine, J. M., Euskirchen, E. S., Mather, S. V., & Zheng, D. (2004). A working framework for quantifying carbon sequestration in disturbed land mosaics. *Environmental Management*, *33*(1), S210–S221. https://doi.org/10.1007/s00267-003-9131-4

Chen, J., Lei, C., & Sciusco, P. (2021). Modeling ecosystem global warming potentials. In *Biophysical Models and Applications in Ecosystem Analysis* (pp. 119–150). Michigan State University Press; JSTOR. https://doi.org/10.14321/j.ctv1h1vc27.11

Euskirchen, E. S., Chen, J., Li, H., Gustafson, E. J., & Crow, T. R. (2002). Modeling landscape net ecosystem productivity (LandNEP) under alternative management regimes. *Ecological Modelling*, *154*(1), 75–91. https://doi.org/10.1016/S0304-3800(02)00052-2

FAO. (2007). *Paying Farmers for Environmental Services*. FAO, 222.

Forster, P., T. Storelvmo, K. Armour, W. Collins, J.-L. Dufresne, D. Frame, D.J. Lunt, T. Mauritsen, M.D. Palmer, & M. Watanabe, M. Wild, and H. Zhang. (2021). The Earth's energy budget, climate feedbacks and climate sensitivity. In *Climate Change 2021: The Physical Science Basis. Contribution of Working Group I to the Sixth Assessment Report of the Intergovernmental Panel on Climate Change* (pp. 923–1054). Cambridge University Press, Cambridge, United Kingdom and New York, NY, USA.

Gellie, N. J., Breed, M. F., Mortimer, P. E., Harrison, R. D., Xu, J., & Lowe, A. J. (2018). Networked and embedded scientific experiments will improve restoration outcomes. *Frontiers in Ecology and the Environment*, *16*(5), 288–294. https://doi.org/10.1002/fee.1810

Gotangco Castillo, C. K., Raymond, L., & Gurney, K. R. (2012). REDD+ and climate: Thinking beyond carbon. *Carbon Management*, *3*(5), 457–466. https://doi.org/10.4155/cmt.12.54

Hlavinka, J., Nauš, J., & Špundová, M. (2013). Anthocyanin contribution to chlorophyll meter readings and its correction. *Photosynthesis Research*, *118*(3), 277–295. https://doi.org/10.1007/s11120-013-9934-y

Hoegh-Guldberg, O., Jacob, D., Taylor, M., Guillén Bolaños, T., Bindi, M., Brown, S., Camilloni, I. A., Diedhiou, A., Djalante, R., Ebi, K., Engelbrecht, F., Guiot, J., Hijioka, Y., Mehrotra, S., Hope, C. W., Payne, A. J., Pörtner, H.-O., Seneviratne, S. I., Thomas, A., … Zhou, G. (2019). The human imperative of stabilizing global climate change at 1.5°C. *Science*, *365*(6459), eaaw6974. https://doi.org/10.1126/science.aaw6974

Homer, C., Dewitz, J., Jin, S., Xian, G., Costello, C., Danielson, P., Gass, L., Funk, M., Wickham, J., Stehman, S., Auch, R., & Riitters, K. (2020). Conterminous United States land cover change patterns 2001–2016 from the 2016 National Land Cover Database. *ISPRS Journal of Photogrammetry and Remote Sensing*, *162*, 184–199. https://doi.org/10.1016/j.isprsjprs.2020.02.019

Hong, C., Burney, J. A., Pongratz, J., Nabel, J. E. M. S., Mueller, N. D., Jackson, R. B., & Davis, S. J. (2021). Global and regional drivers of land-use emissions in 1961–2017. *Nature*, *589*(7843), Article 7843. https://doi.org/10.1038/s41586-020-03138-y

Houspanossian, J., Giménez, R., Jobbágy, E., & Nosetto, M. (2017). Surface albedo raise in the South American Chaco: Combined effects of deforestation and agricultural changes. *Agricultural and Forest Meteorology*, *232*, 118–127. https://doi.org/10.1016/j.agrformet.2016.08.015

Jandaghian, Z., & Akbari, H. (2018). The effect of increasing surface albedo on urban climate and air quality: A detailed study for Sacramento, Houston, and Chicago. *Climate*, *6*(2), Article 2. https://doi.org/10.3390/cli6020019

Kvalevåg, M. M., Myhre, G., Bonan, G., & Levis, S. (2010). Anthropogenic land cover changes in a GCM with surface albedo changes based on MODIS data. *International Journal of Climatology*, *30*(13), 2105–2117. https://doi.org/10.1002/joc.2012

Lenton, T. M., & Vaughan, N. E. (2009). The radiative forcing potential of different climate geoengineering options. *Atmos. Chem. Phys.*, 23.

Lugato, E., Cescatti, A., Jones, A., Ceccherini, G., & Duveiller, G. (2020). Maximising climate mitigation potential by carbon and radiative agricultural land management with cover crops. *Environmental Research Letters*, *15*(9), 094075. https://doi.org/10.1088/1748-9326/aba137

Mahmood, R., Pielke, R. A., Hubbard, K. G., Niyogi, D., Dirmeyer, P. A., McAlpine, C., Carleton, A. M., Hale, R., Gameda, S., Beltrán-Przekurat, A., Baker, B., McNider, R., Legates, D. R., Shepherd, M., Du, J., Blanken, P. D., Frauenfeld, O. W., Nair, U. S., & Fall, S. (2014). Land cover changes and their biogeophysical effects on climate. *International Journal of Climatology*, *34*(4), 929–953. https://doi.org/10.1002/joc.3736

Masson-Delmotte, V., P. Zhai, A. Pirani, S.L. Connors, C. Péan, S. Berger, N. Caud, Y. Chen, L. Goldfarb, M.I. Gomis, M. Huang, K. Leitzell, E. Lonnoy, J.B.R. & Matthews, T.K. Maycock, T. Waterfield, O. Yelekçi, R. Yu, and B. Zhou (eds.). (2021). *IPCC, 2021: Climate Change 2021: The Physical Science Basis. Contribution of Working Group I to the Sixth Assessment Report of the Intergovernmental Panel on Climate Change*. Cambridge University Press, Cambridge, United Kingdom and New York, NY, USA. doi:10.1017/9781009157896

Matos, F. A. R., Magnago, L. F. S., Aquila Chan Miranda, C., de Menezes, L. F. T., Gastauer, M., Safar, N. V. H., Schaefer, C. E. G. R., da Silva, M. P., Simonelli, M., Edwards, F. A., Martins, S. V., Meira-Neto, J. A. A., & Edwards, D. P. (2020). Secondary forest fragments offer important carbon and biodiversity cobenefits. *Global Change Biology*, *26*(2), 509–522. https://doi.org/10.1111/gcb.14824

Matthews, H. D., Weaver, A. J., Meissner, K. J., Gillett, N. P., & Eby, M. (2004). Natural and anthropogenic climate change: Incorporating historical land cover change, vegetation dynamics and the global carbon cycle. *Climate Dynamics*, *22*(5), 461–479. https://doi.org/10.1007/s00382-004-0392-2

McAlpine, C., Ryan, J., Seabrook, L., Thomas, S., Dargusch, P., Syktus, J., Pielke, R., Etter, A., Fearnside, P., & Laurance, W. (2010). More than CO2: A broader paradigm for managing climate change and variability to avoid ecosystem collapse. *Current Opinion in Environmental Sustainability*, *2*(5–6), 334–346. https://doi.org/10.1016/j.cosust.2010.10.001

Michigan State Climatologist's Office. (2013). *Gull Lake (3504). Michigan State University*. Retrived from http://climate. geo.msu.edu/climate_mi/stations/3504/

Myhre, G., Shindell, D., & Pongratz, J. (2014). Anthropogenic and natural radiative forcing. In *Climate change 2013: The physical science basis; Working Group I contribution to the fifth assessment report of the Intergovernmental Panel on Climate Change*, T. Stocker (Ed.), (pp. 659–740). Ludwig-Maximilians-Universität München. https://doi.org/10.1017/CBO9781107415324.018

National Academies of Sciences, Engineering, and Medicine. (2021). *Reflecting Sunlight: Recommendations for Solar Geoengineering Research and Research Governance* (p. 25762). Washington D.C., The National Academies Press. https://doi.org/10.17226/25762

National Research Council (2010). *Understanding the Changing Planet: Strategic Directions for the Geographical Sciences*. Washington D.C., The National Academies Press. https://doi.org/10.17226/12860

National Research Council (2015). *Climate Intervention: Reflecting Sunlight to Cool Earth*. Washington D.C., The National Academies Press. https://doi.org/10.17226/18988

Naudts, K., Chen, Y., McGrath, M. J., Ryder, J., Valade, A., Otto, J., & Luyssaert, S. (2016). Europe's forest management did not mitigate climate warming. *Science*, *351*(6273), 597–600. https://doi.org/10.1126/science.aad7270

Omernik, J. M., & Griffith, G. E. (2014). Ecoregions of the conterminous United States: Evolution of a hierarchical spatial framework. *Environmental Management*, *54*(6), 1249–1266. https://doi.org/10.1007/s00267-014-0364-1

Ouyang, Z., Sciusco, P., Jiao, T., Feron, S., Lei, C., Li, F., John, R., Fan, P., Li, X., Williams, C. A., Chen, G., Wang, C., & Chen, J. (2022). Albedo changes caused by future urbanization contribute to global warming. *Nature Communications*, *13*(1), 3800. https://doi.org/10.1038/s41467-022-31558-z

Peters, W., Jacobson, A. R., Sweeney, C., Andrews, A. E., Conway, T. J., Masarie, K., Miller, J. B., Bruhwiler, L. M. P., Petron, G., Hirsch, A. I., Worthy, D. E. J., van der Werf, G. R., Randerson, J. T., Wennberg, P. O., Krol, M. C., & Tans, P. P. (2007). An atmospheric perspective on North American carbon dioxide exchange: CarbonTracker. *Proceedings of the National Academy of Sciences*, *104*(48), 18925–18930. https://doi.org/10.1073/pnas.0708986104

Pielke, R. A., Pitman, A., Niyogi, D., Mahmood, R., McAlpine, C., Hossain, F., Goldewijk, K. K., Nair, U., Betts, R., Fall, S., Reichstein, M., Kabat, P., & Noblet, N. de. (2011). Land use/land cover changes and climate: Modeling analysis and observational evidence. *Wiley Interdisciplinary Reviews: Climate Change*, *2*(6), 828–850. https://doi.org/10.1002/wcc.144

Schaetzl, R. J., Darden, J. T., & Brandt, D. S. (2009). *Michigan Geography and Geology*. Pearson Custom Publishing. http://catalog.hathitrust.org/api/volumes/oclc/309340740.html

Sciusco, P., Chen, J., Abraha, M., Lei, C., Robertson, G. P., Lafortezza, R., Shirkey, G., Ouyang, Z., Zhang, R., & John, R. (2020). Spatiotemporal variations of albedo in managed agricultural landscapes: Inferences to global warming impacts (GWI). *Landscape Ecology*, *35*(6), 1385–1402. https://doi.org/10.1007/s10980-020-01022-8

Sciusco, P., Chen, J., Giannico, V., Abraha, M., Lei, C., Shirkey, G., Yuan, J., & Robertson, G. P. (2022). Albedo-induced global warming impact at multiple temporal scales within an upper Midwest USA watershed. *Land*, *11*(2), 283. https://doi.org/10.3390/land11020283

Shao, C., Li, L., Dong, G., & Chen, J. (2014). Spatial variation of net radiation and its contribution to energy balance closures in grassland ecosystems. *Ecological Processes*, *3*(1), 7. https://doi.org/10.1186/2192-1709-3-7

Shao, J., Zhou, X., Luo, Y., Li, B., Aurela, M., Billesbach, D., Blanken, P. D., Bracho, R., Chen, J., Fischer, M., Fu, Y., Gu, L., Han, S., He, Y., Kolb, T., Li, Y., Nagy, Z., Niu, S., Oechel, W. C., … Zhang, J. (2016). Direct and indirect effects of climatic variations on the interannual variability in net ecosystem exchange across terrestrial ecosystems. *Tellus B: Chemical and Physical Meteorology*, *68*(1), 30575. https://doi.org/10.3402/tellusb.v68.30575

Smith, P., Martino, D., Cai, Z., O'Mara, F., Rice, C., Scholes, B., Howden, M., McAllister, T., Pan, G., Romanenkov, V., Rose, S., Schneider, U., Towprayoon, S., Wattenbach, M., Rypdal, K., Martino, D., Cai, Z., Gwary, D., Janzen, H., … Sirotenko, O. (2007). Agriculture. In *Climate Change 2007: Mitigation. Contribution of Working Group III to the Fourth Assessment Report of the Intergovernmental Panel on Climate Change* (p. 44). Cambridge University Press, Cambridge, United Kingdom and New York, NY, USA.

Tian, L., Chen, J., & Shao, C. (2018). Interdependent dynamics of LAI-albedo across the roofing landscapes: Mongolian and Tibetan Plateaus. *Remote Sensing*, *10*(7), 1159. https://doi.org/10.3390/rs10071159

Wang, K., Liu, J., Zhou, X., Sparrow, M., Ma, M., Sun, Z., & Jiang, W. (2004). Validation of the MODIS global land surface albedo product using ground measurements in a semidesert region on the Tibetan Plateau. *Journal of Geophysical Research: Atmospheres*, *109*(D5). https://doi.org/10.1029/2003JD004229

Wang, L., Huang, M., & Li, D. (2020). Where are white roofs more effective in cooling the surface? *Geophysical Research Letters*, *47*(15), e2020GL087853. https://doi.org/10.1029/2020GL087853

Wiesner, S., Desai, A. R., Duff, A. J., Metzger, S., & Stoy, P. C. (2022). Quantifying the natural climate solution potential of agricultural systems by combining eddy covariance and remote sensing. *Journal of Geophysical Research: Biogeosciences*, *127*(9), e2022JG006895. https://doi.org/10.1029/2022JG006895

Williamson, P., & Bodle, R. (2014). *Geoengineering in Relation to the Convention on Biological Diversity: Technical and Regulatory Matters.* Montreal, Canada: Convention on Biological Diversity. http://www.deslibris.ca/ID/242834

Xiao, J., Zhuang, Q., Law, B. E., Baldocchi, D. D., Chen, J., Richardson, A. D., Melillo, J. M., Davis, K. J., Hollinger, D. Y., Wharton, S., Oren, R., Noormets, A., Fischer, M. L., Verma, S. B., Cook, D. R., Sun, G., McNulty, S., Wofsy, S. C., Bolstad, P. V., … Torn, M. S. (2011). Assessing net ecosystem carbon exchange of U.S. terrestrial ecosystems by integrating eddy covariance flux measurements and satellite observations. *Agricultural and Forest Meteorology*, *151*(1), 60–69. https://doi.org/10.1016/j.agrformet.2010.09.002

Zarnetske, P. L., Gurevitch, J., Franklin, J., Groffman, P. M., Harrison, C. S., Hellmann, J. J., Hoffman, F. M., Kothari, S., Robock, A., Tilmes, S., Visioni, D., Wu, J., Xia, L., & Yang, C.-E. (2021). Potential ecological impacts of climate intervention by reflecting sunlight to cool Earth. *Proceedings of the National Academy of Sciences*, *118*(15), e1921854118. https://doi.org/10.1073/pnas.1921854118

Zhao, F., Lan, X., Li, W., Zhu, W., & Li, T. (2021). Influence of land use change on the surface albedo and climate change in the Qinling-Daba Mountains. *Sustainability*, *13*(18), 10153. https://doi.org/10.3390/su131810153

Zhao, K., & Jackson, R. B. (2014). Biophysical forcings of land-use changes from potential forestry activities in North America. *Ecological Monographs*, *84*(2), 329–353. https://doi.org/10.1890/12-1705.1

CHAPTER 2. SPATIOTEMPORAL VARIATIONS OF ALBEDO IN MANAGED AGRICULTURAL LANDSCAPES: INFERENCES TO GLOBAL WARMING IMPACT (GWI)

Abstract

Albedo can be used to quantify ecosystem and landscape contributions to local and global climate. Such contributions are conventionally expressed as albedo-induced radiative forcing ($RF_{\Delta\alpha}$) and global warming impact ($GWI_{\Delta\alpha}$). I contextualize the results within landscape carbon production and storage to highlight the importance of changes in albedo for landscape GWI from multiple causes, including net ecosystem production (NEP) and greenhouse gas (GHG) emissions. The main objective is to examine the spatiotemporal changes in albedo ($\Delta\alpha$) in contrasting managed landscapes through calculations of $RF_{\Delta\alpha}$ and $GWI_{\Delta\alpha}$ under different precipitation regimes (i.e., drier *vs* wetter *vs* normal). To do so, I selected five contrasting landscapes within the Kalamazoo River Watershed in southwestern Michigan, USA, as proof of concept. The daily MCD43A3 MODIS (V006) product was used to analyze the inter/ and intra-annual variations of growing season albedo. In addition, the variations of $RF_{\Delta\alpha}$ and $GWI_{\Delta\alpha}$ were computed based on landscape composition and weather conditios. Results show that $RF_{\Delta\alpha}$ (-5.6 W m^{-2}) and $GWI_{\Delta\alpha}$ (-1.3 $MgCO_{2eq}$ ha^{-1} yr^{-1}) were high in forest-dominated landscapes, indicating cooling effects and CO_{2eq} mitigation impacts similar to crops, with magnitudes at forest-dominated landscapes on average 52% stronger than those at cropland-dominated ones. In the landscape with the highest proportion of forest, under drier and wetter conditions, albedo-induced climate benefit potentials (i.e., CO_{2eq} mitigation effects) were reduced by up to 24% and ~30%, respectively, while in one cropland-dominated landscape wetter conditions reduced the climate benefit potentials by 23%. Findings demonstrate that quantifying spatiotemporal changes in albedo in managed landscapes and under different precipitation regimes is essential to understand how landscape modification affects $RF_{\Delta\alpha}$ and $GWI_{\Delta\alpha}$ and thereby contributes to ecosystem-level GWI.

Introduction

Decoupling the causes and consequences of ecosystem functioning and services at multiple spatial scales represents an important scientific frontier in landscape ecology (Antón et al., 2011; Chen et al., 2013; Raudsepp-Hearne et al., 2010; Seidl et al., 2016; Yuan & Chen, 2015). Land use and land cover change (LULCC) caused by human activities (e.g., land uses and management) and natural disturbances (e.g., wildfires) directly affects regional and global climate through the exchange of energy, carbon, water, and greenhouse gases (GHGs) between the land surface and the atmosphere (Bonan, 2016; Bright et al., 2015). Management activities and disturbances such as cultivation, burning, and grazing not only influence GHG emissions but also alter the surface radiation balance (Pielke et al., 2011; Shao et al., 2014). Unfortunately, little effort has been directed towards investigating resulting changes in surface radiation balance (e.g., changes in albedo) at landscape scales (Chen et al., 2004; Euskirchen et al., 2002).

Surface albedo— the fraction of incoming shortwave solar radiation scattered by a surface back to space—is a measurable physical variable that can be used to quantify ecosystem and landscape contributions to local and global climate (Brovkin et al., 2013; Dickinson, 1983; Li et al., 2016; Picard et al., 2012; Storelvmo et al., 2016). Changing surface albedo has been proposed as one of several climate intervention strategies for climate change mitigation (Goosse, 2015; Lenton & Vaughan, 2009; National Research Council et al., 2010) and it is also important for understanding exchanges of energy and mass between terrestrial surfaces and the atmosphere (Merlin, 2013). Albedo is in its early stages of incorporation into climate models, but it is useful for deriving different mechanisms to lower climate warming by potentially increasing the scattering of shortwave solar radiation energy back to space (Lenton & Vaughan, 2009). Although LULCC (e.g., conversions from forest to biofuel, grassland, and cropland) can significantly alter

surface albedo (Bala et al., 2007; Cai et al., 2016), the magnitude of changes depends on vegetation type and canopy structure (Bennett et al., 2006; Tian et al., 2018).

Albedo is also highly correlated with leaf wetness, soil moisture, and soil water content (Henderson-Sellers & Wilson, 1983; Wang et al., 2004)—which are strongly related to precipitation and its temporal distribution—as well as with plant phenology and vegetation structure (Luyssaert et al., 2014), plant or tree height (Betts, 2001), and agricultural practices (Houspanossian et al., 2017), this last scarcely considered (Jeong et al., 2014; Zhang et al., 2013). For example, Culf et al. (1995) reported decreased albedo in forests as a function of darker leaves and darker soils under wet conditions. Berbet and Costa (2003) found that ranchlands were characterized by variable albedo throughout the entire year depending on climatic conditions (e.g., drier *vs* wetter periods), whereas forests were characterized by higher and lower albedo in both dry and wet periods, respectively.

Changes in atmospheric conditions and land mosaics due to LULCC can affect the Earth's radiation balance (Gray, 2007). Radiative forcing (RF) has been widely used to describe this imbalance as changes in the fraction of solar energy reflected by the Earth's surface (Mira et al., 2015), whether anthropogenic or natural (Lenton & Vaughan, 2009). Radiative forcing can thus be used to compare modifications in radiation balance due to atmospheric/surface albedo changes or due to GHG emissions. Previous studies (Akbari et al., 2009; Betts, 2000) have developed methodologies to relate RF to climate regulations equivalents to CO_2 (i.e., CO_{2eq}), used to calculate ecosystem-scale contributions to global warming impacts (GWIs)—a common measure for quantifying RFs of different GHGs and other agents (Forster et al., 2007; Fuglestvedt et al., 2003; Peters et al., 2011). Global warming impact allows one to directly relate anthropogenic activities to GHG emissions (Cherubini et al., 2012; Davin et al., 2007; Haines, 2003; Robertson et al., 2017)

and to understand and quantify the impact of an ecosystem on climate.

Despite escalating efforts to examine the magnitude and dynamics of albedo change due to LULCC, previous studies have focused on albedo, RF, and GWI differences among the cover types within landscapes or regions (Carrer et al., 2018; Chen et al., 2019; Haas et al., 2001; Román et al., 2009). For example, previous studies have shown that deforestation and expanding agricultural lands have played an important role in surface cooling of the northern hemisphere due to increased surface albedo and regeneration of forests after harvesting (Betts, 2001; Govindasamy et al., 2001; Lee et al., 2011). Georgescu et al. (2011) simulated strong cooling effects—equivalent to a reduction in carbon emission of 78 tC ha^{-1}—by increasing the surface albedo of agricultural lands across the central United States. Loarie et al. (2011) demonstrated that introducing sugar cane production into cropland/pasture landscapes of Brazil increased albedo and evapotranspiration, which in turn appeared to cool the local climate. Importantly, to quantify the contribution of LULCC to global warming/cooling, GWI should be computed with reference to albedo due to pre-existing conditions.

Here I examined the spatiotemporal changes of albedo (i.e., $\Delta\alpha$) in contrasting managed landscapes as compared to pre-existing forests through calculations of albedo-induced RF ($\Delta RF_{\Delta\alpha}$) and GWI ($\Delta GWI_{\Delta\alpha}$) under different precipitation regimes (i.e., different weather conditions). I expressed the relationship between landscape $\Delta\alpha$, $\Delta RF_{\Delta\alpha}$, and $GWI_{\Delta\alpha}$ as (Figure 2.1):

$$[\Delta\alpha_c \times \Delta lm_l \times \Delta w_l] \rightarrow \Delta RF_{\Delta\alpha} \rightarrow \Delta GWI_{\Delta\alpha} \quad (2.1)$$

where $\Delta\alpha_c$ is the surface albedo change at cover type *c*, Δlm_l is the variation of land mosaic (i.e., forest- *vs* cropland-dominated) for landscape *l*, Δw_l is the variation of weather conditions for landscape *l*, $\Delta RF_{\Delta\alpha}$ and $\Delta GWI_{\Delta\alpha}$ are the net landscape albedo-induced radiative forcing and global warming impact, respectively.

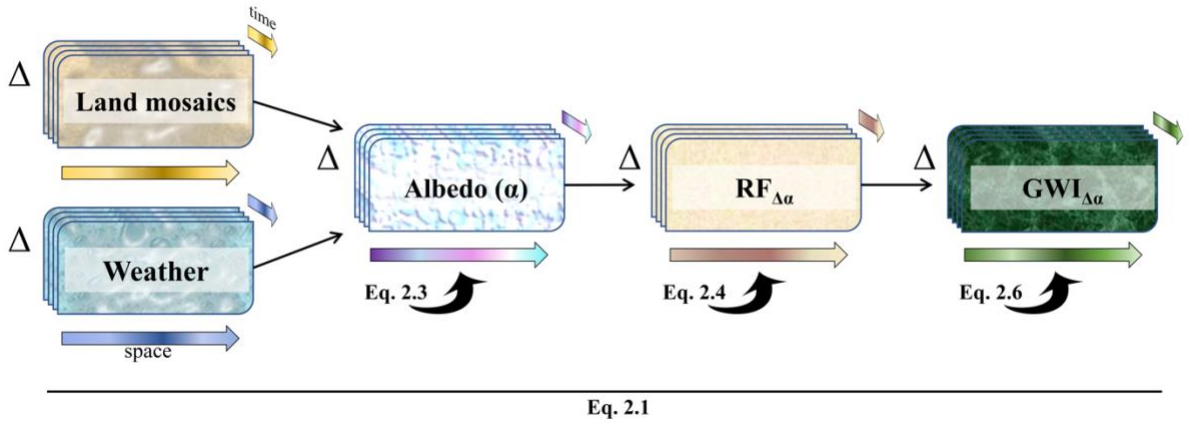

Figure 2.1: Schematic diagram showing the relationship between landscape albedo (α) and albedo-induced radiative forcing ($RF_{\Delta\alpha}$) and global warming impact ($GWI_{\Delta\alpha}$), as outlined at Eq. 2.1. The main hypothesis is that variations (Δ) in land mosaics (i.e., forest- *vs* cropland-dominated landscapes) and weather conditions (i.e., drier v*s* wetter *vs* normal) affect the spatiotemporal variation of α and, hence, the $RF_{\Delta\alpha}$ and $GWI_{\Delta\alpha}$. Figure modified from Sciusco et al., 2000.

More specifically, I aimed to estimate the magnitude and seasonal changes in albedo so that $\Delta GWI_{\Delta\alpha}$ could be assessed at ecosystem, landscape, and watershed scales, and included in ecosystem GWI assessments (Gelfand and Robertson, 2015). I further contextualized my results within landscape C production and storage to highlight the importance of changes in landscape $GWI_{\Delta\alpha}$ from multiple causes, including net ecosystem production (NEP) and GHG emissions. The framework developed in this study (Eq. 2.1 and Figure 2.1) can be applied to any landscape to compute landscape $GWI_{\Delta\alpha}$. To this end, I selected five contrasting landscapes in the Kalamazoo River Watershed of southwestern Michigan, USA, as a proof of concept to investigate inter/ and intra-annual variations of albedo under three different precipitation regimes.

Material & Methods

Study area

I chose five contrasting landscapes in the Kalamazoo River Watershed, located in southwestern Michigan, USA, for proof of concept (Figure 2.2). Within the 5621 km^2 watershed,

the long-term (1981–2010) mean annual temperature is 9.9 °C and the average annual precipitation is 900 mm that is evenly distributed throughout the year (Michigan State Climatologist's Office, 2013). The watershed includes portions of 10 counties: Allegan, Ottawa, Van Buren, Kent, Barry, Kalamazoo, Calhoun, Eaton, Jackson, and Hillsdale. Prior to European settlement, the watershed was dominated by forests (Brown et al., 2000) with interspersed tallgrass prairies, savannas, lakes, wetlands, and oak openings (Chapman & Brewer R, 2008). The watershed however has undergone significant LULCC since then. Present-day forest areas are secondary successional forests that followed their complete harvest by European settlers in the late 1800s (Brown et al., 2000). Today, the watershed consists of cultivated crops, successional forest stands, pasture-hay grasslands, and two urban areas (Kalamazoo and Battle Creek). Medium to coarse texture soils and mesic climate allow continuous recharge of groundwater (Schaetzl et al., 2009).

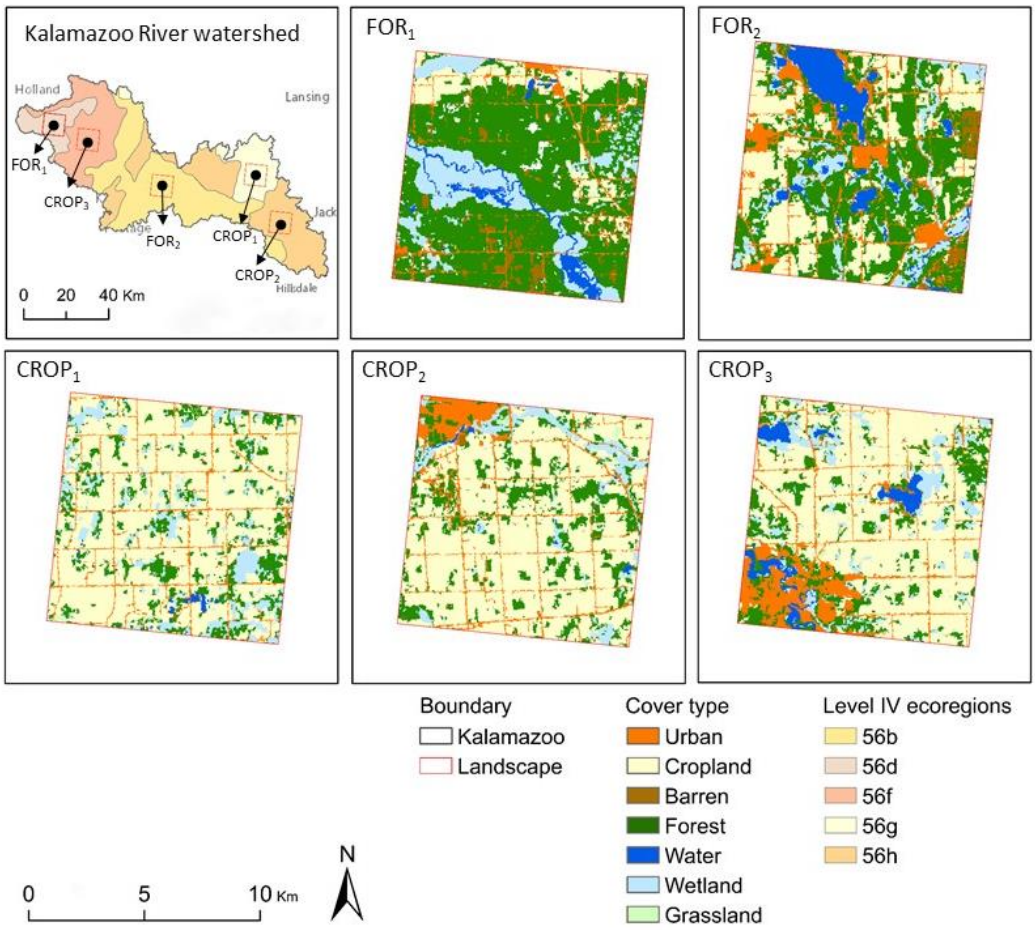

Figure 2.2: Locations of the five equal area landscapes (FOR_1, FOR_2, $CROP_1$, $CROP_2$, $CROP_3$) within the Kalamazoo River Watershed in the southwest Michigan, USA. Each landscape falls within a unique Level IV ecoregion defined by the United States Environmental Protection Agency (U.S. EPA). Basemap sources: *Esri, HERE, Garmin, USGS, Intermap, INCREMENT P, NRCAN, Esri Japan, METI, Esri China (Hong Kong), NOSTRA, © OpenStreetMap contributors, and the GIS User Community.*

I randomly selected five 10,000 ha landscapes (Figure 2.2; Barnes & Spurr, 1998) that represent the main ecoregions (i.e., areas characterized by similar vegetation, with the same type, quality, and quantity of environmental resources; Omernik & Griffith, 2014) of the watershed. The Kalamazoo River Watershed includes three United States Environmental Protection Agency (U.S. EPA) ecoregions (cf. https://www.epa.gov/eco-research/ecoregion-download-files-state-region-5#pane-20): Eastern Temperate Forest (Level I), Mixed Wood Plain (Level II), and Southern Michigan/Northern Indiana Drift Plain (Level III). At a finer scale, five Level IV ecoregions (Table

A1) exist in the watershed: Battle Creek Outwash Plain (56b), Michigan Lake Plain (56d), Lake Michigan Moraines (56f), Lansing Loamy Plain (56g), and Interlobate Dead Ice Moraines (56h). I used the five landscapes to represent the five Level IV ecoregions so that each landscape fell within an individual Level IV ecoregion.

Each landscape has different proportions of urban, cropland, barren, forest, water, wetland, and grassland cover types (Table 2.1). Two of the five landscapes have a higher proportion of forest (FOR_1 highest proportion of forest, and FOR_2 second highest proportion); while the remaining three landscapes are dominated by cropland ($CROP_1$, $CROP_2$, and $CROP_3$, from high to low proportion of cropland, respectively) (Table 2.1).

Table 2.1: Land cover composition of the five landscapes. Bold values indicate the cover type dominating the landscape.

	Landscape				
Cover type	FOR_1	FOR_2	$CROP_1$	$CROP_2$	$CROP_3$
	ha (%)				
Urban	513 (5.2)	1330 (13.3)	545 (5.5)	1047 (10.5)	1341 (13.4)
Cropland	1035 (10.5)	2597 (26.0)	**6807 (68.1)**	**6442 (64.5)**	**5713 (57.2)**
Barren	530 (5.4)	286 (2.9)	49 (0.5)	62 (0.6)	64 (0.6)
Forest	**5672 (57.5)**	**3833 (38.4)**	1415 (14.2)	1670 (16.7)	1477 (14.8)
Water	410 (4.2)	922 (9.2)	56 (0.6)	43 (0.4)	442 (4.4)
Wetland	1669 (16.9)	1012 (10.1)	1101 (11.0)	693 (6.9)	917 (9.2)
Grassland	30 (0.3)	12 (0.1)	21 (0.2)	35 (0.4)	38 (0.4)

Given that forest was the dominant land cover type prior to European settlement within each landscape (Brown et al., 2000), I considered the average albedo of all forest portions within each of the five landscapes during the growing season at 10:30 a.m. local time (UTC -05; i.e., MODIS Terra morning overpass time) as the reference albedo. Thereafter, in each landscape, changes in albedo ($\Delta\alpha$) were obtained by calculating the difference between mean cropland and

mean forest albedos, and then used to calculate $RF_{\Delta\alpha}$ and $GWI_{\Delta\alpha}$.

Landscape structure

The landscape structure of the watershed was quantified from a classified land cover map for 2011 (Figure 2.2) at 30 m spatial resolution, which was produced using the Landsat archives from the United States Geological Survey Earth Explorer and Global Visualization Viewer (GloVis) portals (cf. https://earthexplorer.usgs.gov/). The land cover map was obtained following the Anderson level I classification scheme and included seven land cover types: 1) urban, 2) cropland, 3) barren, 4) forest, 5) water, 6) wetland, and 7) grassland. The details of the accuracy assessment (i.e., producer and user's accuracy for each class type and the overall accuracy in an error matrix) of the classification were provided in Chen et al. (2019).

MODIS albedo

Albedo datasets were obtained from the most recent collection (V006) of the MCD43A3 MODIS Bidirectional Reflectance Distribution Function (BRDF) product (cf. https://doi.org/10.5067/MODIS/MCD43A3.006). MOD43A3 is a daily product at 500 m spatial resolution obtained by inversion of a Bidirectional Reflectance Distribution Function (the BRDF) model against a 16-day moving window of MODIS observations. The BRDF model was then used to derive the black-sky (i.e., directional-hemispherical reflectance) and white-sky (i.e., bi-hemispherical reflectance) albedos (Wang et al., 2014). I only considered snow-free, white-sky albedo (α) at a shortwave length of 0.3–5.0 µm (hereafter, α_{SHO} and expressed in percentage). For each image, the "*Albedo_WSA_shortwave*" (white-sky albedo) band was selected and rescaled to 0–1. Only high-quality data were selected within the "full BRDF inversion" quality band (QA=0). The "*Snow_BRDF_Albedo*" band in the MCD43A2 product was used to filter and exclude pixels with snow albedo retrievals (Chrysoulakis et al., 2018).

MODIS NDVI

Previous studies have thoroughly addressed the importance of snow cover on variability/uncertainty of albedo (Bonan, 2008; Bright et al., 2015; Campbell & Norman, 1998; Iqbal, 2012; Kaye & Quemada, 2017; Liang et al., 2013; Sun et al., 2017; Zhao & Jackson, 2014). Here, I focused on $\Delta\alpha$, $RF_{\Delta\alpha}$, and $GWI_{\Delta\alpha}$ only during the growing season when maximum variability of watershed crop phenology can be related with changes in climatic conditions and human disturbances at the landscape level. Therefore, for each year, I identified the "growing season" during March–October by detecting the greenness onset/offset for the entire Kalamazoo River Watershed. To do so, for each year, I used a 16-day composite time series of the normalized difference vegetation index (NDVI) to detect the inflection points (i.e., dates) when the maximum and minimum change rate of NDVI occurred (Jeong et al., 2011). I obtained NDVI at a 250 m spatial resolution from the most recent collection (V006) of the MYD13Q1 MODIS product (cf. https://doi.org/10.5067/MODIS/MYD13Q1.006). Finally, I divided each growing season (March–October) into three periods (hereafter, seasons)—spring, summer, and fall using astronomical seasons' subdivision (i.e., spring equinox, summer solstice, and fall equinox).

Precipitation data

Daily precipitation data at a 4 km spatial resolution was obtained from the Parameter-elevation Regressions on Independent Slopes Model group (PRISM) AN81d product (c.f http://www.prism.oregonstate.edu/) over the 2012–2017 time-period. I also calculated the cumulative precipitation of the five landscapes during the growing season from March through October. For the time-period considered (e.g., 2012–2017), I then identified three years as drier, wetter, and normal years: 2012, 2016, and 2017, respectively. As a matter of fact, the Midwest of USA experienced 6 weeks of summer drought during June-July in 2012 (Mallya et al., 2013),

resulting in a growing season precipitation of <490 mm. In 2017, the watershed received over 750 mm, while this was ~700 mm (i.e., near average) for 2017. All analysis and processing of albedo, NDVI, and precipitation data were performed on the Google Earth Engine (GEE) platform (Gorelick et al., 2017), where the MODIS products were uploaded, filtered to the date of interest, and clipped to the shape file for each of the five landscapes.

Statistical analysis

I performed analysis of variance (ANOVA) to examine the change in albedo with land cover type and landscape structure within the three-year study period and across three seasons. The following linear model was applied:

$$\alpha_{SHO} = landscape \times cover\ type \times year \times season \quad (2.2)$$

where α_{SHO} is the snow-free white-sky albedo at the shortwave length at a daily step acquired from MODIS at 10:30 a.m. local time (UTC -05); *landscape*, *cover type*, *year*, and *season* are the five equal area landscapes (FOR_1, FOR_2, $CROP_1$, $CROP_2$, $CROP_3$), the seven cover types (Table 2.1) at each landscape, the three years (drier, wetter, and normal), and the three astronomical seasons (spring, summer, and fall), respectively. I also considered the interaction terms among the independent variables in our ANOVA. To test the normality of the data I checked the distribution of the residuals. I then carried out ANOVA and Tukey tests for multiple comparisons using the R-package '*lsmeans'* (R Core Team, 2020).

Radiative forcing (RF) and global warming impact (GWI)

To quantify the potential of landscape radiative forcing (RF) due to albedo, first, I needed to compute the changes in surface albedo ($\Delta\alpha$) due to land mosaic as follows:

$$\Delta\alpha = \alpha_c - \alpha_f \quad (2.3)$$

where α_c and α_f are the changes of α_{SHO} in terms of absolute difference between mean cropland

and mean forest albedos in each of the five landscapes.

I then calculated the albedo-induced RF ($RF_{\Delta\alpha}$; W m^{-2}), which refers to the direct RF at the top-of-atmosphere, by following the algorithms of Carrer et al. (2018):

$$RF_{\Delta\alpha} = -\frac{1}{N}\sum_{d=1}^{N} SW_{in} \times T_a \times \Delta\alpha \quad (2.4)$$

where $RF_{\Delta\alpha}$ is the mean albedo-induced radiative forcing at the top-of-atmosphere over the growing season (t), N is the number of days in the growing season, SW_{in} (W m^{-2}) is the incoming shortwave radiation at the surface, T_a is the upward atmospheric transmittance, and $\Delta\alpha$ is the change in surface albedo (i.e., between mean cropland and mean forest albedos; Eq. 2.3). By multiplying both SW_{in} and $\Delta\alpha$ by T_a, I calculated the instantaneous amount of radiation that leaves the atmosphere at 10:30 a.m. local time (UTC -05). It is worth reiterating that all the variables (i.e., SW_{in}, $\Delta\alpha$, and T_a) refer to the specific time of 10:30 a.m. local time (UTC -05; i.e., MODIS Terra morning overpass time) and were considered to represent daily means. Negative values of $RF_{\Delta\alpha}$ indicate a cooling effect due to the differences between mean cropland and mean forest albedos.

While previous studies used a global annual average value of 0.854 (i.e., 85%) for T_a (Cherubini et al., 2012; Lenton & Vaughan, 2009), I calculated T_a as the ratio of incident shortwave radiation at the top of the atmosphere (SW_{TOA}) to that at the surface (SW_{in}) at 10:30 a.m. local time (UTC -05). By assuming a same value of upward and downward atmospheric transmittances (Carrer et al., 2018), SW_{in} (W m^{-2}) was obtained from a local Eddy Covariance (EC) tower located at one of the Long-term Ecological Research sites at Kellogg Biological Station (42°24´N, 85°24´W) (Abraha et al., 2015), while SW_{TOA} (W m^{-2}) was calculated as:

$$SW_{TOA} = S_{po} \times \cos(\theta) \times d \quad (2.5)$$

where S_{po} is the solar constant (1,360; W m^{-2}), $cos(\theta)$ is the cosine of the solar zenith angle, obtained from the MCD43A2 (V006) MODIS BRDF Albedo Quality product (cf.

https://doi.org/10.5067/MODIS/MCD43A2.006), applying the "*BRDF_Albedo_LocalSolarNoon*" band, and *d* is the mean Earth-Sun distance (km).

I then converted RF into the CO_2 equivalent (CO_{2eq}) by using the GWI algorithms of Bird et al. (2008) and Carrer et al. (2018):

$$GWI_{\Delta\alpha} = \frac{S \times RF_{\Delta\alpha}}{AF \times rf_{CO_2}} \frac{1}{TH} \quad (2.6)$$

where $GWI_{\Delta\alpha}$ is the albedo-induced global warming impact ($kgCO_{2eq}\ m^{-2}\ yr^{-1}$), represented by MODIS α_{SHO} acquisitions at 10:30 a.m. local time (UTC -05), i.e., assuming that the values represent the mean CO_{2eq} mitigation impact of each landscape during the growing season March–October *(t)*, $RF_{\Delta\alpha}$ is the mean albedo-induced RF due to $\Delta\alpha$ over the growing season March-October *(t)* (Eq. 2.4), *S* is cropland area (ha) for which I hypothesized the change of albedo occurred, *AF* is the CO_2 airborne fraction (0.48; i.e., 48%; Muñoz et al., 2010) obtained from the exponential CO_2 decay function (see Bird et al. (2008) for more details), and *TH* is the time horizon of potential global warming fixed at 100 years (Kaye & Quemada, 2017). Lastly, the parameter rf_{CO2}—the marginal RF of CO_2 emissions at the current atmospheric concentration—is kept as a constant at 0.908 W $kgCO_2^{-1}$ (Bright et al., 2015; Carrer et al., 2018; Muñoz et al., 2010).

Negative and positive values of $GWI_{\Delta\alpha}$ indicate CO_{2eq} mitigations and emissions, respectively. I calculated the annual $GWI_{\Delta\alpha}$ as 1/100th of the total CO_{2eq} to normalize to the 100-year time horizon used in the Kyoto Protocol (Boucher et al., 2009). Notably, here I assumed that the same land mosaic in each landscape will be maintained for the duration of 100 years. Previous studies (Akbari et al., 2009; Betts, 2000) have also used a constant AF as opposed to the exponential CO_2 decay function; however, the computed GWIs are similar (Bright et al., 2015).

Results

Two of the five landscapes (FOR_1 and FOR_2) were dominated by forests (Table 2.1), with

a forest coverage of 57.5% in FOR_1 and 38.4% in FOR_2. Wetlands and croplands accounted for 16.9% and 10.5% of landscape, respectively, in FOR_1 (Table 2.1), but only 10.1% and 26% in FOR_2 where urban land was also the highest (13.3%). Croplands were dominant in $CROP_1$, $CROP_2$, and $CROP_3$ (Table 2.1), with 68.1%, 64.5%, and 57.2% of area coverage, respectively. Forest cover ranked the second highest in these landscapes (14.2%, 16.7%, and 14.8%, respectively). Bare soils, grasslands, and water accounted for small portions of all five landscapes.

The entire watershed had an α_{SHO} of 15.9% during the drier (2012) and wetter (2016) years and of 15.6% during the normal (2017) year (Table A2), yielding an overall average of 15.8% with a low inter-annual variation. Each cover type contributed differently to α_{SHO} at the watershed level. In particular, croplands and water bodies showed the highest (16.6%) and lowest (12.1%) α_{SHO}, respectively, with the highest values occurring in both 2012 (16.6%±1.0) and 2016 (16.6%±1.1) for croplands, and the lowest in 2017 (11.9%±3.4) for water. The other cover types showed similar α_{SHO} values, ranging 15.1–15.6% for barren and grassland, 15.2% for urban and forests and 15.4% for wetlands. At the landscape level, α_{SHO} of forest, which was considered as reference, was generally lower than that of croplands. In particular, FOR_1 and FOR_2 landscapes averaged a low α_{SHO} of 14.6% and 13.9%, respectively, whereas $CROP_1$, $CROP_2$, and $CROP_3$ landscapes recorded higher values of 16.7%, 16.4%, and 16.2%, respectively. However, FOR_1 and FOR_2 demonstrated the highest α_{SHO} in 2012 (14.7%±0.8 and 14.1%±2.3, respectively), while $CROP_1$, $CROP_2$, and $CROP_3$ demonstrated the highest α_{SHO} in different years, such as 2016 for $CROP_1$ (17.0%±0.8), 2012 and 2016 for $CROP_2$ (16.5%±0.6), and 2017 for $CROP_3$ (16.3%±1.7). In the forest-dominated landscapes, all cover types showed higher α_{SHO} during the drier year (2012). However, for FOR_2, α_{SHO} values of cropland and barren were high in the wetter year (2016). In the cropland-dominated landscapes, the highest α_{SHO} value (17.1%) was observed in $CROP_3$ (±1.1) for

croplands in 2017, and in $CROP_1$ for both urban (±0.6) and croplands (±0.8) in 2016.

The ANOVA model (R^2=0.64; Table 2.2) indicated that the variation of α_{SHO} was significant (p-value<0.001) among the five landscapes (i.e., ecoregions; ω^2=26.6%) by cover type (i.e., landscape mosaics; ω^2=11.1%) and their interactions (ω^2=5.2%), with year and its interactions explaining <1% of the variation. However, the variation from season (i.e., seasonality; ω^2=15.9%) explained more than cover type.

Table 2.2: Statistical results of analysis of variance (ANOVA) based on the linear model at Eq. 2.3 (dependent variable: α_{SHO}).

Variable	DF	SS	MS	F	p-value	ω^2	R^2
lands.	4	1.869	0.467	3689.660	***	0.266	
seas.	2	1.118	0.559	4414.651	***	0.159	
Cover	6	0.779	0.130	1024.423	***	0.111	
lands. × cover	24	0.371	0.015	121.891	***	0.052	
lands. × seas.	8	0.142	0.018	140.167	***	0.020	
lands. × cover × seas.	48	0.079	0.002	12.962	***	0.011	
year × seas.	4	0.048	0.012	94.672	***	0.007	
cover × seas.	12	0.030	0.003	19.844	***	0.004	
lands. × year	8	0.022	0.003	21.210	***	0.003	
lands. × year × seas.	16	0.020	0.001	9.684	***	0.003	
year	2	0.013	0.007	51.367	***	0.002	
lands. × cover × year	48	0.015	0	2.505	***	0.002	
cover × year	12	0.002	0	1.278		0	
cover × year × seas.	24	0.003	0	1.047		0	
lands. × cover × year × seas.	96	0.011	0	0.887		0	0.64
Residuals	19779	2.505	0				

R^2: R-squared score

ω^2: omega-squared indicating the variance in the dependent variable α_{SHO} accounted for by the independent variables landscape, cover type, year, seasons, and their interactions

Signif. codes: *** p-value < 0.001, ** p-value < 0.0.1, * p-value < 0.05, · p-value < 0.1, " " p-value > 0.1

Forest-dominated landscapes showed lower least square means (LSM) of α_{SHO} ($LSM\alpha_{SHO}$) than cropland-dominated landscapes (Figure 3a) over the three years.

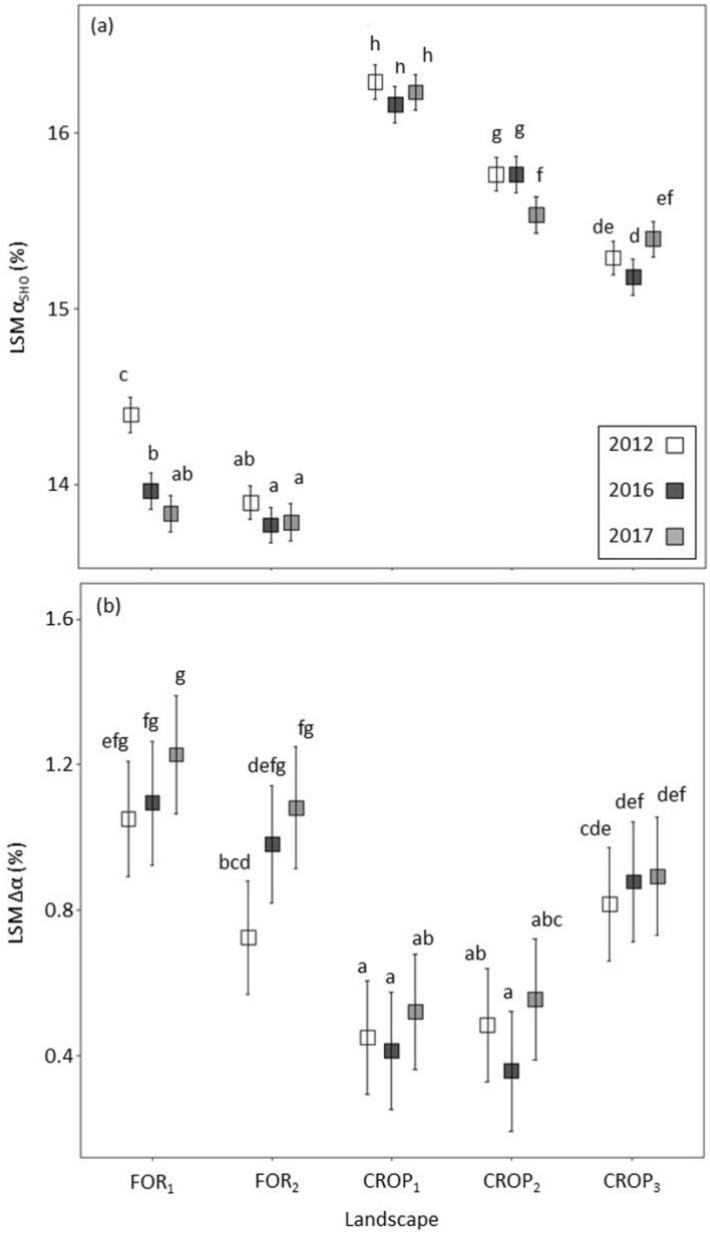

Figure 2.3: Least square means (LSM) multi-comparison analysis of α_{SHO} (a) and $\Delta\alpha_{SHO}$ (b) in 2012 (i.e., drier), 2016 (i.e., wetter), and 2017 (i.e., normal) for each landscape. Boxes indicate the LSM; whiskers represent the lower and upper limits of the 95% family-wise confidence level of the LSM. Boxes sharing the same letters are not significantly different (inter/ and intra-annual, as well as within and among the five landscapes) according to the Tukey honestly significant difference test.

A decreasing interannual trend (between 2012, 2016, and 2017 growing seasons) characterized FOR_1, FOR_2, and $CROP_2$, with FOR_1 showing statistically higher LSMα_{SHO} in the drier year (i.e., 2012); whereas $CROP_2$ showed statistically lower LSMα_{SHO} in the normal year

(i.e., 2017). In addition, differences in LSM between cropland and forest albedos ($LSM_{\Delta\alpha}$) appeared to be higher in FOR_1, FOR_2, and $CROP_3$ (Figure 3b), but with increasing inter-annual trends, than in $CROP_1$ and $CROP_2$. However, only FOR_2 showed statistically lower $LSM_{\Delta\alpha}$ in the drier year (2012) (Figure 2.3b).

Clear seasonal patterns existed in α_{SHO} and were generally lower in spring and autumn than in the summer (Figure 2.4). However, in $CROP_2$, the α_{SHO} of the major cover types (i.e., cropland, forest, urban, and wetland) was the highest in the spring of the drier year. The α_{SHO} of cropland and urban areas in 2017 (a normal year) was also relatively higher in both spring and summer (Figures 2.4c_1-c_3). The interannual variability between the wetter and normal years (Figures 2.4b_1–b_4 and 2.4c_1–c_4, respectively) appeared similar, with small differences between FOR_1 and FOR_2 (e.g., the lowest α_{SHO} occurring in spring in FOR_1 and in autumn in FOR_2).

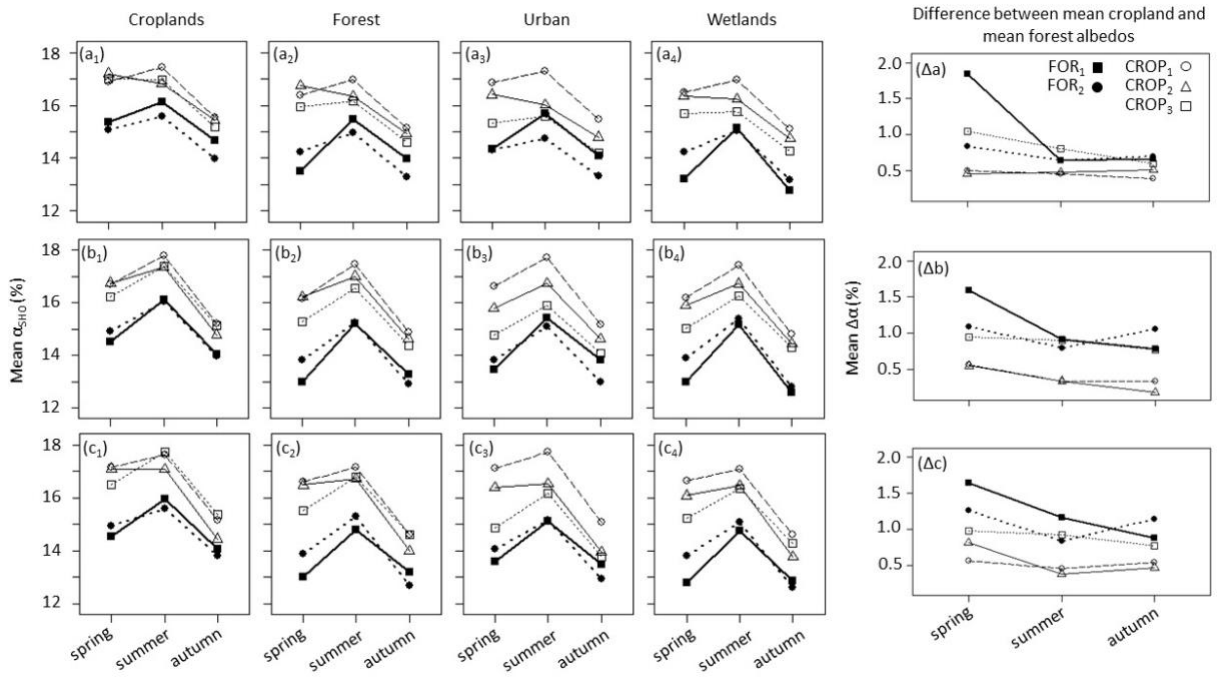

Figure 2.4: Mean α_{SHO} (%) by cover type and season in 2012 (i.e., drier year; a_1–a_4), 2016 (i.e., wetter year; b_1–b_4), and 2017 (i.e., normal year; c_1–c_4) for the five landscapes. Mean of the difference between mean cropland and mean forest albedos ($\Delta\alpha_{SHO}$) for the same years (Δa, Δb, and Δc, respectively) is also shown.

The mean Δα ranged between 0.4% and 2% (i.e., ~1.2% mean difference between mean cropland and mean forest albedos) (Figure 2.4Δa–Δc); however, the intra-annual variability of Δα differed by landscape and year. I found that forest-dominated landscapes (FOR_1 and FOR_2) had higher Δα in spring each year, with the minimum in autumn (FOR_1) and summer (FOR_2) of every year. Cropland-dominated landscapes ($CROP_1$, $CROP_2$ and $CROP_3CROP_3$) showed higher Δα in spring that was more pronounced in 2016 for $CROP_1$ (Figure 2.4Δb), in 2016 and 2017 for $CROP_2$ (Figure 2.4Δb-Δc), and in 2012 for $CROP_3$ (Figure 2.4Δa). However, $CROP_2$ in 2012 was characterized by a different Δα trend—lower in spring and higher in autumn (Figure 2.4Δa). The summer Δα variability among the five landscapes was lower in the drier year (Figure 2.4Δa) and higher in the normal year (Figure 2.4Δc). Two distinct clusters characterized the summer of the wetter year (Figure 2.4Δb), with FOR_1, FOR_2 and $CROP_3$ having an Δα of ≥ 1% and $CROP_1$ and

$CROP_2$ of ≤ 0.5%.

All five landscapes had negative $RF_{\Delta\alpha}$ (Table 2.3 and Figure 2.5a). Among the cropland-dominated landscapes, $CROP_1$ and $CROP_2$ had similar lower magnitude $RF_{\Delta\alpha}$ values, with minimum and maximum values in the wetter and normal years (i.e., 2016 and 2017, respectively), respectively. In particular, $CROP_2$ had $RF_{\Delta\alpha}$ (W m^{-2}) of -1.2 in 2016 and -1.9 in 2017, followed by $CROP_1$ (-1.3 and -2.0) and $CROP_3$ (-2.9 and -3.7). Among the forest-dominated landscapes, FOR_1 showed a similar trend, with minimum and maximum magnitude $RF_{\Delta\alpha}$ in 2016 and 2017 (-3.9 and -5.6, respectively), while FOR_2 had the minimum and maximum magnitude $RF_{\Delta\alpha}$ in the dry and normal years (-2.7 and -2.9, respectively, in 2012 and 2017, respectively).

Table 2.3: Mean (± one standard deviation) change of Δα (%), $RF_{\Delta\alpha}$ (W m^{-2}), and $GWI_{\Delta\alpha}$ ($MgCO_{2eq}$ ha^{-1} yr^{-1}) for each landscape in 2012, 2016, and 2017 growing seasons. Negative and positive values for $RF_{\Delta\alpha}$ and $GWI_{\Delta\alpha}$ indicate cooling and warming effects and CO_{2eq} mitigation and emission impacts due to albedo change, respectively. Percentage changes (%) between 2017 (baseline) and the two extreme weather years (i.e., $diff_{2017\text{-}2012}$ and $diff_{2017\text{-}1016}$, respectively) are also shown. Values with significant decrease (e.g., percent change) are highlighted in bold texts.

	2012			2016			2017			$diff_{2017\text{-}2012}$		$diff_{2017\text{-}2016}$	
	Δ_α	$RF_{\Delta\alpha}$	$GWI_{\Delta\alpha}$	Δ_α	$RF_{\Delta\alpha}$	$GWI_{\Delta\alpha}$	Δ_α	$RF_{\Delta\alpha}$	$GWI_{\Delta\alpha}$	Δ_α	$RF_{\Delta\alpha}$ / $GWI_{\Delta\alpha}$	Δ_α	$RF_{\Delta\alpha}$ / $GWI_{\Delta\alpha}$
FOR_1	1.2(±0.8)	-4.2	-1.0	1.2(±0.8)	-3.9	-0.9	1.3(±0.6)	-5.6	-1.3	**9.0**	**24.0**	**6.1**	**29.9**
FOR_2	0.8(±0.3)	-2.7	-0.6	1.0(±0.4)	-2.9	-0.7	1.1(±2.0)	-2.9	-0.7	28.5	9.0	7.8	1.4
$CROP_1$	0.5(±0.2)	-1.7	-0.4	0.5(±0.3)	-1.3	-0.3	0.5(±0.3)	-2.0	-0.5	9.2	15.6	12.6	32.1
$CROP_2$	0.5(±0.3)	-1.7	-0.4	0.4(±0.2)	-1.2	-0.3	0.6(±1.4)	-1.9	-0.4	19.4	9.9	34.3	33.4
$CROP_3$	0.9(±0.3)	-3.2	-0.7	0.9(±0.6)	-2.9	-0.7	0.9(±0.5)	-3.7	-0.9	6.0	14.9	**1.0**	**23.3**

Δα: change in surface albedo between mean cropland and mean forest albedos

$RF_{\Delta\alpha}$ and $GWI_{\Delta\alpha}$: albedo-induced radiative forcing (W m^{-2}) and global warming impact ($MgCO_{2eq}$ ha^{-1} yr^{-1})

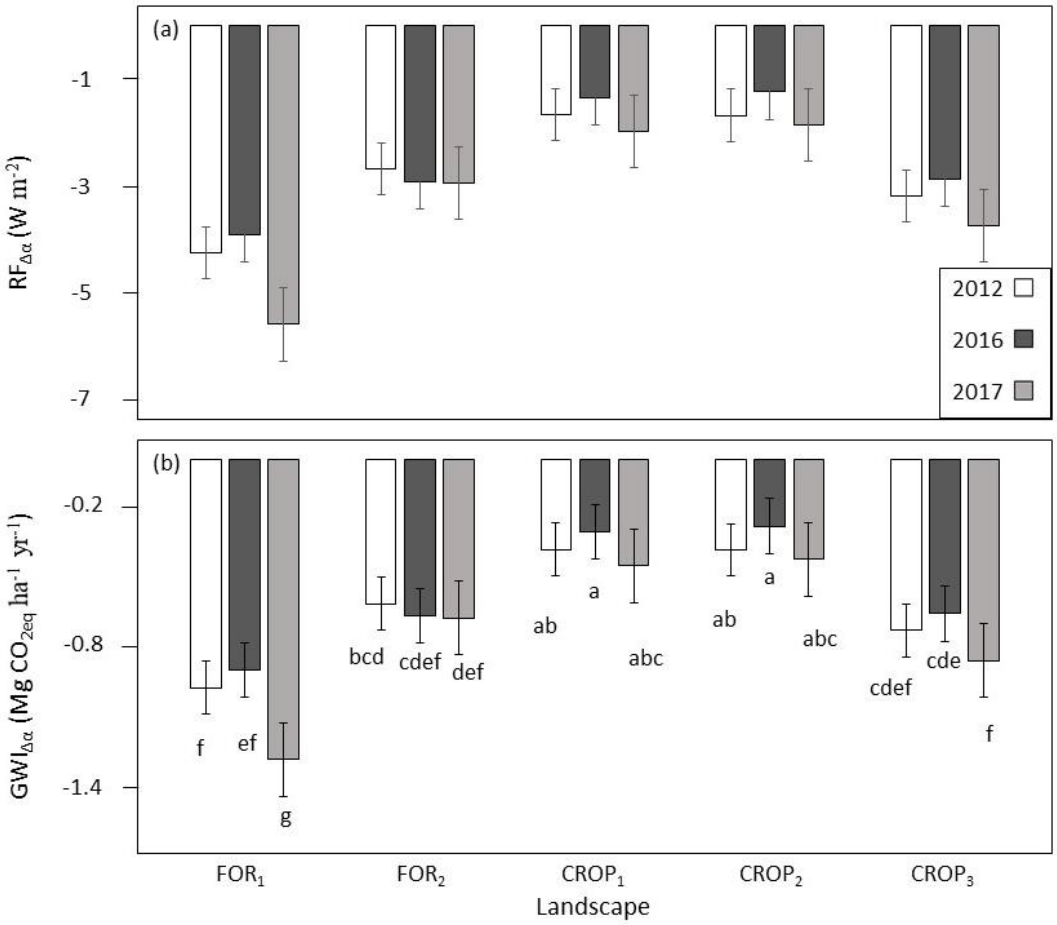

Figure 2.5: Bar chart of albedo-induced radiative forcing ($RF_{\Delta\alpha}$; W m^{-2}) due to the difference between mean cropland and mean forest albedos at the top-of-atmosphere across five landscapes at 10:30 a.m. local time (UTC -05) during the 2012, 2016, and 2017 growing seasons (a). Panel (b) shows the albedo-induced global warming impact ($GWI_{\Delta\alpha}$; $MgCO_{2eq}$ ha^{-1} yr^{-1}) due to the difference between mean cropland and mean forest albedos. Negative values for $RF_{\Delta\alpha}$ and $GWI_{\Delta\alpha}$ indicate cooling effects and CO_{2eq} mitigation impacts, respectively. Bars sharing the same letters are not significantly different (inter/ and intra-annual, as well as within and among the five landscapes) according to the Tukey honestly significant difference test. The three years 2012, 2016, and 2017 refer to drier, wetter, and normal weather conditions, respectively.

As for $RF_{\Delta\alpha}$, all five landscapes showed negative values of $GWI_{\Delta\alpha}$ (Table 2.3 and Figure 2.5b), which had inter/ and intra-annual trends similar to $RF_{\Delta\alpha}$ (Figure 2.5b). In particular, $CROP_1$ and $CROP_2$ had similar lower magnitude $GWI_{\Delta\alpha}$ ($MgCO_{2eq}$ ha^{-1} yr^{-1}) values, with minimum ($CROP_1$ and $CROP_2$: -0.3) and maximum ($CROP_1$: -0.5 and $CROP_2$: -0.4) values in the wet (i.e., 2016) and normal (i.e., 2017) years, respectively, followed by $CROP_3$ (-0.7 and -0.9, respectively).

FOR_1 showed a similar trend, with minimum and maximum magnitude $GWI_{\Delta\alpha}$ in 2016 and 2017 (-0.9 and -1.3, respectively), with statistically higher $GWI_{\Delta\alpha}$ in 2017, while FOR_2 had the minimum and maximum magnitude $GWI_{\Delta\alpha}$ in the drier (2012) and both wetter and normal (2016 and 2017) years (-0.6 and -0.7, respectively) (Table 2.3 and Figure 2.5b).

Taking the normal year (2017) as my baseline, the percentage changes between the normal and drier years (e.g., diff $_{2017\text{-}2012}$), and the normal and wetter years (e.g., diff $_{2017\text{-}2016}$) showed reduced $\Delta\alpha$, $RF_{\Delta\alpha}$, and $GWI_{\Delta\alpha}$ values (Table 2.3). In particular, the decrease in $\Delta\alpha$ was higher in FOR_2, $CROP_1$ $CROP_2$ (28.5%, 9.2%, and 19.4%, respectively) for $diff_{2017\text{-}2012}$ and in $CROP_1$ and $CROP_2$ (12.6% and 34.3%, respectively) for $diff_{2017\text{-}2016}$. FOR_2 decreased the least from baseline in both $RF_{\Delta\alpha}$ and $GWI_{\Delta\alpha}$ compared to all other landscapes, which had the highest decrease in $diff_{2017\text{-}2016}$—FOR_1 (29.9%), $CROP_1$ (32.1%), $CROP_2$ (33.4%), and $CROP_3$ (23.3%). Statistically, reductions in $\Delta\alpha$, $RF_{\Delta\alpha}$, and $GWI_{\Delta\alpha}$ values were all significant in FOR_1 (for both $diff_{2017\text{-}2012}$ and $diff_{2017\text{-}2016}$) and in $CROP_2$ (for $diff_{2017\text{-}2016}$).

Discussion

The main finding of my study is that $RF_{\Delta\alpha}$ and $GWI_{\Delta\alpha}$ play an important role in climate change impact due to landscape mosaics. In particular, I found that forests have lower albedo than croplands, which is in consistent with previous studies. In all five landscapes LULCC from forest to cropland showed a cooling effect with negative $RF_{\Delta\alpha}$ and $GWI_{\Delta\alpha}$ values. The results also show that the difference between mean cropland and mean forest albedos during the three years produces on average ~64%, 65%, and 28% stronger CO_{2eq} mitigation impacts in the landscape with the highest proportion of forest (FOR_1) than in cropland-dominated landscapes ($CROP_1$, $CROP_2$, and $CROP_3$, respectively), presumably due to the lower proportion in cropland (e.g., 10.5% of cropland area) in FOR_1. Additionally, drier weather conditions in 2012 result in the highest albedo in almost

all landscapes, although only significantly higher in one of the forest-dominated (i.e., FOR_1) landscapes, supporting a consensus that drier surfaces reflect more than wetter surfaces. Over the growing season, albedo peaks in summer in all cover types, with lower albedo in spring and autumn due to changes in plant phenology.

Inter and intra-annual changes in albedo

I compared α_{SHO} values among major cover types (i.e., urban, cropland, forest, and wetland), disregarding those with lower proportions (i.e., grassland, water, and barren) due to their negligible contributions to the total landscape α_{SHO}. I observed that croplands and forests had on average 7.8% higher and 0.7% lower albedo than other land covers, respectively. This is in line with previous studies that examined snow-free albedo variations among ecosystems (Chen et al., 2019; Jiao et al., 2017) and across the conterminous United States (Barnes & Roy, 2010). Bonan (Bonan, 2008) showed that forests have lower surface albedo than other cover types, contributing to climate warming. My study indicated that in forest-dominated landscapes (FOR_1 and FOR_2) the average of interannual variation of α_{SHO} was ~2.8% lower than that in cropland-dominated landscapes (Table A2 and Figure 2.3a). Analysis of variance also revealed that the five landscapes (i.e., ecoregions), cover types (i.e., landscape mosaics), and seasons (i.e., seasonality) contributed significantly to the overall variation of α_{SHO}. Specifically, I found that besides the five landscapes, seasons (~16%) contributed by 5% more than cover type (11%) towards variation of α_{SHO} (Table 2.2).

Changes in α_{SHO} due to LULCC have been widely studied (Chrysoulakis et al., 2018); however, its dynamics at ecosystem-to-landscape scales remain unexplored. For example, Zheng et al. (2019) investigated how vegetation changes affect albedo trends without considering the integrated effect of both cover type and seasonality, while Matthews et al. (2003) investigated the

cooling/warming effects of albedo change resulting from deforestation but failed to consider realistic land cover change scenarios. A number of agricultural management practices are known to mitigate climate change (summarized in Smith et al. (2008) and Eagle et al. (2012)), including GHG emission reductions and soil carbon storage, but the potential contribution of albedo change as an ecosystem-scale mitigation factor has not been much addressed. For example, tillage practices, harvest timing, residue management, and winter cover crops can all affect surface reflectance in annual cropping systems (Bright et al., 2015; Kaye & Quemada, 2017; Poeplau & Don, 2015; Robertson et al., 2017) and thus GWI.

To my knowledge, no effort has been made to understand albedo mitigation in terms of both RF and GWI in the context of landscape mosaics characterized by diverse land use type and intensity. Using the framework listed in Eq. 2.1 and Figure 2.1, I was able to integrate spatial (e.g., five landscapes within ecoregions) and temporal (e.g., inter/ and intra-annual) changes as main drivers of α_{SHO} variations. Regardless of land composition, cropland-dominated landscapes showed a higher intra-annual variability of α_{SHO} than forests under drier, wetter, and normal weather conditions (Figure 2.4a–c), likely due to the higher disturbances that croplands experience (i.e., fragmentation, land management, crop variety, and crop seasonality). For example, α_{SHO} can be altered by the differences in leaf structure/properties (Miller et al., 2016) and leaf wetness (Luyssaert et al., 2014), by the difference in management of both perennial and annual crops and by agricultural practices (Bright et al., 2015; Kaye & Quemada, 2017; Robertson et al., 2017).

The LSM multi-comparison analysis showed that dry conditions led FOR_1 to yield statistically higher α_{SHO} compared to wetter and normal conditions. On the other hand, $CROP_2$ showed significantly lower α_{SHO} under normal conditions than under drier and wetter conditions (Figure 2.3a), indicating a different albedo response of forest- and cropland-dominated landscapes

to changes in weather conditions. All other landscapes showed higher α_{SHO} in the drier year (2012) than in the normal and wetter years, although not statistically different.

Albedo-induced radiative forcing ($RF_{\Delta\alpha}$) and global warming impact ($GWI_{\Delta\alpha}$)

I obtained $RF_{\Delta\alpha}$ (W m^{-2}) values that were more representative of the entire growing season through the years 2012, 2016, and 2017. I found that the five landscapes had a negative $RF_{\Delta\alpha}$, indicating a cooling effect. However, such effect was stronger in FOR_1 where it ranged between -3.9 W m^{-2} and -5.6 W m^{-2} (Table 2.3 and Figure 2.5a), followed by $CROP_3$ (-2.9 W m^{-2} and -3.7 W m^{-2}) and FOR_2 (-2.7 W m^{-2} and -2.9 W m^{-2}), while $CROP_1$ and $CROP_2$ were almost similar (ranging between -1.2 W m^{-2} and -1.9 W m^{-2}, respectively). In other words, land mosaics in the landscape with the highest proportion of forest (e.g., FOR_1) leads to a maximum $RF_{\Delta\alpha}$ of -5.6 W m^{-2} (i.e., a cooling effect), which is similar to that hypothesized by Jiao et al. (2017) under the simulated scenario of global deforestation of evergreen broadleaf forests (local magnitude of RF_{TOA} at -5.6 W m^{-2}). Moreover, in this study I was able to investigate $RF_{\Delta\alpha}$ dynamics across three contrasting precipitation regimes—drier (2012), wetter (2016), and normal (2017). The interannual analysis specifically showed that within each landscape, the cooling effect was lower in 2016 and higher in 2017, with the exception of FOR_2, which had a lower cooling effect in 2012 and a higher one in 2017 (e.g., slightly higher than in 2016). In sum, accurate quantification of landscape contribution to the global warming potentials needs input from both landscape composition and climate that directly regulate ecosystem properties.

The $GWI_{\Delta\alpha}$ computations allowed me to estimate the CO_{2eq} mitigation caused by the differences between mean cropland and mean forest albedos. Standardized to the same areas, the greatest contribution of albedo changes to GWI occurred in the FOR_1 ($GWI_{\Delta\alpha}$ = -1.3 $MgCO_{2eq}$ ha^{-1} in 2017; Table 2.3 and Figure 2.5b), whereas the least contribution occurred in $CROP_2$ (-0.3

$MgCO_{2eq}$ ha^{-1} yr^{-1}). These contributions to GWI are of the same order of magnitude as many crop management components. For example, in this same watershed a corn-soybean-wheat rotation managed with a legume cover crop had a net GWI of 0.4 - 0.6 $MgCO_{2eq}$ ha^{-1} yr^{-1} (Robertson, 2000), without considering albedo change due to historical LULCC. Likewise, the net GWI of conventional and no-till cropping systems were similar in magnitude without consideration of albedo; 0.3 to 0.9 $MgCO_{2eq}$ ha^{-1} yr^{-1}, respectively (Gelfand et al., 2013). In several landscapes (FOR_1, FOR_2, and $CROP_3$), $GWI_{\Delta\alpha}$ was sufficient to offset the GWI costs of both N_2O emissions (0.4 $MgCO_{2eq}$ ha^{-1} yr^{-1}) and farming inputs for an alfalfa cropping system (~0.8 $MgCO_{2eq}$ ha^{-1} yr^{-1}; Gelfand et al., 2013).

Surprisingly, the results of interannual variation among the three growing seasons showed that the CO_{2eq} mitigation impact between forest- and cropland-dominated (FOR_1, $CROP_3$) landscapes was statistically different in 2012 and 2016 for FOR_1 (Table 2.3 and Figure 2.5a) and in 2016 for $CROP_3$, suggesting that changes in weather conditions, as seen in my study from drier to normal and from wetter to normal, can affect the CO_{2eq} mitigation impacts of landscapes. Overall, in one of the forest-dominated landscapes (FOR_1) the percent decrease of CO_{2eq} mitigation due to drier and wetter conditions was higher than that of the cropland-dominated landscape $CROP_3$ under wetter conditions (e.g., lower albedo). Specifically, I found that both drier and wetter conditions in FOR_1 could significantly reduce $CO_{2\text{-}eq.}$ mitigation by up to 24% and ~30% (i.e., percentage change), respectively; while the CO_{2eq} mitigation's decreasing in $CROP_3$ was significant under wetter conditions (e.g., 23.3%), which, in both cases, is still enough to offset 11% of the total CO_{2eq} emissions of conventionally tilled corn systems in the same area and under the same climatic conditions (i.e., 2012 and 2016; Abraha et al., 2019). Surprisingly the high decrease in $\Delta\alpha$ (e.g., FOR_1: 9% vs 6.1% and $CROP_3$: 6% vs 1%) under wetter conditions did not lead to a

high decrease in CO_{2eq} mitigation.

Assumptions and limitations

The methodology used in this study represents an analytical approach as a proof of concept of the effects of landscape patches and climatic conditions on $RF_{\Delta\alpha}$ and $GWI_{\Delta\alpha}$ in the context of forest- and cropland-dominant landscapes. However, certain assumptions can be made on the application of our approach. The first is that $RF_{\Delta\alpha}$ is related to land mosaics (e.g., patch composition) derived by land transformation (Muñoz et al., 2010). In fact, the focus of the present study is to measure the changes in $RF_{\Delta\alpha}$ and $GWI_{\Delta\alpha}$ due to conversion of forests to croplands, assuming the existing croplands were forests in the past. I then considered $\Delta\alpha$ using the baseline (forest), which is treated as a reference cover type of the five landscapes, since it was the dominant land cover type of the pre-European settlements (Brown et al., 2000).

A second assumption is related to using *in-situ* incident shortwave radiation at the surface (SW_{in}) for the calculation of upward atmospheric transmittance (T_a). While the literature (Cherubini et al., 2012; Lenton & Vaughan, 2009; Muñoz et al., 2010) refers to T_a as the annual global mean (T_a=0.854; i.e., 85%) for a constant zenith angle of 60°, here I calculated T_a for a given day as the ratio SW_{in}/SW_{TOA}, with SW_{in} obtained from *in-situ* measurements within the study area (Abraha et al., 2015), specifically at the FOR_2 landscape. By avoiding such a default value for T_a (i.e., 0.845), I reduced the error by ~30%. I then assumed that SW_{in} would be the same at all five landscape locations. In fact, unlike previous studies, I calculated $RF_{\Delta\alpha}$ and $GWI_{\Delta\alpha}$ on a relatively small area (i.e., not global/regional) for which the uncertainty error carried by a constant T_a would not have been significant.

A third assumption is related to the time horizon (TH) fixed at 100 years, which is the same time horizon used in the Kyoto Protocol (Boucher et al., 2009). By calculating the annual $GWI_{\Delta\alpha}$

as 1/100 of the total CO_{2eq}, I assumed that, in each landscape, the same land mosaic will be maintained for the duration of 100 years. This choice of TH is a limitation because short time horizons can overemphasize the impacts of albedo, while long time horizons can de-emphasize the impacts (Anderson-Teixeira et al., 2012).

Another limitation of the study is the use of a growing season (March–October) time frame for $RF_{\Delta\alpha}$ and $GWI_{\Delta\alpha}$ rather than an annual period. Previous studies (Bonan, 2008; Bright et al., 2015; Campbell & Norman, 1998; Iqbal, 2012; Kaye & Quemada, 2017; Liang et al., 2013; Sun et al., 2017; Zhao & Jackson, 2014) have addressed the importance of snow cover to variability/uncertainty of albedo between forest and cropland because of the capability of forest stands of masking the snow (e.g., lowing the albedo). Nevertheless, my use of growing season values allowed to better isolate the human disturbance on the landscape through agricultural activities by focusing on the crop phenology and its relationship with climatic conditions. Had I included wintertime albedo, my forest-cropland differences would have been even greater, however, since deciduous forest stands have higher wintertime albedo than cropland due to the presence of bare branches (Anderson et al., 2011; Campbell & Norman, 1998) during winter. On the other hand, from the remote sensing perspective, MODIS snow-albedo retrievals have been demonstrated to be less accurate than acquisitions during the growing season (Wang et al., 2014).

There are also uncertainties associated with user-defined data (Muñoz et al., 2010), such as considering $\Delta\alpha$ as the difference between croplands and forest albedos. AF (i.e., CO_2 airborne fraction) and rf_{CO2} (the marginal RF of CO_2 emissions at the current atmospheric concentration) are estimated to embed errors of ±15% and ±10%, respectively, in the GWI estimation (Akbari et al., 2009; Forster et al., 2007). It is also worth mentioning the uncertainties related to the scale-dependency. In fact, there is a mismatch between the spatial representativeness of MODIS

acquisition pixels (e.g., 500 m) and that of Landsat (30 m), which leads to intrinsic variability of the measurements (Chen et al., 2019; Chrysoulakis et al., 2018). However, as already emphasized in previous studies (Mira et al., 2015; Moustafa et al., 2017), validation techniques provide a reasonable estimate of albedo from MODIS products across homogeneous landscapes (e.g., the two forest- and the three cropland-dominated landscapes).

Lastly, I did not consider the effect of spatial autocorrelation that may affect the significance of the statistic test (Fletcher & Fortin, 2018). Nevertheless, the aim of this study is not to attempt spatial predictions (Feilhauer et al., 2012) of $RF_{\Delta\alpha}$ and $GWI_{\Delta\alpha}$.

Conclusions

My study shows that there are significant contributions (R^2=0.64) to the overall variation in albedo due to landscapes (i.e., ecoregions), cover types (i.e., landscape mosaics), and seasons (i.e., seasonality). Variation in seasons contributes more than landscape composition (~16% and 11%, respectively) in variations of albedo. By integrating spatial (e.g., five landscapes within ecoregions) and temporal (e.g., inter and intra-annual) patterns as main drivers of albedo variation, I found that cropland-dominated landscapes produce a higher intra-annual variability of albedo under drier, wetter, and normal weather conditions, likely due to more frequent disturbances (i.e., management activities). Forest-dominated landscapes have higher albedo in drier and wetter years than that in normal years, whereas only one crop-dominated landscape shows statistically lower albedo under normal conditions than that under drier and wetter ones. This indicates a different response to changes in climatic conditions from forest- and cropland-dominated landscapes. Regarding albedo contributions to cooling/warming effects, I found that cooling effects of $RF_{\Delta\alpha}$ occur in all landscapes but are higher in the landscape with the highest proportion of forests (FOR_1) (e.g., higher differences between mean cropland and mean forest

albedos). The pattern of $GWI_{\Delta\alpha}$ across the five landscapes is similar to that of $RF_{\Delta\alpha}$, with CO_{2eq} mitigation relative to pre-existing forest vegetation higher in FOR_1 and lower in $CROP_1$ and $CROP_2$. I found that in the landscape with the highest proportion of forest (FOR_1) both drier and wetter conditions can significantly reduce CO_{2eq} mitigation by up to 24% and ~30%, respectively; while the reduction of CO_{2eq} mitigation is significant only in one of the cropland-dominated landscapes ($CROP_3$) under wetter conditions (e.g., 23.3% decrease).

REFERENCES

Abraha, M., Chen, J., Chu, H., Zenone, T., John, R., Su, Y.-J., Hamilton, S. K., & Robertson, G. P. (2015). Evapotranspiration of annual and perennial biofuel crops in a variable climate. *GCB Bioenergy*, *7*(6), 1344–1356. https://doi.org/10.1111/gcbb.12239

Abraha, M., Gelfand, I., Hamilton, S. K., Chen, J., & Robertson, G. P. (2019). Carbon debt of field-scale conservation reserve program grasslands converted to annual and perennial bioenergy crops. *Environmental Research Letters*, *14*(2), 024019. https://doi.org/10.1088/1748-9326/aafc10

Akbari, H., Menon, S., & Rosenfeld, A. (2009). Global cooling: Increasing world-wide urban albedos to offset CO_2. *Climatic Change*, *94*(3–4), 275–286. https://doi.org/10.1007/s10584-008-9515-9

Anderson, R. G., Canadell, J. G., Randerson, J. T., Jackson, R. B., Hungate, B. A., Baldocchi, D. D., Ban-Weiss, G. A., Bonan, G. B., Caldeira, K., Cao, L., Diffenbaugh, N. S., Gurney, K. R., Kueppers, L. M., Law, B. E., Luyssaert, S., & O'Halloran, T. L. (2011). Biophysical considerations in forestry for climate protection. *Frontiers in Ecology and the Environment*, *9*(3), 174–182. https://doi.org/10.1890/090179

Anderson-Teixeira, K. J., Snyder, P. K., Twine, T. E., Cuadra, S. V., Costa, M. H., & DeLucia, E. H. (2012). Climate-regulation services of natural and agricultural ecoregions of the Americas. *Nature Climate Change*, *2*(3), 177–181. https://doi.org/10.1038/nclimate1346

Antón, A., Cebrian, J., Heck, K. L., Duarte, C. M., Sheehan, K. L., Miller, M.-E. C., & Foster, C. D. (2011). Decoupled effects (positive to negative) of nutrient enrichment on ecosystem services. *Ecological Applications*, *21*(3), 991–1009. https://doi.org/10.1890/09-0841.1

Bala, G., Caldeira, K., Wickett, M., Phillips, T. J., Lobell, D. B., Delire, C., & Mirin, A. (2007). Combined climate and carbon-cycle effects of large-scale deforestation. *Proceedings of the National Academy of Sciences*, *104*(16), 6550–6555. https://doi.org/10.1073/pnas.0608998104

Barnes, B. V., & Spurr, S. H. (1998). *Forest Ecology* (4th ed.). John Wiley & Sons, New York, 774. ISBN: 978-0-471-30822-5

Barnes, C. A., & Roy, D. P. (2010). Radiative forcing over the conterminous United States due to contemporary land cover land use change and sensitivity to snow and interannual albedo variability. *Journal of Geophysical Research*, *115*(G4). https://doi.org/10.1029/2010JG001428

Bennett, A. F., Radford, J. Q., & Haslem, A. (2006). Properties of land mosaics: Implications for nature conservation in agricultural environments. *Biological Conservation*, *133*(2), 250–264. https://doi.org/10.1016/j.biocon.2006.06.008

Berbet, M. L. C., & Costa, M. H. (2003). Climate change after tropical deforestation: Seasonal variability of surface albedo and its effects on precipitation change. *Journal of Climate*,

16(12), 2099–2104. https://doi.org/10.1175/1520-0442(2003)016<2099:CCATDS>2.0.CO;2

Betts, R. A. (2000). Offset of the potential carbon sink from boreal forestation by decreases in surface albedo. *Nature*, *408*(6809), 187–190. https://doi.org/10.1038/35041545

Betts, R. A. (2001). Biogeophysical impacts of land use on present-day climate: Near-surface temperature change and radiative forcing. *Atmospheric Science Letters*, *2*(1–4), 39–51. https://doi.org/10.1006/asle.2001.0037

Bird, D. N., Kunda, M., Mayer, A., Schlamadinger, B., Canella, L., & Johnston, M. (2008). Incorporating changes in albedo in estimating the climate mitigation benefits of land use change projects. *Biogeosciences Discussions*, *5*(2), 1511–1543. https://doi.org/10.5194/bgd-5-1511-2008

Bonan, G. (2016). *Ecological Climatology: Concepts and Applications* (3rd ed.). Cambridge University Press. https://doi.org/10.1017/CBO9781107339200

Bonan, G. B. (2008). Forests and climate change: Forcings, feedbacks, and the climate benefits of forests. *Science*, *320*(5882), 1444–1449. https://doi.org/10.1126/science.1155121

Boucher, O., Friedlingstein, P., Collins, B., & Shine, K. P. (2009). The indirect global warming potential and global temperature change potential due to methane oxidation. *Environmental Research Letters*, *4*(4), 044007. https://doi.org/10.1088/1748-9326/4/4/044007

Bright, R. M., Zhao, K., Jackson, R. B., & Cherubini, F. (2015). Quantifying surface albedo and other direct biogeophysical climate forcings of forestry activities. *Global Change Biology*, *21*(9), 3246–3266. https://doi.org/10.1111/gcb.12951

Brovkin, V., Boysen, L., Raddatz, T., Gayler, V., Loew, A., & Claussen, M. (2013). Evaluation of vegetation cover and land-surface albedo in MPI-ESM CMIP5 simulations. *Journal of Advances in Modeling Earth Systems*, *5*(1), 48–57. https://doi.org/10.1029/2012MS000169@10.1002/(ISSN)1942-2466.MPIESM1

Brown, D. G., Pijanowski, B. C., & Duh, J. D. (2000). Modeling the relationships between land use and land cover on private lands in the Upper Midwest, USA. *Journal of Environmental Management*, *59*(4), 247–263. https://doi.org/10.1006/jema.2000.0369

Cai, H., Wang, J., Feng, Y., Wang, M., Qin, Z., & B. Dunn, J. (2016). Consideration of land use change-induced surface albedo effects in life-cycle analysis of biofuels. *Energy & Environmental Science*, *9*(9), 2855–2867. https://doi.org/10.1039/C6EE01728B

Campbell, G. S., & Norman, J. M. (1998). *Introduction to Environmental Biophysics* (2nd ed.). Springer, New York, 286.

Carrer, D., Pique, G., Ferlicoq, M., Ceamanos, X., & Ceschia, E. (2018). What is the potential of cropland albedo management in the fight against global warming? A case study based on

the use of cover crops. *Environmental Research Letters*, *13*(4), 044030. https://doi.org/10.1088/1748-9326/aab650

Chapman, K. A. & Brewer R. (2008). *Prairie and Savanna in Southern Lower Michigan: History, Slassification, Ecology*. Michigan Botanic Club, 47, 48.

Chen, J., Brosofske, K. D., Noormets, A., Crow, T. R., Bresee, M. K., Le Moine, J. M., Euskirchen, E. S., Mather, S. V., & Zheng, D. (2004). A working framework for quantifying carbon sequestration in disturbed land mosaics. *Environmental Management*, *33*(1), S210–S221. https://doi.org/10.1007/s00267-003-9131-4

Chen, J., Sciusco, P., Ouyang, Z., Zhang, R., Henebry, G. M., John, R., & Roy, David. P. (2019). Linear downscaling from MODIS to Landsat: Connecting landscape composition with ecosystem functions. *Landscape Ecology*, *34*(12), 2917–2934. https://doi.org/10.1007/s10980-019-00928-2

Chen, J., Wan, S., Henebry, G., Qi, J., Gutman, G., Sun, G., & Kappas, M. (2013). *Dryland East Asia: Land Dynamics Amid Social and Climate Change*. Walter de Gruyter, Berlin, Boston, 470.

Cherubini, F., Bright, R. M., & Strømman, A. H. (2012). Site-specific global warming potentials of biogenic CO_2 for bioenergy: Contributions from carbon fluxes and albedo dynamics. *Environmental Research Letters*, *7*(4), 045902. https://doi.org/10.1088/1748-9326/7/4/045902

Chrysoulakis, N., Mitraka, Z., & Gorelick, N. (2018). Exploiting satellite observations for global surface albedo trends monitoring. *Theoretical and Applied Climatology*. https://doi.org/10.1007/s00704-018-2663-6

Culf, A. D., Fisch, G., & Hodnett, M. G. (1995). The Albedo of Amazonian forest and ranch land. *Journal of Climate*, *8*(6), 1544–1554. https://doi.org/10.1175/1520-0442(1995)008<1544:TAOAFA>2.0.CO;2

Davin, E. L., Noblet-Ducoudré, N. de, & Friedlingstein, P. (2007). Impact of land cover change on surface climate: Relevance of the radiative forcing concept. *Geophysical Research Letters*, *34*(13). https://doi.org/10.1029/2007GL029678

Dickinson, R. E. (1983). Land surface processes and climate—Surface albedos and energy balance. In *Advances in Geophysics* (Vol. 25, pp. 305–353). Elsevier. https://doi.org/10.1016/S0065-2687(08)60176-4

Eagle, A. J., Henry, L. R., Olander, L. P., Haugen-Kozyra, K., Millar, N., & Robertson, G. P. (2012). Greenhouse gas mitigation potential of agricultural land management in the United States: A synthesis of the literature. Technical Working Group on Agricultural Greenhouse Gases (T-AGG) Report, 10–04, 72.

Euskirchen, E. S., Chen, J., Li, H., Gustafson, E. J., & Crow, T. R. (2002). Modeling landscape net ecosystem productivity (LandNEP) under alternative management regimes. *Ecological Modelling*, *154*(1), 75–91. https://doi.org/10.1016/S0304-3800(02)00052-2

Feilhauer, H., He, K. S., & Rocchini, D. (2012). Modeling species distribution using niche-Based proxies derived from composite bioclimatic variables and MODIS NDVI. *Remote Sensing*, *4*(7), 2057–2075. https://doi.org/10.3390/rs4072057

Fletcher, R., & Fortin, M.-J. (2018). Spatial dependence and autocorrelation. In *Spatial Ecology and Conservation Modeling: Applications with R*. Springer International Publishing, 133–168. https://doi.org/10.1007/978-3-030-01989-1_5

Forster, P., Ramaswamy, V., Artaxo, P., Berntsen, T., Betts, R., Fahey, D., Haywood, J., Lean, J., Lowe, D., Myhre, G., Nganga, J., Prinn, R., Raga, G., Schulz, M., Dorland, R., Bodeker, G., Boucher, O., Collins, W., Conway, T., & Whorf, T. (2007). Changes in Atmospheric Constituents and in Radiative Forcing. In *Climate Change 2007: The Physical Science Basis. Contribution of Working Group I to the 4th Assessment Report of the Intergovernmental Panel on Climate Change*. [Solomon, S., D. Qin, M. Manning, Z. Chen, M. Marquis, K.B. Averyt, M.Tignor and H.L. Miller (eds.)]. Cambridge University Press, Cambridge, United Kingdom and New York, NY, USA.

Fuglestvedt, J. S., Berntsen, T. K., Godal, O., Sausen, R., Shine, K. P., & Skodvin, T. (2003). Metrics of climate change: Assessing radiative forcing and emission indices. *Climatic Change*, *58*(3), 267–331. https://doi.org/10.1023/A:1023905326842

Gelfand I Robertson G P. (2015). Mitigation of greenhouse gas emissions in agricultural ecosystems. In *The Ecology of Agricultural Landscapes: Long-Term Research on the Path to Sustainability*. Oxford University Press, New York, 310–339.

Gelfand, I., Sahajpal, R., Zhang, X., Izaurralde, R. C., Gross, K. L., & Robertson, G. P. (2013). Sustainable bioenergy production from marginal lands in the US Midwest. *Nature*, *493*(7433), 514–517. https://doi.org/10.1038/nature11811

Georgescu, M., Lobell, D. B., & Field, C. B. (2011). Direct climate effects of perennial bioenergy crops in the United States. *Proceedings of the National Academy of Sciences*, *108*(11), 4307–4312. https://doi.org/10.1073/pnas.1008779108

Goosse, H. (2015). *Climate System Dynamics and Modeling*. Cambridge University Press, 357.

Gorelick, N., Hancher, M., Dixon, M., Ilyushchenko, S., Thau, D., & Moore, R. (2017). Google Earth Engine: Planetary-scale geospatial analysis for everyone. *Remote Sensing of Environment*, *202*, 18–27. https://doi.org/10.1016/j.rse.2017.06.031

Govindasamy, B., Duffy, P. B., & Caldeira, K. (2001). Land use changes and northern hemisphere cooling. *Geophysical Research Letters*, *28*(2), 291–294. https://doi.org/10.1029/2000GL006121

Gray, V. (2007). Climate change 2007: The physical science basis summary for policymakers. *Energy & Environment*, *18*(3–4), 433–440. https://doi.org/10.1260/095830507781076194

Haas, G., Wetterich, F., & Köpke, U. (2001). Comparing intensive, extensified and organic grassland farming in southern Germany by process life cycle assessment. *Agriculture, Ecosystems & Environment*, *83*(1–2), 43–53. https://doi.org/10.1016/S0167-8809(00)00160-2

Haines, A. (2003). Climate Change 2001: The Scientific Basis. Contribution of Working Group 1 to the Third Assessment report of the Intergovernmental Panel on Climate Change. J. T. Houghton, Y. Ding, D. J. Griggs, M. Noguer, P. J. van der Winden, X. Dai. Cambridge: Cambridge University Press, 2001, pp. 881, £34.95 (HB) ISBN: 0-21-01495-6; £90.00 (HB) ISBN: 0-521-80767-0. *International Journal of Epidemiology*, *32*(2), 321–321. https://doi.org/10.1093/ije/dyg059

Henderson-Sellers, A., & Wilson, M. F. (1983). Surface albedo data for climatic modeling. *Reviews of Geophysics*, *21*(8), 1743–1778. https://doi.org/10.1029/RG021i008p01743

Houspanossian, J., Giménez, R., Jobbágy, E., & Nosetto, M. (2017). Surface albedo raise in the South American Chaco: Combined effects of deforestation and agricultural changes. *Agricultural and Forest Meteorology*, *232*, 118–127. https://doi.org/10.1016/j.agrformet.2016.08.015

Iqbal, M. (2012). *An Introduction To Solar Radiation*. Elsevier, New York, 390.

Jeong, S.-J., Ho, C.-H., Gim, H.-J., & Brown, M. E. (2011). Phenology shifts at start vs. end of growing season in temperate vegetation over the Northern Hemisphere for the period 1982–2008. *Global Change Biology*, *17*(7), 2385–2399. https://doi.org/10.1111/j.1365-2486.2011.02397.x

Jeong, S.-J., Ho, C.-H., Piao, S., Kim, J., Ciais, P., Lee, Y.-B., Jhun, J.-G., & Park, S. K. (2014). Effects of double cropping on summer climate of the North China Plain and neighbouring regions. *Nature Climate Change*, *4*(7), 615–619. https://doi.org/10.1038/nclimate2266

Jiao, T., Williams, C. A., Ghimire, B., Masek, J., Gao, F., & Schaaf, C. (2017). Global climate forcing from albedo change caused by large-scale deforestation and reforestation: Quantification and attribution of geographic variation. *Climatic Change*, *142*(3–4), 463–476. https://doi.org/10.1007/s10584-017-1962-8

Kaye, J. P., & Quemada, M. (2017). Using cover crops to mitigate and adapt to climate change. A review. *Agronomy for Sustainable Development*, *37*(1), 4. https://doi.org/10.1007/s13593-016-0410-x

Lee, X., Goulden, M. L., Hollinger, D. Y., Barr, A., Black, T. A., Bohrer, G., Bracho, R., Drake, B., Goldstein, A., Gu, L., Katul, G., Kolb, T., Law, B. E., Margolis, H., Meyers, T., Monson, R., Munger, W., Oren, R., Paw U, K. T., … Zhao, L. (2011). Observed increase in local cooling effect of deforestation at higher latitudes. *Nature*, *479*(7373), 384–387. https://doi.org/10.1038/nature10588

Lenton, T. M., & Vaughan, N. E. (2009). The radiative forcing potential of different climate geoengineering options. *Atmospheric Chemistry Physiscs*, *9*(15), 5539–5561

Li, B., Gasser, T., Ciais, P., Piao, S., Tao, S., Balkanski, Y., Hauglustaine, D., Boisier, J.-P., Chen, Z., Huang, M., Li, L. Z., Li, Y., Liu, H., Liu, J., Peng, S., Shen, Z., Sun, Z., Wang, R., Wang, T., … Zhou, F. (2016). The contribution of China's emissions to global climate forcing. *Nature*, *531*(7594), 357–361. https://doi.org/10.1038/nature17165

Liang, S., Zhao, X., Liu, S., Yuan, W., Cheng, X., Xiao, Z., Zhang, X., Liu, Q., Cheng, J., Tang, H., Qu, Y., Bo, Y., Qu, Y., Ren, H., Yu, K., & Townshend, J. (2013). A long-term Global LAnd Surface Satellite (GLASS) data-set for environmental studies. *International Journal of Digital Earth*, *6*(sup1), 5–33. https://doi.org/10.1080/17538947.2013.805262

Loarie, S. R., Lobell, D. B., Asner, G. P., Mu, Q., & Field, C. B. (2011). Direct impacts on local climate of sugar-cane expansion in Brazil. *Nature Climate Change*, *1*(2), 105–109. https://doi.org/10.1038/nclimate1067

Luyssaert, S., Jammet, M., Stoy, P. C., Estel, S., Pongratz, J., Ceschia, E., Churkina, G., Don, A., Erb, K., Ferlicoq, M., Gielen, B., Grünwald, T., Houghton, R. A., Klumpp, K., Knohl, A., Kolb, T., Kuemmerle, T., Laurila, T., Lohila, A., … Dolman, A. J. (2014). Land management and land-cover change have impacts of similar magnitude on surface temperature. *Nature Climate Change*, *4*(5), 389–393. https://doi.org/10.1038/nclimate2196

Mallya, G., Zhao, L., Song, X. C., Niyogi, D., & Govindaraju, R. S. (2013). 2012 Midwest drought in the United States. *Journal of Hydrologic Engineering*, *18*(7), 737–745. https://doi.org/10.1061/(ASCE)HE.1943-5584.0000786

Matthews, H. D., Weaver, A. J., Eby, M., & Meissner, K. J. (2003). Radiative forcing of climate by historical land cover change. *Geophysical Research Letters*, *30*(2). https://doi.org/10.1029/2002GL016098

Merlin, O. (2013). An original interpretation of the wet edge of the surface temperature–albedo space to estimate crop evapotranspiration (SEB-1S), and its validation over an irrigated area in northwestern Mexico. *Hydrology and Earth System Sciences*, *17*(9), 3623–3637. https://doi.org/10.5194/hess-17-3623-2013

Michigan State Climatologist's Office. (2013). *Gull Lake (3504). Michigan State University*. Retrived from http://climate. geo.msu.edu/climate_mi/stations/3504/

Miller, J. N., VanLoocke, A., Gomez-Casanovas, N., & Bernacchi, C. J. (2016). Candidate perennial bioenergy grasses have a higher albedo than annual row crops. *GCB Bioenergy*, *8*(4), 818–825. https://doi.org/10.1111/gcbb.12291

Mira, M., Weiss, M., Baret, F., Courault, D., Hagolle, O., Gallego-Elvira, B., & Olioso, A. (2015). The MODIS (collection V006) BRDF/albedo product MCD43D: Temporal course evaluated over agricultural landscape. *Remote Sensing of Environment*, *170*, 216–228. https://doi.org/10.1016/j.rse.2015.09.021

Moustafa, S. E., Rennermalm, A. K., Román, M. O., Wang, Z., Schaaf, C. B., Smith, L. C., Koenig, L. S., & Erb, A. (2017). Evaluation of satellite remote sensing albedo retrievals over the ablation area of the southwestern Greenland ice sheet. *Remote Sensing of Environment, 198*, 115–125. https://doi.org/10.1016/j.rse.2017.05.030

Muñoz, I., Campra, P., & Fernández-Alba, A. R. (2010). Including CO_2-emission equivalence of changes in land surface albedo in life cycle assessment. Methodology and case study on greenhouse agriculture. *The International Journal of Life Cycle Assessment*, *15*(7), 672–681. https://doi.org/10.1007/s11367-010-0202-5

National Research Council (2010). *Understanding the Changing Planet: Strategic Directions for the Geographical Sciences*. Washington D.C., The National Academies Press. https://doi.org/10.17226/12860

Omernik, J. M., & Griffith, G. E. (2014). Ecoregions of the conterminous United States: Evolution of a hierarchical spatial framework. *Environmental Management, 54*(6), 1249–1266. https://doi.org/10.1007/s00267-014-0364-1

Peters, G. P., Aamaas, B., T. Lund, M., Solli, C., & Fuglestvedt, J. S. (2011). Alternative "global warming" metrics in life cycle assessment: A case study with existing transportation data. *Environmental Science & Technology*, *45*(20), 8633–8641. https://doi.org/10.1021/es200627s

Picard, G., Domine, F., Krinner, G., Arnaud, L., & Lefebvre, E. (2012). Inhibition of the positive snow-albedo feedback by precipitation in interior Antarctica. *Nature Climate Change*, *2*(11), 795–798. https://doi.org/10.1038/nclimate1590

Pielke, R. A., Pitman, A., Niyogi, D., Mahmood, R., McAlpine, C., Hossain, F., Goldewijk, K. K., Nair, U., Betts, R., Fall, S., Reichstein, M., Kabat, P., & Noblet, N. de. (2011). Land use/land cover changes and climate: Modeling analysis and observational evidence. *Wiley Interdisciplinary Reviews: Climate Change*, *2*(6), 828–850. https://doi.org/10.1002/wcc.144

Poeplau, C., & Don, A. (2015). Carbon sequestration in agricultural soils via cultivation of cover crops – a meta-analysis. *Agriculture, Ecosystems & Environment*, *200*, 33–41. https://doi.org/10.1016/j.agee.2014.10.024

R Core Team (2020). *R: A Language and Environment for Statistical Computing.* R Foundation for Statistical Computing: Vienna, Austria. https://www.R-project.org/

Raudsepp-Hearne, C., Peterson, G. D., Tengö, M., Bennett, E. M., Holland, T., Benessaiah, K., MacDonald, G. K., & Pfeifer, L. (2010). Untangling the environmentalist's paradox: Why is human well-being increasing as ecosystem services degrade? *BioScience*, *60*(8), 576–589. https://doi.org/10.1525/bio.2010.60.8.4

Robertson, G. P. (2000). Greenhouse gases in intensive agriculture: Contributions of individual gases to the radiative forcing of the atmosphere. *Science*, *289*(5486), 1922–1925. https://doi.org/10.1126/science.289.5486.1922

Robertson, G. P., Hamilton, S. K., Barham, B. L., Dale, B. E., Izaurralde, R. C., Jackson, R. D., Landis, D. A., Swinton, S. M., Thelen, K. D., & Tiedje, J. M. (2017). Cellulosic biofuel contributions to a sustainable energy future: Choices and outcomes. *Science*, *356*(6345), 2324. https://doi.org/10.1126/science.aal2324

Román, M. O., Schaaf, C. B., Woodcock, C. E., Strahler, A. H., Yang, X., Braswell, R. H., Curtis, P. S., Davis, K. J., Dragoni, D., & Goulden, M. L. (2009). The MODIS (collection V005) BRDF/albedo product: Assessment of spatial representativeness over forested landscapes. *Remote Sensing of Environment*, *113*(11), 2476–2498. https://doi.org/10.1016/j.rse.2009.07.009

Schaetzl, R. J., Darden, J. T., & Brandt, D. S. (2009). *Michigan Geography and Geology*. Pearson Custom Publishing. http://catalog.hathitrust.org/api/volumes/oclc/309340740.html

Seidl, R., Spies, T. A., Peterson, D. L., Stephens, S. L., & Hicke, J. A. (2016). Searching for resilience: addressing the impacts of changing disturbance regimes on forest ecosystem services. *Journal of Applied Ecology*, *53*(1), 120–129. https://doi.org/10.1111/1365-2664.12511

Shao, C., Li, L., Dong, G., & Chen, J. (2014). Spatial variation of net radiation and its contribution to energy balance closures in grassland ecosystems. *Ecological Processes*, *3*(1), 7. https://doi.org/10.1186/2192-1709-3-7

Smith, P., Martino, D., Cai, Z., Gwary, D., Janzen, H., Kumar, P., McCarl, B., Ogle, S., O'Mara, F., Rice, C., Scholes, B., Sirotenko, O., Howden, M., McAllister, T., Pan, G., Romanenkov, V., Schneider, U., Towprayoon, S., Wattenbach, M., & Smith, J. (2008). Greenhouse gas mitigation in agriculture. *Philosophical Transactions of the Royal Society B: Biological Sciences*, *363*(1492), 789–813. https://doi.org/10.1098/rstb.2007.2184

Storelvmo, T., Leirvik, T., Lohmann, U., Phillips, P. C. B., & Wild, M. (2016). Disentangling greenhouse warming and aerosol cooling to reveal Earth's climate sensitivity. *Nature Geoscience*, *9*(4), 286–289. https://doi.org/10.1038/ngeo2670

Sun, Q., Wang, Z., Li, Z., Erb, A., & Schaaf, C. B. (2017). Evaluation of the global MODIS 30 arc-second spatially and temporally complete snow-free land surface albedo and reflectance anisotropy dataset. *International Journal of Applied Earth Observation and Geoinformation*, *58*, 36–49. https://doi.org/10.1016/j.jag.2017.01.011

Tian, L., Chen, J., & Shao, C. (2018). Interdependent dynamics of LAI-albedo across the roofing landscapes: Mongolian and Tibetan Plateaus. *Remote Sensing*, *10*(7), 1159. https://doi.org/10.3390/rs10071159

Wang, K., Liu, J., Zhou, X., Sparrow, M., Ma, M., Sun, Z., & Jiang, W. (2004). Validation of the MODIS global land surface albedo product using ground measurements in a semidesert region on the Tibetan Plateau. *Journal of Geophysical Research: Atmospheres*, *109*(D5). https://doi.org/10.1029/2003JD004229

Wang, Z., Schaaf, C. B., Strahler, A. H., Chopping, M. J., Román, M. O., Shuai, Y., Woodcock, C. E., Hollinger, D. Y., & Fitzjarrald, D. R. (2014). Evaluation of MODIS albedo product (MCD43A) over grassland, agriculture and forest surface types during dormant and snow-covered periods. *Remote Sensing of Environment*, *140*, 60–77. https://doi.org/10.1016/j.rse.2013.08.025

Yuan, Z. Y., & Chen, H. Y. H. (2015). Decoupling of nitrogen and phosphorus in terrestrial plants associated with global changes. *Nature Climate Change*, *5*(5), 465–469. https://doi.org/10.1038/nclimate2549

Zhang, Y., Wang, X., Pan, Y., & Hu, R. (2013). Diurnal and seasonal variations of surface albedo in a spring wheat field of arid lands of Northwestern China. *International Journal of Biometeorology*, *57*(1), 67–73. https://doi.org/10.1007/s00484-012-0534-x

Zhao, K., & Jackson, R. B. (2014). Biophysical forcings of land-use changes from potential forestry activities in North America. *Ecological Monographs*, *84*(2), 329–353. https://doi.org/10.1890/12-1705.1

Zheng, L., Zhao, G., Dong, J., Ge, Q., Tao, J., Zhang, X., Qi, Y., Doughty, R. B., & Xiao, X. (2019). Spatial, temporal, and spectral variations in albedo due to vegetation changes in China's grasslands. *ISPRS Journal of Photogrammetry and Remote Sensing*, *152*, 1–12. https://doi.org/10.1016/j.isprsjprs.2019.03.020

APPENDIX

Table A1: Description of the five United States Environmental Protection Agency (US EPA) Level IV ecoregions that fall within the Kalamazoo River Watershed boundary. Additional information can be found online at https://www.epa.gov/eco-research/ecoregion-download-files-state-region-5#pane-20.

US EPA Level IV ecoregions		
Full name	Abbreviation	Features
Battle Creek Outwash Plain	56b	**Landforms**: broad, flat plain, major drainage during the Pleistocene glaciers receding. **Soils**: well-drained loamy soils (pasture) and sandy soils suitable for corn, soybeans, and grain. **Pre-settlement vegetation**: wet and dry tallgrass prairies, oak savanna.
Michigan Lake Plain	56d	**Landforms**: sandy coastal strip with beaches, high dunes, beaches ridges, mucky inter-dune depressions, and swales. **Soils**: excessively-drained (oak and white pine), poorly-drained (marsh grasses, aspen, silver maple), and well-drained sandy soils (pasture, hay, aspen, cherry, oak, white pine). **Pre-settlement vegetation**: pine, hemlock, beech, sugar maple, treeless marshes, lowland hardwood swamps, and tamarack swamp.
Lake Michigan Moraines	56f	**Landforms**: end and ground moraine. **Soils**: well-drained sandy loams soils (row crops, orchards, oak-hickory-sugar maple forests), poorly-drained sandy and clay loams soils (marsh grasses, aspen, silver maple), finer-textured, less permeable soils (beech-sugar maple forests). **Pre-settlement vegetation**: beech, sugar maple, oak, oak savanna, oak-hickory, hemlock.
Lansing Loamy Plain	56g	**Landforms**: ground moraine, well-drained hills, and poorly-drained linear depressions. **Soils**: medium-textured loamy soils (beech-sugar maple forests), sandy soils (pasture or hay), poorly-drained soils (marsh grasses, aspen, silver maple, and swamp white oak). **Pre-settlement vegetation**: beech-sugar maple forests, associated with basswood, black maple, red oak, and white maple forests (ground moraines), oak-hickory forests (drier end moraines), American elm, red ash, silver maple, tamarack, swamp white oak, and wet prairies (poorly drained linear depressions).
Interlobate Dead Ice Moraines	56h	**Landforms**: coarse-textured end moraine, kames, and outwash sands. **Soils**: sandy loams soils (corn, soybeans, and grain), poorly-drained sandy loams soils (marsh grasses, aspen, and silver maple), well-drained soils (pasture and oak-hickory forests). **Pre-settlement vegetation**: oak savanna, oak-hickory forests, wet and dry tallgrass prairies.

Table A2: Mean (± one standard deviation) of α_{SHO} (%) by cover type and landscapes during 2012 (drier), 2016 (wetter) and 2017 (normal). Mean values ($\bar{X}$) among the three years are also reported.

		Cover type							
	year	Urban	Cropland	Barrens	Forest	Water	Wetlands	Grasslands	All
FOR_1	2012	15.1(±0.7)	16.0(±0.7)	14.6(±0.5)	14.6(±0.6)	13.8(±0.6)	14.2(±0.8)	15.4(0)	14.7(±0.8)
	2016	14.7(±0.7)	15.8(±0.9)	14.2(±0.6)	14.3(±0.6)	13.7(±0.4)	14.1(±0.8)	14.9(0)	14.4(±0.9)
	2017	14.7(±0.8)	15.9(±1.0)	14.0(±0.7)	14.1(±0.7)	13.6(±0.5)	14.0(±0.8)	15.0(0)	14.3(±1.0)
	$\bar{X}$	14.8	15.9	14.2	14.3	13.7	14.1	15.1	14.6
FOR_2	2012	14.1(±1.8)	15.2(±1.0)	14.8(±0.6)	14.4(±1.2)	9.3(±3.5)	14.4(±1.1)	14.3(±1.3)	14.1(±2.3)
	2016	14.0(±1.9)	15.3(±1.2)	14.8(±0.7)	14.2(±1.5)	9.1(±3.6)	14.3(±1.2)	13.9(±1.5)	14.0(±2.4)
	2017	13.6(±1.9)	14.8(±1.1)	14.3(±0.7)	13.7(±1.3)	8.7(±3.5)	8.7(±1.2)	13.5(±1.7)	13.5(±2.3)
	$\bar{X}$	13.9	15.1	14.6	14.1	9.0	14.2	13.9	13.9
$CROP_1$	2012	16.8(±0.5)	16.9(±0.7)	16.5(0)	16.4(±0.9)	16.5(±0.1)	16.4(±0.7)	16.3(±1.0)	16.8(±0.7)
	2016	17.1(±0.6)	17.1(±0.8)	16.5(0)	16.6(±1.0)	16.2(±0.4)	16.6(±0.8)	16.1(±1.2)	17.0(±0.8)
	2017	16.9(±0.6)	17.0(±0.7)	16.5(0)	16.5(±0.9)	16.2(±0.2)	16.4(±0.8)	16.0(±1.7)	16.8(±0.8)
	$\bar{X}$	16.9	17.0	16.5	16.5	16.3	16.5	16.1	16.7
$CROP_2$	2012	16.0(±1.0)	16.7(±0.5)	16.0(0)	16.3(±0.5)	15.3(±0.8)	16.1(±0.5)	16.0(0)	16.5(±0.6)
	2016	16.0(±1.0)	16.7(±0.5)	16.3(0)	16.3(±0.6)	15.6(±0.6)	16.1(±0.5)	15.9(0)	16.5(±0.6)
	2017	15.7(±1.1)	16.4(±0.7)	15.9(0)	15.8(±0.6)	15.2(±0.6)	15.6(±0.4)	15.6(0)	16.1(±0.8)
	$\bar{X}$	15.9	16.6	16.1	16.2	15.4	15.9	15.8	16.4
$CROP_3$	2012	15.2(±1.4)	16.8(±0.8)	16.1(±0.6)	15.9(±1.0)	13.1(±1.2)	15.7(±1.1)	16.8(±0.3)	16.2(±1.4)
	2016	15.3(±1.5)	16.8(±0.9)	16.0(±1.1)	15.8(±1.1)	13.0(±1.1)	15.6(±1.2)	16.7(±0.4)	16.2(±1.5)
	2017	15.2(±1.7)	17.1(±1.1)	16.2(±1.8)	15.8(±1.3)	12.9(±1.2)	15.7(±1.4)	17.0(±0.3)	16.3(±1.7)
	$\bar{X}$	15.3	16.9	16.1	15.9	13.0	15.6	16.8	16.2
Watershed	2012	15.4(±1.3)	16.6(±1.0)	15.3(±1.1)	15.4(±1.1)	12.3(±3.4)	15.6(±1.1)	15.8(±1.8)	15.9(±1.5)
	2016	15.3(±1.4)	16.6(±1.1)	15.2(±1.3)	15.3(±1.3)	12.1(±3.5)	15.5(±1.2)	15.7(±1.8)	15.9(±1.6)
	2017	15.0(±1.5)	16.5(±1.2)	14.8(±1.3)	14.9(±1.4)	11.9(±3.4)	15.2(±1.3)	15.4(±2.0)	15.6(±1.7)
	$\bar{X}$	15.2	16.6	15.1	15.2	12.1	15.4	15.6	15.8

α_{SHO}: white-sky shortwave albedo

FOR_1 and FOR_2: forest-dominated landscapes, with proportion of forest of ~58% and 38%, respectively

$CROP_1$, $CROP_2$, and $CROP_3$: cropland-dominated landscapes, with proportion of cropland of 68%, ~65%, and 57%, respectively

CHAPTER 3. ALBEDO-INDUCED GLOBAL WARMING IMPACT AT MULTIPLE TEMPORAL SCALES WITHIN AN UPPER MIDWEST USA WATERSHED

Abstract

Land surface albedo is a significant regulator of climate. Changes in land use worldwide have greatly reshaped landscapes in the recent decades. Deforestation, agricultural development, and urban expansion alter land surface albedo, each with unique influences on shortwave radiative forcing and global warming impact (GWI). Here, I characterize the changes in landscape albedo-induced GWI ($GWI_{\Delta\alpha}$) at multiple temporal scales, with a special focus on the seasonal and monthly $GWI_{\Delta\alpha}$ over a 19-year period for different land cover types in five ecoregions within a watershed in the upper Midwest, USA. The results show that land cover changes from the original forest exhibited a net cooling effect, with contributions of annual $GWI_{\Delta\alpha}$ varying by cover type and ecoregion. Seasonal and monthly variations of the $GWI_{\Delta\alpha}$ showed unique trends over the 19-year period and contributed differently to the total $GWI_{\Delta\alpha}$. Cropland contributed most to cooling the local climate, with seasonal and monthly offsets of 18% and 83%, respectively, of the annual greenhouse gas emissions of maize fields in the same area. Urban areas exhibited both cooling and warming effects. Cropland and urban areas showed significantly different seasonal $GWI_{\Delta\alpha}$ at some ecoregions. The landscape composition of the five ecoregions could cause different net landscape $GWI_{\Delta\alpha}$.

Introduction

Surface albedo—the fraction of incoming shortwave solar radiation scattered by a surface back to space—is a fundamental component of the Earth's surface energy balance (Hollinger et al., 2010; Myhre et al., 2014). Unlike greenhouse gases (GHGs) that regulate climate by disproportionate interception of longwave radiation that affects the Earth's radiation balance, the warming or cooling effects of surface albedo are directly due to changes in the amounts of shortwave radiation reflected back to outer space, and they are instantaneous. Changes in land uses

worldwide have greatly reshaped landscapes over the past 2-3 thousand years, at an escalating rate since the industrial revolution (Kalnay & Cai, 2003; Pielke et al., 2011; Vitousek et al., 1997; Wackernagel et al., 2002), and Earth's surface albedo has changed accordingly, resulting in alterations of the Earth's radiation balance that are partially responsible for the changing climate.

Globally, deforestation, agricultural development—including forest and grassland conversion—and urban expansion are major sources of albedo change (Pielke et al., 2011; Shao et al., 2014), which in turn can directly affect the Earth's radiation balance. Imbalances due to albedo change is described by the albedo-induced radiative forcing ($RF_{\Delta\alpha}$; W m^{-2})—changes in the fraction of solar radiation reflected back to the atmosphere from the surface of the Earth (Mira et al., 2015). For example, according to the Intergovernmental Panel on Climate Change (IPCC; Forster et al., 2021), the RF of well mixed GHGs—i.e., carbon-dioxide (CO_2), methane (CH_4), and nitrous oxide (N_2O)—has a warming effect equivalent to ~+2.91 W m^{-2}, while the $RF_{\Delta\alpha}$ due to land use and land cover change (LUCC) has a cooling effect equivalent to ~-0.20 W m^{-2}. In other words, albedo changes have offset up to ~7% of the energy imbalance caused by well mixed GHGs, with the offsets varying substantially by region. However, such offset is a global average in reference to LULCC, with dominant changes from forest to non-forest since 1750; therefore, the unknown local contributions of $RF_{\Delta\alpha}$ due to LULCC might play an important role in the overall global average climate regulation effects. As a matter of fact, the scientific understanding of the forcing effects of albedo due to LULCC are ranked as medium-low relative to the rich scientific evidence of the forcing effects of GHGs (Myhre et al., 2014). The albedo-induced warming or cooling can also be converted into equivalents of CO_2 (CO_{2eq}) and/or carbon (C_{eq}) atmospheric radiative forcing via the concept of global warming potential (GWP, $kgCO_{2eq}$ m^{-2} yr^{-1}; Bright & Lund, 2021; Stocker et al., 2014) metric—hereinafter referred to as global warming impact (GWI),

to be in line with other studies (Abraha et al., 2021; Sciusco et al., 2020)—and thus can be compared with the climate impact of other GHGs (i.e., biogeochemical GWI). For example, Houspanossian et al. (2017) found that conversion from forests to croplands, forests to pastures, and pastures to croplands in dry subtropical forests of South America offset 12–27 MgC_{eq} ha^{-1} during a 12-year period, or 15% to 55% of the total C emissions due to deforestation. In Europe, Carrer et al. (2018) reported that inclusion of cover crops in annual cropping systems could have cooling effects equivalent to a mitigation of -0.03 MgC_{eq} ha^{-1} yr^{-1}; while Lugato et al. (2020) showed that such mitigation potential due to the inclusion of cover crops could be substantially enhanced by growing high-albedo chlorophyll-deficient cover crops. In southwest Michigan, USA, Chen et al. (2021) estimated that land conversion from forest to maize (*Zea mays*) can provide a cooling equivalent to a mitigation of -0.043 MgC_{eq} ha^{-1} yr^{-1} due to a 0.051 (i.e., 5.1%) increase in albedo. At watershed scale, Sciusco et al. (2020) demonstrated that altered landscapes could produce cooling effects relative to intact native late successional forests typical of pre-European settlement, with a range of -0.1 to -0.4 MgC_{eq} ha^{-1} yr^{-1}, which is the same order of magnitude as many crop management components of GWI (Gelfand et al., 2013; Gelfand & Robertson, 2015).

Despite recognition of the potential importance of albedo modification strategies for regional to global climate mitigation by IPCC (Kauppi & Sedjo, 2003) and stimulating discussions (Cicerone, 2006; Crutzen, 2016) on possible ways of increasing surface albedo to cool the Earth, little effort has been made to understand changes in landscape $RF_{\Delta\alpha}$ or $GWI_{\Delta\alpha}$ in the context of landscape mosaics at broader temporal scales and for multiple anthropogenic LULCC (Chen et al., 2004; Euskirchen et al., 2002; Sciusco et al., 2020). A critical unknown is how different cover types contribute to the total landscape $GWI_{\Delta\alpha}$ at different times of the year. Over the long term

(i.e., years to decades), little is known about whether the intra-annual variations of landscape $GWI_{\Delta\alpha}$ are significant.

Here I build on Sciusco et al. (2020) (i.e., Chapter 2 of this dissertation) to estimate the contributions of $GWI_{\Delta\alpha}$ to the landscape warming or cooling effects at seasonal and monthly time scales over 19 years for multiple ecoregions subtypes. My specific objectives are to quantify for different cover types in different ecoregions of the upper Midwest USA watershed 1) the monthly and seasonal contributions to the total landscape cooling or warming; 2) the variations of $GWI_{\Delta\alpha}$ contributions by cover type, ecoregion, and year; and 3) the magnitude of cooling or warming effects due to land cover change (relative to mature forest cover).

Materials & Methods

Study area and landscape composition

The Kalamazoo River Watershed (5621 km^2; Figure 3.1) is located in southwestern Michigan, USA, and includes portions of 10 counties: Allegan, Barry, Calhoun, Eaton, Hillsdale, Jackson, Kalamazoo, Kent, Ottawa, and Van Buren. Mean annual temperature (1981–2010) is 9.9 °C and average annual precipitation is 900 mm evenly distributed throughout the year (Michigan State Climatologist's Office, 2013). The dominant cover type prior to European settlement in the early 1800s was eastern broadleaved deciduous forest (Brown et al., 2000), with scattered patches of tallgrass prairie, oak savanna, lakes, and wetlands (Chapman & Brewer, 2008). Today, the dominant land cover includes cultivated crops, successional forest stands, pasture-hay grasslands, and two urban areas (Kalamazoo and Battle Creek). Medium to coarse texture soils and mesic climate allow continuous recharge of groundwater (Schaetzl et al., 2009).

Within the watershed, there are five United States Environmental Protection Agency (U.S. EPA) Level IV ecoregions (Figure 3.1), which are defined as areas characterized by unique

combinations of physiographic, geologic, pedologic, botanic, hydrologic, and climatic characteristics (Omernik & Griffith, 2014). Level IV ecoregions have the greatest resolution, and they are Battle Creek Outwash Plain (56b); Michigan Lake Plain (56d); Lake Michigan Moraines (56f); Lansing Loamy Plain (56g); and Interlobate Dead Ice Moraines (56h). For further details, see U.S. EPA at https://www.epa.gov/eco-research/level-iii-and-iv-ecoregions-continental-united-states.

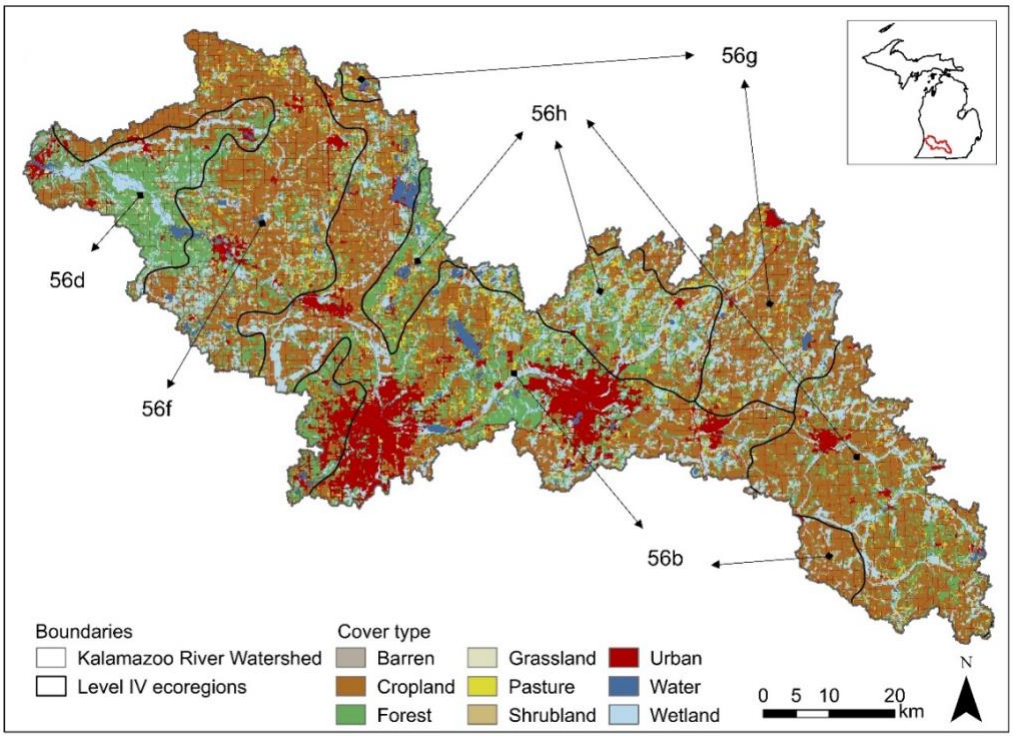

Figure 3.1: The study area of the five United States Environmental Protection Agency (U.S. EPA) Level IV ecoregions and the nine National Land Cover Database (NLCD) cover type classes within the Kalamazoo River Watershed in 2001.

In this study I used the National Land Cover Database (NLCD; Homer et al., 2020; Yang et al., 2018), which provides twenty land cover classes—consequently grouped into nine classes: barren, cropland, forest, grassland, pasture, shrubland, urban, water, and wetland—at 30 m spatial resolution, and with an overall accuracy ranging between 80% and 90%, in the central and western U.S.. Land cover classifications from NLCD are available for the years 2001, 2004, 2006, 2008,

2011, 2013, and 2016. Because land cover maps from NLCD are not obtained annually, unlike albedo data (see next section *Intra-annual changes in albedo*), for years where NLCD data are not available, land cover was assumed similar to previous year. For example, the land cover map for 2002 was assumed to be the same as that of 2001, and for 2017–2019 I assumed the land cover had no significant changes.

Intra-annual changes in albedo

I obtained albedo data at 10:30 a.m. local time (UTC -05; i.e., MODIS Terra morning overpass time) at 500 m spatial resolution at daily time-step for 2001–2019 from the most recent collection (V006) of the MODIS Bidirectional Reflectance Distribution Function (BRDF) MCD43A3 product (cf. https://lpdaac.usgs.gov/products/mcd43d42v006/). The MCD43A3 product was produced by the inversion of a BRDF model against a 16-day moving window of MODIS observations and it contains both the black-sky (i.e., directional-hemispherical reflectance) and white-sky (i.e., bi-hemispherical reflectance) albedos (Wang et al., 2014). I considered white-sky surface albedo (α) at a shortwave length of 0.3–5.0 μm by growing season and month during 2001–2019. For each image, I selected the "*Albedo_WSA_shortwave*" (i.e., white-sky albedo) band and rescaled it to 0–1. For quality control, I applied the quality band "*BRDF_Albedo_Band_Mandatory_Quality_shortwave*" (i.e., the full BRDF inversion) (Chrysoulakis et al., 2018; Sciusco et al., 2020) by filtering out pixels not meeting the control protocols. I then used an additional quality band (i.e., "*Snow_BRDF_Albedo*") from the MCD43A2 product (accessed at https://lpdaac.usgs.gov/products/mcd43a2v061/) to further filter and select quality snow-albedo retrievals in the MCD43A3 product.

Growing season and monthly albedos (α_{gs} and α_{mo}, respectively) at 10:30 a.m. local time (UTC -05) were derived by stacking (i.e., median image composite) the daily images into growing

seasons or months by year. Specifically, α_{gs} accounted for 19 composites (2001–2019), while α_{mo} accounted for 11 composites (January–December, over the 19-year period, less March, which was not considered because few images were available, due likely to the high cloud cover in this month). I applied the same methodology as Jeong et al. (2011) and Sciusco (2020) to identify the growing season for each year. Briefly, I used the enhanced vegetation index (EVI) to identify the growing season by detecting the EVI inflection points (i.e., the dates) when maximum and minimum change rate in greenness occurred over the entire watershed. I obtained 16-day composite time series of EVI at a 250 m spatial resolution from the most recent collection (V006) of the MODIS MYD13Q1 product (cf. https://lpdaac.usgs.gov/products/myd13q1v006/). Similar to the quality control protocols for albedo product, I filtered and selected only good quality EVI pixels by applying the quality band "*SummaryQA*" from the MYD13Q1 product. Both albedo and EVI acquisitions referred to approximately 10:30 a.m. and 1:00 p.m. local time (UTC -05), respectively, when MODIS (Terra and Aqua, respectively) passes over the study area.

I employed the Google Earth Engine platform (Gorelick et al., 2017) to analyze and process all datasets, while ArcMap (v. 10.6) was used to perform the zonal statistical analysis to calculate the proportion of NLCD cover types within each MODIS pixel and to extract α_{gs} and α_{mo} values by pixel before statistical analysis in RStudio v.1.2.5033 (R Core Team, 2020).

Albedo-induced global warming impact ($GWI_{\Delta\alpha}$)

I employed the linear downscaling approach of Chen et al. (2019) to estimate surface albedo of cover type *i* ($\hat{\alpha}_{si}$) at each MODIS pixel. Briefly, for a MODIS pixel, $\hat{\alpha}_{si}$ is considered as the sum of surface albedo of cover type *i* (α_{si}) within each MODIS pixel, as follows:

$$\hat{\alpha}_{si}(t) = \left[\sum\left(k_i \times \hat{\alpha}_{si}(t)\right)\right] + \varepsilon_t \quad (3.1)$$

where $\hat{\alpha}_{si}$ is the estimated surface albedo of cover type *i* for a time-period *(t)* (i.e., GS: *t* = 2001–2019 and monthly: *t* = January–December, less March), k_i is the proportion (0–1) of cover type in each MODIS pixel, and ε_t represents model residuals.

The calculation of landscape albedo-induced radiative forcing ($RF_{\Delta\alpha}$) and global warming impact ($GWI_{\Delta\alpha}$) is based on the change in surface albedo due to land cover conversion. This is normally considered as the surface albedo difference ($\Delta\alpha_s$) between a cover type *i* and the native vegetation cover type (i.e., the reference; Sciusco et al., 2020), here forest as the dominant land cover type prior to European settlement (Brown et al., 2000). Thus, the surface albedo difference of cover type *i* ($\Delta\alpha_{si}$) for growing season and monthly periods and for each ecoregion at 10:30 a.m. local time (UTC -05) is calculated as:

$$\Delta_{\alpha_{si}} = (\hat{\alpha}_{si} - \hat{\alpha}_{sf}) \quad (3.2)$$

where $\hat{\alpha}_{si}$ and $\hat{\alpha}_{sf}$ are the estimated surface albedos of cover type *i* and of the reference forest *f* for growing season and monthly periods and for each ecoregion. I assumed that all land conversions occurred from forest to cropland, pasture, or urban—with the exception of barren, grassland, and shrubland (in low percentage within the study area), and current water and wetland covers (i.e., for which we excluded conversion from forest). I calculated $\Delta\alpha_{si}$ only when the proportion of a cover type *i* was ≥ 80% of the 500 m MODIS pixel. Hence, only cropland, forest, pasture, and urban covers will be considered in this study.

I then used $\Delta\alpha_{si}$ to calculate the instantaneous albedo-induced radiative forcing at the top-of-atmosphere ($RF_{\Delta\alpha}$; W m^{-2}) using the solar radiation at the Earth's surface, as follows (Bright et al., 2012; Xu et al., 2020):

$$RF_{\Delta\alpha} = -(SW_{TOA} \times \Delta\alpha_p) \quad (3.3)$$

where SW_{TOA} is the incident shortwave radiation at the top-of-atmosphere (TOA) and $\Delta\alpha_p$ is the change in planetary albedo. Changes in planetary albedo ($\Delta\alpha_p$) are linearly related to changes in surface albedo ($\Delta\alpha_{si}$) as follows (Bright et al., 2012; Cherubini et al., 2012; Lenton & Vaughan, 2009; Muñoz et al., 2010):

$$\Delta\alpha_p = f_a \times \Delta\alpha_{si} \quad (3.4)$$

where f_a is a two-way atmospheric transmittance parameter that accounts for both the reflection and absorption of solar radiation through the atmosphere, and it can be decomposed into downward and upward transmittance coefficients as follows (Lenton & Vaughan, 2009):

$$f_a = K_T \times T_a \quad (3.5)$$

where the clearness index K_T is the fraction (i.e., %) of SW_{TOA} reaching the Earth's surface, T_a is the upward atmospheric transmittance factor (i.e., the fraction of the radiation reflected by the Earth's surface back at the top-of-atmosphere). In turn, T_a is calculated as:

$$T_a = \frac{SW_{in}}{SW_{TOA}} \quad (3.6)$$

where SW_{in} and SW_{TOA} are the incident shortwave radiation at the surface and at TOA, respectively. By replacing Eqs. 3.4, 3.5 and 3.6 in 3.3, I obtained the following equation (Bright et al., 2012; Carrer et al., 2018; Xu et al., 2020):

$$RF_{\Delta\alpha} = -(SW_{in} \times K_T \times \Delta\alpha_{si}) \quad (3.7)$$

where $RF_{\Delta\alpha}$ (W m^{-2}) is the landscape albedo-induced radiative forcing at the top-of-atmosphere at 10:30 a.m. local time (UTC -05), SW_{in}, K_T, and $\Delta\alpha_{si}$ are the incident shortwave radiation at the surface, the clearness index, and the surface albedo difference between a cover type *i* and the reference forest for growing season and monthly periods and for each ecoregion, respectively. The incident shortwave radiation at the surface (SW_{in}) and the clearness index (K_T) were derived from the solar and meteorological dataset NASA POWER (Sparks, 2020) at daily time-step for multiple

locations (i.e., five Level IV ecoregions) within the Kalamazoo River Watershed. I then averaged SW_{in} and K_T values to match the 19 growing seasons and the 11 months. I also calculated $RF_{\Delta\alpha}$ by using the upward atmospheric transmittance factor (T_a; Eq. 3.6) as in Carrer et al. (2018) and Sciusco et al. (2020), although the differences in $RF_{\Delta\alpha}$ calculated with the use of K_T and T_a were negligible, so I decided to only report $RF_{\Delta\alpha}$ calculated with K_T (Eq. 3.7). Positive or negative values of $RF_{\Delta\alpha}$ indicate warming or cooling effects, respectively.

Lastly, I calculated the landscape $GWI_{\Delta\alpha}$ (Bright et al., 2012; Carrer et al., 2018; Xu et al., 2020) as follows:

$$GWI_{\Delta\alpha} = \left(\frac{A \times RF_{\Delta\alpha}}{AF(t) \times rf_{CO_2}} \frac{1}{TH}\right) \quad (3.8)$$

where $GWI_{\Delta\alpha}$ ($kgCO_{2eq}$ m^{-2} yr^{-1}) is the landscape albedo-induced global warming impact for growing season and monthly periods and for each ecoregion at 10:30 a.m. local time (UTC -05), A is the area for which the hypothesized albedo change occurred (here normalized to 1 m^2), $AF(t)$ is the CO_2 airborne fraction that remains in the atmosphere at time (t) following a single pulse emission, rf_{CO_2} is the marginal RF for CO_2 emissions at a given atmospheric concentration, and TH represents the time horizon of global warming. The parameter $AF(t)$ is modeled with an exponential function through multi-model impulse response function analysis (Joos et al., 2013) as follows:

$$AF(t) = a_0 + \sum_{i=1}^{3} \left[a_i e^{-t/\tau_i}\right] \quad (3.9)$$

where t represents the time in years, a_i and τ_i are the fitted coefficients representing the decay of CO_2 pulse emission in the atmosphere over time. The recommended mean coefficients obtained from the multi-model impulse response function analysis are: a_0=0.2173 (the fraction of CO_2 that remains permanently in the atmosphere); a_1=0.2240; a_2=0.2824; a_3=0.2763; τ_1=394.4; τ_2=36.54; and τ_3=4.304 (Joos et al., 2013).

Lastly, rf_{CO_2} is kept as a constant at 0.908 W $kgCO_2^{-1}$ (Bright et al., 2015; Carrer et al., 2018; Muñoz et al., 2010), while *TH* is fixed at 100 years (i.e., the number of time steps the GWI is then divided by; Boucher et al., 2009; Kaye & Quemada, 2017).

With Eq. 3.8 I calculate the equivalent $RF_{\Delta\alpha}$ that a unit area of *A* would have at global scale. Positive or negative values of $GWI_{\Delta\alpha}$ indicate effects equivalent to CO_2 emission or mitigation, respectively. Here I report results of landscape seasonal and monthly $GWI_{\Delta\alpha}$ ($GWI_{\Delta\alpha gs}$ and $GWI_{\Delta\alpha mo}$, respectively) expressed with units of MgC_{eq} ha^{-1} gs^{-1} and MgC_{eq} ha^{-1} mo^{-1}, respectively, and referred to at 10:30 a.m. local time (UTC -05). Positive or negative values of $GWI_{\Delta\alpha}$ indicate effects equivalent to C emissions or mitigations, respectively.

Contributions of land cover change to $GWI_{\Delta\alpha}$

I performed a nested analysis of variance (ANOVA) with repeated measurements (i.e., growing season and monthly periods) to quantify the contribution to landscape $GWI_{\Delta\alpha}$ by cover type and ecoregion for the growing season and monthly periods. Specifically, I looked at contributions among and within the five ecoregions, with two linear models:

$$GWI_{\Delta\alpha}(t) = (ecoregion \times cover\ type)(t) \quad (3.9)$$

$$GWI_{\Delta\alpha}(t) = cover\ type\ (t) \quad (3.10)$$

where *ecoregion* refers to the five Level IV ecoregions (i.e., 56b, 56d, 56f, 56g, and 56h) and *cover type* refers to the three cover types (i.e., cropland, pasture, and urban) used to determine the albedo difference from the reference forest (Eq. 3.2) for growing season and monthly periods and for each ecoregion. Prior to running the ANOVA, I checked for normal distribution of the residuals (i.e., normality and heteroscedasticity assumptions) and outliers, and performed the Mauchly's test (i.e., sphericity assumption) when necessary. Wherever the sphericity assumption was violated, I applied the Greenhouse-Geisser corrections. I then calculated the generalized eta-squared (η^2)

(Bakeman, 2005) to examine the variance of dependent variable $GWI_{\Delta\alpha}$ by ecoregion, cover type and their interactions. Lastly, I carried out a post-hoc Tukey test analysis to see whether differences in the least square means (LSMs) of $GWI_{\Delta\alpha}$ among and within cover type and ecoregions were significant. All analyses were carried out in RStudio v. 1.2.5033 (R Core Team, 2020), using the R-packages "*ez*", "*nlme*", "*multcomp*", and "*lsmeans*" (Hothorn et al., 2020; Lawrence, 2016; Lenth, 2018; Pinheiro et al., 2017).

Results

Land use land cover change

The dominant land cover types in the Kalamazoo River Watershed, cropland, forest, pasture, and urban cover, underwent detectable changes during 2001–2016 (Table 3.1).

Table 3.1: Land cover composition in ha (%) of the Kalamazoo River Watershed and net gain (+) and loss (-) for each cover type during the period 2001–2016.

	Land cover composition		Land cover gain (+) or loss (–)
	ha(%)		
Cover type	2001	2016	2001–2016
Cropland	215869(40.90)	215155(40.80)	-714(-0.33)
Forest	115393(21.90)	113893(21.60)	-1500(-1.30)
Pasture	28382(5.40)	27296(5.20)	-1087(-3.83)
Urban	66759(12.70)	68743(13.00)	+1984(+2.89)

Declines were highest in forest (1500 ha, -1.3%), followed by pasture (1087 ha, -3.83%) and cropland (714 ha, -0.33%). Gains occurred in urban cover type (~2000ha, ~+3%). Cropland, forest, and pasture were converted into a variety of cover types (Table 3.2): cropland was primarily converted into urban (1157 ha), pasture (776 ha), and forest (137 ha), forest was largely converted into urban (515 ha) and cropland (164 ha), while pasture was mostly converted into cropland (1456 ha) and urban (197 ha).

Table 3.2: Pivot table showing the land cover conversion in ha of each cover type during the period 2001–2016 across the Kalamazoo River Watershed. Values underlined indicate the main land conversions, while "*" indicates no land conversion.

	Land cover conversion (ha) 2001–2016				
2001 \ 2016	Cropland	Forest	Pasture	Urban	$Total_{2001}$
Cropland	212802*	<u>137</u>	<u>776</u>	<u>1157</u>	214872
Forest	<u>164</u>	113337*	9	<u>515</u>	114025
Pasture	<u>1456</u>	57	26467*	<u>197</u>	28176
Urban	16	21	8	66704*	66748
$Total_{2016}$	214437	113552	27259	68573	423821

Albedo and GWI$\Delta\alpha$ in time and space

The linear downscaling model (Eq. 3.1) showed that each cover type contributed differently to total α_{gs} (adj. R^2=0.995) and α_{mo} (adj. R^2=0.745) (Table A3). The four cover types had an overall average α_{gs} of 0.16±0.013, with cropland having the highest α_{gs} at 0.17±0.002, followed closely by pasture (0.16±0.003), and urban and forest (0.15±0.004) covers (Table A4). On the other hand, the α_{mo} (overall average: 0.23±0.134) had a higher variation than α_{gs} and was higher in January, February, and December with a maximum of 0.46±0.109 in February (Table A4). Other months exhibited lower α_{mo}, with a minimum of 0.14±0.017 in November. Cropland and pasture had the highest α_{mo} (0.28±0.183 and 0.25±0.156, respectively). However, the remaining cover types ranked differently for α_{mo} than for α_{gs}, decreasing in the order urban (0.22±0.119) and forest (0.19±0.080). As with α, $\Delta\alpha$ varied substantially across cover types but it was relatively constant within a cover type among the ecoregions (Table A5 and Figure 3.2a-b). In particular, $\Delta\alpha_{gs}$ ranged from -0.001±0.003 for urban to 0.026±0.004 for cropland cover (Table A5 and Figure 3.2a), while $\Delta\alpha_{mo}$ had higher variation and ranged from 0.024±0.040 for urban to 0.089±0.108 for cropland cover (Table A5 and Figure 3.2b).

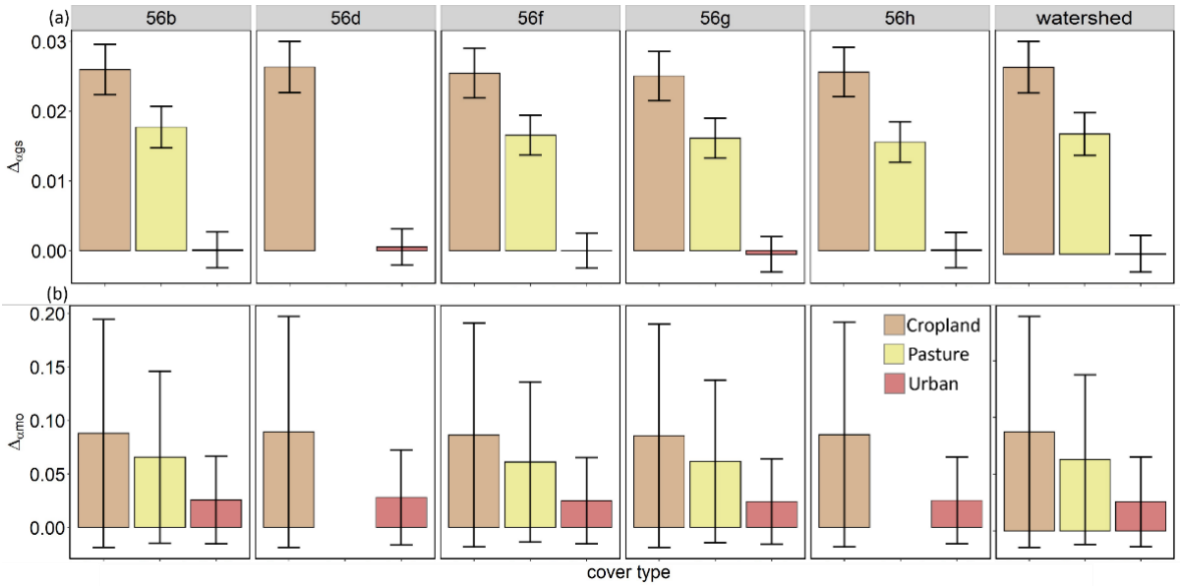

Figure 3.2: Albedo difference between a cover type *i* and the forest for (a) growing season ($\Delta\alpha_{gs}$) and (b) monthly ($\Delta\alpha_{mo}$) periods, respectively, within the five Level IV ecoregions and the entire Kalamazoo River Watershed during 2001–2019 (see Table A5 in the Appendix).

The average $GWI_{\Delta\alpha}$ showed an overall cooling effect (Table A6 and Figure 3.3a-b) for most cover types, with the exception for urban, which showed neutral effects.

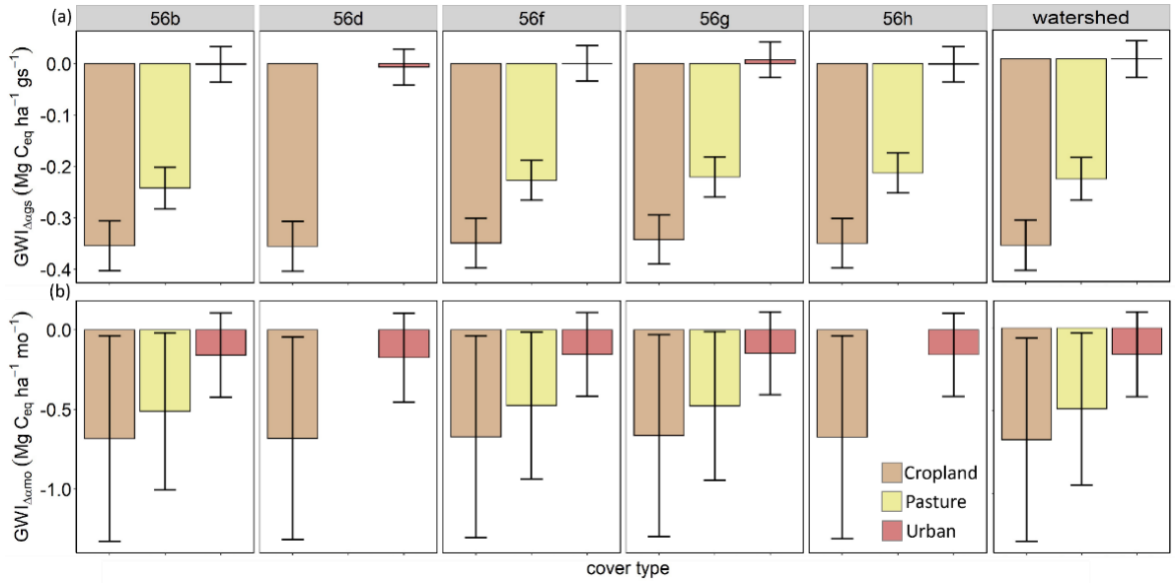

Figure 3.3: Albedo-induced global warming impact ($GWI_{\Delta\alpha}$) for (a) growing season ($GWI_{\Delta\alpha gs}$, MgC_{eq} ha^{-1} gs^{-1}) and (b) monthly ($GWI_{\Delta\alpha mo}$, MgC_{eq} ha^{-1} mo^{-1}) periods, respectively, within the five Level IV ecoregions and the entire Kalamazoo River Watershed during 2001–2019 (see Table A6 in Appendix).

Overall, cropland cover type had seasonal and monthly average cooling effects equivalent to -0.35±0.05 MgC_{eq} ha^{-1} gs^{-1} and -0.68±0.61 MgC_{eq} ha^{-1} mo^{-1}, respectively (Table A6 and Figure 3.3a-b), with highest cooling effects equivalent to -0.47 MgC_{eq} ha^{-1} gs^{-1} (in 2015 for Ecoregions 56b, 56d, 56f, and 56h; Tables A7.1-A7.2-A7.3-A7.5) and -2.15 MgC_{eq} ha^{-1} mo^{-1} (in February for Ecoregion 56b; Table A8.1), for the two periods, respectively. These cooling effects represented ~26% and ~68% more than the seasonal and monthly annual averages, respectively. On the other hand, urban cover (seasonal and monthly averages effects equivalent to -0.001±0.034 MgC_{eq} ha^{-1} gs^{-1} and -0.158±0.256 MgC_{eq} ha^{-1} mo^{-1}, respectively; Table A6), was the only cover type showing neutral effects.

All three cover types showed similar trends in $GWI_{\Delta\alpha gs}$ during 2001–2019 across the five ecoregions (Tables A7.1–A7.5 and Figure 3.4a) with similar rises and falls from the average of $GWI_{\Delta\alpha gs}$ values.

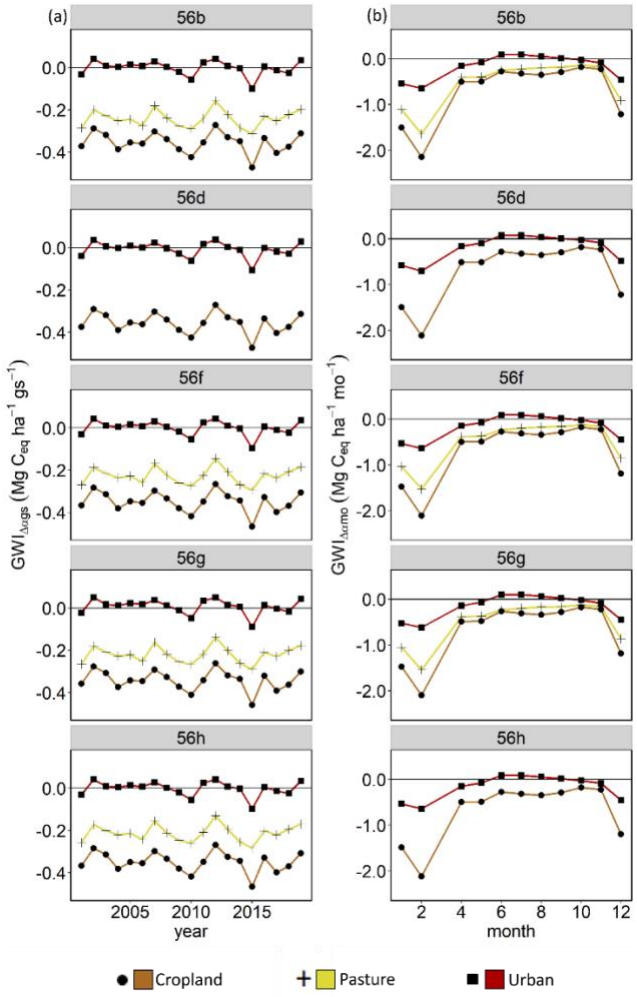

Figure 3.4: Albedo-induced global warming impact ($GWI_{\Delta\alpha}$) for a given cover type within the five Level IV ecoregions. Panels (a) and (b) represent the $GWI_{\Delta\alpha}$ for the growing season ($GWI_{\Delta\alpha gs}$; MgC_{eq} ha^{-1} gs^{-1}; during 2001–2019) and monthly ($GWI_{\Delta\alpha mo}$; MgC_{eq} ha^{-1} mo^{-1}; during January–December, less March) periods, respectively. Positive and negative values of $GWI_{\Delta\alpha gs}$ and $GWI_{\Delta\alpha mo}$ indicate warming and cooling effects, respectively, equivalent to carbon (C_{eq}; emission and mitigation, respectively) during 19-year growing season and months, respectively.

For cropland, cooling effects of $GWI_{\Delta\alpha gs}$ ranged between -0.39 and -0.47 MgC_{eq} ha^{-1} gs^{-1}, -0.25 and -0.31 MgC_{eq} ha^{-1} gs^{-1} for pasture, and -0.01 and -0.11 MgC_{eq} ha^{-1} gs^{-1} for urban. Urban was the only cover type showing also warming effects of $GWI_{\Delta\alpha gs}$ that raged between 0.01 and 0.05 MgC_{eq} ha^{-1} gs^{-1}. The inter-monthly variation of $GWI_{\Delta\alpha mo}$ for cropland, pasture, and urban cover showed similar trends with higher cooling effects in January, February, and December (Tables A8.1–A8.5 and Figure 3.4b). Among these cover types, the highest cooling occurred in

cropland (-0.18 to -2.15 MgC_{eq} ha^{-1} mo^{-1}), followed by pasture (-0.13 to -1.64 MgC_{eq} ha^{-1} mo^{-1}) and urban (-0.02 to -0.470 MgC_{eq} ha^{-1} mo^{-1}) cover. For the three cover types, $GWI_{\Delta\alpha mo}$ was relatively constant from April–November; however, urban had slightly bell-shaped trends with small warming effects in June and July (0.01 to 0.1 MgC_{eq} ha^{-1} mo^{-1}; Tables A8.1–A8.5 and Figure 3.4b) and cropland had an inverted bell-shaped trend with slight rises in June and October. Lastly, pasture (in Ecoregions 56b-56f-56g) had relatively constant trend. The variation among ecoregions in $GWI_{\Delta\alpha gs}$ was significant ($p<0.001$) by ecoregion, cover type, and their interactions (ANOVA model in Eq. 3.9; Table A9), while the variation in $GWI_{\Delta\alpha mo}$ was significant ($p<0.001$) only by cover type. Neither years nor months were significant for $GWI_{\Delta\alpha}$. Most of the variation in $GWI_{\Delta\alpha gs}$ was explained by cover type (η^2=~95%), followed by the interaction between ecoregions and cover type (η^2=~52%) and ecoregions (η^2=32%). In comparison, the variation in $GWI_{\Delta\alpha mo}$ was almost equally explained by ecoregion, cover type, and their interactions, although only cover type was significant (η^2=~24% at $p<0.001$). The variation in both $GWI_{\Delta\alpha gs}$ and $GWI_{\Delta\alpha mo}$ within ecoregions (Eq. 3.10; Table A9), however, was significant ($p<0.001$) by cover type, which explained more of the variation in $GWI_{\Delta\alpha gs}$ (η^2=99%) than in $GWI_{\Delta\alpha mo}$ (η^2=65%).

A post-hoc Tukey test analysis (Figure 3.5a-b) showed that, within each ecoregion, the least square means (LSMs) for $GWI_{\Delta\alpha gs}$ had low variability and were significantly different among the cover types (Figure 3.5a). The LSMs for $GWI_{\Delta\alpha mo}$ were more variable, and many cover types had statistically similar means (Figure 3.5b). Among ecoregions, the LSMs of cropland $GWI_{\Delta\alpha gs}$ at Ecoregion 56g were significantly different from those at Ecoregions 56b and 56d, while the LSMs of urban $GWI_{\Delta\alpha gs}$ at Ecoregion 56g were significantly different from those at Ecoregion ecoregions 56d; however, no significant differences in their LSMs for $GWI_{\Delta\alpha mo}$ were observed (Figure 3.5b).

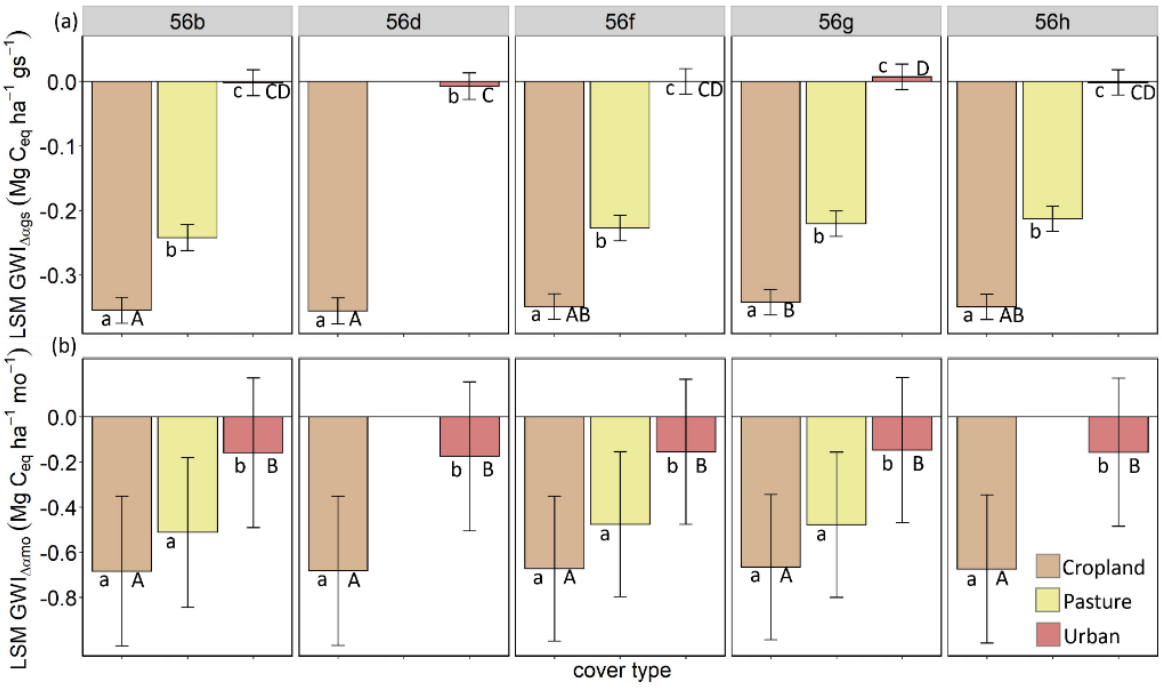

Figure 3.5: The least square means (LSMs) multi-comparison analysis of albedo-induced global warming impact ($GWI_{\Delta\alpha}$) for a given cover type across the five Level IV ecoregions for the (a) growing season ($GWI_{\Delta\alpha gs}$; MgC_{eq} ha^{-1} gs^{-1}; during 2001–2019) and (b) monthly ($GWI_{\Delta\alpha mo}$; MgC_{eq} ha^{-1} mo^{-1}; during January–December, less March) periods, respectively. Whiskers represent the lower and upper limits of the 95% family-wise confidence level of the LSMs. Bars sharing the same letters are not significantly different according to the post-hoc Tukey test analysis. Lowercase letters indicate differences among cover types within the five ecoregions, while uppercase letters indicate differences of same cover type among the five ecoregions.

The overall $GWI_{\Delta\alpha}$ contribution from different seasons and months varied by cover type, and it was exclusively higher during the non-growing season (NGS) than during the growing season (GS) months for all ecoregions (Table A10 and Figure 3.6), with the NGS months being characterized by only cooling effects (Table A11). As a general trend, the highest contributions were in February the lowest in October. Specifically, during the NGS, urban (at all ecoregions) contributed the most to the total cooling effect (between 18% and 31%), followed by pasture (at Ecoregions 56b-56f-56g; contribution between 14% and 25%), and cropland (at all ecoregions; contribution between 14% and 24%). It is worth noting that, during GS months, no cover type had a contribution >8% (i.e., 1/12 of the annual total). Nevertheless, climate regulations of urban (for

all ecoregions) were close to the overall mean value of 8% in April, while cropland (at all ecoregions) and pasture (at Ecoregions 56b, 56f, and 56g) in April and May.

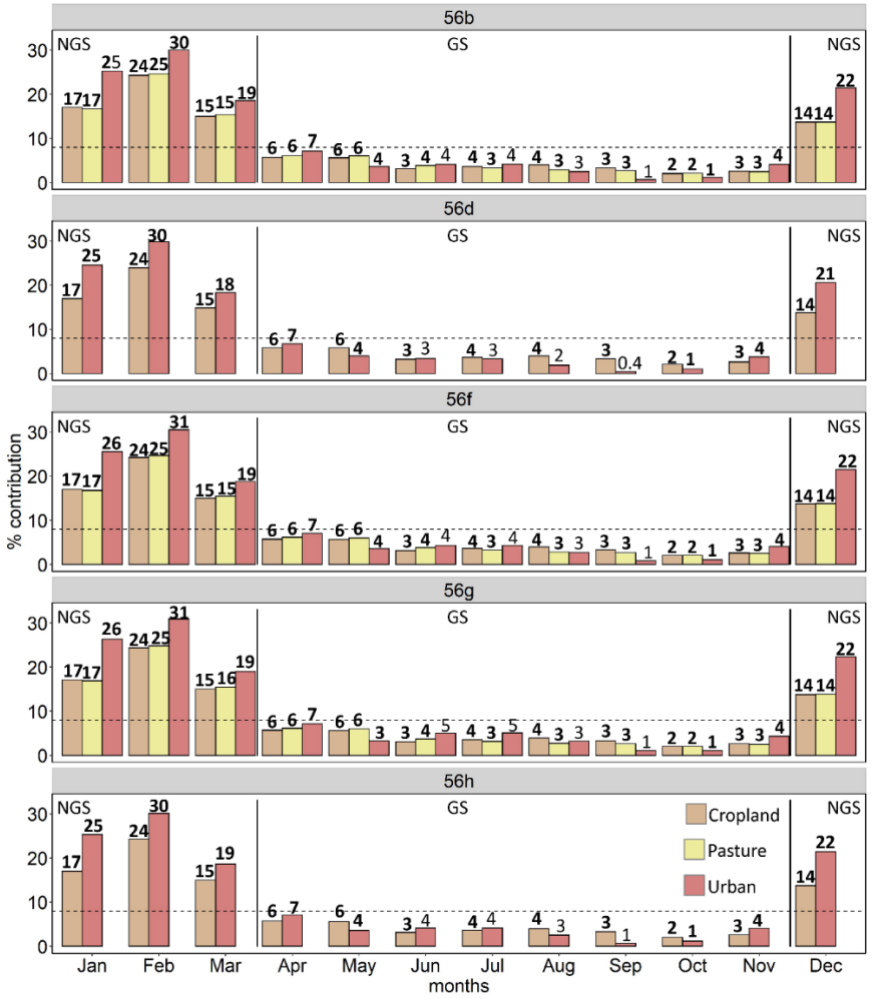

Figure 3.6: Percent contribution of albedo-induced global warming impact ($GWI_{\Delta\alpha}$) to cooling (values in bold) or warming effects by season and month periods for major cover types in the five Level IV ecoregions. The horizontal dashed line represents the average contribution ~8% (i.e., 1/12 of the annual total); the solid vertical lines separate the non-growing season (NGS) from the growing season (GS) months. Values of March were missing and gap-filled as the mean $GWI_{\Delta\alpha}$ of February and April.

Discussion

My results show that albedo-induced global warming impact ($GWI_{\Delta\alpha}$) accounts for significant climate cooling (i.e., C_{eq} mitigation) effects due to land cover changes and land mosaic. Individual contributions varied by cover type, ecoregion, and season/month, with cropland

showing the highest cooling effects, followed by pasture; while urban showed both cooling and warming effects, the latter only during the growing season months. Overall, the cooling effects of monthly $GWI_{\Delta\alpha}$ were higher than the seasonal ones, most likely due to the substantial influence of snow cover on land surface albedo (Li et al., 2018) or different vegetation surfaces (e.g., due to management practices). For the same reason, seasonal analysis showed that the cooling contributions during the non-growing season months were higher than during the growing season months.

My results seem to be promising in the context of climate regulation potentials of albedo changes due to land cover changes and land mosaic. Nevertheless, several assumptions and limitations to my study could benefit GWI computations elsewhere in managed landscapes.

Cooling effects

During the 19-year period, the highest cooling effect of seasonal and monthly $GWI_{\Delta\alpha}$ of cropland were equivalent to -0.47 MgC_{eq} ha^{-1} gs^{-1} in 2015 for Ecoregions 56b, 56d, 56f, and 56h, and -2.15 MgC_{eq} ha^{-1} mo^{-1} in February for Ecoregion 56b, respectively. In comparison, Abraha et al. (2019)—accounting for GHGs using whole-system lifecycle analysis—found emissions of 2.6 MgC_{eq} ha^{-1} yr^{-1} over eight years in Conservation Reserve Program (CRP) grasslands converted to maize. Thus, the seasonal and monthly maximum albedo-induced cooling effects from cropland represent (i.e., offset) 18% and ~83%, respectively, of the annual C_{eq} over the eight years from CRP grasslands converted to maize fields. By only considering the cumulative highest cooling effects due to both seasonal and monthly $GWI_{\Delta\alpha}$, the albedo climate benefits would completely offset the annual emissions due to grassland converted to maize over the eight years. Moreover, the cropland cooling effects mentioned above are more than enough to offset the annual net biogeochemical GWI—i.e., warming effects due to the net contributions from CO_2, CH_4, and N_2O

at 0.31 MgC_{eq} ha^{-1} yr^{-1}—produced by annual crop systems (i.e., maize-soybean-wheat rotation) under conventional tillage management of the same area (Robertson, 2000).

Variable effects

Urban areas appeared to have either cooling or warming effects depending on time scale examined. Unlike cropland cover type, which had cooling effects during summer months, mostly due to changes in vegetation over the growing season (Hammerle et al., 2007; Kuusinen et al., 2016; Lukeš et al., 2014; Rechid et al., 2009; Zheng et al., 2019), urban cover type had warming effects over the growing season months and cooling effects during the rest of the year. More specifically, the highest seasonal and monthly warming effects, equivalent to 0.05 MgC_{eq} ha^{-1} gs^{-1} in 2002 and 2012 and to ~0.1 MgC_{eq} ha^{-1} mo^{-1} in June–July, respectively, at Ecoregion 56g, are equivalent to ~29% and 45% of the annual net ecosystem production (NEP) of deciduous forest stands in northern Michigan (Curtis et al., 2002). On the other hand, the maximum monthly cooling effect of urban landscapes was equivalent to -0.7 MgC_{eq} ha^{-1} mo^{-1} (in February at Ecoregion 56h), which is between 16% and 32% the estimated C_{eq} offset (i.e., between 2.2 MgC_{eq} ha^{-1} and 4.4 MgC_{eq} ha^{-1}) induced by an increase in albedo of 0.01 (i.e., 1%) across major cities in the U.S. over a 50-year period (Zheng et al., 2019). Such results are important, considering that the watershed includes two major urban centers, Kalamazoo and Battle Creek, with a total population of >500,000 people in 2010 (Chen et al., 2021), and, as previous studies predicted, the total built-up areas in the whole state of Michigan will increase >50% until 2030, with the urban areas alone representing >70% of this increase (Messina, 2008).

Intra- and interannual variability of albedo and GWI$\Delta\alpha$

Despite my expectation that intra- and inter-annual variability of surface albedo would vary due to seasonality and climatic conditions (Sciusco et al., 2020), I did not find significant

differences in interannual variation of Δα, and thus $GWI_{\Delta\alpha}$. For example, each cover type showed unique interannual trends that appeared to be similar during the seasonal and monthly periods. However, I found that during growing season, $GWI_{\Delta\alpha}$ of cropland and urban cover types was not the same in every ecoregion, which emphasizes that cover types may contribute differently depending on the location. In other words, changes in landscape composition in the five ecoregions could cause different net landscape $GWI_{\Delta\alpha}$. For example, contrasting landscape compositions among the five ecoregions lead to different cumulative cooling effects during the growing season over 19 years; this value varied from -6.89 MgC_{eq} ha^{-1} gs^{-1} to -11.36 MgC_{eq} ha^{-1} gs^{-1} at Ecoregions 56d and 56b, respectively. At monthly scale, as another example, landscape composition produced cumulative cooling effects of -9.14 MgC_{eq} ha^{-1} mo^{-1} to -14.89 MgC_{eq} ha^{-1} mo^{-1} at Ecoregions 56h and 56b, respectively.

My results also suggest that a total forest loss of ~680 ha due to conversion to cropland and urban (i.e., the main cover type classes within the watershed) during 2001–2016 led to seasonal and monthly cooling effects at watershed scale that, on average, were equivalent to ~-179 MgC_{eq} gs^{-1} and ~-374 MgC_{eq} mo^{-1}, respectively.

Seasonal percent contribution to the total cooling and warming

In line with other studies (Abraha et al., 2021), the largest contribution to the overall total seasonal $GWI_{\Delta\alpha}$ came from the non-growing season months, during which all the cover types exhibited cooling effects, which varied in magnitude depending on the ecoregion. Once again, urban was the only cover type that contributed to warming effects in the growing season, generally following a decreasing trend going from June–September and with similar magnitude. However, despite the interest of my study being far from investigating importance of urban albedo modifications in the context of urban heat island effects, my results further imply the need for

future research on the same line as what other studies currently highlight: the importance of increasing the surface albedo of urban components (e.g., pavements, roofs, walls) as climate regulation strategy to solve urban energy budget and building energy demand (Jandaghian & Akbari, 2018; Zheng et al., 2019). However, the seasonal analysis clearly confirmed that the contributions to the total landscape cooling or warming effect varied by ecoregion, resulting in either net cooling/warming or in a net neutral effect of the albedo climate benefits at landscape scale.

Assumptions and limitations

Several assumptions and limitations in my study could benefit GWI computations elsewhere in managed landscapes. A first assumption is related to the choice of the time horizon (TH, Eq. 3.8) fixed at a 100-year period. The choice of either short or long-time horizons can either over- or de-accentuate albedo-induced global warming impact ($GWI_{\Delta\alpha}$) values (Anderson-Teixeira et al., 2012). Specifically, by keeping TH fixed at 100 years, I assume that the land cover composition of the study area will remain the same for the next 100 years, although it is likely that the land cover over the next 100 years will be very different. However, by setting TH=100, I put our study in line with the Kyoto Protocol (Boucher et al., 2009; Sciusco et al., 2020).

There is also uncertainty associated with the spatial resolution of MODIS products. The albedo MODIS product employed in this work has a pixel with a nominal spatial resolution of 500 m, which has been shown not to properly match the effective spatial resolution (usually much higher than the nominal one; Moreno-Ruiz et al., 2019; Zhou et al., 2019). However, despite previous studies attempts to analyze the effective spatial resolution of the MODIS albedo product (Campagnolo et al., 2016; Hovi et al., 2019), they were only based on a single homogeneous area.

For areas characterized by substantial land surface heterogeneity, like the one presented in this work, the effective spatial representativeness of the pixel is hard to determine (Zhou et al., 2019).

My study investigates the contribution of land mosaics due to land transformation on $GWI_{\Delta\alpha}$ in the context of climate change mitigations by considering forest cover type as the reference for the entire study area (Brown et al., 2000). However, without other references my calculations cannot estimate forests' contribution to $GWI_{\Delta\alpha}$, which hinders a comprehensive synthesis of the total climate emission or mitigation of the watershed considering that the low albedo of forests contributes to climate warming (Bonan, 2008). Moreover, regarding indirect biophysical effects, forests' role in mitigating climate change is multifaced and recent studies demonstrated how re- and afforestation strategies can increase low level cloud cover formation, which, depending on forest type, results in cooling effects on the planet (Duveiller et al., 2021). Lastly, analyzing land transformation with reference to forest is only one method. For example, for other studies and policymakers the main focus is on land transformation in the context of bioenergy conversions (Abraha et al., 2021) and land management practices to compare landscape dynamics to agriculture (Cai et al., 2016; Davin et al., 2014; Sieber et al., 2020).

The MODIS BRDF function is the composite of a 16-day period (He et al., 2018) with albedo values from a single snapshot at 10:30 a.m. local time (UTC -05; i.e., MODIS Terra morning overpass time). However, there is increasing evidence showing diurnal variations of albedo (He et al., 2018; Wang et al., 2015) under different sky conditions. This means that albedo values at 10:30 a.m. local time (UTC -05) are likely different from the daily averages. Nevertheless, MODIS albedo products are soundly validated as well as widely accepted for retrieving albedo from other remote sensing products (Cescatti et al., 2012; He et al., 2012; Liu et al., 2009; Roman et al., 2013; Stroeve et al., 2005; Wang et al., 2014) and present an overall

accuracy of RMSE ~0.02 and maximum error of ~0.04, compared to *in-situ* measurements (Wang et al., 2004).

Lastly, I considered growing season and monthly albedo at 10:30 a.m. local time (UTC -05) by computing their median composite, which prevented me from accounting for the effects of land surface characteristics (i.e., vegetation properties, such as leaf area index, and landscape heterogeneity) on spatiotemporal variation of albedo within patches of the same type. This represents a limitation, as during the growing season, vegetation cover and canopy structure and albedo are negatively correlated, due to different capacity of the canopy to absorb incoming solar radiation (Tian et al., 2018). My cover type categories did not reflect these differences, so future efforts will be needed to quantify such differences, including the use of other remote sensing metrics and instantaneous measurements (Giannico et al., 2018).

Conclusions

In conclusion, I found that albedo-induced global warming impact ($GWI_{\Delta\alpha}$) accounted for a significant amount of landscape climate mitigation due to land use land cover changes, although its contributions varied by cover type, ecoregion, and season/month. Over the 19-year period, conversion of forest to cropland resulted in the highest amount of climate cooling compared with conversions to other land cover types, whether measured seasonally or monthly. Conversion of forest to urban cover showed a warming effect during June–September and a cooling effect in the other months. Each season or month contributed to the annual total $GWI_{\Delta\alpha}$ very differently and can result in either net cooling or warming or in a near-neutral albedo climate benefits.

REFERENCES

Abraha, M., Chen, J., Hamilton, S. K., Sciusco, P., Lei, C., Shirkey, G., Yuan, J., & Robertson, G. P. (2021). Albedo-induced global warming impact of Conservation Reserve Program grasslands converted to annual and perennial bioenergy crops. *Environmental Research Letters*, *16*(8), 084059. https://doi.org/10.1088/1748-9326/ac1815

Abraha, M., Gelfand, I., Hamilton, S. K., Chen, J., & Robertson, G. P. (2019). Carbon debt of field-scale conservation reserve program grasslands converted to annual and perennial bioenergy crops. *Environmental Research Letters*, *14*(2), 024019. https://doi.org/10.1088/1748-9326/aafc10

Anderson-Teixeira, K. J., Snyder, P. K., Twine, T. E., Cuadra, S. V., Costa, M. H., & DeLucia, E. H. (2012). Climate-regulation services of natural and agricultural ecoregions of the Americas. *Nature Climate Change*, *2*(3), 177–181. https://doi.org/10.1038/nclimate1346

Kauppi, P.; Sedjo, R. Technological and economic potential of options to enhance, maintain, and manage biological carbon reservoirs and geo-engineering. In *Economics of Forestry*; Sedjo, R.A., Ed.; Routledge: London, UK, 2003; pp. 373–416. ISBN 978-1-315-18268-1.

Bakeman, R. (2005). Recommended effect size statistics for repeated measures designs. *Behavior Research Methods*, *37*(3), 379–384. https://doi.org/10.3758/BF03192707

Bonan, G. B. (2008). Forests and climate change: Forcings, feedbacks, and the climate benefits of forests. *Science*, *320*(5882), 1444–1449. https://doi.org/10.1126/science.1155121

Boucher, O., Friedlingstein, P., Collins, B., & Shine, K. P. (2009). The indirect global warming potential and global temperature change potential due to methane oxidation. *Environmental Research Letters*, *4*(4), 044007. https://doi.org/10.1088/1748-9326/4/4/044007

Bright, R. M., Cherubini, F., & Strømman, A. H. (2012). Climate impacts of bioenergy: Inclusion of carbon cycle and albedo dynamics in life cycle impact assessment. *Environmental Impact Assessment Review*, *37*, 2–11. https://doi.org/10.1016/j.eiar.2012.01.002

Bright, R. M., & Lund, M. T. (2021). CO_2-equivalence metrics for surface albedo change based on the radiative forcing concept: A critical review. *Atmospheric Chemistry and Physics*, *21*(12), 9887–9907. https://doi.org/10.5194/acp-21-9887-2021

Bright, R. M., Zhao, K., Jackson, R. B., & Cherubini, F. (2015). Quantifying surface albedo and other direct biogeophysical climate forcings of forestry activities. *Global Change Biology*, *21*(9), 3246–3266. https://doi.org/10.1111/gcb.12951

Brown, D. G., Pijanowski, B. C., & Duh, J. D. (2000). Modeling the relationships between land use and land cover on private lands in the Upper Midwest, USA. *Journal of Environmental Management*, *59*(4), 247–263. https://doi.org/10.1006/jema.2000.0369

Cai, H., Wang, J., Feng, Y., Wang, M., Qin, Z., & B. Dunn, J. (2016). Consideration of land use change-induced surface albedo effects in life-cycle analysis of biofuels. *Energy & Environmental Science*, *9*(9), 2855–2867. https://doi.org/10.1039/C6EE01728B

Campagnolo, M. L., Sun, Q., Liu, Y., Schaaf, C., Wang, Z., & Román, M. O. (2016). Estimating the effective spatial resolution of the operational BRDF, albedo, and nadir reflectance products from MODIS and VIIRS. *Remote Sensing of Environment*, *175*, 52–64. https://doi.org/10.1016/j.rse.2015.12.033

Carrer, D., Pique, G., Ferlicoq, M., Ceamanos, X., & Ceschia, E. (2018). What is the potential of cropland albedo management in the fight against global warming? A case study based on the use of cover crops. *Environmental Research Letters*, *13*(4), 044030. https://doi.org/10.1088/1748-9326/aab650

Cescatti, A., Marcolla, B., Santhana Vannan, S. K., Pan, J. Y., Román, M. O., Yang, X., Ciais, P., Cook, R. B., Law, B. E., Matteucci, G., Migliavacca, M., Moors, E., Richardson, A. D., Seufert, G., & Schaaf, C. B. (2012). Intercomparison of MODIS albedo retrievals and in situ measurements across the global FLUXNET network. *Remote Sensing of Environment*, *121*, 323–334. https://doi.org/10.1016/j.rse.2012.02.019

Chapman, K. A., & Brewer, R. (2008). *Prairie and Savanna in Southern Lower Michigan: History, Classification, Ecology*. Michigan Botanic Club, 47, 48

Chen, J., Brosofske, K. D., Noormets, A., Crow, T. R., Bresee, M. K., Le Moine, J. M., Euskirchen, E. S., Mather, S. V., & Zheng, D. (2004). A working framework for quantifying carbon sequestration in disturbed land mosaics. *Environmental Management*, *33*(1), S210–S221. https://doi.org/10.1007/s00267-003-9131-4

Chen, J., Lei, C., & Sciusco, P. (2021). Modeling ecosystem global warming potentials. In *Biophysical Models and Applications in Ecosystem Analysis* (pp. 119–150). Michigan State University Press; JSTOR. https://doi.org/10.14321/j.ctv1h1vc27.11

Chen, J., Sciusco, P., Ouyang, Z., Zhang, R., Henebry, G. M., John, R., & Roy, David. P. (2019). Linear downscaling from MODIS to Landsat: Connecting landscape composition with ecosystem functions. *Landscape Ecology*, *34*(12), 2917–2934. https://doi.org/10.1007/s10980-019-00928-2

Cherubini, F., Bright, R. M., & Strømman, A. H. (2012). Site-specific global warming potentials of biogenic CO_2 for bioenergy: Contributions from carbon fluxes and albedo dynamics. *Environmental Research Letters*, *7*(4), 045902. https://doi.org/10.1088/1748-9326/7/4/045902

Chrysoulakis, N., Mitraka, Z., & Gorelick, N. (2018). Exploiting satellite observations for global surface albedo trends monitoring. *Theoretical and Applied Climatology*. https://doi.org/10.1007/s00704-018-2663-6

Cicerone, R. J. (2006). Geoengineering: Encouraging research and overseeing implementation. *Climatic Change*, *77*(3–4), 221–226. https://doi.org/10.1007/s10584-006-9102-x

Crutzen, P. J. (2016). Albedo enhancement by stratospheric sulfur injections: A contribution to resolve a policy dilemma? An editorial essay. In P. J. Crutzen & H. G. Brauch (Eds.), *Paul J. Crutzen: A Pioneer on Atmospheric Chemistry and Climate Change in the Anthropocene* (pp. 217–225). Springer International Publishing. https://doi.org/10.1007/978-3-319-27460-7_11

Curtis, P. S., Hanson, P. J., Bolstad, P., Barford, C., Randolph, J. C., Schmid, H. P., & Wilson, K. B. (2002). Biometric and eddy-covariance based estimates of annual carbon storage in five eastern North American deciduous forests. *Agricultural and Forest Meteorology*, *113*(1), 3–19. https://doi.org/10.1016/S0168-1923(02)00099-0

Davin, E. L., Seneviratne, S. I., Ciais, P., Olioso, A., & Wang, T. (2014). Preferential cooling of hot extremes from cropland albedo management. *Proceedings of the National Academy of Sciences*, *111*(27), 9757–9761. https://doi.org/10.1073/pnas.1317323111

Duveiller, G., Filipponi, F., Ceglar, A., Bojanowski, J., Alkama, R., & Cescatti, A. (2021). Revealing the widespread potential of forests to increase low level cloud cover. *Nature Communications*, *12*(1), 4337. https://doi.org/10.1038/s41467-021-24551-5

Euskirchen, E. S., Chen, J., Li, H., Gustafson, E. J., & Crow, T. R. (2002). Modeling landscape net ecosystem productivity (LandNEP) under alternative management regimes. *Ecological Modelling*, *154*(1), 75–91. https://doi.org/10.1016/S0304-3800(02)00052-2

Forster, P., Ramaswamy, V., Artaxo, P., Berntsen, T., Betts, R., Fahey, D., Haywood, J., Lean, J., Lowe, D., Myhre, G., Nganga, J., Prinn, R., Raga, G., Schulz, M., Dorland, R., Bodeker, G., Boucher, O., Collins, W., Conway, T., & Whorf, T. (2007). Changes in Atmospheric Constituents and in Radiative Forcing. In *Climate Change 2007: The Physical Science Basis. Contribution of Working Group I to the 4th Assessment Report of the Intergovernmental Panel on Climate Change*. [Solomon, S., D. Qin, M. Manning, Z. Chen, M. Marquis, K.B. Averyt, M.Tignor and H.L. Miller (eds.)]. Cambridge University Press, Cambridge, United Kingdom and New York, NY, USA.

Gelfand I. & Robertson G. P. (2015). Mitigation of greenhouse gas emissions in agricultural ecosystems. In *The Ecology of Agricultural Landscapes: Long-Term Research on the Path to Sustainability*. Oxford University Press, New York, 310–339.

Gelfand, I., Sahajpal, R., Zhang, X., Izaurralde, R. C., Gross, K. L., & Robertson, G. P. (2013). Sustainable bioenergy production from marginal lands in the US Midwest. *Nature*, *493*(7433), 514–517. https://doi.org/10.1038/nature11811

Giannico, V., Chen, J., Shao, C., Ouyang, Z., John, R., & Lafortezza, R. (2018). Contributions of landscape heterogeneity within the footprint of eddy-covariance towers to flux measurements. *Agricultural and Forest Meteorology*, *260–261*, 144–153. https://doi.org/10.1016/j.agrformet.2018.06.004

Gorelick, N., Hancher, M., Dixon, M., Ilyushchenko, S., Thau, D., & Moore, R. (2017). Google Earth Engine: Planetary-scale geospatial analysis for everyone. *Remote Sensing of Environment*, *202*, 18–27. https://doi.org/10.1016/j.rse.2017.06.031

Hammerle, A., Haslwanter, A., Tappeiner, U., Cernusca, A., & Wohlfahrt, G. (2007). Leaf area controls on energy partitioning of a mountain grassland. *Biogeosciences Discussions*, *4*(5), 3607–3638. https://doi.org/10.5194/bgd-4-3607-2007

He, T., Liang, S., Wang, D., Wu, H., Yu, Y., & Wang, J. (2012). Estimation of surface albedo and directional reflectance from Moderate Resolution Imaging Spectroradiometer (MODIS) observations. *Remote Sensing of Environment*, *119*, 286–300. https://doi.org/10.1016/j.rse.2012.01.004

He, T., Wang, D., & Qu, Y. (2018). Land surface albedo. In *Comprehensive Remote Sensing* (pp. 140–162). Elsevier. https://doi.org/10.1016/B978-0-12-409548-9.10370-7

Hollinger, D. Y., Ollinger, S. V., Richardson, A. D., Meyers, T. P., Dail, D. B., Martin, M. E., Scott, N. A., Arkebauer, T. J., Baldocchi, D. D., Clark, K. L., Curtis, P. S., Davis, K. J., Desai, A. R., Dragoni, D., Goulden, M. L., Gu, L., Katul, G. G., Pallardy, S. G., U, K. T. P., … Verma, S. B. (2010). Albedo estimates for land surface models and support for a new paradigm based on foliage nitrogen concentration. *Global Change Biology*, *16*(2), 696–710. https://doi.org/10.1111/j.1365-2486.2009.02028.x

Homer, C., Dewitz, J., Jin, S., Xian, G., Costello, C., Danielson, P., Gass, L., Funk, M., Wickham, J., Stehman, S., Auch, R., & Riitters, K. (2020). Conterminous United States land cover change patterns 2001–2016 from the 2016 National Land Cover Database. *ISPRS Journal of Photogrammetry and Remote Sensing*, *162*, 184–199. https://doi.org/10.1016/j.isprsjprs.2020.02.019

Hothorn, T., Bretz, F., Westfall, P., Heiberger, R. M., Schuetzenmeister, A., & Scheibe, S. (2020). *Multcomp: Simultaneous Inference in General Parametric Models*. https://CRAN.R-project.org/package=multcomp

Houspanossian, J., Giménez, R., Jobbágy, E., & Nosetto, M. (2017). Surface albedo raise in the South American Chaco: Combined effects of deforestation and agricultural changes. *Agricultural and Forest Meteorology*, *232*, 118–127. https://doi.org/10.1016/j.agrformet.2016.08.015

Hovi, A., Lindberg, E., Lang, M., Arumäe, T., Peuhkurinen, J., Sirparanta, S., Pyankov, S., & Rautiainen, M. (2019). Seasonal dynamics of albedo across European boreal forests: Analysis of MODIS albedo and structural metrics from airborne LiDAR. *Remote Sensing of Environment*, *224*, 365–381. https://doi.org/10.1016/j.rse.2019.02.001

Jandaghian, Z., & Akbari, H. (2018). The effect of increasing surface albedo on urban climate and air quality: A detailed study for Sacramento, Houston, and Chicago. *Climate*, *6*(2), 19. https://doi.org/10.3390/cli6020019

Jeong, S.-J., Ho, C.-H., Gim, H.-J., & Brown, M. E. (2011). Phenology shifts at start vs. end of growing season in temperate vegetation over the Northern Hemisphere for the period 1982–2008. *Global Change Biology*, *17*(7), 2385–2399. https://doi.org/10.1111/j.1365-2486.2011.02397.x

Joos, F., Roth, R., Fuglestvedt, J. S., Peters, G. P., Enting, I. G., von Bloh, W., Brovkin, V., Burke, E. J., Eby, M., Edwards, N. R., Friedrich, T., Frölicher, T. L., Halloran, P. R., Holden, P. B., Jones, C., Kleinen, T., Mackenzie, F. T., Matsumoto, K., Meinshausen, M., … Weaver, A. J. (2013). Carbon dioxide and climate impulse response functions for the computation of greenhouse gas metrics: A multi-model analysis. *Atmospheric Chemistry and Physics*, *13*(5), 2793–2825. https://doi.org/10.5194/acp-13-2793-2013

Kalnay, E., & Cai, M. (2003). Impact of urbanization and land-use change on climate. *Nature*, *423*(6939), 828–850. https://doi.org/10.1038/nature01675

Kaye, J. P., & Quemada, M. (2017). Using cover crops to mitigate and adapt to climate change. A review. *Agronomy for Sustainable Development*, *37*(1), 4. https://doi.org/10.1007/s13593-016-0410-x

Kuusinen, N., Stenberg, P., Korhonen, L., Rautiainen, M., & Tomppo, E. (2016). Structural factors driving boreal forest albedo in Finland. *Remote Sensing of Environment*, *175*, 43–51. https://doi.org/10.1016/j.rse.2015.12.035

Lawrence, M. A. (2016). *Ez: Easy Analysis and Visualization of Factorial Experiments*. https://CRAN.R-project.org/package=ez

Lenth, R. (2018). *Lsmeans: Least-Squares Means*. https://CRAN.R-project.org/package=lsmeans

Lenton, T. M., & Vaughan, N. E. (2009). The radiative forcing potential of different climate geoengineering options. *Atmos. Chem. Phys.*, 23.

Li, Q., Ma, M., Wu, X., & Yang, H. (2018). Snow cover and vegetation-induced decrease in global albedo from 2002 to 2016. *Journal of Geophysical Research: Atmospheres*, *123*(1), 124–138. https://doi.org/10.1002/2017JD027010

Liu, J., Schaaf, C., Strahler, A., Jiao, Z., Shuai, Y., Zhang, Q., Roman, M., Augustine, J. A., & Dutton, E. G. (2009). Validation of Moderate Resolution Imaging Spectroradiometer (MODIS) albedo retrieval algorithm: Dependence of albedo on solar zenith angle. *Journal of Geophysical Research: Atmospheres*, *114*(D1). https://doi.org/10.1029/2008JD009969

Lugato, E., Cescatti, A., Jones, A., Ceccherini, G., & Duveiller, G. (2020). Maximising climate mitigation potential by carbon and radiative agricultural land management with cover crops. *Environmental Research Letters*, *15*(9), 094075. https://doi.org/10.1088/1748-9326/aba137

Lukeš, P., Rautiainen, M., Manninen, T., Stenberg, P., & Mõttus, M. (2014). Geographical gradients in boreal forest albedo and structure in Finland. *Remote Sensing of Environment*, *152*, 526–535. https://doi.org/10.1016/j.rse.2014.06.023

Welsh, W. F.; Brown, D. G.; Messina, J. P. Land use and cover. In *Michigan Geography and Geology*; Schaetzl, R. J., Darden, J. T., Brandt, D., Eds.; Pearson Custom Publishing: Boston, MA, USA, 2009; pp. 446–457; ISBN 0-536-98716-5.

Michigan State Climatologist's Office. (2013). *Gull Lake (3504). Michigan State University*. Retrieved from http://climate. geo.msu.edu/climate_mi/stations/3504/

Mira, M., Weiss, M., Baret, F., Courault, D., Hagolle, O., Gallego-Elvira, B., & Olioso, A. (2015). The MODIS (collection V006) BRDF/albedo product MCD43D: Temporal course evaluated over agricultural landscape. *Remote Sensing of Environment*, *170*, 216–228. https://doi.org/10.1016/j.rse.2015.09.021

Moreno-Ruiz, J. A., García-Lázaro, J. R., Arbelo, M., & Riaño, D. (2019). A comparison of burned area time series in the Alaskan boreal forests from different remote sensing products. *Forests*, *10*(5), 363. https://doi.org/10.3390/f10050363

Muñoz, I., Campra, P., & Fernández-Alba, A. R. (2010). Including CO_2-emission equivalence of changes in land surface albedo in life cycle assessment. Methodology and case study on greenhouse agriculture. *The International Journal of Life Cycle Assessment*, *15*(7), 672–681. https://doi.org/10.1007/s11367-010-0202-5

Myhre, G.; Shindell, D.; Pongratz, J. Anthropogenic and natural radiative forcing. In *Climate Change 2013: The Physical Science Basis. Working Group I Contribution to the Fifth Assessment Report of the Intergovernmental Panel on Climate Change*; Stocker, T.F., Ed.; Cambridge University Press: Cambridge, UK; New York, NY, USA, 2014; pp. 659–740; ISBN 978-1-107-41532-4.

Omernik, J. M., & Griffith, G. E. (2014). Ecoregions of the conterminous United States: Evolution of a hierarchical spatial framework. *Environmental Management*, *54*(6), 1249–1266. https://doi.org/10.1007/s00267-014-0364-1

Pielke, R. A., Pitman, A., Niyogi, D., Mahmood, R., McAlpine, C., Hossain, F., Goldewijk, K. K., Nair, U., Betts, R., Fall, S., Reichstein, M., Kabat, P., & Noblet, N. de. (2011). Land use/land cover changes and climate: Modeling analysis and observational evidence. *Wiley Interdisciplinary Reviews: Climate Change*, *2*(6), 828–850. https://doi.org/10.1002/wcc.144

Pinheiro J, Douglas B, Saikat DR, Deepayan S, Siem Heisterkamp, Bert VW, & R-core. (2017). *Nlme: Linear and Nonlinear Mixed Effects Models*. https://CRAN.R-project.org/package=nlme

R Core Team (2020). *R: A Language and Environment for Statistical Computing*. R Foundation for Statistical Computing: Vienna, Austria. https://www.R-project.org/

Rechid, D., Raddatz, T. J., & Jacob, D. (2009). Parameterization of snow-free land surface albedo as a function of vegetation phenology based on MODIS data and applied in climate modelling. *Theoretical and Applied Climatology*, *95*(3), 245–255. https://doi.org/10.1007/s00704-008-0003-y

Robertson, G. P. (2000). Greenhouse gases in intensive agriculture: Contributions of individual gases to the radiative forcing of the atmosphere. *Science*, *289*(5486), 1922–1925. https://doi.org/10.1126/science.289.5486.1922

Roman, M. O., Gatebe, C. K., Shuai, Y., Wang, Z., Gao, F., Masek, J. G., He, T., Liang, S., & Schaaf, C. B. (2013). Use of in situ and airborne multiangle data to assess MODIS- and Landsat-based estimates of directional reflectance and albedo. *IEEE Transactions on Geoscience and Remote Sensing*, *51*(3), 1393–1404. https://doi.org/10.1109/TGRS.2013.2243457

Schaetzl, R. J., Darden, J. T., & Brandt, D. S. (2009). *Michigan Geography and Geology*. Pearson Custom Publishing. http://catalog.hathitrust.org/api/volumes/oclc/309340740.html

Sciusco, P., Chen, J., Abraha, M., Lei, C., Robertson, G. P., Lafortezza, R., Shirkey, G., Ouyang, Z., Zhang, R., & John, R. (2020). Spatiotemporal variations of albedo in managed agricultural landscapes: Inferences to global warming impacts (GWI). *Landscape Ecology*, *35*(6), 1385–1402. https://doi.org/10.1007/s10980-020-01022-8

Shao, C., Li, L., Dong, G., & Chen, J. (2014). Spatial variation of net radiation and its contribution to energy balance closures in grassland ecosystems. *Ecological Processes*, *3*(1), 7. https://doi.org/10.1186/2192-1709-3-7

Sieber, P., Ericsson, N., Hammar, T., & Hansson, P.-A. (2020). Including albedo in time-dependent LCA of bioenergy. *GCB Bioenergy*, *12*(6), 410–425. https://doi.org/10.1111/gcbb.12682

Sparks A. (2020). *nasapower: NASA-POWER Data for R*. https://CRAN.R-project.org/package=nasapower

Stocker, T.F.; Qin, D.; Plattner, G.-K.; Tignor, M.M.B.; Allen, S.K.; Boschung, J.; Nauels, A.; Xia, Y.; Bex, V.; Midgley, P.M. *Climate Change 2013: The Physical Science Basis. Contribution of Working Group I to the Fifth Assessment Report of IPCC the Intergovernmental Panel on Climate Change*; Stocker, T., Qin, D., Plattner, G.-K., Tignor, M., Allen, S., Boschung, J., Nauels, A., Xia, Y., Bex, V., Midgley, P., Eds.; Cambridge University Press: Cambridge, UK; New York, NY, USA, 2014; p. 1535; ISBN 978-1-107-66182-0.

Stroeve, J., Box, J. E., Gao, F., Liang, S., Nolin, A., & Schaaf, C. (2005). Accuracy assessment of the MODIS 16-day albedo product for snow: Comparisons with Greenland in situ measurements. *Remote Sensing of Environment*, *94*(1), 46–60. https://doi.org/10.1016/j.rse.2004.09.001

Tian, L., Chen, J., & Shao, C. (2018). Interdependent dynamics of LAI-albedo across the roofing landscapes: Mongolian and Tibetan Plateaus. *Remote Sensing*, *10*(7), 1159. https://doi.org/10.3390/rs10071159

Vitousek, P. M., Mooney, H. A., Lubchenco, J., & Melillo, J. M. (1997). Human domination of Earth's ecosystems. *Science*, *277*, 7. https://doi.org/10.1126/science.277.5325.494

Wackernagel, M., Schulz, N. B., Deumling, D., Linares, A. C., Jenkins, M., Kapos, V., Monfreda, C., Loh, J., Myers, N., Norgaard, R., & Randers, J. (2002). Tracking the

ecological overshoot of the human economy. *Proceedings of the National Academy of Sciences*, *99*(14), 9266–9271. https://doi.org/10.1073/pnas.142033699

Wang, D., Liang, S., He, T., Yu, Y., Schaaf, C., & Wang, Z. (2015). Estimating daily mean land surface albedo from MODIS data. *Journal of Geophysical Research: Atmospheres*, *120*(10), 4825–4841. https://doi.org/10.1002/2015JD023178

Wang, K., Liu, J., Zhou, X., Sparrow, M., Ma, M., Sun, Z., & Jiang, W. (2004). Validation of the MODIS global land surface albedo product using ground measurements in a semidesert region on the Tibetan Plateau. *Journal of Geophysical Research: Atmospheres*, *109*(D5). https://doi.org/10.1029/2003JD004229

Wang, Z., Schaaf, C. B., Strahler, A. H., Chopping, M. J., Román, M. O., Shuai, Y., Woodcock, C. E., Hollinger, D. Y., & Fitzjarrald, D. R. (2014). Evaluation of MODIS albedo product (MCD43A) over grassland, agriculture and forest surface types during dormant and snow-covered periods. *Remote Sensing of Environment*, *140*, 60–77. https://doi.org/10.1016/j.rse.2013.08.025

Xu, X., Swei, O., Xu, L., Schlosser, C. A., Gregory, J., & Kirchain, R. (2020). Quantifying location-specific impacts of pavement albedo on radiative forcing using an analytical approach. *Environmental Science & Technology*, *54*(4), 2411–2421. https://doi.org/10.1021/acs.est.9b04556

Yang, L., Jin, S., Danielson, P., Homer, C., Gass, L., Bender, S. M., Case, A., Costello, C., Dewitz, J., Fry, J., Funk, M., Granneman, B., Liknes, G. C., Rigge, M., & Xian, G. (2018). A new generation of the United States National Land Cover Database: Requirements, research priorities, design, and implementation strategies. *ISPRS Journal of Photogrammetry and Remote Sensing*, *146*, 108–123. https://doi.org/10.1016/j.isprsjprs.2018.09.006

Zheng, L., Zhao, G., Dong, J., Ge, Q., Tao, J., Zhang, X., Qi, Y., Doughty, R. B., & Xiao, X. (2019). Spatial, temporal, and spectral variations in albedo due to vegetation changes in China's grasslands. *ISPRS Journal of Photogrammetry and Remote Sensing*, *152*, 1–12. https://doi.org/10.1016/j.isprsjprs.2019.03.020

Zhou, H., Liang, S., He, T., Wang, J., Bo, Y., & Wang, D. (2019). Evaluating the spatial representativeness of the MODerate Resolution Image Spectroradiometer albedo product (MCD43) at AmeriFlux sites. *Remote Sensing*, *11*(5), 547. https://doi.org/10.3390/rs11050547

APPENDIX

Table A3: Summary table for the overall linear downscaling models (Eq. 3.1) for the estimated $\hat{\alpha}_{gs}$ and $\hat{\alpha}_{mo}$ (dependent variables) across the entire Kalamazoo River Watershed. Values in bold indicate the cover types considered in this study.

	Variable	Estimates	SE	t	p-value	DF	adj. R^2
$\hat{\alpha}_{gs}$	barren	0.152	0.000	1340.300	***	9	0.995
	cropland	**0.174**	**0.000**	**26281.727**	*******		
	forest	**0.145**	**0.000**	**13171.109**	*******		
	grassland	0.129	0.000	1347.355	***		
	pasture	**0.165**	**0.000**	**5715.941**	*******		
	shrubland	0.138	0.000	653.438	***		
	urban	**0.145**	**0.000**	**10926.929**	*******		
	water	0.091	0.000	2815.767	***		
	wetland	0.154	0.000	12248.465	***		
$\hat{\alpha}_{mo}$	barren	0.237	0.003	93.220	***	9	0.745
	cropland	**0.283**	**0.000**	**1904.740**	*******		
	forest	**0.185**	**0.000**	**745.962**	*******		
	grassland	0.171	0.002	76.378	***		
	pasture	**0.260**	**0.001**	**398.528**	*******		
	shrubland	0.149	0.005	32.996	***		
	urban	**0.215**	**0.000**	**715.211**	*******		
	water	0.183	0.001	251.948	***		
	wetland	0.215	0.000	766.229	***		

Signif. codes: *** p-value < 0.001, ** p-value < 0.01, * p-value < 0.05, · p-value < 0.1, " " p-value > 0.1
$\hat{\alpha}_{gs}$ and $\hat{\alpha}_{mo}$: estimated whites-sky shortwave albedo for growing season and monthly periods, respectively

Table A4: Mean (± one standard deviation) for $\hat{\alpha}_{gs}$ and $\hat{\alpha}_{mo}$ during 2001–2019 for the four cover types. Average values ($\bar{X}$) across the four cover types ($\bar{X}_{cover\ type}$) and for the 19-year growing seasons ($\bar{X}_{gs}$) and the 11-month ($\bar{X}_{mo}$) periods are also shown.

		Cover type				
Time-period		Cropland	Forest	Pasture	Urban	$\bar{X}_{cover\ type}$
$\hat{\alpha}_{gs}$	2001	0.171(±0.002)	0.143(±0.001)	0.163(±0.001)	0.145(±0.001)	0.156(±0.013)
	2002	0.174(±0.001)	0.152(±0.001)	0.166(±0.001)	0.149(±0.002)	0.160(±0.011)
	2003	0.169(±0.001)	0.146(±0.001)	0.162(±0.001)	0.145(±0.001)	0.155(±0.012)
	2004	0.172(±0.002)	0.144(±0.001)	0.161(±0.001)	0.143(±0.002)	0.155(±0.014)
	2005	0.171(±0.002)	0.145(±0.001)	0.162(±0.001)	0.144(±0.002)	0.156(±0.013)
	2006	0.172(±0.002)	0.146(±0.001)	0.165(±0.001)	0.145(±0.002)	0.157(±0.014)
	2007	0.170(±0.001)	0.148(±0.001)	0.160(±0.001)	0.146(±0.001)	0.156(±0.011)
	2008	0.171(±0.001)	0.147(±0.001)	0.163(±0.001)	0.146(±0.001)	0.157(±0.012)
	2009	0.174(±0.002)	0.146(±0.002)	0.166(±0.001)	0.148(±0.002)	0.158(±0.014)
	2010	0.172(±0.002)	0.141(±0.002)	0.161(±0.001)	0.145(±0.002)	0.155(±0.014)
	2011	0.175(±0.002)	0.149(±0.001)	0.166(±0.001)	0.147(±0.002)	0.159(±0.013)
	2012	0.170(±0.001)	0.150(±0.001)	0.161(±0.001)	0.147(±0.001)	0.157(±0.010)
	2013	0.168(±0.001)	0.145(±0.001)	0.160(±0.001)	0.144(±0.001)	0.154(±0.012)
	2014	0.172(±0.002)	0.147(±0.001)	0.167(±0.001)	0.147(±0.002)	0.158(±0.013)
	2015	0.169(±0.002)	0.134(±0.002)	0.156(±0.001)	0.142(±0.002)	0.150(±0.015)
	2016	0.171(±0.001)	0.147(±0.001)	0.163(±0.001)	0.147(±0.002)	0.157(±0.012)
	2017	0.170(±0.002)	0.141(±0.001)	0.159(±0.001)	0.142(±0.002)	0.153(±0.014)
	2018	0.168(±0.002)	0.141(±0.001)	0.156(±0.001)	0.143(±0.001)	0.152(±0.013)
	2019	0.173(±0.001)	0.151(±0.001)	0.164(±0.001)	0.148(±0.001)	0.159(±0.012)
	$\bar{X}_{gs}$	0.171(±0.002)	0.145(±0.004)	0.162(±0.003)	0.146(±0.002)	0.156(±0.013)
$\hat{\alpha}_{mo}$	Jan	0.575(±0.013)	0.320(±0.012)	0.504(±0.013)	0.413(±0.008)	0.453(±0.111)
	Feb	0.579(±0.013)	0.333(±0.012)	0.516(±0.013)	0.408(±0.008)	0.459(±0.109)
	Apr	0.162(±0.002)	0.129(±0.002)	0.155(±0.002)	0.139(±0.002)	0.147(±0.015)
	May	0.175(±0.002)	0.146(±0.002)	0.169(±0.002)	0.150(±0.001)	0.160(±0.014)
	Jun	0.178(±0.001)	0.163(±0.001)	0.177(±0.001)	0.158(±0.001)	0.169(±0.010)
	Jul	0.179(±0.001)	0.160(±0.001)	0.173(±0.001)	0.155(±0.001)	0.167(±0.011)
	Aug	0.177(±0.002)	0.153(±0.001)	0.166(±0.001)	0.149(±0.002)	0.161(±0.013)
	Sep	0.170(±0.002)	0.145(±0.001)	0.160(±0.001)	0.144(±0.001)	0.155(±0.012)
	Oct	0.156(±0.001)	0.136(±0.001)	0.151(±0.001)	0.138(±0.001)	0.145(±0.010)
	Nov	0.158(±0.002)	0.119(±0.002)	0.147(±0.002)	0.134(±0.002)	0.140(±0.017)
	Dec	0.530(±0.013)	0.277(±0.012)	0.463(±0.014)	0.374(±0.008)	0.411(±0.110)
	$\bar{X}_{mo}$	0.276(±0.183)	0.189(±0.080)	0.253(±0.156)	0.215(±0.119)	0.233(±0.134)

$\hat{\alpha}_{gs}$ and $\hat{\alpha}_{gs}$: estimated whites-sky shortwave albedo (α) for growing season and monthly periods, respectively

Table A5: Mean (± one standard deviation) of $\Delta\alpha_{gs}$ and $\Delta\alpha_{mo}$ for a given cover type within the five Level IV ecoregions during 2001–2019. Average values ($\bar{X}$) of each cover type for the entire Kalamazoo River Watershed ($\bar{X}_w$) are also shown.

		Level IV ecoregions					
	Cover type	56b	56d	56f	56g	56h	$\bar{X}_w$
$\Delta\alpha_{gs}$	Cropland	0.026(±0.004)	0.026(±0.004)	0.025(±0.004)	0.025(±0.004)	0.026(±0.004)	0.026(±0.004)
	Pasture	0.018(±0.003)	–	0.017(±0.003)	0.016(±0.003)	0.016(±0.003)	0.017(±0.003)
	Urban	0.000(±0.003)	0.001(±0.003)	0.000(±0.003)	-0.001(±0.003)	0.000(±0.003)	0.000(±0.003)
$\Delta\alpha_{mo}$	Cropland	0.088(±0.106)	0.089(±0.108)	0.086(±0.105)	0.086(±0.104)	0.087(±0.105)	0.087(±0.102)
	Pasture	0.066(±0.080)	–	0.061(±0.075)	0.062(±0.076)	–	0.063(±0.075)
	Urban	0.026(±0.041)	0.028(±0.044)	0.025(±0.040)	0.024(±0.040)	0.025(±0.041)	0.026(±0.040)

$\Delta\alpha_{gs}$ and $\Delta\alpha_{mo}$: albedo difference between a cover type *i* and the reference forest at growing season and monthly periods, respectively

"–": no data available

Table A6: Mean (± one standard deviation) of $GWI_{\Delta\alpha gs}$ (MgC_{eq} ha^{-1} gs^{-1}) and $GWI_{\Delta\alpha mo}$ (MgC_{eq} ha^{-1} mo^{-1}) for a given cover type within the five Level IV ecoregions during 2001–2019. Average values ($\bar{X}$) of each cover type for the entire Kalamazoo River Watershed ($\bar{X}_w$) are also shown. Positive and negative values of $GWI_{\Delta\alpha}$ indicate warming and cooling effects, respectively, equivalent to carbon (C_{eq}; emission and mitigation, respectively).

		Level IV ecoregions					
	Cover type	56b	56d	56f	56g	56h	$\bar{X}_w$
$GWI_{\Delta\alpha gs}$	Cropland	-0.354(±0.049)	-0.356(±0.049)	-0.349(±0.048)	-0.342(±0.048)	-0.349(±0.048)	-0.350(±0.047)
	Pasture	-0.242(±0.040)	–	-0.227(±0.039)	-0.220(±0.039)	-0.213(±0.039)	-0.225(±0.040)
	Urban	-0.002(±0.035)	-0.007(±0.035)	0.000(±0.034)	-0.007(±0.035)	-0.001(±0.034)	-0.001(±0.034)
$GWI_{\Delta\alpha mo}$	Cropland	-0.683(±0.646)	-0.682(±0.636)	-0.672(±0.635)	-0.665(±0.634)	-0.674(±0.638)	-0.675(±0.614)
	Pasture	-0.512(±0.494)	–	-0.475(±0.461)	-0.478(±0.469)	–	-0.488(±0.460)
	Urban	-0.159(±0.265)	-0.175(±0.280)	-0.155(±0.262)	-0.147(±0.260)	-0.157(±0.262)	-0.158(±0.256)

$GWI_{\Delta\alpha gs}$ and $GWI_{\Delta\alpha mo}$: albedo-induced global warming impact ($GWI_{\Delta\alpha}$) at growing season and monthly periods, respectively
"–": no data available

Table A7.1: Growing season albedo-induced global warming impact ($GWI_{\Delta\alpha gs}$, MgC_{eq} ha^{-1} gs^{-1}) during 2001–2019 for Ecoregion 56b. Underlined values indicate the cumulative $GWI_{\Delta\alpha gs}$ value for the entire ecoregion over the 19-year period. Major peaks (↑) and decreases (↓) from the $GWI_{\Delta\alpha gs}$ average are also shown. Positive and negative values of $GWI_{\Delta\alpha gs}$ indicate growing season warming and cooling effects, respectively, equivalent to carbon (C_{eq}; emission and mitigation, respectively) during 2001–2019.

		$GWI_{\Delta\alpha gs}$ (MgC_{eq} ha^{-1} gs^{-1})			
Ecoregion	GS	Cropland	Pasture	Urban	$Tot._{cover\ type}$
	2001	-0.37	$-0.29^{\downarrow}$	-0.03	-0.69
	2002	$-0.29^{\uparrow}$	$-0.20^{\uparrow **}$	$0.04^{\uparrow **}$	-0.45
	2003	$-0.32^{\uparrow **}$	-0.23	0.01	-0.54
	2004	-0.39	-0.25	0.00	-0.64
	2005	-0.35	-0.24	0.01	-0.58
	2006	-0.36	$-0.27^{\downarrow *}$	0.01	-0.63
	2007	$-0.30^{\uparrow}$	$-0.18^{\uparrow}$	$0.03^{\uparrow}$	-0.46
	2008	-0.34	-0.24	0.00	-0.58
	2009	-0.39	$-0.28^{\downarrow}$	-0.02	-0.68
	2010	$-0.42^{\downarrow}$	$-0.29^{\downarrow}$	-0.06	-0.77
56b	2011	-0.35	-0.24	$0.02^{\uparrow *}$	-0.57
	2012	$-0.27^{\uparrow *}$	$-0.16^{\uparrow *}$	$0.04^{\uparrow **}$	-0.39
	2013	-0.33	-0.22	0.01	-0.55
	2014	-0.35	$-0.28^{\downarrow}$	0.00	-0.64
	2015	$-0.47^{\downarrow **}$	$-0.31^{\downarrow **}$	-0.10	-0.89
	2016	-0.33	-0.23	0.00	-0.56
	2017	$-0.40^{\downarrow *}$	-0.25	-0.01	-0.67
	2018	-0.37	-0.22	-0.03	-0.62
	2019	$-0.31^{\uparrow}$	$-0.20^{\uparrow **}$	$0.03^{\uparrow}$	-0.48
	$Tot._{2001–2019}$	-6.73	-4.60	-0.03	<u>-11.36</u>
	$\bar{X}_{2001–2019}$	-0.35	-0.24	0.00	

GS: growing season
"*" and "**": min and max decrease/peak, respectively
"–": no data available

Table A7.2: Growing season albedo-induced global warming impact ($GWI_{\Delta\alpha gs}$, MgC_{eq} ha^{-1} gs^{-1}) during 2001–2019 for Ecoregion 56d. Underlined values indicate the cumulative $GWI_{\Delta\alpha gs}$ value for the entire ecoregion over the 19-year period. Major peaks (↑) and decreases (↓) from the $GWI_{\Delta\alpha gs}$ average are also shown. Positive and negative values of $GWI_{\Delta\alpha gs}$ indicate growing season warming and cooling effects, respectively, equivalent to carbon (C_{eq}; emission and mitigation, respectively) during 2001–2019.

		$GWI_{\Delta\alpha gs}$ (MgC_{eq} ha^{-1} gs^{-1})			
Ecoregion	GS	Cropland	Pasture	Urban	$Tot._{cover\ type}$
	2001	-0.37	–	$-0.04^{\downarrow *}$	-0.41
	2002	$-0.29^{\uparrow}$	–	$0.04^{\uparrow **}$	-0.25
	2003	$-0.32^{\uparrow **}$	–	0.01	-0.31
	2004	$-0.39^{\downarrow *}$	–	0.00	-0.39
	2005	-0.35	–	0.01	-0.34
	2006	-0.36	–	0.00	-0.36
	2007	$-0.30^{\uparrow}$	–	$0.02^{\uparrow *}$	-0.28
	2008	-0.34	–	0.00	-0.34
	2009	-0.39	–	-0.03	-0.42
	2010	$-0.43^{\downarrow}$	–	$-0.06^{\downarrow}$	-0.49
56d	2011	-0.36	–	0.02	-0.34
	2012	$-0.27^{\uparrow *}$	–	$0.04^{\uparrow **}$	-0.23
	2013	-0.33	–	0.00	-0.33
	2014	-0.35	–	-0.01	-0.36
	2015	$-0.47^{\downarrow **}$	–	$-0.11^{\downarrow **}$	-0.58
	2016	-0.34	–	0.00	-0.34
	2017	$-0.40^{\downarrow}$	–	-0.02	-0.42
	2018	-0.38	–	-0.03	-0.40
	2019	$-0.31^{\uparrow}$	–	0.03	-0.28
	$Tot._{2001–2019}$	-6.76		-0.13	<u>-6.89</u>
	$\bar{X}_{2001–2019}$	-0.36		-0.01	

GS: growing season
"*" and "**": min and max decrease/peak, respectively
"–": no data available

Table A7.3: Growing season albedo-induced global warming impact ($GWI_{\Delta\alpha gs}$, MgC_{eq} ha^{-1} gs^{-1}) during 2001–2019 for Ecoregion 56f. Underlined values indicate the cumulative $GWI_{\Delta\alpha gs}$ value for the entire ecoregion over the 19-year period. Major peaks (↑) and decreases (↓) from the $GWI_{\Delta\alpha gs}$ average are also shown. Positive and negative values of $GWI_{\Delta\alpha gs}$ indicate growing season warming and cooling effects, respectively, equivalent to carbon (C_{eq}; emission and mitigation, respectively) during 2001–2019.

		$GWI_{\Delta\alpha gs}$ (MgC_{eq} ha^{-1} gs^{-1})			
Ecoregion	GS	Cropland	Pasture	Urban	$Tot._{cover\ type}$
	2001	-0.37	$-0.27^{\downarrow}$	$-0.03^{\downarrow}$	-0.67
	2002	$-0.28^{\uparrow}$	$-0.19^{\uparrow **}$	$0.04^{\uparrow **}$	-0.43
	2003	$-0.31^{\uparrow **}$	-0.22	0.01	-0.52
	2004	-0.38	-0.24	0.01	-0.61
	2005	-0.35	-0.23	0.02	-0.56
	2006	-0.35	$-0.26^{\downarrow *}$	0.01	-0.60
	2007	$-0.30^{\uparrow}$	$-0.17^{\uparrow}$	$0.03^{\uparrow}$	-0.44
	2008	-0.33	-0.22	0.00	-0.55
	2009	-0.38	$-0.26^{\downarrow *}$	$-0.02^{\downarrow *}$	-0.66
	2010	$-0.42^{\downarrow}$	$-0.27^{\downarrow}$	$-0.05^{\downarrow}$	-0.75
56f	2011	-0.35	-0.23	$0.03^{\uparrow *}$	-0.55
	2012	$-0.27^{\uparrow *}$	$-0.14^{\uparrow *}$	$0.04^{\uparrow **}$	-0.37
	2013	-0.32	-0.21	0.01	-0.52
	2014	-0.34	$-0.27^{\downarrow}$	0.00	-0.62
	2015	$-0.47^{\downarrow **}$	$-0.29^{\downarrow **}$	$-0.10^{\downarrow **}$	-0.86
	2016	-0.33	-0.22	0.01	-0.54
	2017	$-0.40^{\downarrow *}$	-0.24	-0.01	-0.64
	2018	-0.37	-0.21	$-0.02^{\downarrow *}$	-0.60
	2019	$-0.31^{\uparrow **}$	$-0.18^{\uparrow}$	$0.04^{\uparrow **}$	-0.46
	$Tot._{2001–2019}$	-6.63	-4.31	0.00	<u>-10.94</u>
	$\bar{X}_{2001–2019}$	-0.35	-0.23	0.00	

GS: growing season
"*" and "**": min and max decrease/peak, respectively
"–": no data available

Table A7.4. Growing season albedo-induced global warming impact ($GWI_{\Delta\alpha gs}$, MgC_{eq} ha^{-1} gs^{-1}) during 2001–2019 for Ecoregion 56g. Underlined values indicate the cumulative $GWI_{\Delta\alpha gs}$ value for the entire ecoregion over the 19-year period. Major peaks (↑) and decreases (↓) from the $GWI_{\Delta\alpha gs}$ average are also shown. Positive and negative values of $GWI_{\Delta\alpha gs}$ indicate growing season warming and cooling effects, respectively, equivalent to carbon (C_{eq}; emission and mitigation, respectively) during 2001–2019.

		$GWI_{\Delta\alpha gs}$ (MgC_{eq} ha^{-1} gs^{-1})			
Ecoregion	GS	Cropland	Pasture	Urban	$Tot._{cover\ type}$
	2001	-0.36	$-0.26^{\downarrow}$	$-0.02^{\downarrow *}$	-0.65
	2002	$-0.28^{\uparrow}$	$-0.18^{\uparrow **}$	$0.05^{\uparrow *}$	-0.41
	2003	$-0.31^{\uparrow **}$	-0.21	0.02	-0.50
	2004	-0.37	-0.23	0.01	-0.59
	2005	-0.34	-0.22	0.02	-0.54
	2006	-0.35	$-0.25^{\downarrow}$	0.02	-0.58
	2007	$-0.29^{\uparrow}$	$-0.16^{\uparrow}$	$0.04^{\uparrow *}$	-0.42
	2008	-0.33	-0.22	0.01	-0.53
	2009	-0.37	$-0.25^{\downarrow *}$	-0.01	-0.64
	2010	$-0.41^{\downarrow}$	$-0.27^{\downarrow}$	$-0.05^{\downarrow}$	-0.73
56g	2011	-0.34	-0.22	0.03	-0.52
	2012	$-0.26^{\uparrow *}$	$-0.14^{\uparrow *}$	$0.05^{\uparrow **}$	-0.35
	2013	-0.32	-0.20	0.02	-0.51
	2014	-0.34	$-0.26^{\downarrow}$	0.01	-0.59
	2015	$-0.46^{\downarrow **}$	$-0.29^{\downarrow **}$	$-0.09^{\downarrow **}$	-0.84
	2016	-0.32	-0.21	0.01	-0.52
	2017	$-0.39^{\downarrow *}$	-0.23	0.00	-0.62
	2018	-0.36	-0.20	-0.02	-0.58
	2019	$-0.30^{\uparrow}$	$-0.18^{\uparrow **}$	$0.04^{\uparrow *}$	-0.44
	$Tot._{2001–2019}$	-6.50	-4.19	0.14	<u>-10.54</u>
	$\bar{X}_{2001–2019}$	-0.34	-0.22	0.01	

GS: growing season
"*" and "**": min and max decrease/peak, respectively
"–": no data available

Table A7.5: Growing season albedo-induced global warming impact ($GWI_{\Delta\alpha gs}$, MgC_{eq} ha^{-1} gs^{-1}) during 2001–2019 for Ecoregion 56h. Underlined values indicate the cumulative $GWI_{\Delta\alpha gs}$ value for the entire ecoregion over the 19-year period. Major peaks (↑) and decreases (↓) from the $GWI_{\Delta\alpha gs}$ average are also shown. Positive and negative values of $GWI_{\Delta\alpha gs}$ indicate growing season warming and cooling effects, respectively, equivalent to carbon (C_{eq}; emission and mitigation, respectively) during 2001–2019.

		$GWI_{\Delta\alpha gs}$ (MgC_{eq} ha^{-1} gs^{-1})			
Ecoregion	GS	Cropland	Pasture	Urban	$Tot._{cover\ type}$
	2001	-0.37	-0.26	$-0.03^{\downarrow}$	-0.65
	2002	$-0.28^{\uparrow}$	$-0.17^{\uparrow **}$	$0.04^{\uparrow}$	-0.42
	2003	$-0.31^{\uparrow **}$	-0.20	0.01	-0.51
	2004	-0.38	-0.22	0.00	-0.60
	2005	-0.35	-0.21	$0.01^{\uparrow *}$	-0.55
	2006	-0.35	$-0.24^{\downarrow *}$	0.01	-0.59
	2007	$-0.30^{\uparrow}$	$-0.16^{\uparrow}$	$0.03^{\uparrow}$	-0.43
	2008	-0.33	-0.21	0.00	-0.54
	2009	-0.38	$-0.25^{\downarrow}$	$-0.02^{\downarrow *}$	-0.65
	2010	$-0.42^{\downarrow}$	$-0.26^{\downarrow}$	$-0.06^{\downarrow}$	-0.73
56h	2011	-0.35	-0.21	$0.02^{\uparrow}$	-0.53
	2012	$-0.27^{\uparrow *}$	$-0.13^{\uparrow *}$	$0.04^{\uparrow **}$	-0.36
	2013	-0.33	-0.20	0.01	-0.51
	2014	-0.34	$-0.25^{\downarrow}$	0.00	-0.60
	2015	$-0.47^{\downarrow **}$	$-0.28^{\downarrow **}$	$-0.10^{\downarrow **}$	-0.85
	2016	-0.33	-0.20	0.01	-0.53
	2017	$-0.40^{\downarrow *}$	-0.22	$-0.01^{\downarrow}$	-0.63
	2018	-0.37	-0.19	$-0.02^{\downarrow *}$	-0.59
	2019	$-0.31^{\uparrow **}$	$-0.17^{\uparrow **}$	$0.03^{\uparrow}$	-0.44
	$Tot._{2001–2019}$	-6.64	-4.04	-0.02	<u>-10.71</u>
	$\bar{X}_{2001–2019}$	-0.35	-0.21	0.00	

GS: growing season
"*" and "**": min and max decrease/peak, respectively
"–": no data available

Table A8.1: Monthly albedo-induced global warming impact ($GWI_{\Delta\alpha mo}$, MgC_{eq} ha^{-1} mo^{-1}) during January–December for Ecoregion 56b. Underlined values indicate the cumulative $GWI_{\Delta\alpha mo}$ value for the entire ecoregion over the 11-month period. Positive and negative values of $GWI_{\Delta\alpha mo}$ indicate monthly warming and cooling effects, respectively, equivalent to carbon (C_{eq}; emission and mitigation, respectively) during the 19-year period.

		$GWI_{\Delta\alpha mo}$ (MgC_{eq} ha^{-1} mo^{-1})			
Ecoregion	Month	Cropland	Pasture	Urban	$Tot._{cover\ type}$
56b	Jan	-1.50	-1.11	-0.54	-3.16
	Feb	-2.15	-1.64	-0.64	-4.43
	Apr	-0.50	-0.41	-0.15	-1.06
	May	-0.50	-0.40	-0.08	-0.98
	Jun	-0.28	-0.26	0.09	-0.45
	Jul	-0.32	-0.22	0.09	-0.45
	Aug	-0.35	-0.19	0.05	-0.49
	Sep	-0.29	-0.18	0.01	-0.46
	Oct	-0.18	-0.14	-0.02	-0.34
	Nov	-0.23	-0.17	-0.09	-0.48
	Dec	-1.21	-0.91	-0.46	-2.58
	$Tot._{Jan–Dec}$	-7.52	-5.63	-1.75	<u>-14.89</u>
	$\bar{X}_{Jan–Dec}$	-0.68	-0.51	-0.16	

"–": no data available

Table A8.2: Monthly albedo-induced global warming impact ($GWI_{\Delta\alpha mo}$, MgC_{eq} ha^{-1} mo^{-1}) during January–December for Ecoregion 56d. Underlined values indicate the cumulative $GWI_{\Delta\alpha mo}$ value for the entire ecoregion over the 11-month period. Positive and negative values of $GWI_{\Delta\alpha mo}$ indicate monthly warming and cooling effects, respectively, equivalent to carbon (C_{eq}; emission and mitigation, respectively) during the 19-year period.

		$GWI_{\Delta\alpha mo}$ (MgC_{eq} ha^{-1} mo^{-1})			
Ecoregion	Month	Cropland	Pasture	Urban	$Tot._{cover\ type}$
56d	Jan	-1.49	–	-0.58	-2.07
	Feb	-2.11	–	-0.70	-2.82
	Apr	-0.51	–	-0.16	-0.67
	May	-0.51	–	-0.09	-0.60
	Jun	-0.28	–	0.08	-0.20
	Jul	-0.32	–	0.08	-0.25
	Aug	-0.35	–	0.04	-0.31
	Sep	-0.29	–	0.01	-0.28
	Oct	-0.18	–	-0.02	-0.21
	Nov	-0.23	–	-0.09	-0.32
	Dec	-1.21	–	-0.48	-1.70
	$Tot._{Jan–Dec}$	-7.50		-1.92	**-9.42**
	$\bar{X}_{Jan–Dec}$	-0.68		-0.17	

"–": no data available

Table A8.3: Monthly albedo-induced global warming impact ($GWI_{\Delta\alpha mo}$, MgC_{eq} ha^{-1} mo^{-1}) during January–December for Ecoregion 56f. Underlined values indicate the cumulative $GWI_{\Delta\alpha mo}$ value for the entire ecoregion over the 11-month period. Positive and negative values of $GWI_{\Delta\alpha mo}$ indicate monthly warming and cooling effects, respectively, equivalent to carbon (C_{eq}; emission and mitigation, respectively) during the 19-year period.

		$GWI_{\Delta\alpha mo}$ (MgC_{eq} ha^{-1} mo^{-1})			
Ecoregion	Month	Cropland	Pasture	Urban	$Tot._{cover\ type}$
	Jan	-1.48	-1.04	-0.53	-3.05
	Feb	-2.11	-1.53	-0.64	-4.27
	Apr	-0.50	-0.38	-0.15	-1.03
	May	-0.49	-0.37	-0.08	-0.94
	Jun	-0.27	-0.24	0.09	-0.42
	Jul	-0.32	-0.20	0.09	-0.42
56f	Aug	-0.34	-0.17	0.06	-0.46
	Sep	-0.29	-0.16	0.02	-0.43
	Oct	-0.18	-0.13	-0.02	-0.33
	Nov	-0.23	-0.16	-0.09	-0.47
	Dec	-1.19	-0.85	-0.45	-2.49
	$Tot._{Jan–Dec}$	-7.39	-5.23	-1.70	<u>-14.32</u>
	$\bar{X}_{Jan–Dec}$	-0.67	-0.48	-0.15	

"–": no data available

Table A8.4: Monthly albedo-induced global warming impact ($GWI_{\Delta\alpha gs}$, MgC_{eq} ha^{-1} mo^{-1}) during January–December for Ecoregion 56g. Underlined values indicate the cumulative $GWI_{\Delta\alpha mo}$ value for the entire ecoregion over the 11-month period. Positive and negative values of $GWI_{\Delta\alpha mo}$ indicate monthly warming and cooling effects, respectively, equivalent to carbon (C_{eq}; emission and mitigation, respectively) during the 19-year period.

		$GWI_{\Delta\alpha mo}$ (MgC_{eq} ha^{-1} mo^{-1})			
Ecoregion	Month	Cropland	Pasture	Urban	$Tot._{cover\ type}$
	Jan	-1.47	-1.05	-0.53	-3.05
	Feb	-2.10	-1.54	-0.62	-4.26
	Apr	-0.49	-0.38	-0.14	-1.01
	May	-0.48	-0.37	-0.07	-0.92
	Jun	-0.26	-0.23	0.10	-0.40
	Jul	-0.31	-0.20	0.10	-0.40
56g	Aug	-0.34	-0.17	0.06	-0.44
	Sep	-0.28	-0.16	0.02	-0.42
	Oct	-0.18	-0.13	-0.02	-0.32
	Nov	-0.22	-0.16	-0.09	-0.47
	Dec	-1.19	-0.86	-0.45	-2.49
	$Tot._{Jan–Dec}$	-7.31	-5.26	-1.62	<u>-14.19</u>
	$\bar{X}_{Jan–Dec}$	-0.66	-0.48	-0.15	

"–": no data available

Table A8.5: Monthly albedo-induced global warming impact ($GWI_{\Delta\alpha mo}$, MgC_{eq} ha^{-1} mo^{-1}) during January–December for Ecoregion 56h. Underlined values indicate the cumulative $GWI_{\Delta\alpha mo}$ value for the entire ecoregion over the 11-month period. Positive and negative values of $GWI_{\Delta\alpha mo}$ indicate monthly warming and cooling effects, respectively, equivalent to carbon (C_{eq}; emission and mitigation, respectively) during the 19-year period.

		$GWI_{\Delta\alpha mo}$ (MgC_{eq} ha^{-1} mo^{-1})			
Ecoregion	Month	Cropland	Pasture	Urban	$Tot._{cover\ type}$
56h	Jan	-1.48	–	-0.54	-2.02
	Feb	-2.12	–	-0.64	-2.76
	Apr	-0.50	–	-0.15	-0.65
	May	-0.49	–	-0.08	-0.57
	Jun	-0.27	–	0.09	-0.19
	Jul	-0.32	–	0.09	-0.23
	Aug	-0.35	–	0.05	-0.29
	Sep	-0.29	–	0.01	-0.27
	Oct	-0.18	–	-0.02	-0.20
	Nov	-0.23	–	-0.09	-0.31
	Dec	-1.20	–	-0.46	-1.65
	$Tot._{Jan–Dec}$	-7.41		-1.73	<u>-9.14</u>
	$\bar{X}_{Jan–Dec}$	-0.67		-0.16	

"–": no data available

Table A9: Nested analysis of variance (ANOVA with repeated measurements), among and within ecoregions, based on the linear models at Eqs. 3.9 and 3.10. Dependent variables: $GWI_{\Delta\alpha gs}$ and $GWI_{\Delta\alpha mo}$ (MgC_{eq} ha^{-1} gs^{-1}/mo^{-1}).

		Variable	DF	SS	MS	F	p-value	η^2 (%)
Among Ecoregion	$GWI_{\Delta\alpha gs}$	Ecoregions	4	0.00	0.00	860.57	***	32.04[a]
		Cover type	1	5.80	5.80	4786.41	***	94.81
		Ecoregions × Cover type	4	0.00	0.00	182.84	***	51.83[a]
		Residuals	162	0.02	0.00			
	$GWI_{\Delta\alpha mo}$	Ecoregions	4	0.01	0.00	24.17		28.53[a]
		Cover type	1	7.34	7.34	19.05	***	23.52
		Ecoregions × Cover type	4	0.00	0.00	3.61		25.61[a]
		Residuals	90	3.86	0.39			
Within Ecoregion	$GWI_{\Delta\alpha gs}$	Cover type	2	5.94	2.97	12185	***	99.00
		Residuals	245	0.06	0.00			
	$GWI_{\Delta\alpha mo}$	Cover type	2	7.47	2.67	122.80	***	65.40
		Residuals	130	3.95	0.03			

$GWI_{\Delta\alpha gs}$ and $GWI_{\Delta\alpha mo}$: albedo-induced global warming impact ($GWI_{\Delta\alpha}$) at growing season and monthly periods, respectively
Signif. codes: *** p-value < 0.001, ** p-value < 0.01, * p-value < 0.05, · p-value < 0.1, p-value > 0.1
η^2: generalized eta squares indicating the variance in the dependent variable (i.e., $GWI_{\Delta\alpha}$) accounted for by the independent variables (i.e., ecoregion, cover type, and their interactions)
"a": η^2 values obtained from the Mauchly's test of sphericity by applying the Greenhouse-Geisser correction

Table A10: Overall percent contribution and percent contribution higher than the average (>8%; i.e., 1/12th of the total, i.e., equal contribution across the 12-month period) of albedo-induced global warming impact ($GWI_{\Delta\alpha}$) by non-growing season and growing season in the five Level IV ecoregions. Cooling effects showing the contributions higher than the average are underlined.

	Overall contribution (%)					Contribution higher than the average (%)				
	Level IV ecoregions									
months	56b	56d	56f	56g	56h	56b	56d	56f	56g	56h
NGS	73	75	73	73	74	<u>100</u>	<u>100</u>	<u>100</u>	<u>100</u>	<u>100</u>
GS	27	25	27	27	26	0	0	0	0	0

NGS: non-growing season months (January, February, March, and December)
GS: growing season months (April–November)

Table A11: Percent contribution higher than the average (>8%; i.e., 1/12th of the total, i.e., equal contribution across the 12-month period) of albedo-induced global warming impact ($GWI_{\Delta\alpha}$) by non-growing season and growing season for cropland, pasture, and urban in the five Level IV ecoregions.

		Contribution higher than the average (%)		
		Cover type		
Ecoregion	Months	Cropland	Pasture	Urban
56b	NGS	100	100	100
	GS	0	0	0
56d	NGS	100	–	100
	GS	0	–	0
56f	NGS	100	100	100
	GS	0	0	0
56g	NGS	100	100	100
	GS	0	0	0
56h	NGS	100	–	100
	GS	0	–	0

NGS: non-growing season months (January, February, March, and December)
GS: growing season months (April–November)
"–": no data available

Table A12.1: Growing season albedo-induced radiative forcing ($RF_{\Delta\alpha gs}$, W m^{-2}) during 2001–2019 for Ecoregion 56b. Underlined values indicate the cumulative $RF_{\Delta\alpha gs}$ value for the entire ecoregion over the 19-year period. Positive and negative values of $RF_{\Delta\alpha gs}$ indicate growing season warming and cooling effects, respectively.

		$RF_{\Delta\alpha gs}$ (W m^{-2})			
Ecoregion	GS	Cropland	Pasture	Urban	$Tot._{cover\ type}$
	2001	-5.08	-3.91	-0.44	-9.43
	2002	-3.93	-2.73	0.57	-6.10
	2003	-4.35	-3.12	0.12	-7.35
	2004	-5.28	-3.44	0.04	-8.67
	2005	-4.83	-3.33	0.19	-7.97
	2006	-4.91	-3.74	0.10	-8.55
	2007	-4.13	-2.48	0.38	-6.22
	2008	-4.63	-3.27	0.03	-7.87
	2009	-5.27	-3.79	-0.28	-9.34
	2010	-5.79	-3.96	-0.78	-10.53
56b	2011	-4.83	-3.29	0.33	-7.79
	2012	-3.71	-2.14	0.56	-5.28
	2013	-4.50	-3.05	0.10	-7.45
	2014	-4.76	-3.89	-0.05	-8.70
	2015	-6.46	-4.27	-1.37	-12.10
	2016	-4.55	-3.15	0.06	-7.64
	2017	-5.52	-3.44	-0.18	-9.14
	2018	-5.11	-3.03	-0.35	-8.49
	2019	-4.26	-2.71	0.47	-6.49
	$Tot._{2001–2019}$	-91.90	-62.73	-0.48	<u>-155.11</u>
	$\bar{X}_{2001–2019}$	-4.84	-3.30	-0.025	

GS: growing season
"–": no data available

Table A12.2: Growing season albedo-induced radiative forcing ($RF_{\Delta\alpha gs}$, W m^{-2}) during 2001–2019 for Ecoregion 56d. Underlined values indicate the cumulative $RF_{\Delta\alpha gs}$ value for the entire ecoregion over the 19-year period. Positive and negative values of $RF_{\Delta\alpha gs}$ indicate growing season warming and cooling effects, respectively.

		$RF_{\Delta\alpha gs}$ (W m^{-2})			
Ecoregion	GS	Cropland	Pasture	Urban	$Tot._{cover\ type}$
	2001	-5.11	–	-0.52	-5.64
	2002	-3.96	–	0.50	-3.46
	2003	-4.36	–	0.08	-4.28
	2004	-5.32	–	-0.04	-5.36
	2005	-4.83	–	0.13	-4.69
	2006	-4.94	–	0.00	-4.94
	2007	-4.13	–	0.32	-3.81
	2008	-4.65	–	-0.04	-4.69
	2009	-5.31	–	-0.37	-5.68
	2010	-5.80	–	-0.84	-6.64
56d	2011	-4.86	–	0.23	-4.62
	2012	-3.70	–	0.52	-3.18
	2013	-4.50	–	0.05	-4.45
	2014	-4.79	–	-0.14	-4.92
	2015	-6.47	–	-1.44	-7.90
	2016	-4.58	–	-0.01	-4.59
	2017	-5.52	–	-0.24	-5.76
	2018	-5.12	–	-0.39	-5.51
	2019	-4.27	–	0.39	-3.88
	$Tot._{2001–2019}$	-92.21		-1.80	<u>-94.00</u>
	$\bar{X}_{2001–2019}$	-4.85		-0.095	

GS: growing season
"–": no data available

Table A12.3: Growing season albedo-induced radiative forcing ($RF_{\Delta\alpha gs}$, W m^{-2}) during 2001–2019 for Ecoregion 56f. Underlined values indicate the cumulative $RF_{\Delta\alpha gs}$ value for the entire ecoregion over the 19-year period. Positive and negative values of $RF_{\Delta\alpha gs}$ indicate growing season warming and cooling effects, respectively.

		$RF_{\Delta\alpha gs}$ (W m^{-2})			
Ecoregion	GS	Cropland	Pasture	Urban	$Tot._{cover\ type}$
	2001	-5.00	-3.69	-0.41	-9.10
	2002	-3.87	-2.56	0.59	-5.84
	2003	-4.28	-2.94	0.15	-7.08
	2004	-5.21	-3.23	0.07	-8.36
	2005	-4.75	-3.12	0.22	-7.65
	2006	-4.84	-3.53	0.12	-8.25
	2007	-4.05	-2.30	0.41	-5.94
	2008	-4.55	-3.07	0.05	-7.57
	2009	-5.19	-3.56	-0.26	-9.01
	2010	-5.71	-3.73	-0.74	-10.18
56f	2011	-4.76	-3.09	0.35	-7.50
	2012	-3.64	-1.97	0.59	-5.03
	2013	-4.43	-2.86	0.13	-7.15
	2014	-4.69	-3.68	-0.03	-8.41
	2015	-6.37	-4.02	-1.32	-11.70
	2016	-4.47	-2.95	0.09	-7.34
	2017	-5.44	-3.22	-0.14	-8.80
	2018	-5.04	-2.83	-0.31	-8.18
	2019	-4.18	-2.52	0.49	-6.21
	$Tot._{2001–2019}$	-90.48	-58.87	0.04	<u>-149.31</u>
	$\bar{X}_{2001–2019}$	-4.76	-3.10	0.002	

GS: growing season
"–": no data available

Table A12.4: Growing season albedo-induced radiative forcing ($RF_{\Delta\alpha gs}$, W m^{-2}) during 2001–2019 for Ecoregion 56g. Underlined values indicate the cumulative $RF_{\Delta\alpha gs}$ value for the entire ecoregion over the 19-year period. Positive and negative values of $RF_{\Delta\alpha gs}$ indicate growing season warming and cooling effects, respectively.

		$RF_{\Delta\alpha gs}$ (W m^{-2})			
Ecoregion	GS	Cropland	Pasture	Urban	$Tot._{cover\ type}$
	2001	-4.90	-3.61	-0.31	-8.81
	2002	-3.78	-2.46	0.69	-5.55
	2003	-4.19	-2.84	0.23	-6.81
	2004	-5.10	-3.12	0.17	-8.05
	2005	-4.68	-3.03	0.31	-7.40
	2006	-4.73	-3.43	0.24	-7.92
	2007	-3.98	-2.21	0.50	-5.69
	2008	-4.46	-2.98	0.16	-7.29
	2009	-5.08	-3.47	-0.14	-8.70
	2010	-5.61	-3.65	-0.65	-9.90
56g	2011	-4.66	-2.97	0.47	-7.16
	2012	-3.57	-1.88	0.67	-4.79
	2013	-4.35	-2.77	0.22	-6.90
	2014	-4.58	-3.58	0.09	-8.07
	2015	-6.26	-3.95	-1.23	-11.44
	2016	-4.38	-2.86	0.19	-7.05
	2017	-5.34	-3.13	-0.05	-8.53
	2018	-4.95	-2.75	-0.24	-7.94
	2019	-4.11	-2.42	0.59	-5.94
	$Tot._{2001–2019}$	-88.70	-57.13	1.91	<u>-143.92</u>
	$\bar{X}_{2001–2019}$	-4.67	-3.01	0.100	

GS: growing season
"–": no data available

Table A12.5: Growing season albedo-induced radiative forcing ($RF_{\Delta\alpha gs}$, W m^{-2}) during 2001–2019 for Ecoregion 56h. Underlined values indicate the cumulative $RF_{\Delta\alpha gs}$ value for the entire ecoregion over the 19-year period. Positive and negative values of $RF_{\Delta\alpha gs}$ indicate growing season warming and cooling effects, respectively.

		$RF_{\Delta\alpha gs}$ (W m^{-2})			
Ecoregion	GS	Cropland	Pasture	Urban	$Tot._{cover\ type}$
	2001	-5.00	-3.51	-0.43	-8.94
	2002	-3.88	-2.36	0.56	-5.67
	2003	-4.28	-2.74	0.12	-6.91
	2004	-5.20	-3.00	0.05	-8.16
	2005	-4.77	-2.91	0.19	-7.49
	2006	-4.84	-3.31	0.10	-8.06
	2007	-4.07	-2.12	0.38	-5.81
	2008	-4.56	-2.88	0.04	-7.41
	2009	-5.19	-3.37	-0.27	-8.83
	2010	-5.71	-3.55	-0.76	-10.01
56h	2011	-4.77	-2.86	0.34	-7.29
	2012	-3.66	-1.79	0.56	-4.89
	2013	-4.44	-2.67	0.11	-7.00
	2014	-4.69	-3.47	-0.04	-8.20
	2015	-6.36	-3.86	-1.33	-11.56
	2016	-4.48	-2.77	0.07	-7.18
	2017	-5.44	-3.02	-0.17	-8.63
	2018	-5.04	-2.66	-0.34	-8.03
	2019	-4.20	-2.32	0.47	-6.05
	$Tot._{2001–2019}$	-90.61	-55.17	-0.34	<u>-146.12</u>
	$\bar{X}_{2001–2019}$	-4.77	-2.90	-0.018	

GS: growing season
"–": no data available

Table A13.1: Monthly albedo-induced radiative forcing ($RF_{\Delta\alpha mo}$, W m^{-2}) during January–December for Ecoregion 56b. Underlined values indicate the cumulative $RF_{\Delta\alpha mo}$ value for the entire ecoregion over the 11-month period. Positive and negative values of $RF_{\Delta\alpha mo}$ indicate monthly warming and cooling effects, respectively.

		$RF_{\Delta\alpha mo}$ (W m^{-2})			
Ecoregion	Month	Cropland	Pasture	Urban	$Tot._{cover\ type}$
	Jan	-20.51	-15.17	-7.40	-43.08
	Feb	-29.29	-22.39	-8.80	-60.48
	Apr	-6.87	-5.55	-2.08	-14.51
	May	-6.80	-5.50	-1.07	-13.37
	Jun	-3.80	-3.49	1.21	-6.08
	Jul	-4.39	-3.01	1.21	-6.19
56b	Aug	-4.80	-2.63	0.73	-6.70
	Sep	-3.98	-2.46	0.19	-6.25
	Oct	-2.46	-1.88	-0.34	-4.69
	Nov	-3.12	-2.27	-1.21	-6.60
	Dec	-16.55	-12.44	-6.28	-35.27
	$Tot._{Jan–Dec}$	-102.58	-76.80	-23.84	<u>-203.22</u>
	$\bar{X}_{Jan–Dec}$	-9.33	-6.98	-2.17	

"–": no data available

Table A13.2: Monthly albedo-induced radiative forcing ($RF_{\Delta\alpha mo}$, W m^{-2}) during January–December for Ecoregion 56d. Underlined values indicate the cumulative $RF_{\Delta\alpha mo}$ value for the entire ecoregion over the 11-month period. Positive and negative values of $RF_{\Delta\alpha mo}$ indicate monthly warming and cooling effects, respectively.

		$RF_{\Delta\alpha mo}$ (W m^{-2})			
Ecoregion	Month	Cropland	Pasture	Urban	$Tot._{cover\ type}$
56d	Jan	-20.35	–	-7.89	-28.24
	Feb	-28.84	–	-9.59	-38.43
	Apr	-6.95	–	-2.17	-9.11
	May	-6.95	–	-1.27	-8.22
	Jun	-3.85	–	1.07	-2.78
	Jul	-4.42	–	1.06	-3.35
	Aug	-4.80	–	0.59	-4.21
	Sep	-3.99	–	0.12	-3.87
	Oct	-2.47	–	-0.33	-2.80
	Nov	-3.15	–	-1.21	-4.36
	Dec	-16.57	–	-6.61	-23.19
	$Tot._{Jan–Dec}$	-102.34		-26.22	<u>-128.56</u>
	$\bar{X}_{Jan–Dec}$	-9.30		-2.38	

"–": no data available

Table A13.3: Monthly albedo-induced radiative forcing ($RF_{\Delta\alpha mo}$, W m^{-2}) during January–December for Ecoregion 56f. Underlined values indicate the cumulative $RF_{\Delta\alpha mo}$ value for the entire ecoregion over the 11-month period. Positive and negative values of $RF_{\Delta\alpha mo}$ indicate monthly warming and cooling effects, respectively.

		$RF_{\Delta\alpha mo}$ (W m^{-2})			
Ecoregion	Month	Cropland	Pasture	Urban	$Tot._{cover\ type}$
	Jan	-20.17	-14.16	-7.30	-41.63
	Feb	-28.77	-20.85	-8.72	-58.34
	Apr	-6.79	-5.21	-2.01	-14.01
	May	-6.73	-5.09	-1.02	-12.84
	Jun	-3.74	-3.21	1.22	-5.73
	Jul	-4.31	-2.73	1.23	-5.80
56f	Aug	-4.70	-2.36	0.76	-6.29
	Sep	-3.90	-2.24	0.23	-5.92
	Oct	-2.43	-1.76	-0.30	-4.49
	Nov	-3.08	-2.14	-1.16	-6.38
	Dec	-16.28	-11.62	-6.15	-34.04
	$Tot._{Jan–Dec}$	-100.89	-71.36	-23.22	<u>-195.46</u>
	$\bar{X}_{Jan–Dec}$	-9.17	-6.49	-2.11	

"–": no data available

Table A13.4: Monthly albedo-induced radiative forcing ($RF_{\Delta\alpha mo}$, W m^{-2}) during January–December for Ecoregion 56g. Underlined values indicate the cumulative $RF_{\Delta\alpha mo}$ value for the entire ecoregion over the 11-month period. Positive and negative values of $RF_{\Delta\alpha mo}$ indicate monthly warming and cooling effects, respectively.

		$RF_{\Delta\alpha mo}$ (W m^{-2})			
Ecoregion	Month	Cropland	Pasture	Urban	$Tot._{cover\ type}$
	Jan	-20.09	-14.34	-7.18	-41.60
	Feb	-28.63	-21.09	-8.42	-58.14
	Apr	-6.66	-5.22	-1.95	-13.83
	May	-6.55	-5.11	-0.89	-12.54
	Jun	-3.61	-3.16	1.37	-5.40
	Jul	-4.20	-2.67	1.38	-5.50
56g	Aug	-4.62	-2.32	0.88	-6.05
	Sep	-3.84	-2.21	0.30	-5.75
	Oct	-2.39	-1.74	-0.29	-4.42
	Nov	-3.05	-2.14	-1.17	-6.36
	Dec	-16.18	-11.77	-6.09	-34.04
	$Tot._{Jan–Dec}$	-99.83	-71.74	-22.06	<u>-193.64</u>
	$\bar{X}_{Jan–Dec}$	-9.08	-6.52	-2.01	

"–": no data available

Table A13.5: Monthly albedo-induced radiative forcing ($RF_{\Delta\alpha mo}$, W m^{-2}) during January–December for Ecoregion 56h. Underlined values indicate the cumulative $RF_{\Delta\alpha mo}$ value for the entire ecoregion over the 11-month period. Positive and negative values of $RF_{\Delta\alpha mo}$ indicate monthly warming and cooling effects, respectively.

		$RF_{\Delta\alpha mo}$ (W m^{-2})			
Ecoregion	Month	Cropland	Pasture	Urban	$Tot._{cover\ type}$
56h	Jan	-20.25	–	-7.33	-27.58
	Feb	-28.92	–	-8.72	-37.64
	Apr	-6.76	–	-2.05	-8.81
	May	-6.69	–	-1.04	-7.73
	Jun	-3.74	–	1.20	-2.54
	Jul	-4.34	–	1.20	-3.14
	Aug	-4.73	–	0.73	-4.01
	Sep	-3.92	–	0.19	-3.73
	Oct	-2.43	–	-0.33	-2.76
	Nov	-3.07	–	-1.19	-4.26
	Dec	-16.32	–	-6.21	-22.53
	$Tot._{Jan–Dec}$	-101.18		-23.55	<u>-124.73</u>
	$\bar{X}_{Jan–Dec}$	-9.20		-2.14	

"–": no data available

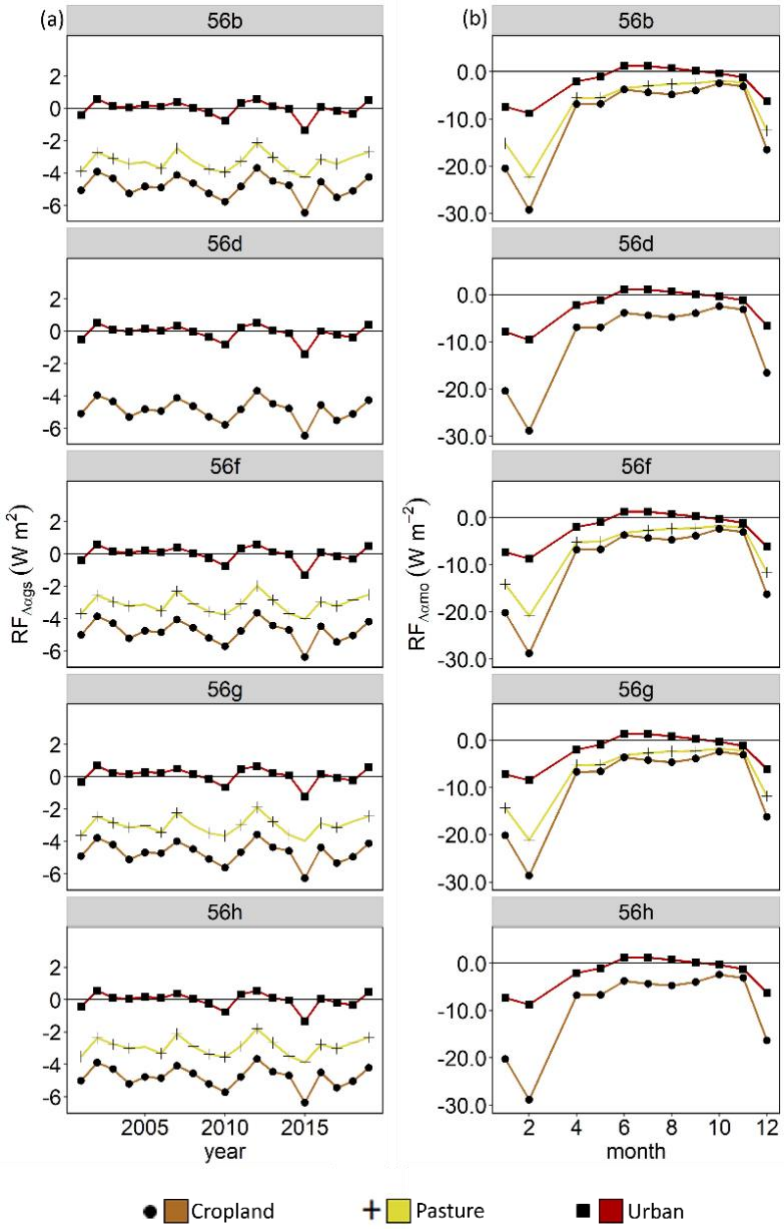

Figure A1: Albedo-induced radiative forcing ($RF_{\Delta\alpha}$) for the five Level IV ecoregions. Panels (a) and (b) represent the $RF_{\Delta\alpha}$ for the growing season ($RF_{\Delta\alpha gs}$; 2001–2019) and monthly ($RF_{\Delta\alpha mo}$; January–December, less March) periods, respectively. Positive and negative values of $RF_{\Delta\alpha gs}$ and $RF_{\Delta\alpha mo}$ indicate warming and cooling effects, respectively, during 19-year growing season and months, respectively.

CHAPTER 4. MODELING THE MAIN KEY INFLUENCES ON THE NET ECOSYSTEM EXCHANGE (NEE) FLUXES: INFERENCES TO CLIMATE REGULATION POTENTIALS DUE TO LAND USE HISTORY AT BIOENERGY CROPPING SYSTEMS IN SOUTHWESTERN MICHIGAN

Abstract

Land use and land cover and associated management history can substantially affect the net carbon (C) sink/source nature of a landscape. Here I examined the contribution of interannual variation of main key influences affecting the net C uptake/emission during 2018–2021 growing seasons, under different land use history and management, using both *in-situ* and remote sensing data. The results show that interannual variations of key influences to the net ecosystem exchange (NEE) depend on the cover type and growing season, with a unique seasonal pattern observed in maize. Specifically, the ranking, number, and magnitude of key influences to the net growing season NEE varied by cover type, highlighting the different nature of bioenergy crops (i.e., annual *vs* perennial and monoculture *vs* polyculture). Among the three bioenergy crops considered, maize contributes the most to net C uptakes, with magnitudes ranging between -9.4 and -22.8 gC m^{-2} d^{-1}. Lastly, I show the capability of fine-resolution optical and radar remote sensing to improve forecasts (depending on the site and the date considered) of growing season NEE at maize cover type as proof of concept. Further work may benefit from coupling these estimates with emissions from other greenhouse gases (GHGs), as well as by extending the analysis to non-growing season to improve our understanding of the role that land use history and management have on climate warming/cooling.

Introduction

As stated in the Sixth Assessment Report (AR6) by the Intergovernmental Panel on Climate Change (IPCC), adaptation and mitigation strategies to climate change are essential to limit global warming to 1.5 °C in order to achieve sustainable development (Bezner et al., 2022). Agricultural cropping systems represent a conspicuous percentage (~50%) of worldwide land cover and for decades now croplands have been investigated to improve our understanding of the ecosystem

functions and services they provide, especially in the context of adaptations and mitigations strategies (Barrios et al., 2018). Both adaptation and mitigation strategies fall within several foci. Just to mention a few: that of well-mixed greenhouse gasses (GHGs)—i.e., carbon dioxide (CO_2), methane (CH_4), and nitrous oxide (N_2O)—emissions, representing the sink/source nature of a system; soil and water conservation; grassland quality; crop yield; biodiversity. Regarding the former, given the well-established scientific knowledge of the contributions of GHGs to global warming, understanding whether a system behaves as sink or source is of fundamental interest for many research studies and of particular importance for policy makers. For instance, according to the IPCC, global agricultural activities in 2019 were responsible for emissions equivalent to 13 $GtCO_2$, which represented ~22% of the total net anthropogenic GHG emissions (Shukla et al., 2022). Researchers agree that the CO_2 sink/source nature of agricultural crop systems is a complex function of various physical, biophysical, and physiological drivers, as well as the type of cropping system (i.e., food *vs* fuel crops). In turn, such drivers are strongly influenced by land management (e.g., agronomic practices), land use history and change (e.g., conversion of croplands to grasslands), weather conditions (e.g., frequency and intensity of precipitation events and high/low temperature periods), etc. (Abraha & Hamilton, et al., 2018; Liu & Greaver, 2009; Tongwane & Moeletsi, 2018). Hence, it is important to measure all those drivers and their role in altering ecosystem CO_2 balances, especially in the anticipation of future climate projections. The U.S. Midwest is well suited to investigate these drivers because it contains land cover mosaics including agricultural crops that vary in their type of crop, land use history and change, and weather conditions. Moreover, in the Midwest, future climate scenarios point to increase in frequency of heavy precipitation events and droughts, leading to more variable water availability for agriculture and natural plant communities (Hayhoe et al., 2010).

One mitigation option in the context of agricultural cropping systems is the use of bioenergy crops—the use of biomass for direct generation of energy rather than food or feed—to enhance the carbon (C) debt payback (i.e., offset between C emissions and mitigations). However, the C debt payback of bioenergy crops has been shown to be strongly influenced by land use history and farm management practices (Forster et al., 2021). Here I estimate the main key influences to CO_2 uptake/emission across three different bioenergy cropping systems (i.e., maize, prairie, and switchgrass) during four years of growing seasons by using both *in-situ* and remote sensing approach. In particular, I aim to: (i) investigate the main key influences (e.g., soil water content, air temperature, leaf area index, vegetation height, etc.) to interannual variations of net ecosystem exchange (NEE) fluxes, expressed as $gC\ m^{-2}$; and (ii) to use multi-sensor remote sensing approach to forecast NEE for maize during 2021 growing season, drawing inferences to the net growing season C uptake/emissions under different land use history and due to main stages of maize's growth development. While the analysis of the main key influences to NEE was carried out across three different bioenergy crops (i.e., maize, restored prairie, and switchgrass), the focus of the forecast of NEE was only on maize as a proof of concept because it was the only cover type whose growth development stages fall entirely within the *in-situ* data collection timeframe and it is not expected to show major intra-annual variation of NEE due to its mono-culture and highly genetically bred nature.

Materials & Methods

Study area

I considered six study sites (42°24′ N, 85°24′ W, 288 m a.s.l.; Figure 4.1ab) located at the Great Lakes Bioenergy Research Center (GLBRC) of the Kellogg Biological Station (KBS), in southwestern Michigan, USA. The sites are characterized by humid continental temperate climate

with mean annual (1981–2010) air temperature of 9.9 °C and mean total annual precipitation of 1027 mm (Abraha et al., 2019). Soils are Typic Hapludalfs, well-drained sandy loams (Abraha et al., 2016; Thoen, 1990). Mean air temperature and total precipitation are 19.7°C and 523 mm, respectively, with highest temperatures in July (Bhardwaj et al., 2011).

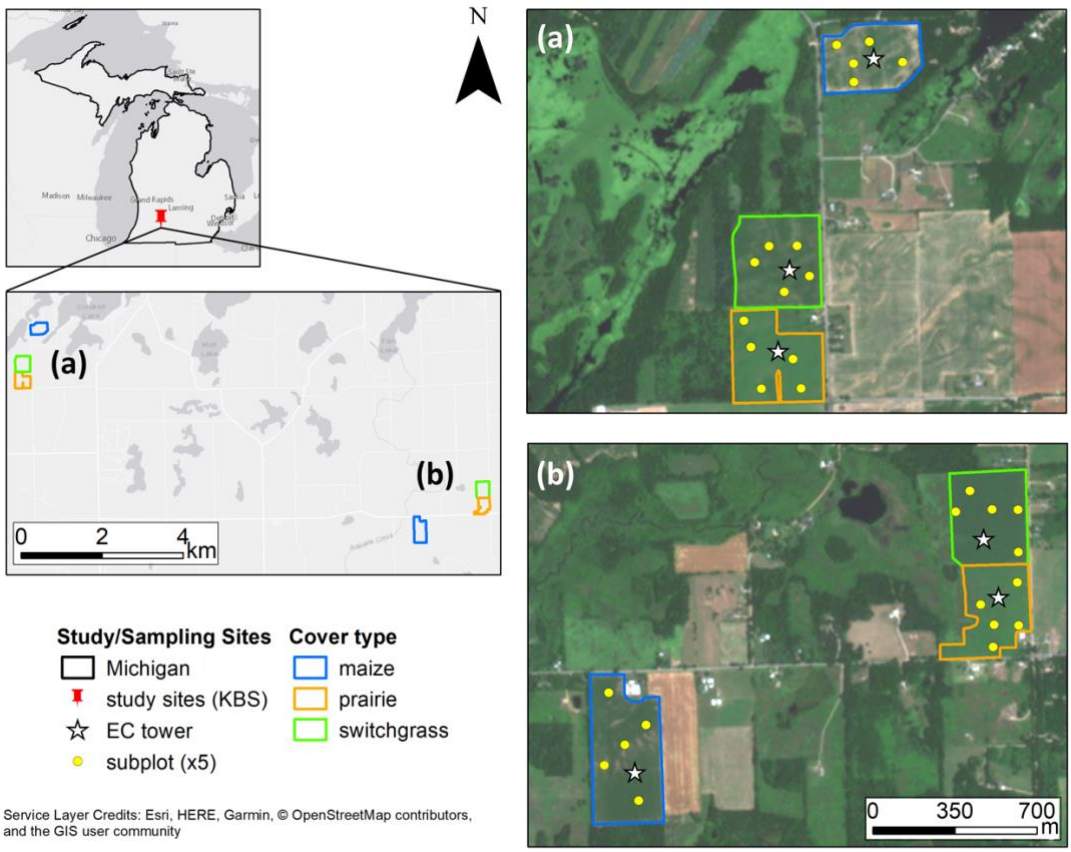

Figure 4.1: Location of the study area at the Kellogg Biological Station (KBS), in southwest Michigan, USA. Panels (a) and (b) refer to the historically cultivated as agricultural land (AGR) and the Conservation Reserve Program (CRP) sites, each with three bioenergy crops: no-till continuous maize (*Zea mays*; in blue), restored prairie (in orange), and switchgrass (*Panicum virgatum*; in green). The location of the seven Eddy Covariance (EC) flux towers (white star symbol), as well as the five subplots (yellow solid circles) are also shown.

The study sites are clustered into two groups, depending on their land use and management history: the historically cultivated as agricultural lands (hereafter indicated with the prefix "AGR"; Figure 4.1a) and the Conservation Reserve Program (hereafter indicated with the prefix "CRP"; Figure 4.1b) sites. The AGR sites were managed as conventionally-tilled agricultural corn-soybean

rotations, while the CRP sites were managed as grasslands (*Bromus inermis*; i.e., the dominant species), for 22 years (Abraha et al., 2019). In 2009, both groups (i.e., AGR and CRP) were then converted to their present land cover types, which include no-till continuous maize (*Zea mays*), restored prairie, and switchgrass (*Panicum virgatum*), hereinafter indicated as M, P, and S and using the final nomenclature as AGR-M/P/S and CRP-M/P/S, respectively. I considered the growing season of four years (i.e., 2018–2021) as study period of the present research. However, given the different phenologies of -M/P/S, for each of the three cover types, start and end of season (SoS and EoS, respectively) were selected considering the period between the first four days in row of uptake (SoS) and release (EoS) of carbon dioxide (CO_2), respectively. Further details about the SoS and EoS are outlined in the next section.

Net ecosystem exchange of CO_2

The exchange in CO_2 fluxes between terrestrial ecosystems and the atmosphere are referred to as net ecosystem exchange (NEE; $gCO_2\ m^{-2}\ d^{-1}$). The monitoring of NEE is carried out at field level via the use of Eddy Covariance (EC) flux towers (Abraha & Gelfand, et al., 2018). In this study, each site included one EC system (Figure 4.1ab), which carried a LI-7500 open-path infrared gas analyzer (IRGA, LI-COR Bioscience, Lincoln, NE) for measurements of both CO_2 and water (H_2O) concentration, and a CSAT3 three-dimensional sonic anemometer (Campbell Scientific Inc. CSI, Logan, UT) for measurements of wind speed and direction. Half-hourly meteorological measurements of incoming and outgoing solar radiation, air temperature, and relative humidity were also measured at each site using sensors like CNR1 (Kipp & Zonen, Delft, The Netherlands) and HMP45C (CSI). On each tower, the EC sensors are mounted at about 1.5–2 m above the vegetation canopy and logged at 10Hz using a Campbell CR5000 datalogger. Half-hourly fluxes were processed in "*EdiRe*" for screening out-of-range data due to bad weather,

sensors, and/or logger malfunction as well as de-spiking. For full data quality control details, refer to Zenone et al. (2011) and Abraha et al. (2015). Given the discrepancy in time acquisition between NEE fluxes and field data, I considered cumulative daily NEE fluxes, so that to match them with *in-situ* data collected during each field visit (Table A14).

During the study period, planting dates for AGR-/CRP-M were roughly around the first week of May, which roughly coincided to the start of the summer fieldwork campaigns. However, the phenological stages of maize differs from those of prairie and of switchgrass. Hence, I considered the growing seasons during 2018–2021 of the present study. Yearly growing seasons were obtained by detecting the SoS and EoS (i.e., first four days in row of CO_2 uptake and release, respectively; Table A15 and Figure A2ab). Specifically, when the detected NEE SoS day was posterior to the first day of field visit, the NEE on DOY "*d*" (NEE_d) was assumed to be the starting point for the cumulative NEE calculation. For example, the SoS for the AGR-M field in 2018 was on DOY 164 (i.e., June 13th; Table A15), while the first day of field visit in 2018 was on DOY 152 (i.e., June 1st; Table A14), hence the $NEE_{AGR\text{-}M164}$ was equal to NEE_{164} (i.e., the NEE on June 13th). On the other hand, when the SoS day was prior to the first day of field visit, I summed the daily NEE up to the field visit on DOY "*d*". For example, SoS for AGR-P field in 2018 was on DOY 142 (May 22nd; Table A15), while the first day of field visit in 2018 was on DOY 152 (June 1st; Table A14); hence, I calculated the $NEE_{AGR\text{-}P142}$ as the cumulative NEE from DOY 142 to 152 (i.e., $NEE_{AGR\text{-}P142}$ to $NEE_{AGR\text{-}P152}$), as shown below:

$$NEE_{152} = \sum_{SoS}^{n} NEE_d \quad (4.1)$$

where *SoS* is the DOY of start of season, prior to the DOY of first field visit (*n*), and NEE_d is the daily net ecosystem exchange (at DOY *d*).

In this study, I report the results in the context of C uptake/emission, with units of gC m^{-2}

per day (d^{-1}) or growing season (gs^{-1}), defined as negative and positive NEE for net C uptake from and emission to the atmosphere, respectively.

In-situ variables

Summer fieldwork campaigns at the six AGR and CRP sites were conducted from May through August during 2018–2021, at five pre-existing subplots (Figure 4.1ab). The six sites were visited roughly every ~14 days, depending on the weather conditions (Table A14), between 10 a.m. and 3 p.m. local time (UTC -05), with a growing summer average of ~6-8 visits per each site. During the field visit, at subplot level (Figure 4.1ab), I collected variables, such as leaf area index (LAI; m^2 m^{-2}), Soil and Plant Analysis Development index (SPAD index; an index of leaf chlorophyll content; Hlavinka et al., 2013), vegetation height (Ht; m), and soil water content (SWC; %). Specifically, LAI, SPAD, and SWC were measured using the LP-80 ceptometer (METER ACCUPAR), the SPAD-502DL (KONICA MINOLTA), and the HydroSense II (Campbell Scientific), respectively. For each day of visit, at each of the five subplots, I took three repeated measurements, for a total of 105 measurements (then averaged to 35, per subplot), per day of visit. All the measurements were assumed to represent daily values to be matched with cumulative daily NEE and remote sensing imagery acquisitions.

In addition to LAI, SPAD, Ht, and SWC, I also acquired other ancillary data such as mean daily air temperature (T_{air}; °C), daily relative humidity (RH; %), and mean daily photosynthetically active radiation (PAR; μmol m^{-2} d^{-1}), which were provided by the LTER meteorological station at KBS (Robertson, 2020) and were assumed to not vary significantly by site, due to their close proximity. Lastly, I used T_{air} and RH to calculate daily vapor pressure deficit (VPD; kPa), another hypothesized driver to NEE. Vapor pressure deficit was calculated as follows (Chen et al., 2021):

$$VPD = e_s - e_a \quad (4.2)$$

where e_s and e_a are the saturation and actual vapor pressure (kPa), respectively. Saturation vapor pressure can then be estimated for temperatures above 0 °C (Monteith & Unsworth, 2013) as follows:

$$e_s = 0.6118e^{(\frac{17.502T_{air}}{T_a+240.97})} \quad (4.3)$$

where T_{air} is the mean daily air temperature (°C). On the other hand, the actual vapor pressure is calculated as follows:

$$e_a = 0.000462E_aT_{air_K} \quad (4.4)$$

where E_a is the actual vapor density (kg m^{-3}) and T_{airK} is the mean daily air temperature in Kelvin (K). The actual vapor density (E_a) is then calculated as:

$$E_a = \frac{E_sRH}{100} \quad (4.5)$$

where E_s is the saturation vapor density (kg m^{-3}) and RH is the relative humidity (%). Lastly, the saturation vapor density is obtained as follows:

$$E_s = \frac{e_s}{0.000462T_{air_K}} \quad (4.6)$$

where e_s is the saturation vapor pressure (Eq. 4.3) and T_{airK} is the mean daily air temperature (K).

Remote sensing products

In addition to NEE fluxes and biophysical and physical *in-situ* data, I employed remote sensing imagery, namely, Sentinel-2 (optical) and Sentinel-1 (synthetic aperture radar), hereafter S2 and S1. Remote sensing imagery were acquired over the study area (Figure 4.1a,b) during the 2018–2021 growing seasons, by choosing images that had closest acquisition dates to those of the field visits (Table A14).

S2 consists of a constellation of two polar-orbiting satellites (Sentinel-2A and Sentinel-2B), in the same sun-synchronous orbit that carry a multispectral instrument (MSI) with 12 multispectral bands (cf. https://sentinels.copernicus.eu/web/sentinel/user-guides/sentinel-2-

msi/resolutions/spatial). Under cloud-free conditions, a single S2 satellite (i.e., A or B) has a revisit time of ~10 days at the equator, while ~5 days with A and B satellites together, with overpass time at 10:30 a.m. local time (UTC -05). Although S2 is offered at multiple spatial resolutions of 10, 20, and 60 m, here I used a spatial resolution of 20 m. The images were downloaded from the online catalog Copernicus Open Access Hub (c.f. https://scihub.copernicus.eu/dhus/#/home, accessed on July 2022) of the European Space Agency, as level 2A (i.e., surface reflectance) over the study area. Where level 2A was not available, I downloaded level 1C (i.e., top-of-atmosphere; TOA) images that were then atmospherically corrected to obtain surface reflectance by using the default settings of the Sen2Cor (v. 2.5.5) algorithm (Müller-Wilm et al., 2020). Specifically, I considered the spectral bands in the blue (B; "*B02*"; 492.4 nm), green (G; "*B03*"; 560 nm), red (R; "*B04*"; 665 nm), red-edge (RE; "*B07*"; 783 nm), near-infrared (NIR; "*B8A*"; 865 nm), and short-wave infrared (SWIR1; "*B11*"; 1614 nm; and SWIR2; "*B12*"; 2202 nm). I then used the "*SCL*" (i.e., scene classification layer), "*CLDPRB*" (i.e., cloud probability), and "*B8A*" bands to create a cloud-/cloud shadow mask for each image following this approach: https://developers.google.com/earth-engine/tutorials/community/sentinel-2-s2cloudless.

Lastly, in order to investigate major stages of the maize's growth development, I calculated vegetation indices (S2-VIs), such as the enhanced vegetation index 2 (EVI2; Jiang et al., 2008), the green chlorophyll index (CIg; Clevers & Gitelson, 2013), and the shortwave infrared (SWIR) normalized difference water index ($NDWI_{SWIR}$), as follows:

$$EVI2 = 2.5 \cdot \frac{\rho_{NIR} - \rho_R}{\rho_{NIR} + 2.4 \cdot \rho_R + 1} \quad (4.7)$$

$$CIg = \frac{\rho_{RE}}{\rho_G} - 1 \quad (4.8)$$

$$NDWI_{SWIR} = \frac{\rho_{NIR} - \rho_{SWIR}}{\rho_{NIR} + \rho_{SWIR}} \quad (4.9)$$

where ρ is the surface reflectance in the near-infrared (*NIR*), red (*R*), red-edge (*RE*), green (*G*), and shortwave infrared (*SWIR1* and *SWIR2*).

Regarding S1, it consists of a constellation of two polar-orbit satellites (Sentinel-1A and Sentinel-1B) carrying a C-band (5.4 GHz) synthetic aperture radar (SAR). The SARs acquire data with dual polarization (dual-pol; VV and VH) backscatter at a nominal spatial resolution of 10 m and with a combined (i.e., S1- A and B together) revisit time of ~5 days, in both ascending and descending orbits. Since ascending and descending orbit pass directions strongly affect the intensity of the backscatter due to different view angles, I used only S-1B images with ascending orbit pass night-time, i.e., 11:30 p.m. local time (UTC -05), over the study area and during 2018–2021 growing seasons. The S1-B images were downloaded from the ESA online catalog Copernicus Open Access Hub: I downloaded the dual-pol (VV and VH) Level-1 Ground Range Detected (GRD) product in the interferometric wide (IW) swath mode images. I then used the Sentinel application platform (SNAP; v.9.0.0) to develop a semi-automated workflow to extract sigma nought (σ°) polarization intensity backscatter (i.e., S1-σ°)—used for the calculation of S1-σ° ratios, arithmetic calculations, and the radar vegetation index (RVI)—and the S1 polarimetric SAR (S1-PolSAR) decomposition coefficients, such as Entropy, Alpha, and Anisotropy (i.e., H-α-A) (Nasirzadehdizaji et al. 2019). The main steps in the generic processing workflow were (i) radiometric calibration, (ii) orbit correction, (iii) polarimetric matrices calculation (only for S1-PolSAR analysis), (iv) speckle filtering, (v) geometric correction, and (vi) σ° calculations (only for S1-σ°) and PolSAR analysis (only for S1-PolSAR). Further details about the S1 processing workflow can be found in Nasirzadehdizaji et al. (2019).

Regarding the S1-σ° intensity ratios, arithmetic calculations, and the RVI they were calculated as follows 9):

$$ratio1 = \frac{\sigma^{\circ}_{VH}}{\sigma^{\circ}_{VV}} \quad (4.10)$$

$$ratio2 = \frac{\sigma^{\circ}_{VV} - \sigma^{\circ}_{VH}}{\sigma^{\circ}_{VV} + \sigma^{\circ}_{VH}} \quad (4.11)$$

$$intensity1 = \sigma^{\circ}_{VH} - \sigma^{\circ}_{VV} \quad (4.12)$$

$$intensity2 = \sigma^{\circ}_{VV} + \sigma^{\circ}_{VH} \quad (4.13)$$

$$RVI = \frac{4\sigma^{\circ}_{VH}}{\sigma^{\circ}_{VV} + \sigma^{\circ}_{VH}} \quad (4.14)$$

where σ°_{VH} and σ°_{VV} are the intensity backscatters in VH and VV polarizations, respectively (Nasirzadehdizaji et al., 2019).

On the other hand, the S1-PolSAR decomposition coefficients considered in this study were Entropy (H) and Alpha (α), which are used to extract average parameters from polarimetric SAR data (Cloude & Pottier, 1996). Specifically, the H-α parameters indicate the randomness of the scatter and the scattering type (i.e., surface, double-bounce, and volume), respectively. As already mentioned, in order to compute the S1-PolSAR decomposition, I needed to calculate the dual-pol covariance matrix C_2, which is generally expressed as:

$$C_2 = \begin{bmatrix} C_{11} & C_{12} \\ C_{21} & C_{22} \end{bmatrix} \quad (4.15)$$

where the dual-pol S1 mode (i.e., VV and VH) is represented by the diagonal elements C_{11} and C_{22}, while the cross-pol mode (i.e., VV-VH and VH-VV) is represented by the elements C_{12} and C_{21}. For Sentinel-1 data, the dual-pol covariance matrix is calculated as:

$$\langle C \rangle_{dual} = \begin{bmatrix} \langle S_{VV} S^{*}_{VV} \rangle & \langle S_{VV} S^{*}_{VH} \rangle \\ \langle S_{VH} S^{*}_{VV} \rangle & \langle S_{VH} S^{*}_{VH} \rangle \end{bmatrix} \quad (4.16)$$

where *S* indicates the scattering in *VV* and *VH* polarizations, while the asterisk (*) indicates the complex conjugation.

Once I obtained the final images with S2-VIs and S1-σ°, RVI, and H-α, I used RStudio

v.2022.07.1 to extract the pixel values at subplot level (Figure 4.1).

Interannual variability of field variables

I performed the non-parametric Kruskal-Wallis test (with Bonferroni adjustment to the p-value, with critical value of 0.01) to evaluate interannual variability of field variable (i.e., LAI, SPAD, Ht, SWC, and NEE) during the 2018 through 2021 growing seasons (i.e., pairwise variable–year, for each pair combination of year), across maize, prairie, and switchgrass. Specifically, the interannual analysis was carried out as follows:

$$y_c = GS_{2018\text{–}2021} \tag{4.17}$$

where y_c is the individual field variable (i.e., LAI, SPAD, Ht, SWC, and NEE) at the cover type *c* (i.e., maize, prairie, and switchgrass) and $GS_{2018–2021}$ is the growing season during 2018–2021. In this way, I was able to investigate whether a variable *y*, at a cover type *c*, significantly differed during 2018–2021 growing seasons. I then employed the Wilcoxon rank sum test as post-hoc test to identify the growing season during which a variable y_c significantly differed (using Bonferroni adjustment to the p-value, with critical value of 0.01). Both Kruskal-Wallis and Wilcoxon tests were carried out using the R functions "*kruskal.test*" and "*pairwise.wilcox.test*", respectively, from the R-package "*stats*".

Main key influences on NEE dynamics

I investigated the main key influence(s) to NEE by fitting three different types of models: Generalized Linear Model (GLM), Multi-Layer Perceptron (MLP), and Random Forest (RF). The equation expressing the relationships between independent variables, representing both structural attributes (i.e., LAI, SPAD, and Ht) and influences (i.e., SWC, Tair, PAR, and VPD), and the dependent variable NEE is the following:

$$NEE = f(LAI,\ SPAD, Ht, SWC, T_{air}, PAR, VPD) \tag{4.18}$$

where *LAI*, *SPAD*, *Ht*, and *SWC* are the leaf area index, SPAD index, soil water content (%), and vegetation height (m), respectively, measured at subplot level; while T_{air}, *PAR*, and *VPD* are the mean daily air temperature (°C), mean daily photosynthetically active radiation (μmol m^{-2} d^{-1}), and vapor pressure deficit (kPa), respectively, measured at tower level and assumed to be homogeneous across sites, due to their close proximity. I then applied transformations to some of the independent variables to overcome for their non-linear relationship with the dependent variable. Practically, the specific transformation was chosen after plotting independent *vs* dependent variables in a "1-1 xy plot". For example, when plotted against *NEE*, the *LAI* variable showed to be reciprocal to *NEE* and to resemble an exponential curve; therefore, it was transformed as "$\frac{1}{1+e^{-LAI}}$". Similarly, T_{air} and *VPD* showed to be reciprocal to *NEE*, while the logarithmic (i.e., "$\frac{1}{\log(T_{air})}$") and square root (i.e., "$\frac{1}{\sqrt{VPD}}$") transformations, respectively, were applied. Lastly, a logarithmic transformation was applied to *SWC* as well (i.e., "log (SWC)").

I split the entire dataset into training (i.e., 80%) and test (i.e., 20%) and I ran the three models on standardized variable values, after removing any missing value. For the MLP and RF models, tuning model parameters were estimated employing a 10-fold cross validation using the R function "*train*" from the R-package "*caret*" (Khun, 2021), while the packages "*neuralnet*" and "*ranger*" (Günther & Fritsch, 2010; Wright & Ziegler, 2017) were used to fit the MLP and RF, respectively. Once the three models were fitted, I calculated the goodness of fit and prediction measures, such as the R-squared score (R^2), which provides information about the amount of dataset variation explained by the model, and the root mean squared error (RMSE), which gives an indication of the accuracy of models predictions within the data range used for fitting, and the magnitude of deviation of predictions from observed values. Both R^2 and RMSE were calculated using the R function "*model_performance*" from the R-package "*DALEX*" (Biecek, 2018). Lastly,

I evaluated variable-importance measure and the partial-dependence (PD) profiles of the main driver(s), for each of the explanatory variables to the NEE at each cover type. Variable-importance measures were obtained by employing a permutation-based evaluation, using RMSE as model performance measure, while PD profiles were obtained by calculating the individual dependence of an instance-level prediction on an explanatory variable. Both variable-importance and PD profiles were carried out using the R function "*model_parts*" from the R-package "*DALEX*".

Bayesian dynamic linear model for maize's NEE

In this section I explain how I forecast one growing season (2021) of NEE (gC m^{-2} d^{-1}) for maize at both AGR and CRP farms using a regression-based Bayesian Dynamic Linear Model (BDLM). A BDLM is a special state-space model in which the regression model is used to investigate dependencies of state variables (i.e., observed variables at a given time *t*) related to different observations. A BDLM is made up of two different models: an observation model and a process model. The former describes the relationship between the observed variable and its current state, while the latter shows the dynamic and stochastic variations within the system. Mathematically, the BLDM used in this work is described as follows (Wang et al., 2019):

observation model:

$$Y_t = F_t\theta_t + v_t, \;\; v_t \sim N(0, V_t) \tag{4.19}$$

process model:

$$\theta_t = G_t\theta_{t-1} + w_t, \;\; w_t \sim N(0, W_t) \tag{4.20}$$

where Y_t is the observation vector (NEEs for 2018, 2019, and 2020 in this case), F_t and G_t are the observation and evolution matrices, respectively, θ_t is the state parameter vector, and v_t and w_t are the observational and evolution errors—w_t indicates the stochastic changes in state parameters from *t-1* to *t*. Lastly, both v_t and w_t are described by a Gaussian distribution (with mean 0 and

variance V_t and W_t, respectively). In other words, V_t and W_t represent the priors of both the observation and the process models, which are described as follows:

priors:

$$V_t \sim \Gamma(1,1) \tag{4.21}$$

$$W_t \sim \Gamma(1,1) \tag{4.22}$$

where Γ indicates the gamma distribution with mean and variance of 1.

In case of forecasting, in the BLDM context, the residuals are modeled through the autoregressive model, which describes the relationship between previous (*t-1*) and current (*t*) values of the state parameter. The prior distribution of θ_t at a time *t* is defined as:

$$P(\theta_t|D_t) \sim N(\mu_t, \sigma_t) \tag{4.23}$$

where μ_t and σ_t are initial conditions of the state parameter $P(\theta_t|D_t)$ mean and variance, while *D* is the state of information. Prior distribution of the $P(\theta_{t+1}|D_t)$ state parameter, at a time *t+1*, is the following:

$$P(\theta_{t+1}|D_t) \sim N(\mu_{t+1}, \sigma_{t+1}) \tag{4.24}$$

with μ_{t+1} obtained as follows:

$$\mu_{t+1} = \mu_{t-1} + \beta_1 \mu_{t-1} \tag{4.25}$$

and the following model non-informative (i.e., weak) prior for initial condition:

$$\beta_1 \sim N(0, 0.00001) \tag{4.26}$$

After choosing the best performing model (i.e., the one with the least RMSE and the highest R^2), among GLM, MLP, and RF, I used the best explanatory variable(s), identified from the variable-importance and partial-dependence (PD) profiles analysis, as best candidates to be main key influences to NEE for the forecast. Two kinds of forecast were performed: (i) using actual biophysical/physical *in-situ* variables as explanatory for maize; and (ii) using both S2-VIs and S1-

σ°, RVI, and S1-PolSAR as substitutes for the *in-situ* observations. Both forecasts were produced for only for maize during the 2021 growing season. Specifically, the variable replacement was based on the best correlation between *in-situ* and remote sensing variables, by using the Spearman's Rho (ρ) correlation coefficients (R function "*rcorr*" from the "*Hmisc*" R-package; Harrel, 2021), which were also used to investigate multicollinearity between the variables. Only statistically significant (p-value<0.05) coefficients were considered. For the BDLM, I used the R function "*ecoforecastR*" and "*rjags*" (Plummer, 2003).

Results

Interannual variation

Growing season lengths varied by the three cover types, four years, and two farms (i.e., AGR and CRP; Table 4.1 and Figure A2a,b).

Table 4.1: Day of the year indicating the start and the end of the growing seasons during 2018–2021 at the historically cultivated as agricultural lands (AGR) and the Conservation Reserve Program (CRP) sites. Start and end of the growing season (i.e., SoS and EoS, respectively) were obtained on the first four days in row of negative and positive NEE (i.e., CO_2 uptake from and emission to the atmosphere), respectively.

	2018			2019			2020			2021			mean 2018–2021
site	SoS	EoS	#days	SoS	EoS	#days	SoS	EoS	#days	SoS	EoS	#days	#days
AGR-M	164	256	93	172	270	98	166	270	105	163	254	92	96.0
AGR-P	142	236	95	147	253	107	150	244	95	127	249	123	104.0
AGR-S	142	262	121	153	270	118	150	270	121	143	263	121	119.2
CRP-M	164	244	81	173	270	99	179	274	96	178	261	84	89.0
CRP-P	115	236	122	130	253	124	109	270	162	101	263	163	141.8
CRP-S	142	244	103	153	253	101	122	274	153	149	274	126	119.8

SoS: start of season (DOY)
EoS: end of season (DOY)
#days: length of growing season in number of days (EoS-SoS+1)

On average, maize showed the shortest growing season length (~93 days), followed by switchgrass (~120 days) and prairie (~123 days) cover types. Regarding the interannual variation, growing season length showed to vary by year, with AGR-C ranging between 91 to 104 days in 2021 and 2020, respectively, and with CRP-C ranging between 80 to 98 days in 2018 and 2019, respectively, with an intra-annual average of 96 days and 89 days at AGR-C and CRP-C,

respectively. On the other hand, prairie cover type had a minimum and maximum growing season length of 94 days (in 2018 and 2020) and 122 days (in 2021), at AGR, and of 121 days (in 2018) and 162 days (in 2021), at CRP, with an intra-annual average of 104 days and 141.8 days at AGR and CRP, respectively. Lastly, switchgrass cover type showed a growing season length ranging between a minimum of 117 days (in 2019) to a maximum of 120 days (in 2018, 2020, and 2021), at AGR, and a minimum and maximum length of 100 days (in 2019) and 152 days (in 2020), respectively, at CRP, with an intra-annual average of 119.2 days and 119.8 days at AGR and CRP, respectively.

Regarding the *in-situ* measurements, across cover types and farms, highest interannual variation was observed in SPAD index, on average higher in maize cover type (45.41±3; Table 4.1), SWC on average higher in switchgrass cover type (17.83±4; %), and NEE, on average higher in maize (-577±77; gC m^{-2} gs^{-1}), while least variation was observed in LAI (higher in prairie cover type: 3.37±1), Ht (higher in maize: 1.14), and Ta (higher in switchgrass cover type: 21±1; °C).

Table 4.2: Interannual mean (± one standard deviation) for LAI, SPAD index, Ht (m), SWC (%), Ta (°C), and NEE (gC m-2 d-1) at the historically cultivated as agricultural lands (AGR) and the Conservation Reserve Program (CRP) sites, for maize (M), prairie (P), and Switchgrass (S), during 2018–2021 (i.e., '18–'21) growing seasons. NEE is also reported as cumulative values (i.e., ΣNEE) over the '18–'21 growing seasons. Averages by cover type–farm and by cover type are also shown.

	Interannual by cover type and farm								
		Averages							
Farm	Cover t.	LAI	SPAD	Ht	SWC	NEE	ΣNEE	days	GS
AGR	M	2.1(±1.3)	41.7(±9.5)	1.3(±1.0)	20.5(±6.4)	-6.0(±5.0)	-556	93	'18
	P	1.9(±1.2)	34.6(±5.2)	1.1(±0.5)	22.7(±8.0)	-4.6(±3.6)	-442	95	
	S	2.4(±1.5)	31.5(±5.3)	1.0(±0.4)	24.1(±6.5)	-3.1(±3.1)	-375	121	
	M	1.8(±1.4)	44.3(±9.2)	1.1(±0.7)	16.4(±7.7)	-5.0(±3.8)	-494	98	'19
	P	3.8(±1.4)	34.1(±5.3)	1.0(±0.5)	16.28(±10.8)	-4.3(±3.6)	-465	107	
	S	2.4(±0.7)	33.9(±4.4)	1.05(±0.3)	18.0(±11.4)	-3.1(±3.0)	-360	118	
	M	2.0(±1.5)	46.4(±8.5)	1.1(±0.8)	18.9(±4.0)	-6.7(±4.5)	-654	105	'20
	P	3.0(±1.4)	28.8(±4.9)	0.9(±0.4)	18.9(±8.5)	-3.3(±3.2)	-411	95	
	S	2.7(±0.8)	31.9(±3.5)	1.0(±0.3)	19.2(±7.1)	-2.9(±2.5)	-375	121	
	M	2.1(±1.8)	49.9(±9.3)	1.3(±1.0)	17.8(±5.4)	-7.4(±5.1)	-682	92	'21
	P	2.3(±1.1)	31.3(±4.7)	0.9(±0.3)	18.6(±6.2)	-2.6(±2.3)	-319	123	
	S	2.2(±1.0)	35.4(±3.1)	1.1(±0.5)	20.7(±4.4)	-2.3(±2.7)	-276	121	
CRP	M	2.0(±1.1)	40.5(±9.3)	1.2(±0.8)	14.6(±6.9)	-5.7(±4.2)	-461	81	'18
	P	2.7(±1.2)	34.0(±5.5)	1.1(±0.4)	16.2(±7.8)	-2.2(±2.7)	-272	122	
	S	3.1(±1.3)	36.6(±3.9)	1.1(±0.3)	15.9(±6.4)	-5.0(±3.9)	-520	103	
	M	1.9(±1.4)	45.5(±12.9)	1.0(±0.8)	15.9(±7.2)	-6.5(±4.3)	-607	99	'19
	P	4.9(±1.5)	33.7(±5.9)	1.1(±0.4)	15.2(±8.5)	-2.5(±3.5)	-371	124	
	S	4.6(±1.9)	38.5(±4.6)	1.1(±0.5)	17.9(±8.7)	-4.4(±3.6)	-440	101	
	M	2.5(±2.1)	47.4(±9.9)	1.0(±0.8)	11.9(±4.5)	-6.5(±4.0)	-541	96	'20
	P	4.9(±2.3)	29.8(±5.2)	1.0(±0.3)	13.7(±10.1)	-2.2(±2.6)	-347	162	
	S	4.4(±1.3)	38.8(±3.4)	1.1(±0.4)	9.2(±4.6)	-3.7(±3.2)	-505	153	
	M	1.7(±1.6)	47.6(±9.5)	1.2(±1.0)	13.5(±5.0)	-7.4(±3.9)	-618	84	'21
	P	3.4(±1.8)	32.2(±4.2)	1.0(±0.4)	11.7(±6.2)	-2.2(±2.1)	-354	163	
	S	3.8(±2.1)	38.7(±9.0)	1.3(±0.5)	17.8(±9.2)	-3.4(±3.5)	-433	126	
		Averages by cover type–farm							
AGR	M	2.0(±0.1)	45.6(±3.5)	1.2(±0.1)	18.4(±1.8)	-6.3(±1.0)	-597(±55)	96.0	'18–'21
	P	2.7(±0.8)	32.2(±2.7)	1.0(±0.1)	19.1(±2.7)	-3.7(0.9)	-409(±64)	104.0	
	S	2.5(±0.2)	33.2(±1.8)	1.0(±0.1)	20.5(±2.7)	-2.8(±0.4)	-347(±48)	119.2	
CRP	M	2.0(±0.3)	45.2(±3.3)	1.1(±0.1)	14.0(±1.7)	-6.3(±0.8)	-557(±68)	89.0	
	P	4.0(±1.1)	32.4(±1.9)	1.0(±0.1)	14.2(±2.0)	-2.3(0.2)	-336(±44)	141.8	
	S	4.0(±0.7)	38.1(±1.0)	1.2(±0.1)	15.2(±4.1)	-4.1(±0.7)	-474(±44)	112.8	
		Averages by cover type							
	M	2.0(±0.2)	45.4(±3.1)	1.1(±0.1)	16.2(±2.9)	-6.3(±0.9)	-577(±77)	92.5	'18–'21
	P	3.4(±1.1)	32.3(±2.2)	1.0(±0.1)	16.7(±3.4)	-3.0(±1.0)	-373(±64)	122.9	
	S	3.2(±0.9)	35.6(±3.0)	1.1(±0.1)	17.8(±4.3)	-3.5(±0.9)	-411(±81)	175.6	

GS: growing seasons during 2018–2021
days: number of days during GS
LAI: leaf area index (m^2 m^{-2})
SPAD: Soil and Plant Analysis Development index (SPAD index; unitless)
Ht: vegetation height (m)
SWC: soil water content (%)
Tair: air temperature (°C)
PPT: cumulative precipitation (mm)
NEE: net ecosystem exchange (gC m^{-2} d^{-1})

Among the three cover types, on average, maize showed the highest magnitude of growing

season NEE, followed by switchgrass and prairie (Table 4.2). Specifically, cumulative NEE values at maize were 35% and 29% higher than those of prairie and switchgrass, respectively; while daily NEE values were 52% and 45% higher than those of prairie and switchgrass, respectively. Same was true for magnitudes of growing season NEE by cover type and by farm, during 2018–2021, where maize NEE values were 31% and 42% (at AGR) and 40% and 15% (CRP) higher than those of prairie and switchgrass, respectively. Regarding the remaining cover types, the magnitudes of growing season NEE for prairie were 15% higher than those for switchgrass at AGR farm. However, opposite magnitudes were observed at CRP farm (i.e., NEE of switchgrass 29% higher than that of prairie). Same was true for the interannual magnitudes of growing season NEE, with maize cover type showing higher magnitudes than those of prairie and switchgrass, with the exception for NEE of maize at CRP on 2018, which was 11% lower than that of switchgrass.

In regard of seasonal variations of data collected at subplot level, overall, LAI and Ht showed increasing trends (Figures A3.1abc and A3.3abc), at the three cover types and at both farms, which appeared to be similar among the four years, with the exception of LAI at CRP-M in 2020 (Figure A3.1a), at CRP-P in 2018 and 2019 (Figure A3.1b), and at CRP-S in 2019 (Figure A3.1c). On the other hand, seasonal variations of SPAD index increased at both AGR-/CRP-M (Figure A3.2a), while stable for prairie and switchgrass at AGR-/CRP- (Figure A3.2bc). Lastly, SWC was the only variable showing seasonal patterns that varied by farm, cover type, and year (Figure A3.4abc).

The non-parametric Kruskal-Wallis rank sum test showed whether the variation of LAI, SPAD index, Ht, SWC, and NEE at the three cover types were statistically significant (i.e., Bonferroni adjustment, with critical value of 0.01) during 2018–2021 (Table A15). In particular, interannual variations of LAI, SWC, and NEE were statistically significant (p-value<0.05) at

prairie and switchgrass, while SPAD index showed statistical significance at all three cover types. On the other hand, Ht did not show any significant interannual variations. By employing the non-parametric Wilcoxon rank sum test, I was able to investigate for which pairwise (i.e., 2018-2019, 2018-2020, etc.) the five variables were statistically different (Bonferroni adjusted, with critical value of 0.01), among cover types (Table A16 and Figure A4). For instance, for maize cover type, SPAD index was the only variable showing statistically significant (Bonferroni adjusted, with critical value of 0.01) interannual variations (between the pairwise 2018-2020 and 2018-2021). At prairie cover type, LAI statistically differed between the pairwise 2018-2019, 2018-2020, 2019-2021, and 2020-20201, followed by SPAD index (between the pairwise 2018-2020, 2018-2021, 2019-2020, and 2020-2021), NEE (between the pairwise 2018-2021 and 2020-2021), and SWC (between the pairwise 2018-2021). As already shown by the Kruskal-Wallis, and then confirmed by the Wilcoxon rank sum test, Ht did not show any significant interannual variation in any of the pairwise comparisons.

Key drivers of growing season NEE

I investigated the relationships hypothesized at Eq. 4.18 for the main key driver(s) to NEE by fitting three different models, such as the generalized linear model (GLM), the multi-layer perceptron (MLP; Figure A5), and the random forest (RF). The 10-fold cross validation for the model training parameters produced different architectures of the MLP (Table A17 and Figure A5) and RF (Table A17) models.

All three models showed to perform well in modeling maize NEE. However, overall, the RF model showed the best performance (Table 4.3 and Figure 4.2).

Table 4.3: Model performance (R^2 and RMSE) of the generalized linear model (GLM), the multi-layer perceptron (MLP), and the random forest (RF) for maize, prairie, and switchgrass. The models chosen for this study are highlighted in bold.

Cover type	Model	R^2	RMSE
Maize	GLM	0.92	18.48
	MLP	0.95	13.97
	RF	**0.97**	**10.22**
Prairie	GLM	0.01	24.64
	MLP	-1.31	37.60
	RF	**0.61**	**15.45**
Switchgrass	GLM	0.41	22.15
	MLP	0.72	15.18
	RF	**0.90**	**8.91**

R^2: R-squared score
RMSE: root-mean squared error

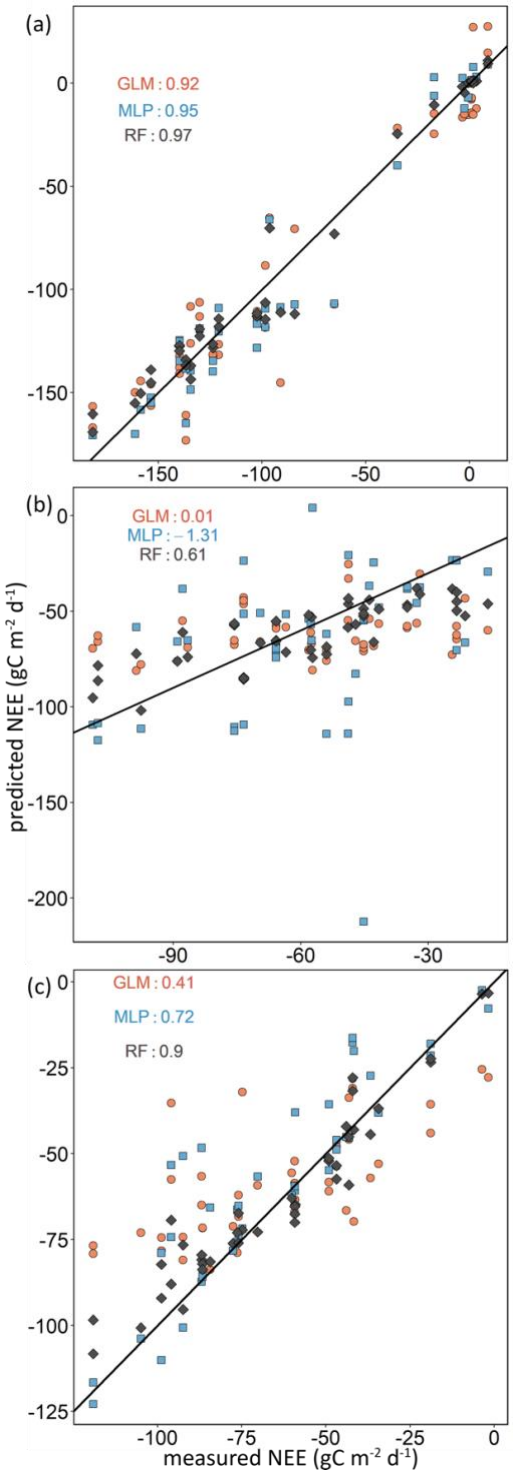

Figure 4.2: Scatterplots of predicted *vs* measured net ecosystem exchange (NEE; gC m^{-2} d^{-1}) values by the generalized linear model (GLM, solid orange circles), multilayer perceptron (MLP, solid light blue squares) model, and random forest (RF, solid black diamonds) models for (a) maize, (b) prairie, and (c) switchgrass during the 2018–2021 growing seasons. Black solid diagonal lines show the 1:1 relationship. The R-squared score models' goodness of fit is also shown.

On the other hand, while the GLM model performed well at maize (R^2=0.92 and RMSE=18.48; Table 4.3, Figure 4.2a, and Table A18), it did a poor job at switchgrass (R^2=0.41 and RMSE=22.15; Table 4.3, Figure 4.2c, and Table A18) and prairie (R^2=0.01 and RMSE=24.64; Table 4.3, Figure 4.2b, and Table A18). Lastly, the MLP was performed well and better than the GLM for maize (R^2=0.95 and RMSE=13.97), followed by switchgrass (R^2=0.72 and RMSE=15.18), but it did a poor job in predicting NEE in prairie (R^2=-0.21 and RMSE=37.60). Accordingly, I focus on the results of the NEE predictions using RF model only.

Overall (i.e., averages by cover type during 2018–2021), predicted magnitude of NEE were the same as the measured ones (Table 4.4).

Table 4.4: Predicted and measured values of the net ecosystem exchange (NEE; gC m^{-2} d^{-1}) at the historically cultivated as agricultural lands (AGR) and the Conservation Reserve Program (CRP) sites during 2018–2021 growing seasons (GS). Averages by cover type–farm and by cover type only are also shown.

Averages by cover type, farm, and year							
Farm	Cover t.		Predicted		Measured		GS
		days	averages	daily	averages	daily	
AGR	M	4	-64.3	-16.1	-66.0	-16.5	'18
	P	5	-80.4	-16.1	-84.2	-16.8	
	S	4	-55.1	-13.8	-54.0	-13.5	
	M	5	-82.9	-16.6	-81.7	-16.3	'19
	P	6	-72.2	-12.0	-77.0	-12.8	
	S	6	-56.2	-9.4	-55.9	-9.3	
	M	5	-74.4	-14.9	-76.3	-15.3	'20
	P	5	-71.6	-14.3	-73.0	-14.6	
	S	5	-60.9	-12.2	-60.1	-12.0	
	M	7	-79.1	-11.3	-81.6	-11.7	'21
	P	7	-45.7	-6.5	-45.0	-6.4	
	S	7	-42.0	-6.0	-40.6	-5.8	
CRP	M	5	-76.0	-15.2	-75.3	-15.1	'18
	P	4	-48.3	-12.1	-42.9	-10.7	
	S	3	-75.1	-25.0	-78.9	-26.3	
	M	4	-90.3	-22.6	-91.0	-22.8	'19
	P	5	-74.8	-15.0	-71.6	-14.3	
	S	5	-73.9	-14.8	-74.9	-15.0	
	M	5	-64.3	-12.9	-62.5	-12.5	'20
	P	5	-67.2	-13.4	-67.1	-13.4	
	S	4	-74.8	-18.7	-76.9	-19.2	
	M	7	-68.2	-9.7	-65.8	-9.4	'21
	P	7	-47.8	-6.8	-46.2	-6.6	
	S	7	-57.4	-8.2	-57.3	-8.2	
Averages by cover type and farm							
AGR	M	5	-75.2	-14.3	-76.4	-14.6	'18–'21
	P	6	-67.5	-11.7	-69.8	-12.1	
	S	6	-53.6	-9.7	-52.7	-9.6	
CRP	M	5	-74.7	-14.2	-73.6	-14.0	
	P	5	-59.5	-11.3	-57.0	-10.8	
	S	5	-70.3	-14.8	-72.0	-15.2	
Averages by cover type							
	M	5	-74.9	-14.3	-75.0	-14.3	'18–'21
	P	6	-63.5	-11.5	-63.4	-11.5	
	S	6	-61.9	-12.1	-62.3	-12.2	

days: number of days of field measurements

The interannual variations of predicted NEE values for maize were always higher than those for prairie and switchgrass, with the exception for the years 2018 and 2020. Overall, predicted NEE values for maize were 15% and 17% higher than those for prairie and switchgrass, respectively; by considering the averages by cover type and by farms, predicted NEE values for maize were 10% and 29% (AGR) and 20% and 6% (CRP) higher than those for prairie and

switchgrass, respectively.

Seasonal predictions appeared to be very accurate for maize cover type, at both AGR and CRP farms (Figure A6a), with the exception on early August 2018-2020-2021 (at AGR) and on late July and August 2018, on early August 2019, and on July 2020-2021 (at CRP). Overall accurate predictions were also obtained at switchgrass cover type, at both AGR and CRP farms (Figure A6c), with some exceptions on late July 2018, June and early July 2019, early June and August 2020, and July-August 2021 (at AGR), and on late June-July 2018, and early July 2020 (at CRP). Regarding prairie cover type, overall, less accurate predictions were obtained at both AGR and CRP farms (Figure A6b).

Despite the model performance, for each cover type, the three models showed unique hierarchy of the importance of the main key influence(s) to NEE (Figure 4.3). For example, at maize cover type, main key influences to NEE were LAI and Ht for the GLM model, while Ht became the main key influence for both the MLP and RF models. Nevertheless, Ht resulted the leading key influence to NEE for all the three models. Regarding prairie cover type, little key influences' variability was observed for the GLM model, while PAR and Ht resulted more important for the MLP one, equally followed by the remaining variables. Lastly, only VPD appeared to be the main key influence to NEE for the RF model. Regarding switchgrass cover type, for the GLM model, LAI and SWC resulted the main key influences to NEE, while the remaining variables showed similar magnitudes; Ht, slightly followed by VPD, Ta, PAR, SWC, and LAI for MLP model; Ht followed by Ta, LAI, PAR, VPD, and SWC and SPAD as least, for the RF model.

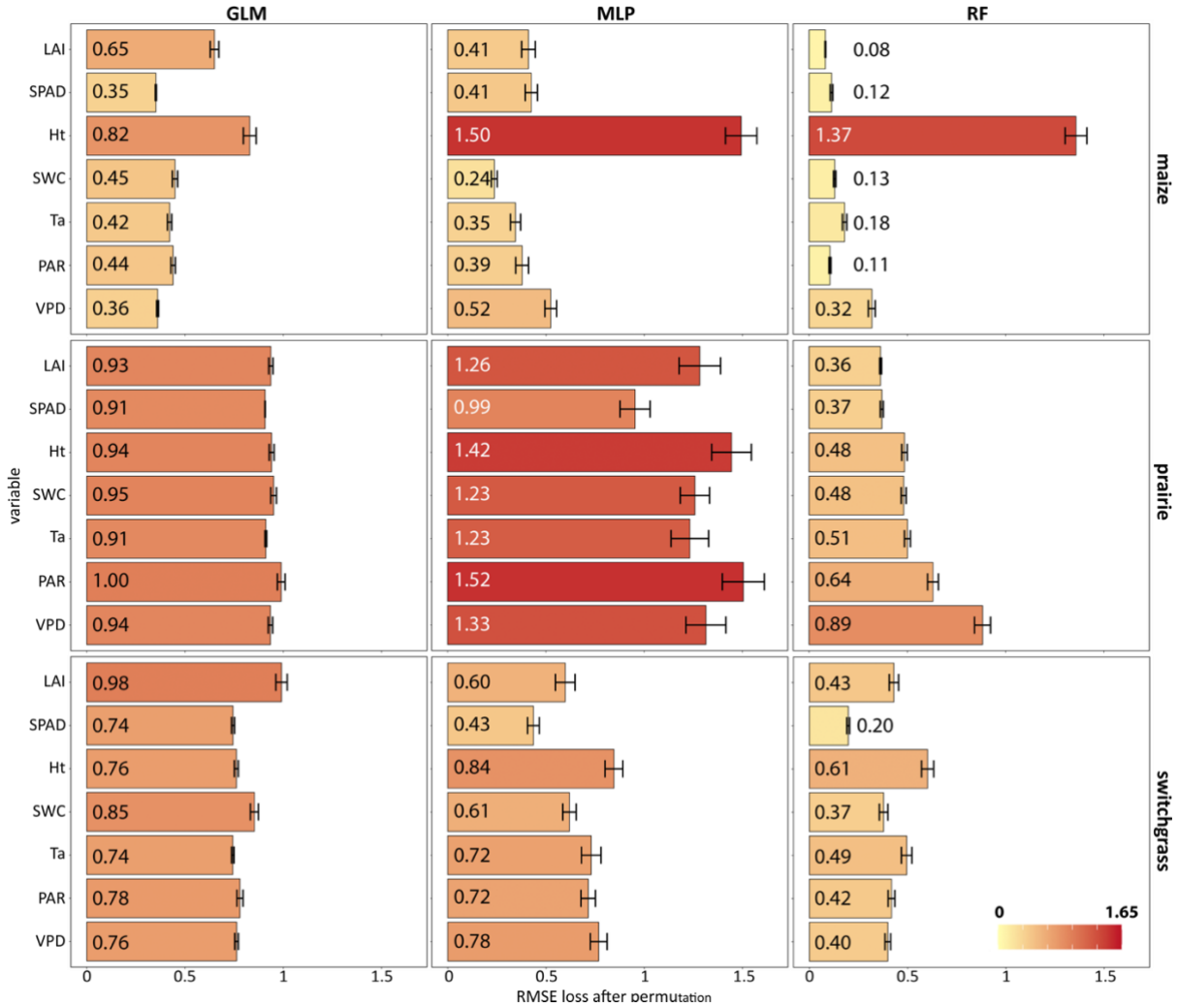

Figure 4.3: Standardized mean variable importance for generalized linear model (GLM), multilayer perceptron (MLP), and random forest (RF) models at maize, prairie, and switchgrass cover types, during 2018–2021 growing seasons. Bar plots indicate the median values of the variable importance for the seven independent variables leaf area index (LAI), Soil Plant Analysis Development index (SPAD index), soil water content (SWC), vegetation height (Ht), mean air temperature (Ta), photosynthetic active radiation (PAR), and vapor pressure deficit (VPD), calculated using 50 permutations and the root-mean square error (RMSE) loss function. The error bars indicate the standard deviation across the permutations. The darker the colors of the bars the higher the variable importance in predicting net ecosystem exchange (NEE; gC m^{-2} d^{-1}).

By only considering the RF model, the partial-dependence profiles showed us the sign (i.e., positive, negative, or null), as well as the magnitude, of each variable (Figure A7). Specifically, by only focusing on the main key influence on NEE, for maize and switchgrass cover types, Ht showed negative sign—i.e., as maize's height increases, the more negative is NEE (increasing in C uptake) until reaching a plateau. However, at maize cover type, such plateau is reached for higher magnitudes of NEE. On the other hand, VPD showed positive sign—i.e., the higher the VPD the more positive NEE is (lower the C uptake).

Growing season NEE forecast at maize cover type

The most associated structural attribute to NEE employed in the *in-situ* Bayesian Dynamic Linear Model (BDLM; at Eqs. 4.19–4.26) for NEE forecast at maize cover type was vegetation height (Ht). The forecast was carried out for the 2021 growing season, during which NEE fluxes were measured over a total of 7 days (May 27, June 10, June 24, July 8, July 21, August 4, and August 20; Table A14). During such period, I was able to monitor some of the stages of maize's growth development (Figure A8)—i.e., vegetative (V) and reproductive (R) stages—starting from the elongation stages of the *n* root whorls (i.e., V1 through V13), tasseling (VT), silking (R1), blister (R2), and milk (R3) stages (Nleya, 2019). From the NEE perspective, and considering AGR- and CRP- farms together, such stages were characterized by net-neutral C emission (on May 27), a slight net C emission (on June 10), a near-neutral C uptake (on June 24), and a net C uptake increasing in magnitude from June 8 to August 4, while decreasing on August 20 (Figure A8). The *in-situ* BDLM analysis showed that forecasts at maize slightly varied by farm sites as well as by the stage of maize's development. For instance, when the two farms were considered together, less accurate (i.e., either under and over estimation) forecasts were obtained on late May, June, early July, and on late August (Table A20 and Figure A9). However, when looking at individual farms,

low accuracy forecasts (i.e., RMSE 20% higher) were obtained on late May, and early July at AGR, while on late May, and early June, at CRP. Nevertheless, whether AGR and CRP were considered together or not, forecasts at the very start and the very end of the fieldwork season period tended to show poor performances (i.e., RMSEs between 30±22 and 48±22, respectively).

Regarding the BDLM using remote sensing variables, the selection of the key variables—S2-VIs, S1-σ°, RVI, and S1-PolSAR decomposition coefficients—was based on the Spearman's ρ correlation analysis (i.e., high significant correlation) between Ht and both S2 and S1 variables (Table A19). However, for the purpose of this study, we considered the four S2 VIs (EVI2, CIg, NDWI1 and NDWI2), three S1 σ° variables (RVI, Ratio1, Intensity2), and two S1-PolSAR variables (entropy and alpha). The remote sensing BDLM analysis showed that forecasts highly varied by type of remote sensing variable employed (Figure A10), with EVI2, CIg, and Alpha performing better than the rest. Hence, only results from EVI2, CIg, and Alpha at AGR and CRP farms and both farms together were reported. The use of EVI2 in BDLM showed differential performance by site and date t (Table A20 and Figure A11.1). For example, predictions at AGR were less accurate, almost across the whole growing season, than those at CRP. When the two farms were considered together, the forecasts performance improved. Similar pattern was observed for CIg (Table 20 and Figure A11.2): less accurate predictions were obtained at AGR, while overall better forecasts were obtained at CRP and when both farms were considered together. Specifically, main improvements (compared to Ht) at AGR were obtained thanks to EVI2 and CIg on June 24 (RMSE reduced by 80% and 65%, respectively) and on August 20 (RMSE reduced by 29% and 17%), respectively, with predictions switching from overestimating to underestimating net C uptake (Tables A20-A21 and Figures 11.1-11.2). At CRP, the use of EVI2 contributed to a better forecast on June 10 (RMSE reduced by 26% but still overestimating), July 8 (RMSE reduced by

29% but still underestimating), and August 20 (RMSE reduced by 55% but still overestimating), while the use of CIg contributed to a better forecast on May 27 (RMSE reduced by 18% but still overestimating), June 10 (RMSE reduced by 32% (but still overestimating), and August 20 (RMSE reduced by 75%). On the other hand, the use of Alpha brought to similar forecast performances between AGR and CRP, with the only improvements on July 8 (RMSE reduced by 31% but still underestimating) and August 20 (RMSE reduced by 64% but slightly underestimating) at AGR- and CRP-, respectively (Tables A20-A21; Figure A11.3). Still, forecasts improved when both farms were considered together—EVI2: on June 10 (RMSE reduced by 40% but still overestimating), July 8 (RMSE reduced by 9%) and August 20 (RMSE reduced by 51% but still overestimating); CIg: on July 8 (RMSE reduced by 22% but slightly underestimating) and August 20 (RMSE reduced by 52% but still overestimating); and Alpha: on August 20 (RMSE reduced by 78% but slightly underestimating).

Discussion

My results showed that the three cover types were characterized by different growing season lengths, with maize and prairie cover types having the shortest and longest growing seasons, respectively. The interannual variations of the main controlling drivers to NEE varied by cover type and growing season considered reflecting the nature of each crop related to the land use history, management, and length of the study period. Maize cover type showed the highest net C uptake, which, despite it did not show significant interannual variation, it varied in magnitude depending on the land use history considered. Moreover, each cover type showed unique hierarchy of main controlling drivers to NEE, which varied in number and magnitude depending on the nature of the cover type, in other words, monoculture *vs* polyculture and annual *vs* perennial.

Interannual variation of main key drivers

The interannual analysis showed that the *in-situ* variables varied by cover type and year considered. For instance, vegetation height was the only variable not showing significant interannual variation the reason of which could be likely because of the well-established (since 2010) perennial crops and same variety of maize used during such a short time-period (i.e., 2018–2021). Moreover, at such time scale, we were not able to investigate possible biotic or abiotic constraints (i.e., sources of stress), such as the extreme weather events (i.e., drought) which could cause changes in crop vegetation height (Aslam et al., 2022; Hajibabaee et al., 2012). Among the three cover types, maize was the only one showing non-significant interannual variations of leaf area index and soil water content, probably due to the monoculture and highly genetically bred characteristic of this row crop. Contemporary maize hybrid tends not to vary by across the field, neither from one year to the next one, in both leaf structure and canopy cover, plant height, and root system. On the other hand, both prairie—the North American tallgrass prairie is dominated by diverse mix of perennial "cool season" (C_3) and "warm season" (C_4) grass and forb species—and switchgrass (perennial C_4 grass) showed significant interannual variations of the *in-situ* variables (i.e., prairie: LAI and SWC; switchgrass: SWC).

Special mention should be reserved for the leaf chlorophyll content (SPAD index), which was the only variable that varied at the three cover types, with prairie showing interannual variations at almost every year pairwise. Previous studies have highlighted various constraints can affect the plant chlorophyll content, including thermal and humidity conditions, management, and applications of mineral fertilizers. For example, Szulc et al. (2021) showed that growing maize in direct sowing as well as applying mineral fertilizers (i.e., N and NP) in critical stages of growth could affect the leaf greenness and chlorophyll content. Moreover, the highly interannual variation

of leaf chlorophyll content at prairie could be due to the polyculture nature of this cover type, which resulted into a sampling of more diversified plant species during the field campaigns.

Interannual variation and magnitude of growing season C uptake

Similar to the key influences, the interannual variation of growing season NEE depended on the cover type and the year examined. For instance, at maize cover type, on average, NEE did not vary significantly during 2018–2021 growing seasons, while significant were the interannual differences of NEE at prairie and switchgrass cover types. Such results could be supported by the more regular interannual growth phases of maize—i.e., annual and genetically bred hybrid—compared to the perennial (i.e., prairie and switchgrass) and polyculture (i.e., prairie) ones. However, our results were contrasting to those reported by previous studies (Abraha et al., 2018) in which it was shown that less interannual variation in NEE was observed in perennial crops. Such discrepancy could possibly arise since I only considered growing season NEE, while previous studies also took into account the non-growing season. This difference is important because, in terms of NEE magnitude, negative and positive growing season NEE indicate net C uptake and emission, respectively. By only considering growing season NEE, I considered the net C uptake of the three cover types. As a matter of fact, all three cover types showed negative growing season NEE (i.e., net C uptake during 2018–2021). The highest C uptake was observed in maize cover type, with same magnitudes at both farms. Such values were in contrast with those reported by Abraha et al. (2018), during an 8-year study period, where AGR sites showed to have significantly higher C uptake than CRP ones. The reason for such discrepancy is because my predictions of growing season NEE were carried out for the summer fieldwork time-period only (other than the fact of not taking into account non-growing season days). When looking at the full growing season (i.e., start to end of the season, calculated by considering the first four days in row

of CO_2 uptake and release, respectively), my results were similar to those at Abraha et al. (2018), with maize C uptakes (cumulative uptakes) higher at AGR (i.e., ΣNEE: -597±55 gC m^{-2}; -6.3±1.0 gC m^{-2} d^{-1}) than those at CRP (i.e., ΣNEE: -557±68 gC m^{-2}; -6.3±0.8 gC m^{-2} d^{-1}), however I did not investigate if such differences were significant or not.

Higher magnitudes of NEE are observed at AGR, compared to CRP, because maintaining lands for 20 years under the Conservation Reserve Program, resulted in an increase of labile C pool in the soil (first 10 cm), which was twofold that of soils that were formerly tilled (Abraha et al., 2018). In other words, higher labile C pools result in net C emissions, and hence in lower magnitude of net C uptake, during growing season as well as during the non-growing season.

On the other hand, daily averages (over a 14-day period) of the net C uptake showed to be similar (i.e., predicted NEE at -14 gC m^{-2} d^{-1}) to those observed by Wagle et al. (2018) over a 7-day period for maize in the Texas High Plains (at -14.8±1.14 gC m^{-2} d^{-1}) and within the range or slightly smaller than those for irrigated (from -15 to -17 gC m^{-2} d^{-1}) and rainfed (from -13 to -18 gC m^{-2} d^{-1}) maize fields in Nebraska.

The two perennial cover types exhibited lower C uptake, of a magnitude equal to 11.5 gC m^{-2} d^{-1} and 12.2 gC m^{-2} d^{-1}, at prairie and switchgrass, compared to 14.3 gC m^{-2} d^{-1} of maize cover type. However, in the context of land use history, predicted C uptakes were higher for prairie than switchgrass at AGR, while opposite trends was observed at CRP, where C uptake of switchgrass were higher than those of prairie (except for 2019). Again, similar results were reported by Abraha et al. (2018), where prairie appeared to have significantly higher C uptakes than switchgrass at AGR, right after following conversion in 2010, while switchgrass gained higher C uptakes after about three years following the conversion in 2010. Overall, the cumulative predicted and actual net C uptakes of the three cover types presented in this study might have higher magnitudes than

those observed by other studies since we either considered the summer fieldwork campaign or the growing season time-period only, instead of accounting for non-growing seasons as well.

Main key drivers of growing season NEE

The three model comparative analysis allowed me to investigate the structural attribute associated to NEE, during 2018–2021 growing seasons. Regardless of the best final model selected, the amount and the magnitude of the drivers considered, strongly varied by cover type. Overall, prairie and switchgrass cover types showed highest number of main explanatory variable to NEE, while maize cover type had the lowest one. Again, this finding can be expected given the perennial (for both prairie and switchgrass) and polyculture (for prairie) nature of such crops, compared to the annual genetically bred row crop such as maize. Nevertheless, according to the random forest model, the most relevant explanatory variable for NEE at maize cover type was vegetation height. This finding could be likely explained by the monoculture and highly genetically bred nature of hybrids of maize, for which the C sink/source condition is directly related to the plant's height (i.e., aboveground biomass). On the other hand, in line with other studies (Wagle et al., 2018), I found that climatic variables (e.g., air temperature, photosynthetic active radiation, and vapor pressure deficit) did not significantly associate with NEE during 2018–2021. Interestingly, for the model selected, I found that leaf area index had almost zero control on growing season NEE. Such result is in contrast with other studies, according to which, leaf area index was found to be an important driver to NEE at maize, under different management (irrigated vs. rain-fed (Safa et al., 2019). Similarly, Wagle et al. (2018) showed that higher magnitudes of growing season NEE at maize are influenced by the higher leaf area index values. A different story came out from the analysis of prairie cover type, which, according to the random forest model, showed to have multiple main explanatory variables associated with growing season NEE. In

particular, the strongest explanatory variable appeared to be vapor pressure deficit, followed by photosynthetic active radiation, daily air temperature, soil water content, and vegetation height, while SPAD index and leaf area index appeared to have less magnitude. I think that the main reason for more than one single key driver, compared to maize, is that, in a perennial polyculture set-up, carbon fluxes are influenced by plant diversity at both single species scale and community-wide scale, due to the diversified photosynthetic and respiration rates of different photosynthetic pathways (C_3 *vs* C_4; Kohli et al., 2021). Lastly, switchgrass showed the highest number of key drivers, such as vegetation height and daily air temperature, slightly followed by vapor pressure deficit, leaf area index, soil water content, and photosynthetic active radiation. For instance, switchgrass is a perennial warm-season C_4 grass, which has been shown to be sensitive to moisture stress (Stahlheber et al., 2020). Moreover, depending on the ecotypes considered, crop's morphological traits, precipitation, and soil water availability have been shown to influence switchgrass ecophysiology (Wullschleger et al., 2010).

Forecast of growing season C uptake in maize

The Bayesian Dynamic Linear Models using the *in-situ* variable (i.e., vegetation height) as main key driver to NEE produced results that varied depending on the land use history considered (i.e., AGR or CRP). Generally, the models overestimated the net C uptake during the early stages of maize development, while underestimated the net C uptake on early July. While overestimates were higher at CRP (between 24 and 41 gC m^{-2} d^{-1} less than the actual C uptake measured) than those at AGR, underestimates were lower at CRP (of about 48 gC m^{-2} d^{-1} less than the actual C uptake measured) than AGR. Nevertheless, despite the land use history considered, models' performances were poor (i.e., high RMSE) at the very beginning of the forecast window, due to the nature of the BDLM, which bases estimates at the step *t+1* on those at the step *t*, where no

previous estimate was available. The use of remote sensing variables in the BDLMs brought to some improvements in forecasting the net C uptake/emission; however, the overall forecast did not benefit much from the remote sensing analysis (Tables A20-A21 and Figures A11.1–A11.3). At the historically cultivated as agricultural lands sites, improvements in forecasting were obtained from EVI2 and CIg on June 24 and on August 20, likely due to the sensitivity of the two optical indices to changes in vegetation greenness and canopy chlorophyll content during the canopy closure and senescence. Regarding the radar PolSAR decomposition coefficient Alpha (i.e., type of scattering: surface *vs* double-bounce *vs* volume), improvements were obtained on July 8. Unlike optical vegetation indices, PolSAR decomposition coefficients provide information about the structure of the target (i.e., vegetation) thanks to the differentiation of scattering type (i.e., surface, double-bounce, and volume scattering), which can be related to the changes in maize canopy structure during the flowering and grain-filling stages. At the previously Conservation Reserve Program site, the employment of EVI2 and CIg VIs brought to an improvement of forecasting on May 27 (CIg only), June 10 (both EVI2 and CIg), on July 8 (only EVI2) and on August 20 (both EVI2 and CIg). On the other hand, the use of Alpha improved forecasting on August 20. Lastly, when both land use histories were considered together, I found that improvements were on June 10 (EVI2 only), July 8 (both EVI2 and CIg), and August 20 (EVI2, CIg, and Alpha).

Limitations and potential implications

One limitation of the present study is the choice of the growing season as time-period of my analysis. The reason of limiting the analysis to the growing season only, derived by the fact that the *in-situ* variables could only be collected during such period (i.e., roughly from May to August). However, by doing so, I ignored the net outgoing fluxes (i.e., CO_2 emissions) during the non-growing season period. For that reason, my results showed NEE values that were higher in

magnitude, and so contrasting with other studies (Abraha et al., 2018). A further limitation, and potential implication, to my study is given by the need to integrate the analysis within a more comprehensive framework, through for example, a life cycle assessment (LCA) analysis (i.e., other sources of CO_2 emission), which would help with a better understanding the impact (and magnitude) of land use history and land management in the context of climate benefit potentials due to various sources of GHG emission. For example, net magnitudes of ecosystem sink/source should also account for the CO_2 emitted due to harvesting (i.e., grain, stover, and biomass), other than the CO_2 uptake by the crops during the growing season—i.e., the so-called adjusted net ecosystem exchange (NEE_{adj}; Abraha et al., 2018). Depending on the land use history, NEE_{adj} might result in higher/lower CO_2 emissions, due to higher/lower exported yield, coupled with lower/higher magnitude of NEE, respectively. Moreover, a more comprehensive calculation of NEE_{adj} must also include the emissions due to agronomic practices (e.g., N_2O emissions due to N fertilization), which are related to soil microbial communities and the readily available C source (Abraha & Gelfand, et al., 2018; Gelfand et al., 2015) as well as the mitigations due to the employment of bioenergy crops as alternative source of energy to fuel (Abraha et al., 2019).

Conclusion

Land use and land cover and associated management history can substantially affect the net C sink/source nature of a landscape. The three cover types accounted for conspicuous climate benefit potentials (i.e., net C uptake) due to land use history during the growing season. Specifically, looking at individual cover type, maize had the highest net C uptake, which was higher in magnitude at the conservation reserve program land than the one established on historically cultivated agricultural lands. Prairie cover type showed the second-highest climate benefit potentials, slightly followed by switchgrass cover type, although differences due to land

cover history were not remarkable. Each cover type showed unique main key influences involved in the magnitude of net C uptake/emission, which reflected the nature of the crop considered, whether annual *vs* perennial and monoculture *vs* polyculture. Net C uptake/emission at Maize cover type were mainly influenced by vegetation height, while multiple key influences were involved in the C uptake/emission at prairie and switchgrass. Lastly, the employment of fine spatial resolution (20 m) optical and radar satellite imagery provides distinct contribution (i.e., site and date dependent) to improving forecasts of daily net C uptake/emission during 2021 growing season. Generally, the two optical vegetation indices (i.e., EVI2 and CIg) contributed to improving the forecasts at various stages of the maize's growth development (i.e., germination/emergence, seedling, flowering/grain-filling, and senescence), where changes were expressed in terms of change in surface reflectance (i.e., greenness and canopy chlorophyll content). On the other hand, the radar polarimetric SAR (PolSAR) decomposition coefficient (i.e., Alpha) helped improving the forecasts of the mid/late growing season stages, where changes were expressed in terms of structural features of maize. In conclusion, further work is needed to improve understanding the magnitude of land use history and land management in the context of climate warming/cooling, for example, by couple our estimates with other GHGs in an LCA framework, as well as by extending the analysis to non-growing season.

REFERENCES

Abraha, M., Chen, J., Chu, H., Zenone, T., John, R., Su, Y.-J., Hamilton, S. K., & Robertson, G. P. (2015). Evapotranspiration of annual and perennial biofuel crops in a variable climate. *GCB Bioenergy*, *7*(6), 1344–1356. https://doi.org/10.1111/gcbb.12239

Abraha, M., Gelfand, I., Hamilton, S. K., Chen, J., & Robertson, G. P. (2018). Legacy effects of land use on soil nitrous oxide emissions in annual crop and perennial grassland ecosystems. *Ecological Applications*, *28*(5), 1362–1369. https://doi.org/10.1002/eap.1745

Abraha, M., Gelfand, I., Hamilton, S. K., Chen, J., & Robertson, G. P. (2019). Carbon debt of field-scale conservation reserve program grasslands converted to annual and perennial bioenergy crops. *Environmental Research Letters*, *14*(2), 024019. https://doi.org/10.1088/1748-9326/aafc10

Abraha, M., Gelfand, I., Hamilton, S. K., Shao, C., Su, Y.-J., Robertson, G. P., & Chen, J. (2016). Ecosystem water-use efficiency of annual corn and perennial grasslands: Contributions from land-use history and species composition. *Ecosystems*, *19*(6), 1001–1012. https://doi.org/10.1007/s10021-016-9981-2

Abraha, M., Hamilton, S. K., Chen, J., & Robertson, G. P. (2018). Ecosystem carbon exchange on conversion of Conservation Reserve Program grasslands to annual and perennial cropping systems. *Agricultural and Forest Meteorology*, *253–254*, 151–160. https://doi.org/10.1016/j.agrformet.2018.02.016

Aslam, M., Rahman, W. U., Abbas, M., Jafar, H. M. A., Ali, R., Raza, S., Shah, S. A., & Ali, S. (2022). Mitigating the drought stress through potassium application in corn. *Annals of the Romanian Society for Cell Biology*, *26*(01), 671–689.

Barrios, E., Valencia, V., Jonsson, M., Brauman, A., Hairiah, K., Mortimer, P. E., & Okubo, S. (2018). Contribution of trees to the conservation of biodiversity and ecosystem services in agricultural landscapes. *International Journal of Biodiversity Science, Ecosystem Services & Management*, *14*(1), 1–16. https://doi.org/10.1080/21513732.2017.1399167

Bezner, K., R., T. Hasegawa, R. Lasco, I. Bhatt, D. Deryng, A. Farrell, H. Gurney-Smith, H. Ju, S. Lluch-Cota, F. Meza, & G. Nelson, H. Neufeldt, and P. Thornton. (2022). 2022: Food, fibre and other ecosystem products. In *Climate Change 2022: Impacts, Adaptation and Vulnerability. Contribution of Working Group II to the Sixth Assessment Report of the Intergovernmental Panel on Climate Change* (pp. 713–906). Cambridge University Press, Cambridge, UK and New York, NY, USA. https://doi.org/10.1017/9781009325844.007

Bhardwaj, A. K., Zenone, T., Jasrotia, P., Robertson, G. P., Chen, J., & Hamilton, S. K. (2011). Water and energy footprints of bioenergy crop production on marginal lands: Land marginality effects on water and energy use. *GCB Bioenergy*, *3*(3), 208–222. https://doi.org/10.1111/j.1757-1707.2010.01074.x

Biecek, P. (2018). *DALEX: Explainers for Complex Predictive Models in R. The Journal of machine Learning Research*, 3245–3249.

Chen, J., Lei, C., & Sciusco, P. (2021). Modeling ecosystem global warming potentials. In *Biophysical Models and Applications in Ecosystem Analysis* (pp. 119–150). Michigan State University Press; JSTOR. https://doi.org/10.14321/j.ctv1h1vc27.11

Clevers, J. G. P. W., & Gitelson, A. A. (2013). Remote estimation of crop and grass chlorophyll and nitrogen content using red-edge bands on Sentinel-2 and -3. *International Journal of Applied Earth Observation and Geoinformation*, *23*, 344–351. https://doi.org/10.1016/j.jag.2012.10.008

Cloude, S. R., & Pottier, E. (1996). A review of target decomposition theorems in radar polarimetry. *IEEE Transactions on Geoscience and Remote Sensing*, *34*(2), 498–518. https://doi.org/10.1109/36.485127

Forster, P., T. Storelvmo, K. Armour, W. Collins, J.-L. Dufresne, D. Frame, D.J. Lunt, T. Mauritsen, M.D. Palmer, & M. Watanabe, M. Wild, and H. Zhang. (2021). 2021: The Earth's energy budget, climate feedbacks, and climate sensitivity. In *Climate Change 2021: The Physical Science Basis. Contribution of Working Group I to the Sixth Assessment Report of the Intergovernmental Panel on Climate Change* [Masson-Delmotte, V., P. Zhai, A. Pirani, S.L. Connors, C. Péan, S. Berger, N. Caud, Y. Chen, L. Goldfarb, M.I. Gomis, M. Huang, K. Leitzell, E. Lonnoy, J.B.R. Matthews, T.K. Maycock, T. Waterfield, O. Yelekçi, R. Yu, and B. Zhou (eds.)]. Cambridge University Press, Cambridge, United Kingdom and New York, NY, USA, pp. 923–1054, https://doi.org/10.1017/9781009157896.009.

Gelfand, I., Cui, M., Tang, J., & Robertson, G. P. (2015). Short-term drought response of N_2O and CO_2 emissions from mesic agricultural soils in the US midwest. *Agriculture, Ecosystems & Environment*, *212*, 127–133. https://doi.org/10.1016/j.agee.2015.07.005

Günther, F., & Fritsch, S. (2010). *neuralnet: Training of Neural Networks*. *The R Journal*, *2*(1), 30. https://doi.org/10.32614/RJ-2010-006

Hajibabaee, M., Azizi, F., & Zargari, K. (2012). Effect of drought stress on some morphological, physiological and agronomic traits in various foliage corn hybrids. *American-Eurasian Journal of Agricultural & Environmental Sciences*, *12*(7), 890–896. https://doi.org/10.5829/idosi.aejaes.2012.12.07.1751

Harrel, F. E. J. (2021). *Hmisc: Harrell Miscellaneous. R package version 4.6-0.* https://CRAN.R-project.org/package=Hmisc

Hayhoe, K., VanDorn, J., Croley, T., Schlegal, N., & Wuebbles, D. (2010). Regional climate change projections for Chicago and the US Great Lakes. *Journal of Great Lakes Research*, *36*, 7–21. https://doi.org/10.1016/j.jglr.2010.03.012

Hlavinka, J., Nauš, J., & Špundová, M. (2013). Anthocyanin contribution to chlorophyll meter readings and its correction. *Photosynthesis Research*, *118*(3), 277–295. https://doi.org/10.1007/s11120-013-9934-y

Jiang, Z., Huete, A. R., Didan, K., & Miura, T. (2008). Development of a two-band enhanced vegetation index without a blue band. *Remote Sensing of Environment, 112*(10), 3833–3845. https://doi.org/10.1016/j.rse.2008.06.006

Khun, M. (2021). *Caret: Classification and Regression Training. R package version 6.0-90.* https://CRAN.R-project.org/package=caret

Kohli, M., Henning, J. A., Borer, E. T., Kinkel, L., & Seabloom, E. W. (2021). Foliar fungi and plant diversity drive ecosystem carbon fluxes in experimental prairies. *Ecology Letters*, *24*(3), 487–497. https://doi.org/10.1111/ele.13663

Liu, L., & Greaver, T. L. (2009). A review of nitrogen enrichment effects on three biogenic GHGs: The CO_2 sink may be largely offset by stimulated N_2O and CH_4 emission. *Ecology Letters*, *12*(10), 1103–1117. https://doi.org/10.1111/j.1461-0248.2009.01351.x

Monteith, J. L., & Unsworth, M. H. (2013). *Principles of Environmental Physics: Plants, Animals, and the Atmosphere* (4th ed). Elsevier, Academic Press.

Müller-Wilm, U., Devignot, O., & Pessiot, L. (2020). *S2 MPC: Sen2Cor Configuration and User Manual*. http://step.esa.int/thirdparties/sen2cor/2.9.0/docs/S2-PDGS-MPC-L2A-SUM-V2.9.0.pdf

Nasirzadehdizaji, R., Balik Sanli, F., Abdikan, S., Cakir, Z., Sekertekin, A., & Ustuner, M. (2019). Sensitivity analysis of multi-temporal sentinel-1 SAR parameters to crop height and canopy coverage. *Applied Sciences*, *9*(4), Article 4. https://doi.org/10.3390/app9040655

Nleya, T., Chungu, C., & Kleinja, J. (2016). Corn growth and development. *Grow Corn Best Management Practices*, 10.

Plummer, M. (2003). *JAGS: A Program for Analysis of Bayesian Graphical Models Using Gibbs Sampling*. *Working Papers*, 8.

Robertson, G. (2020). *LTER Meteorological Stations at the Kellogg Biological Station, Hickory Corners, MI (1988 to 2020)*. https://doi.org/10.6073/pasta/4c30523bae14c4340e4d9c90e72f90c4

Safa, B., Arkebauer, T. J., Zhu, Q., Suyker, A., & Irmak, S. (2019). Net ecosystem exchange (NEE) simulation in maize using artificial neural networks. *IFAC Journal of Systems and Control*, *7*, 100036. https://doi.org/10.1016/j.ifacsc.2019.100036

Shukla, P. R., J. Skea, R. Slade, A. Al Khourdajie, R. van Diemen, D. McCollum, M. Pathak, S. Some, P. Vyas, R. Fradera, M. Belkacemi, & A. Hasija, G. Lisboa, S. Luz, J. Malley, (eds.). (2022). IPCC, 2022: Summary for Policymaker. In *Climate Change 2022: Mitigation of Climate Change. Contribution of Working Group III to the Sixth Assessment Report of the Intergovernmental Panel on Climate Change*. Cambridge University Press, Cambridge, UK and New York, NY, USA. doi: 10.1017/9781009157926.001

Stahlheber, K. A., Lindquist, J., Drogosh, P. D., Pennington, D., & Gross, K. L. (2020). Predicting productivity: A trait-based analysis of variability in biomass yield among switchgrass feedstock cultivars. *Agriculture, Ecosystems & Environment*, *300*, 106980. https://doi.org/10.1016/j.agee.2020.106980

Szulc, P., Bocianowski, J., Nowosad, K., Zielewicz, W., & Kobus-Cisowska, J. (2021). SPAD leaf greenness index: Green mass yield indicator of maize (Zea mays L.), genetic and agriculture practice relationship. *Plants*, *10*(5), 830. https://doi.org/10.3390/plants10050830

Thoen, G. F. (1990). *Soil Survey of Barry County, Michigan*. *14*, US Government Printing Office.

Tongwane, M. I., & Moeletsi, M. E. (2018). A review of greenhouse gas emissions from the agriculture sector in Africa. *Agricultural Systems*, *166*, 124–134. https://doi.org/10.1016/j.agsy.2018.08.011

Wagle, P., Gowda, P. H., Moorhead, J. E., Marek, G. W., & Brauer, D. K. (2018). Net ecosystem exchange of CO_2 and H_2O fluxes from irrigated grain sorghum and maize in the Texas High Plains. *Science of The Total Environment*, *637–638*, 163–173. https://doi.org/10.1016/j.scitotenv.2018.05.018

Wang, H., Zhang, Y.-M., Mao, J.-X., Wan, H.-P., Tao, T.-Y., & Zhu, Q.-X. (2019). Modeling and forecasting of temperature-induced strain of a long-span bridge using an improved Bayesian dynamic linear model. *Engineering Structures*, *192*, 220–232. https://doi.org/10.1016/j.engstruct.2019.05.006

Wright, M. N., & Ziegler, A. (2017). ranger: A fast implementation of random forests for high dimensional data in C++ and R. *Journal of Statistical Software*, *77*(1). https://doi.org/10.18637/jss.v077.i01

Wullschleger, S. D., Davis, E. B., Borsuk, M. E., Gunderson, C. A., & Lynd, L. R. (2010). Biomass production in switchgrass across the United States: Database description and determinants of yield. *Agronomy Journal*, *102*(4), 1158–1168. https://doi.org/10.2134/agronj2010.0087

Zenone, T., Chen, J., Deal, M. W., Wilske, B., Jasrotia, P., Xu, J., Bhardwaj, A. K., Hamilton, S. K., & Philip Robertson, G. (2011). CO2 fluxes of transitional bioenergy crops: Effect of land conversion during the first year of cultivation. *GCB Bioenergy*, *3*(5), 401–412. https://doi.org/10.1111/j.1757-1707.2011.01098.x

APPENDIX

Table A14: Dates of summer fieldwork visits and Sentinel-1 and -2 acquisitions at the six historically cultivated as agricultural lands (AGR) and the Conservation Reserve Program (CRP) sites, during 2018–2021 growing seasons.

2018			2019			2020			2021		
fieldwork	S1	S2	fieldwork	S1	S2	fieldwork	S1	S2	fieldwork	S1	S2
–	–	–	–	–	–	–	–	–	05/27	05/22	05/22
06/01	06/07	06/28	06/11	06/14	06/12	06/09	06/08	06/06	06/10	06/15	06/11
06/21	06/19	06/17	06/25	06/26	06/27	06/22	06/20	06/21	06/23	06/27	06/16
07/09	07/13	07/07	067/09	07/08	07/07	07/08	07/02	07/06	07/08	07/09	07/06
07/24	07/25	07/17	07/23	07/20	07/22	07/21	07/14	07/21	07/21	07/21	07/26
08/08	08/06	08/01	08/07	08/13	08/11	08/05	08/26	08/05	08/04	08/02	08/05
08/31	08/30	08/31	08/20	08/25	08/21	08/19	08/19	08/20	08/19-20*	08/26	06/15-25

"–": no fieldwork visit

* fieldwork visit was split into two consecutive days due to weather conditions

Table A15: Non-parametric Kruskal-Wallis rank sum test for the five variables leaf area index (LAI; m^2 m^{-2}), SPAD index, vegetation height (Ht; m), soil water content (SWC; %), and net ecosystem exchange (NEE; gC m^{-2} d^{-1}), for the pairs "cover type-growing season".

		Kruskal-Wallis rank sum test		
pairs (-growing season)	variable	χ^2	p-value	df
maize		1.859		
prairie	LAI	49.742	***	
switchgrass		9.407	*	
maize		20.344	***	
prairie	SPAD	31.309	***	
switchgrass		12.360	**	
maize		2.955		
prairie	Ht	8.015		3
switchgrass		3.667		
maize		3.009		
prairie	SWC	9.527	*	
switchgrass		17.200	***	
maize		1.302		
prairie	NEE	25.864	***	
switchgrass		22.600	***	

Signif. codes: *** p-value < 0.001, ** p-value < 0.01, * p-value < 0.05, · p-value < 0.1, " " p-value > 0.1

Table A16: Non-parametric Wilcoxon rank sum test for the five variables leaf area index (LAI; m^2 m^{-2}), SPAD index, vegetation height (Ht; m), soil water content (SWC; %), and net ecosystem exchange (NEE; gC m^{-2} d^{-1}) for the pairwise "2018–2021 growing seasons".

		Wilcoxon rank sum test														
		LAI			SPAD			Ht			SWC			NEE		
Cover t.		2018	2019	2020	2018	2019	2020	2018	2019	2020	2018	2019	2020	2018	2019	2020
M	2019		–	–		–	–		–	–		–	–		–	–
	2020			–	**		–			–			–			–
	2021				***											
P	2019	***	–	–		–	–		–	–		–	–		–	–
	2020	***		–	***	***	–			–			–			–
	2021		***	*	*	.	*				*				***	***
S	2019		–	–		–	–		–	–		–	–		–	–
	2020	·		–			–			–	***		–			–
	2021				**								**	***		***

Signif. codes: *** p-value < 0.001, ** p-value < 0.01, * p-value < 0.05, · p-value < 0.1, " " p-value > 0.1

Table A17: Hyperparameters used for the tuning of the multi-layer perceptron (MLP) and random forest (RF) models following a 10-fold cross validation. The designs were selected based on the least root-mean squared error (RMSE; leading to model convergence), the R-squared scores (R^2), and the mean absolute error (MAE).

	MLP				RF					
	Hidden layers	RMSE	R^2	MAE	m_{try}	S_{rule}	Nod. size	RMSE	R^2	MAE
Maize	4-5-7	0.25	0.93	0.17	7	Variance	1	0.18	0.97	0.13
Prairie	7-4-6	1.14	0.24	0.85	7	Max stat	1	0.56	0.70	0.46
Switchgrass	7-6-4	0.45	0.82	0.33	6	Max stat	1	0.35	0.89	0.26

m_{try}: the number of variables to consider at any given split.
S_{rule}: the splitting rule to use during tree construction.
Nod. size: the minimal node size

Table A18: Summary table for the generalized linear models (GLM; at Eq. 4.17) for the NEE (dependent variable) across maize, prairie, and switchgrass, at both the historically cultivated as agricultural lands (AGR) and the Conservation Reserve Program (CRP) sites.

cover type	variable	estimate	SE	t-test	p-value	R^2
Maize	Intercept	-0.005	0.028	-0.194		0.93
	LAI	-0.390	0.059	-6.642	***	
	SPAD	-0.036	0.036	-0.979	·	
	SWC	0.194	0.029	6.661	***	
	Ht	-0.556	0.062	-8.997	***	
	Ta	-0.164	0.032	-5.200	***	
	PAR	-0.189	0.041	-4.668	***	
	VPD	-0.064	0.040	-1.605	·	
Prairie	Intercept	-0.022	0.071	-0.311		0.08
	LAI	0.167	0.078	2.145	*	
	SPAD	0.013	0.074	0.174		
	SWC	0.197	0.073	2.678	**	
	Ht	-0.179	0.079	-2.263	*	
	Ta	-0.064	0.087	-0.734	·	
	PAR	-0.296	0.100	-2.972	**	
	VPD	0.162	0.105	1.533	·	
Switchgrass	Intercept	0.049	0.059	0.820	·	0.32
	LAI	-0.476	0.094	-5.056	***	
	SPAD	0.098	0.065	1.506	·	
	SWC	0.306	0.065	4.690	***	
	Ht	-0.143	0.090	-1.586	·	
	Ta	-0.089	0.073	-1.232	·	
	PAR	-0.197	0.084	-2.362	*	
	VPD	-0.160	0.086	-1.850	·	

Signif. codes: *** p-value < 0.001, ** p-value < 0.01, * p-value < 0.05, · p-value < 0.1, " " p-value > 0.1
NEE: net ecosystem exchange (g C m^{-2} d^{-1}) during 2018–2021 growing seasons
AGR: agriculturally cultivated farms
CRP: conservations reserve program farms

Table A19: Spearman's (ρ) correlation coefficients between the *in-situ* field data and the optical Sentinel-2 vegetation indices (S2-VIs) and the radar Sentinel-1 sigma nought (i.e., σ°) polarization intensity backscatter (S1-σ°) and polarimetric SAR decomposition coefficients (S1-PolSAR) remote sensing variables, at maize cover type, during 2018–2021 growing seasons. Only statistically significance (i.e., p-value<0.05) coefficients are shown. Positive and negative values indicate positive and negative correlations, respectively. Values in bold indicate the remote sensing variables used for the Bayesian Dynamic Linear Models (BDLMs).

			Spearman's (ρ) coefficients			
Cover type	Remote sensing output		LAI	SPAD	Ht	SWC
Maize	S2-VIs	EVI2	0.83	0.54	**0.90**	–
		CIgreen	0.83	0.50	**0.86**	–
		NDWI1	0.62	0.42	**0.77**	–
		NDWI2	0.78	0.52	**0.87**	-0.18
	S1-backscatter	RVI	0.33	0.20	**0.30**	–
		Ratio1	0.33	0.20	**0.30**	–
		Ratio2	-0.33	-0.20	-0.30	–
		Intensity1	-0.25	-0.16	-0.34	-0.20
		Intensity2	0.41	0.26	**0.48**	0.22
	S1 PolSAR coefficients	Entropy	0.58	0.35	**0.62**	–
		Alpha	0.58	0.35	**0.59**	–

"–": p-values > 0.05
S2-VIs: Sentienk-2 vegetation indices
S1-backscatter: Sentinel-1 backscatter and intensity values
S1-PolSAR: Sentinel-1 polarimetric SAR decomposition coefficients

Table A20: Root-mean squared error (RMSE, i.e., accuracy of the forecast, mean (± standard deviation)) of forecasted net ecosystem exchange (NEE; gC m^{-2} d^{-1}) values using both in-situ variables (i.e., vegetation height; Ht) and remote sensing outputs (i.e., EVI2, CIg, and Alpha).

	Ht			EVI2			CIg			Alpha		
date	AGR&CRP	AGR	CRP	AGR&CRP	AGR	CRP	AGR&CRP	AGR	CRP	AGR&CRP	AGR	CRP
May 25	30(±22)	41(±24)	48(±22)	35(±18)	84(0)	53(±20)	38(±24)	79(±2)	40(±25)	44(±30)	68(±23)	64(±24)
June 9	23(±1)	24(±1)	31(±1)	14(±4)	35(±14)	23(±6)	23(±1)	39(±11)	21(±1)	39(±9)	53(±6)	55(±5)
June 22	17(±2)	12(±3)	21(±2)	39(±11)	2(±2)	35(±8)	41(±9)	4(±1)	36(±8)	37(±4)	44(±10)	45(±3)
July 7	17(±11)	53(±13)	19(±11)	16(±7)	61(±18)	15(±10)	13(±11)	79(±15)	19(±12)	28(±5)	37(±9)	27(±3)
July 20	10(±5)	9(±5)	10(±5)	24(±10)	11(±6)	17(±11)	19(±13)	16(±9)	15(±4)	13(±8)	11(±5)	11(±9)
August 3	10(±6)	10(±13)	10(±8)	18(±6)	86(±9)	21(±5)	50(±8)	88(±11)	60(±7)	35(±9)	50(±3)	50(±7)
August 18	43(±7)	31(±3)	48(±5)	21(±4)	22(±10)	21(±3)	20(±11)	25(±11)	12(±7)	10(±6)	37(±4)	17(±6)

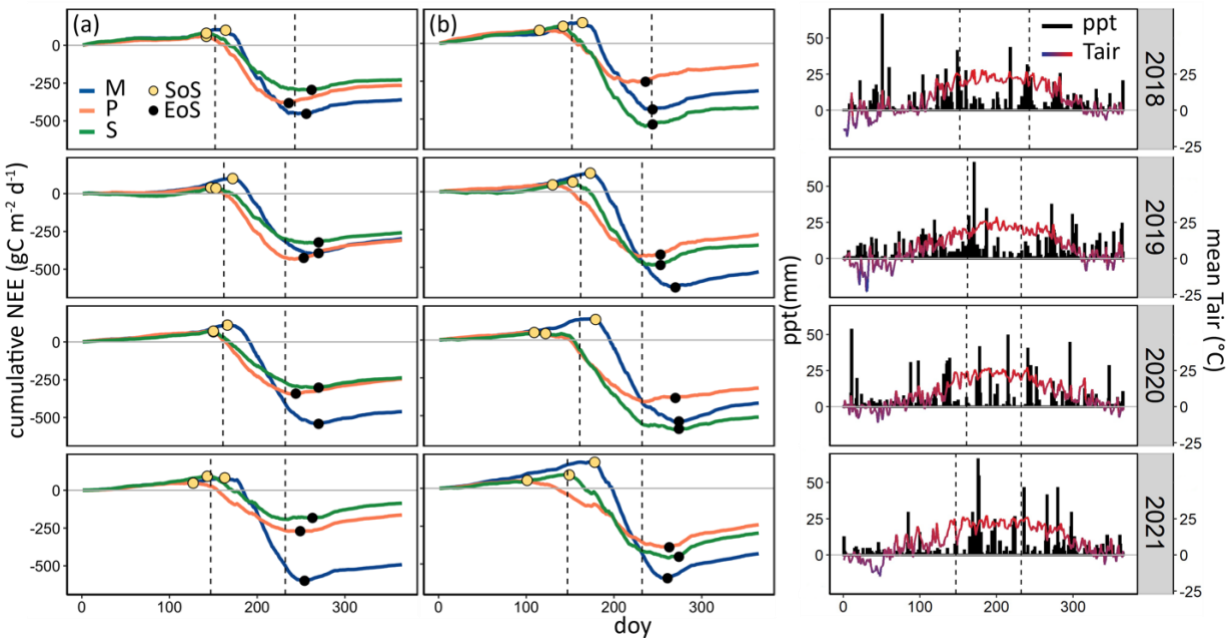

Figure A2: Cumulative net ecosystem exchange (NEE; gC m^{-2} d^{-1}) during 2018–2021 growing seasons across (a) the historically cultivated as agricultural lands (AGR) and (b) the Conservation Reserve Program (CRP) sites, at maize (M), prairie (P), and switchgrass (S) cover types. Solid yellow and black circles indicate the start of the growing season (SoS) and the end of the growing season (EoS), respectively, calculated as the first four days in row of negative (i.e., CO_2 uptake) and positive (i.e., CO_2 emission) NEE, respectively. Vertical black dashed lines indicate the start and the end dates of the summer fieldwork campaigns (see Table A14) during 2018–2021. Daily precipitation (mm) and mean air temperature (°C) values are also shown.

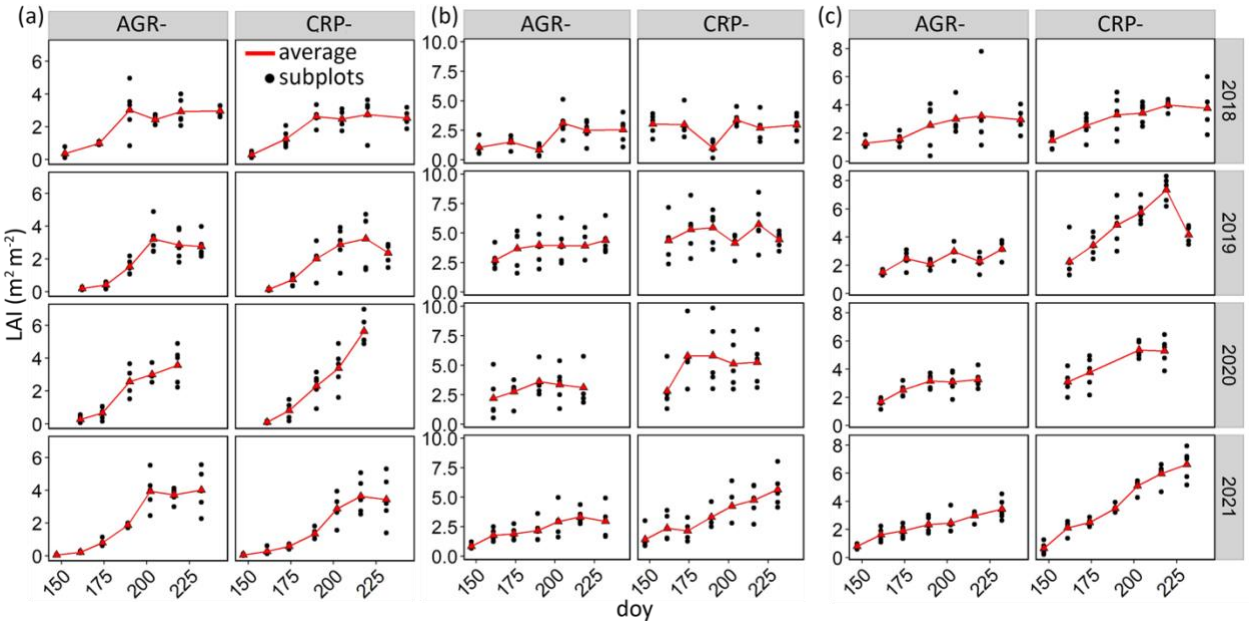

Figure A3.1: Growing season trends of leaf area index (LAI; m^2 m^{-2}) at (a) maize, (b) prairie, and (c) switchgrass cover types, during 2018–2021 growing seasons. Black full circles indicate measurements at subplot (×5) level, while red solid lines and triangles refer to average values.

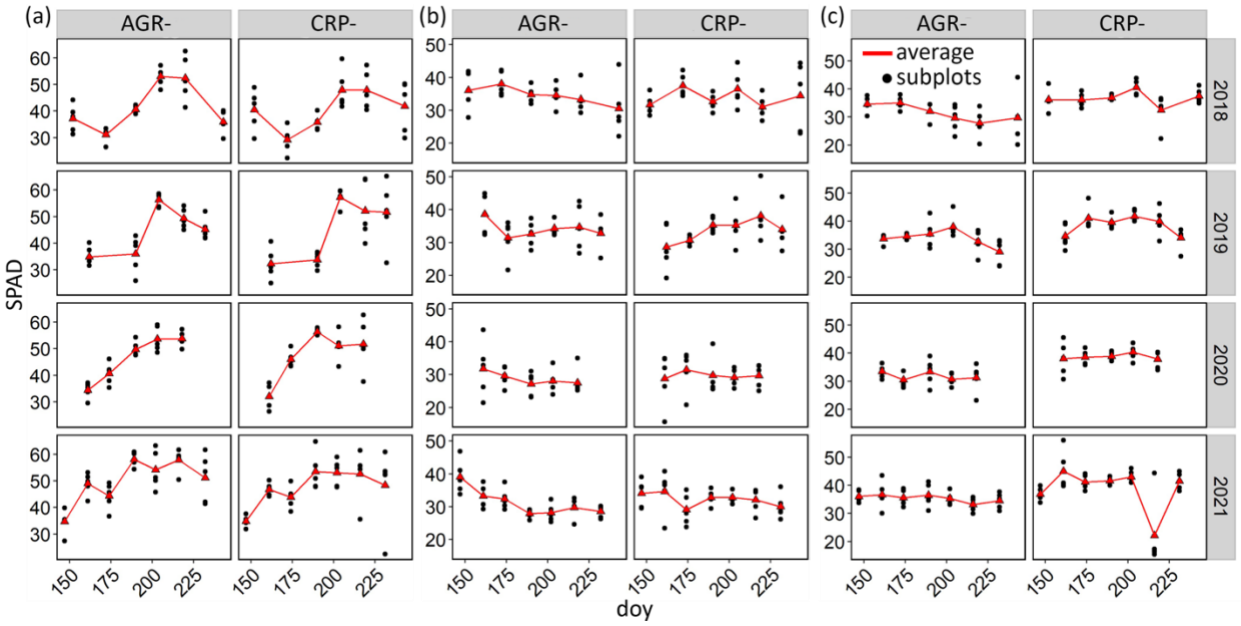

Figure A3.2: Growing season trends of Soil and Plant Analysis Development index (SPAD; unitless) at (a) maize, (b) prairie, and (c) switchgrass cover types, during 2018–2021 growing seasons. Black full circles indicate measurements at subplot (×5) level, while red lines/triangles refer to average values.

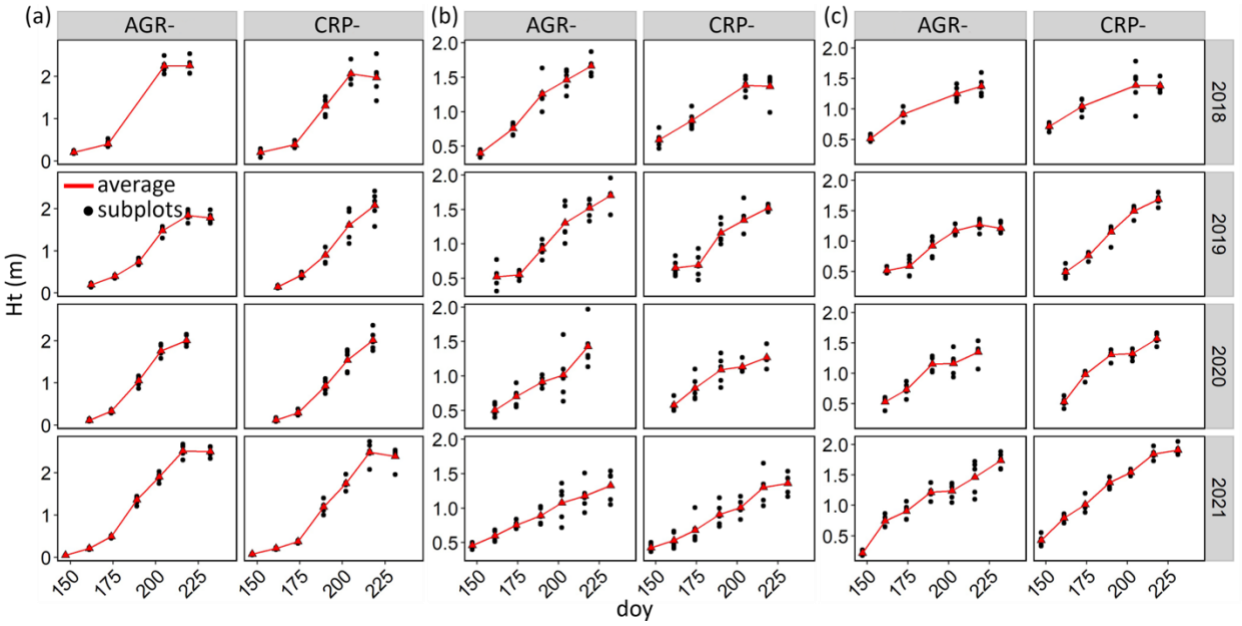

Figure A3.3: Growing season trends of vegetation height (Ht; m) at (a) maize, (b) prairie, and (c) switchgrass cover types, during 2018–2021 growing seasons. Black full circles indicate measurements at subplot (×5) level, while red lines/triangles refer to average values.

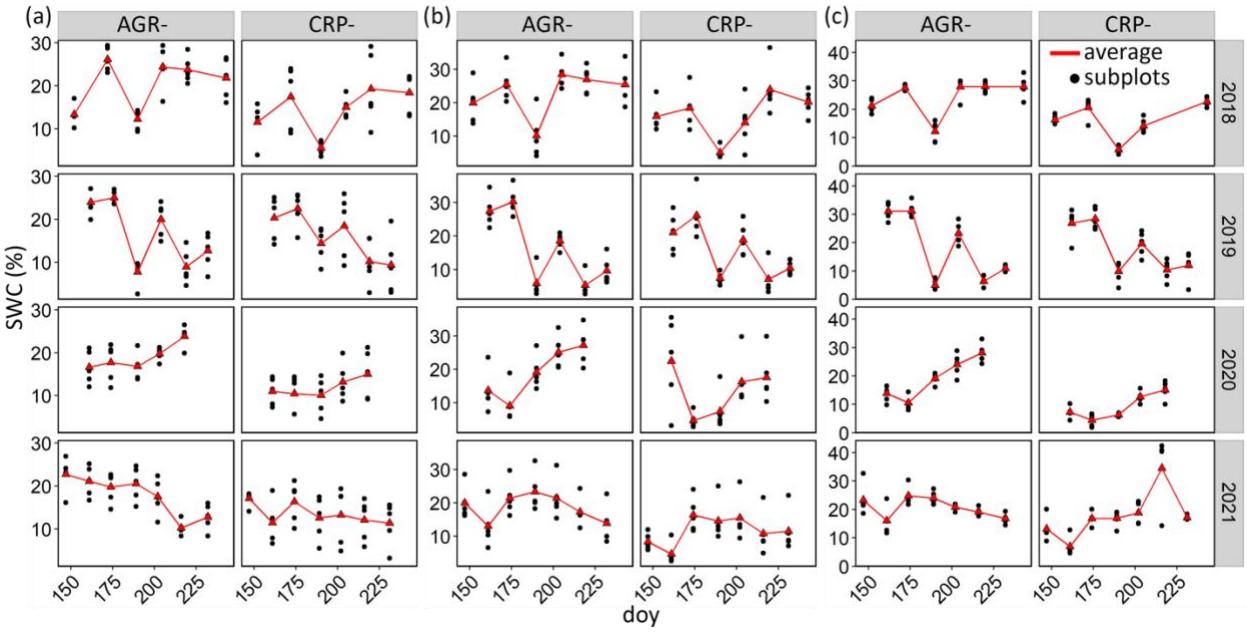

Figure A3.4: Growing season trends of soil water content (SWC; %) at (a) maize, (b) prairie, and (c) switchgrass cover types, during 2018–2021 growing seasons. Black full circles indicate measurements at subplot (×5) level, while red lines/triangles refer to average values.

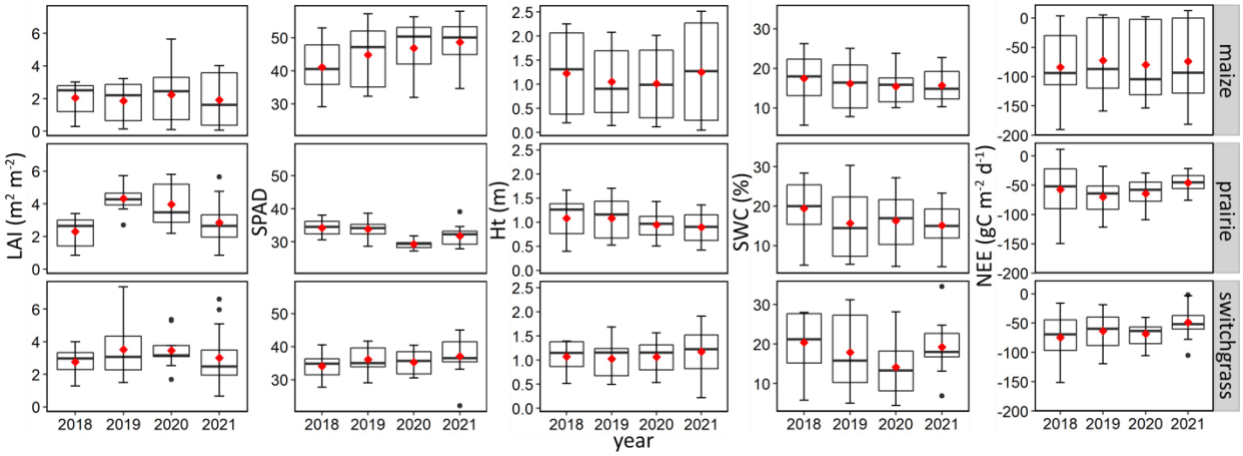

Figure A4: Boxplot of the five variables leaf area index (LAI; m^2 m^{-2}), Soil and Plant Analysis Development index (SPAD; unitless), vegetation height (Ht; m), soil water content (SWC; %), and net ecosystem exchange (NEE; gC m^{-2} d^{-1}) during 2018–2021 growing seasons. Each box represents the 1st (Q1) and 3rd (Q3) quartiles of the interquartile distribution (IQR). The horizontal line and the red diamonds indicate the distribution median (Q2) and mean, respectively. The whiskers represent the limits (minimum and maximum) of the IQR (5% and 95%, respectively), while the black solid points represent the outliers.

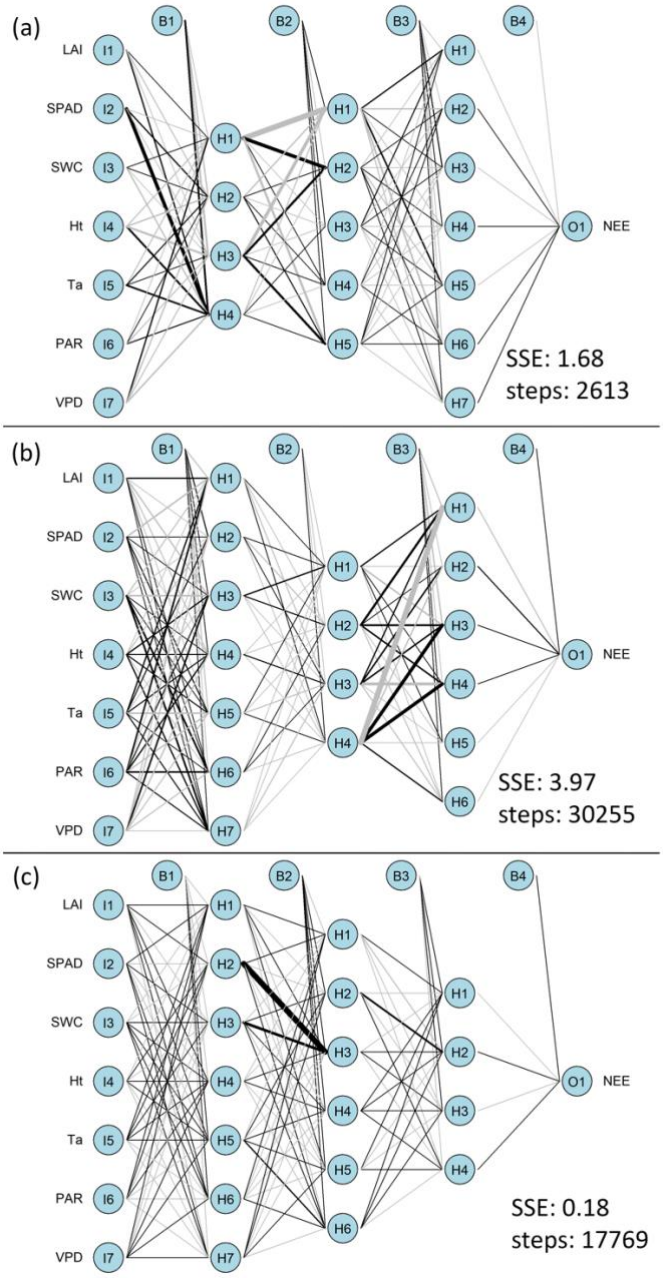

Figure A5: Feed-forward Multi-Layer Perceptron (MLP) neural network for (a) maize, (b) prairie, and (c) switchgrass cover types, during 2018–2021 growing seasons. Each model is composed of one input layer ("*I*"; left-hand side of the graph), represented by the seven independent variables—i.e., leaf area index (LAI), Soil and Plant Analysis Development index (SPAD), soil water content (SWC), vegetation height (Ht), mean air temperature (Ta), photosynthetic active radiation (PAR), and vapor pressure deficit (VPD); three hidden layers ("*H*"; middle side of the graph); and one output layer ("*O*"; right-hand side of the graph) represented by the dependent variable net ecosystem exchange (NEE). Line thickness and color represent the magnitude (i.e., the thicker the line the higher the weight magnitude) and the sign (i.e., black = positive, grey = negative) of the weights. Models' sum of square errors (SSE) and number of steps (i.e., iterations) are also reported.

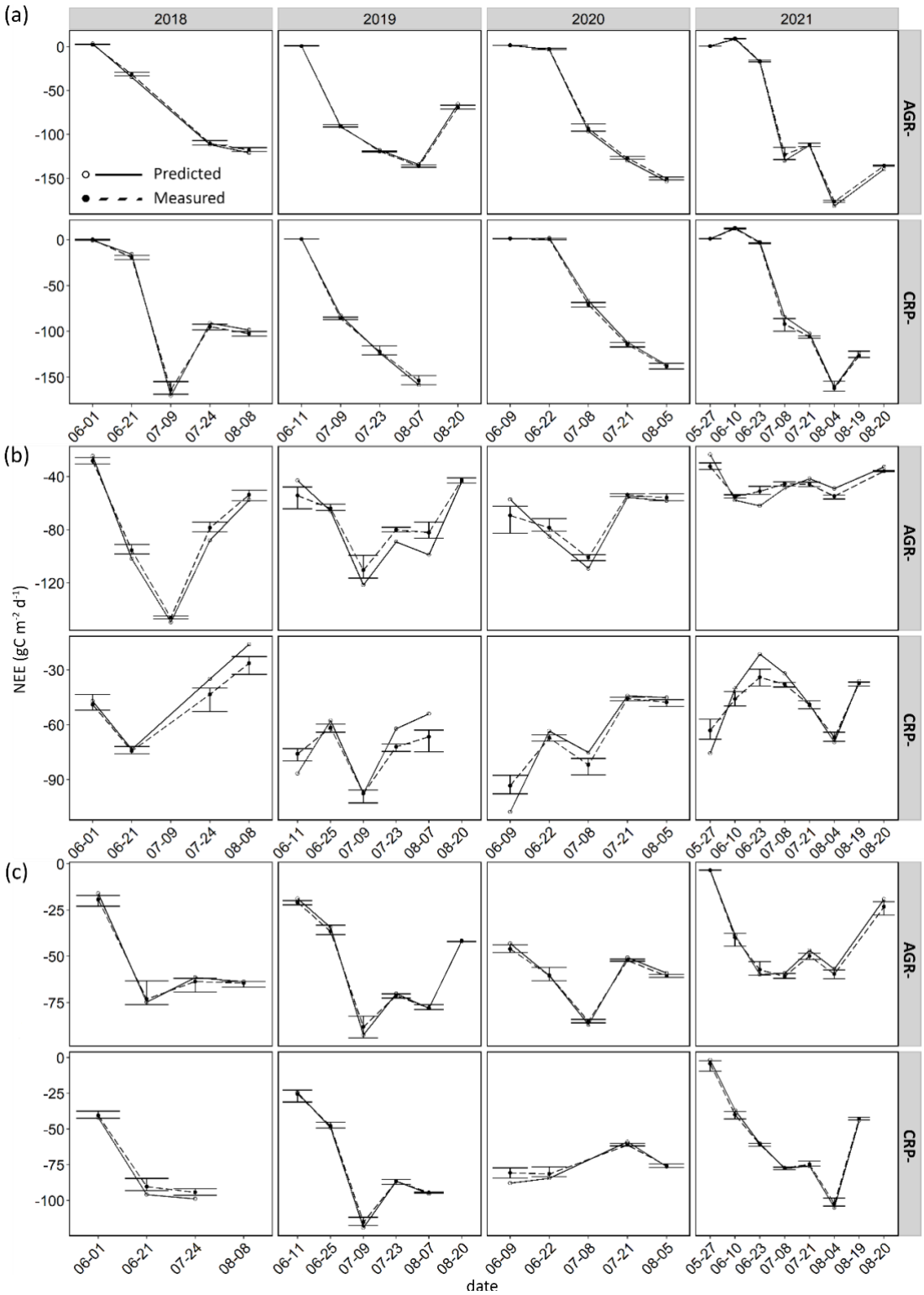

Figure A6: Predicted (Random Forest model; solid black lines and empty circles) and measured (dashed black lines and full black circles) values of the net ecosystem exchange (NEE; gC m^{-2} d^{-1}) at (a) maize, (b) prairie, and (c) switchgrass cover types, during the 2018–2021 growing seasons. Error bars indicate the minimum and maximum values across the five subplots.

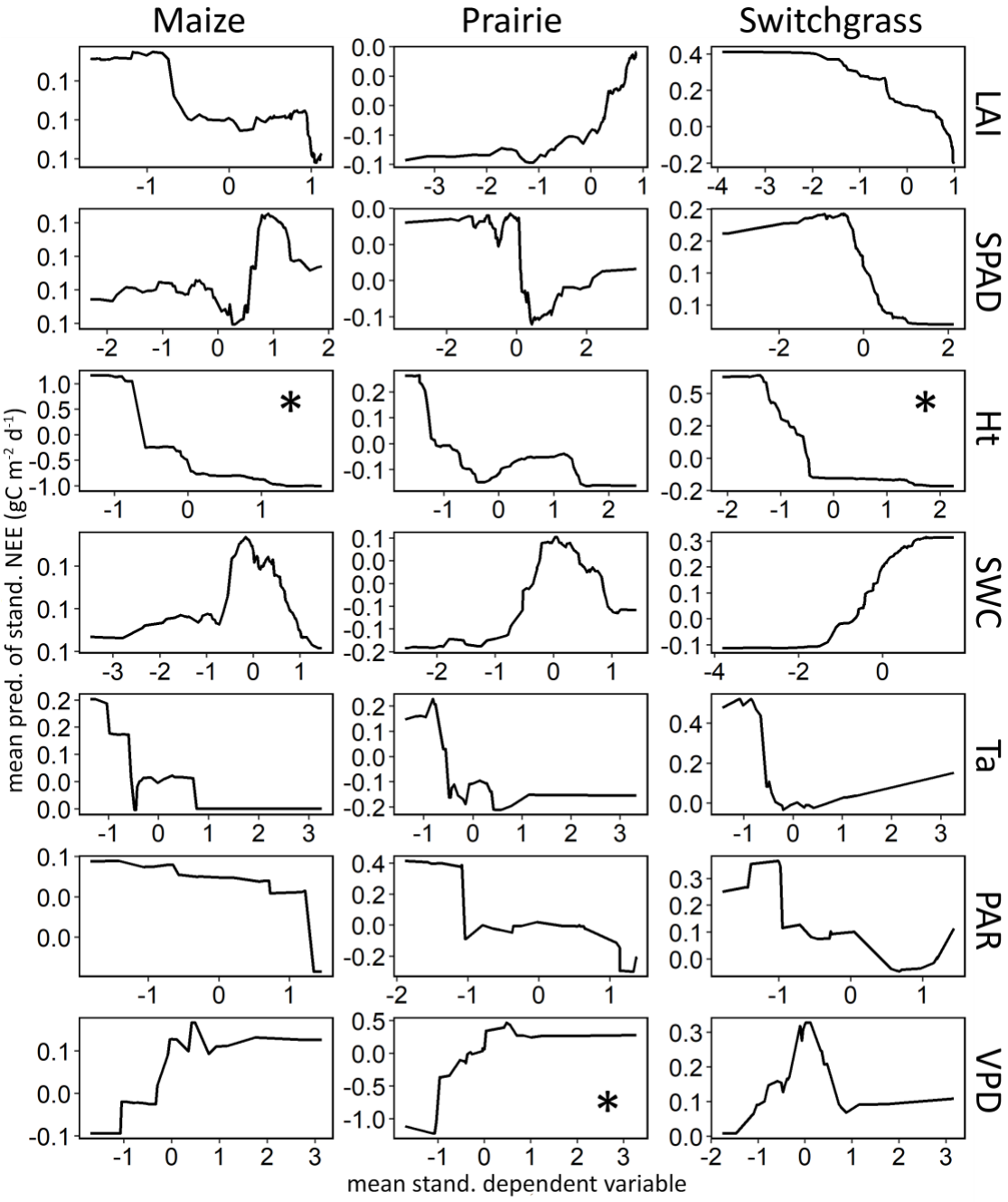

Figure A7: Partial-dependence (PD) profiles showing mean predictions of standardized net ecosystem exchange (NEE; gC m^{-2} d^{-1}) values from the Random Forest (RF) model as function of variations in mean standardized leaf area index (LAI), SPAD index (SPAD), vegetation height (Ht), soil water content (SWC), , mean air temperature (Ta), photosynthetic active radiation (PAR), and vapor pressure deficit (VPD) at maize, prairie, and switchgrass. Asterisks indicate the dominant key drivers, as highlighted by the variable importance at Figure 4.3. PD profiles show individual dependence (positive, negative, or null) of an instance-level prediction on an explanatory variable.

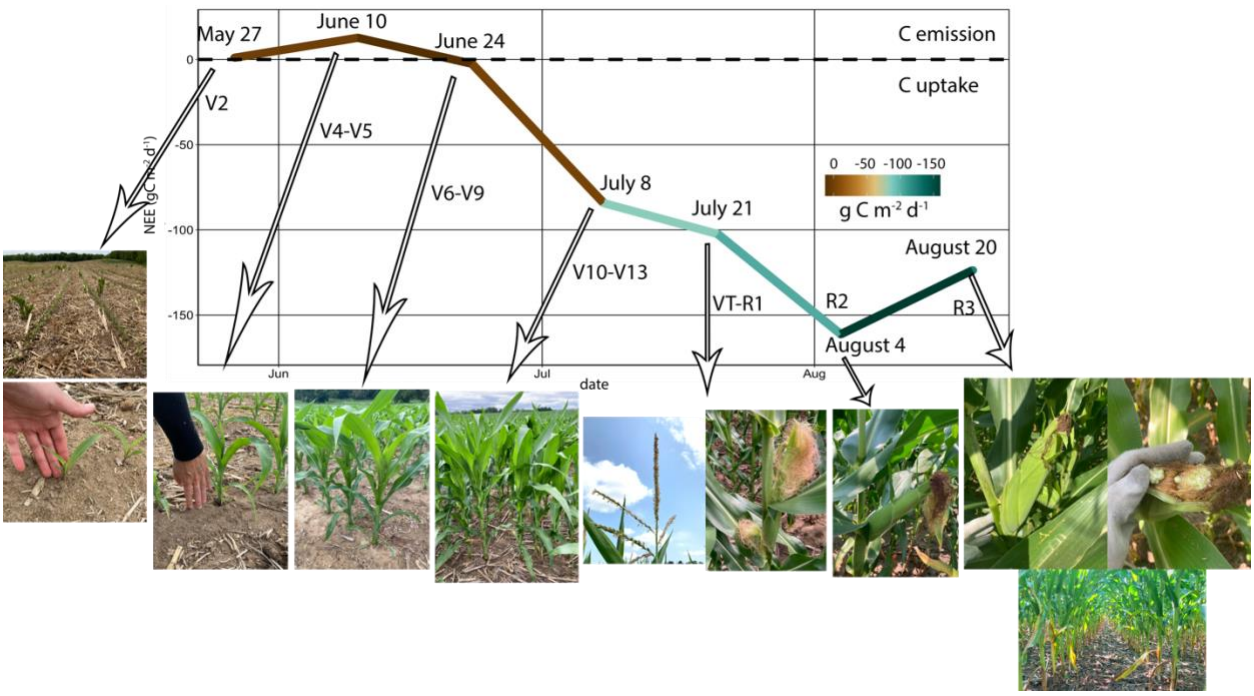

Figure A8: Stages of maize's growth development and net ecosystem exchange (NEE; gC m^{-2} d^{-1}). Photos were taken during the summer field visits in 2021 and represent the typical stages of growth at both the historically cultivated as agricultural lands (AGR) and the Conservation Reserve Program (CRP) sites. For the meaning of each stage (i.e., V and R), refer to the main text.

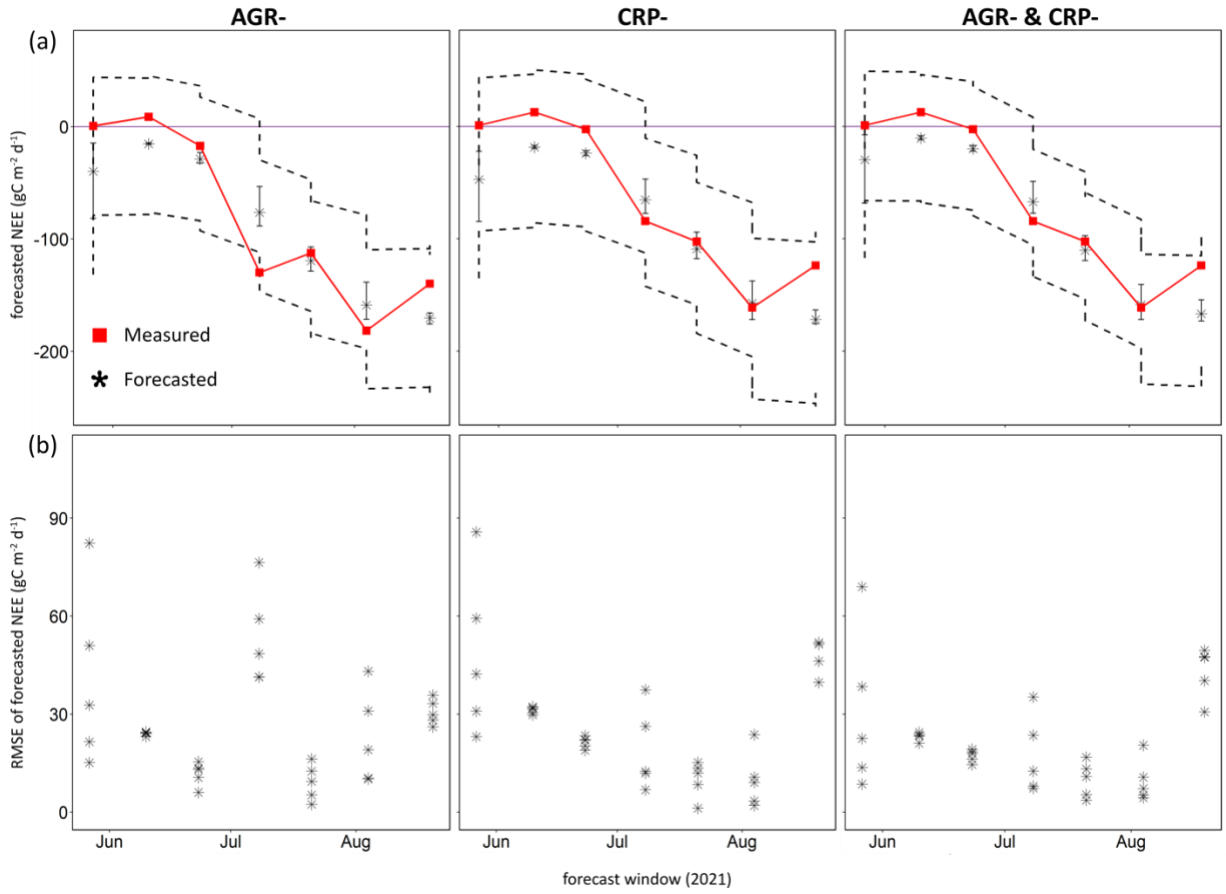

Figure A9: (a) Forecast of the net ecosystem exchange (NEE; gC m^{-2} d^{-1}) for maize cover type, during 2021 growing season, at the historically cultivated as agricultural lands (AGR), the Conservation Reserve Program (CRP), and at both sites together, using Bayesian Dynamic Linear Model (BDLM) with *in-situ* variables. Full red squares and black asterisks represent the measured and forecasted (± min and max at the 5 subplots) NEE values; while black dashed lines indicate the 95% confidence intervals (CI). (b) Root-mean square error (RMSE) of the forecasted NEE indicating accuracy of the forecast.

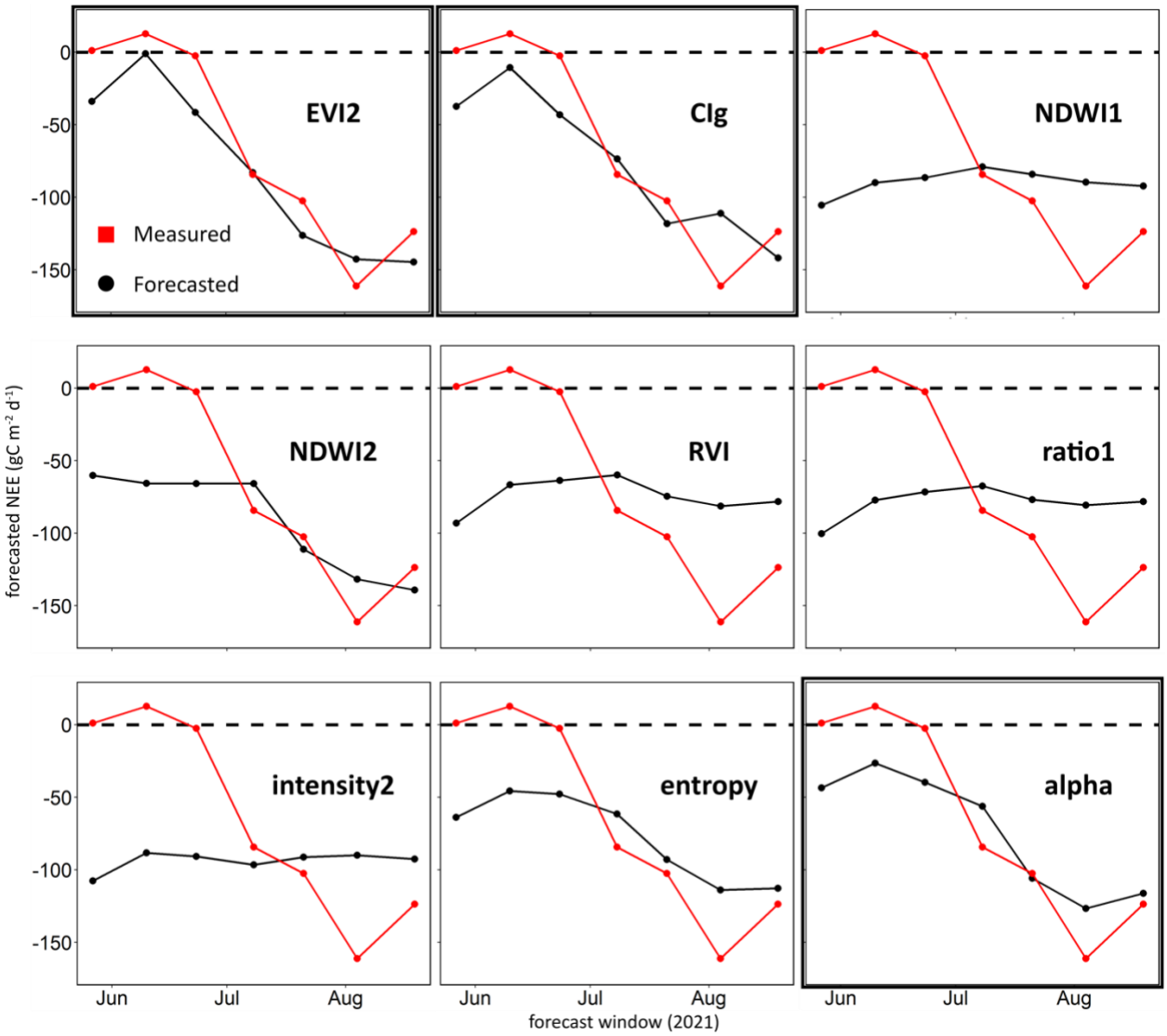

Figure A10: Mean forecasts of the net ecosystem exchange (NEE; gC m^{-2} d^{-1}) for maize cover type, at the historically cultivated as agricultural lands (AGR) and the Conservation Reserve Program (CRP) sites together, during 2021 growing season using Sentinel-2 vegetation indices (EVI2, CIg, NDWI1, and NDWI2), Sentinel-1 polarization intensity backscatters (RVI, ratio1, and intensity2), and Sentinel-1 Polarimetric SAR decomposition coefficients (Entropy and Alpha). Full red circles represent the actual NEE values in 2021. Black bounding boxes indicate the remote sensing outputs selected for the analysis.

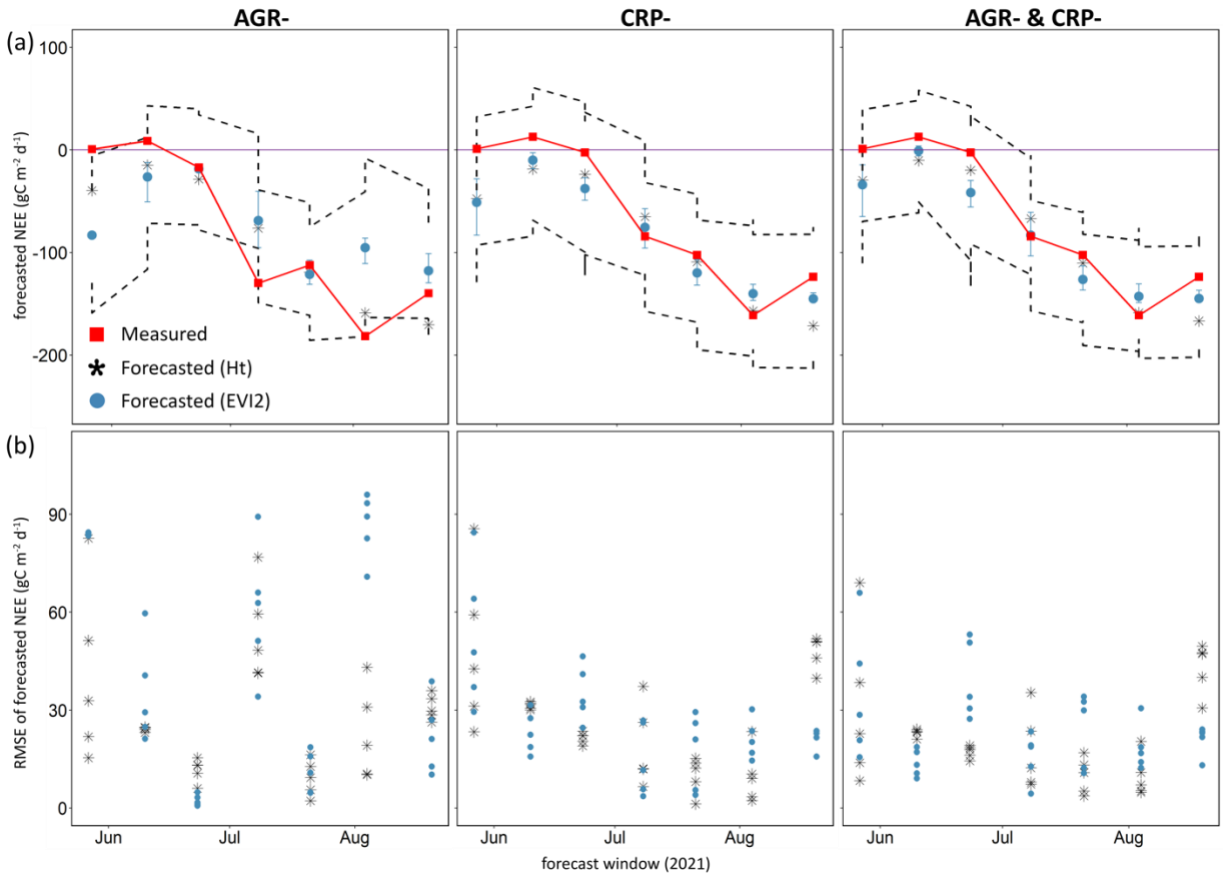

Figure A11.1: (a) Forecast of the net ecosystem exchange (NEE; gC m^{-2} d^{-1}) for maize cover type, during 2021 growing season, at the historically cultivated as agricultural lands (AGR), the Conservation Reserve Program (CRP), and at both sites together, using Bayesian Dynamic Linear Model (BDLM) with the remote sensing variable EVI2. Full red squares represent the measured NEE values, while black asterisks and full blue circles represent the forecasted (± min and max at the 5 subplots) NEE values using Ht and EVI2, respectively. Black dashed lines indicate the 95% confidence intervals (CI). (b) Comparison of the root-mean square error (RMSE; i.e., accuracy of the forecast) of the forecasted NEE using Ht (black asterisk) and EVI2 (full blue circles).

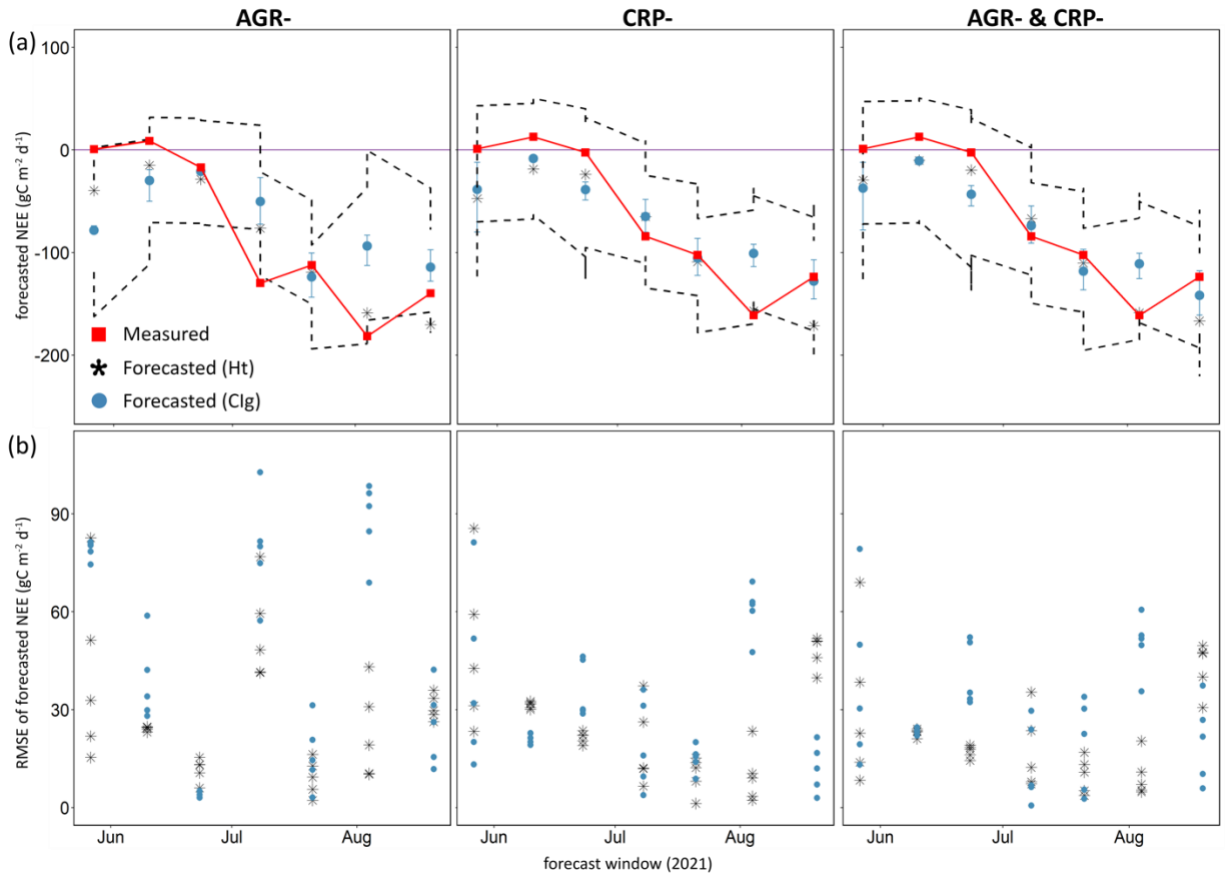

Figure A11.2: (a) Forecast of the net ecosystem exchange (NEE; gC m^{-2} d^{-1}) for maize cover type, during 2021 growing season, at the historically cultivated as agricultural lands (AGR), the Conservation Reserve Program (CRP), and at both sites together, using Bayesian Dynamic Linear Model (BDLM) with the remote sensing variable CIg. Full red squares represent the measured NEE values, while black asterisks and full blue circles represent the forecasted (± min and max at the 5 subplots) NEE values using Ht and CIg, respectively. Black dashed lines indicate the 95% confidence intervals (CI). (b) Comparison of the root-mean square error (RMSE; i.e., accuracy of the forecast) of the forecasted NEE using Ht (black asterisk) and CIg (full blue circles).

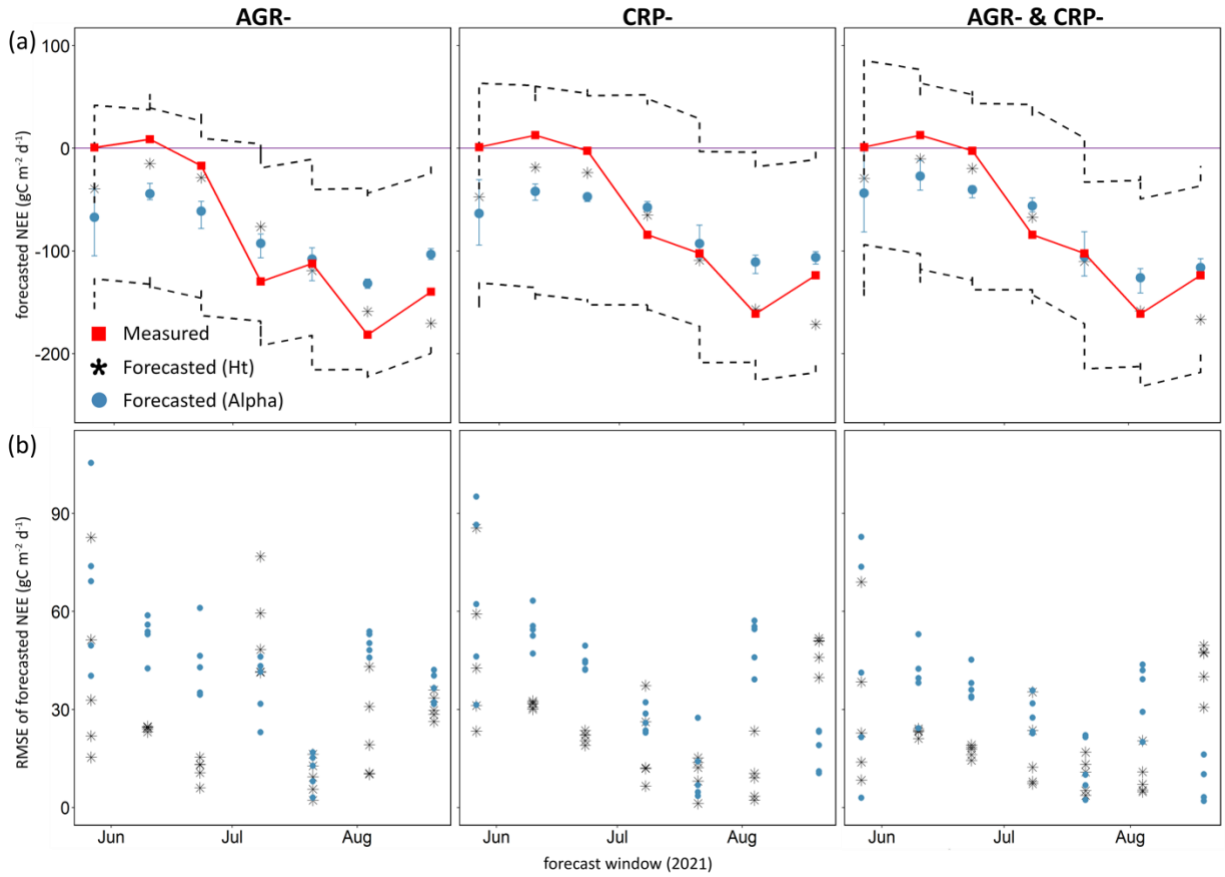

Figure A11.3: (a) Forecast of the net ecosystem exchange (NEE; gC m^{-2} d^{-1}) for maize cover type, during 2021 growing season, at the historically cultivated as agricultural lands (AGR), the Conservation Reserve Program (CRP), and at both sites together, using Bayesian Dynamic Linear Model (BDLM) with the remote sensing variable Alpha. Full red squares represent the measured NEE values, while black asterisks and full blue circles represent the forecasted (± min and max at the 5 subplots) NEE values using Ht and Alpha, respectively. Black dashed lines indicate the 95% confidence intervals (CI). (b) Comparison of the root-mean square error (RMSE; i.e., accuracy of the forecast) of the forecasted NEE using Ht (black asterisk) and Alpha (full blue circles).

CHAPTER 5. CONCLUSIONS

Lessons learned from my research

This dissertation is the result of investigations onto the biogeophysical and biogeochemical mechanisms involved in climate regulation potentials (i.e., warming/cooling effects) as mitigation strategies to global warming, in the context of ecosystem functioning and landscape ecology. The research explores the effects of (i) landscape mosaic and composition on surface albedo changes (Chapters 2 and 3), and (ii) land use history and recent management on net ecosystem exchange fluxes of bioenergy crops (Chapter 4).

Results from Chapters 2 and 3 showed the potential of spatiotemporal variations of surface albedo to cool the local climate, with different magnitudes, depending on weather conditions, major land cover types, and time of the year (growing season *vs* non-growing season) considered. Results from Chapter 4 showed that the inter-annual variation of main biophysical and physical controlling drivers to net ecosystem exchange (NEE) fluxes, with pattern, magnitude, and importance varying by bioenergy crop and growing season considered. Results also showed the capability of fine-resolution optical and radar remote sensing imagery to improve forecasts of growing season NEE of maize as a bioenergy crop.

Major Contributions

Agricultural landscapes have represented the main subject of several environmental research studies that, besides food and feed production, focused on assessing their roles as a carbon sink/source. The Kalamazoo River Watershed has been subjected to intensive land use and land cover changes after the European settlements, which brought to the present characteristic highly managed agricultural land mosaics (Brown et al., 2000). The analysis of biogeophysical and biogeochemical mechanisms across contrasting landscapes and ecoregions, makes the present research a unique study that fills some gaps in the current landscape ecology and ecosystem science

as well as global warming research. Chapter 2 provides a proof of concept to quantify the ecosystem and landscape contribution to local and global climate through the analysis of spatiotemporal changes of surface albedo across five equal area landscapes, in southwestern Michigan, USA, and during three scenarios led by precipitation events (i.e., wet *vs* dry *vs* normal). Chapter 3 extends the analysis at Chapter 2 to the entire Kalamazoo River Watershed for a 19-year period, by looking at the contribution of major cover types, compared to original land uses, during both growing season and non-growing season (i.e., the effects of snow *vs* snow-free surface albedo). Chapter 4 presents the climate regulations of the net ecosystem exchange (NEE) fluxes of three major bioenergy crops under different land use history and management by analyzing the main biophysical and physical controlling drivers to NEE using a comparison of three models.

Several major contributions derive from the first two Chapters. First, this study provides a novel methodology for quantifying the landscape contribution to local and global climate by considering changes in surface albedo due to the co-existence of multiple land cover types (i.e., major land covers composing the land mosaic) within the same landscape. In contrast, previous studies only considered the land cover transformation (i.e., prior *vs* posterior land cover classes) as main driver to changes in surface albedo (Bala et al., 2007; Barnes et al., 2013; Bonan, 2008). Moreover, the first two Chapters contributed on building scientific knowledge in regard of the applied methodology to translate changes in surface albedo into albedo-induced radiative forcing (i.e., cooling/warming effects) and into its CO_2-equivalent (i.e., mitigation/emission effects), so that to be consistent with current IPCC emission metric approaches. In my opinion, such contribution is of fundamental importance because a major challenge of current research to translate albedo changes into CO_2-equivalent mitigation/emission effects is the lack of universal time dependency following the perturbation in albedo change. In other words, a methodology

producing a metric that is true equivalent to CO_2 emissions still does not exist (Bright & Lund, 2021).

The three-model comparison approach employed in Chapter 4, along with the methodology based on both *in-situ* and remote sensing imagery, contributed to the overall need to investigate major controlling drivers to the variations of ecosystem carbon budget (i.e., C uptake/emission). Therefore, it is fundamental to understand the importance and magnitude of controlling drivers to the C uptake/emission across cropping systems. As major contribution, Chapter 4 sheds light on multivariate unexplored controlling drivers as well as pattern-processes of NEE fluxes of three different bioenergy crops. Few are the studies found in the literature that deal with environmental controls on CO_2 exchange across cropping systems (e.g., Hernandez-Ramirez et al., 2011). Moreover, while it has been generally established that available light, ambient temperature, and precipitation patterns represent key controlling drivers of CO_2 fluxes (Griffis et al., 2003; Law et al., 2002; Pingintha et al., 2010; Reverter et al., 2010), the relationships have only been examined separately as single factors (Hernandez-Ramirez et al., 2011).

Recommendations for Future Research

This dissertation represents a collection of three complementary research works, each of which focused on mitigation strategies in the context of global warming research. Recommendations for further research needed could fill the knowledge gaps of the present research.

For instance, I proposed the Kalamazoo River Watershed and its different portions within ecoregion boundaries as proof of concept for my research. Similarly, previous works have been carried out to estimate cooling/warming effects due to surface albedo changes over the conterminous United States (CONUS) (Barnes et al., 2013; Barnes & Roy, 2008, 2010), by

considering boundaries at Ecoregion level and remote sensing albedo data. However, no effort has been made to put the results in the context of landscape composition and mosaic. Therefore, further effort is needed to adapt the proposed methodology to other study cases, within and outside the US. Moreover, with the research presented at Chapters 2 and 3, I investigated the contribution of land mosaics due to land transformation on albedo-induced GWI by considering forest cover type as the reference for the entire study area (Brown et al., 2000). However, such methodology precludes from estimating forests' contribution to albedo-induced GWI, hindering a comprehensive synthesis of the total climate mitigation/emission of the watershed considering that the low albedo of forests contributes to climate warming (Bonan, 2008).

Regarding Chapter 4, additional work should not be limited only to the growing season analysis. In fact, the exclusion of non-growing season fluxes entails the omission of net outgoing fluxes (e.g., GHG emissions, water vapor fluxes, upwelling reflectances), with the result of producing partial understanding of the full story. Furthermore, additional work could focus on critical stages of the maize's growth development during growing season. For example, other studies showed that fluctuations in available light during the most photosynthetically active phase of maize's canopy could represent the main controlling driver to CO_2 uptake (Hernandez-Ramirez et al., 2011). Hence, there is the need to integrate this work with seasonal analysis, to include, for example, early *vs* peak *vs* late growing season. Extending the analysis to not only consider the growing season period, would also help better investigate the magnitude of C ecosystem response to several climatic events, which it has been generally shown to depend on lagged effects (e.g., weather preceding the growing season), and not only on the current event (Archibald & Kirton, 2009). For example, factors like air and soil temperature, radiation, and vapor pressure deficit play different role (i.e., importance) to the CO_2 uptake depending on the time scale considered (Suyker

& Verma, 2012).

In light of the present study's findings, I think that there are still several challenges ahead. To start with, there is the need to translate such findings into key concepts for policy makers, who ultimately have the role to bridge scientific knowledge with society (i.e., communities and organizations) and to help them to address environmental concerns. As demonstrated by my research, out there, there are valuable options to mitigate the effect of climate change and global warming. However, one big challenge is that the trade-off space within which the mitigation options interact is still not readily described. For instance, the main challenge related to the assessment of albedo as mitigation strategy comes from the use of a measure like radiative forcing (RF; W m^{-2}), which can be hard to digest for many decision-makers, who currently deal with currency of CO_2-equivalent emissions (Bright & Lund, 2021). In addition to that, many researchers express the albedo RFs in terms of their CO_2-equivalent effects; however, by employing non-standard methods for calculating it, like there is for well-mixed greenhouse gas ones. In turn, there is confusion even within the scientific community. Moreover, despite scientists have been employing the use of pulse emission metrics (i.e., global warming impact) for years, this field is highly evolving and changing. As result, there is a lot of confusion and misunderstanding about how human modifications to the landscape can be translated into something tangible, such as, warming/cooling and emission/mitigation.

On the other hand, I find essential the need to keep in mind what the manager perspectives might be. For instance, in my humble opinion, in a mindset driven by the sole economic and productive interest, the perceived knowledge about the magnitude with which the management of the landscape is affecting its warming/cooling and emission/mitigation status, is not that useful. For example, telling a farmer how much warming/cooling and emission/mitigation derive from

their management practices and/or their choice of land use, due to the consequent change in both surface albedo and CO_2 fluxes, might be relevant to their economic/political calculus. However, if such knowledge was accompanied by incentives, similar to how it works for the carbon score and credit, its impact would be more meaningful. In part, some research studies are already leaning towards this way of delivering scientific information. For example, in urban settings, some studies have compared the cooling effects derived by higher urban albedo in terms of money saved from the reduced air-conditioning costs.

To conclude, future research will help to fill those gaps, as long as there is a corresponding framework for new policies coming along with it.

REFERENCES

Archibald, S. A., Kirton, A., Van der Merwe, M. R., Scholes, R. J., Williams, C. A., & Hanan, N. (2009). Drivers of inter-annual variability in net ecosystem exchange in a semi-arid savanna ecosystem, South Africa. *Biogeosciences*, *6*(2), 251-266.

Bala, G., Caldeira, K., Wickett, M., Phillips, T. J., Lobell, D. B., Delire, C., & Mirin, A. (2007). Combined climate and carbon-cycle effects of large-scale deforestation. *Proceedings of the National Academy of Sciences*, *104*(16), 6550–6555. https://doi.org/10.1073/pnas.0608998104

Barnes, C. A., & Roy, D. P. (2008). Radiative forcing over the conterminous United States due to contemporary land cover land use albedo change. *Geophysical Research Letters*, *35*(9). https://doi.org/10.1029/2008GL033567

Barnes, C. A., & Roy, D. P. (2010). Radiative forcing over the conterminous United States due to contemporary land cover land use change and sensitivity to snow and interannual albedo variability. *Journal of Geophysical Research*, *115*(G4), G04033. https://doi.org/10.1029/2010JG001428

Barnes, C. A., Roy, D. P., & Loveland, T. R. (2013). Projected surface radiative forcing due to 2000–2050 land-cover land-use albedo change over the eastern United States. *Journal of Land Use Science*, *8*(4), 369–382. https://doi.org/10.1080/1747423X.2012.667453

Bonan, G. B. (2008). Forests and climate change: Forcings, feedbacks, and the climate benefits of forests. *Science*, *320*(5882), 1444–1449. https://doi.org/10.1126/science.1155121

Bright, R. M., & Lund, M. T. (2021). CO_2-equivalence metrics for surface albedo change based on the radiative forcing concept: A critical review. *Atmospheric Chemistry and Physics*, *21*(12), 9887–9907. https://doi.org/10.5194/acp-21-9887-2021

Brown, D. G., Pijanowski, B. C., & Duh, J. D. (2000). Modeling the relationships between land use and land cover on private lands in the Upper midwest, USA. *Journal of Environmental Management*, *59*(4), 247–263. https://doi.org/10.1006/jema.2000.0369

Griffis, T. J., Black, T. A., Morgenstern, K., Barr, A. G., Nesic, Z., Drewitt, G. B., Gaumont-Guay, D., & McCaughey, J. H. (2003). Ecophysiological controls on the carbon balances of three southern boreal forests. *Agricultural and Forest Meteorology*, *117*(1), 53–71. https://doi.org/10.1016/S0168-1923(03)00023-6

Hernandez-Ramirez, G., Hatfield, J. L., Parkin, T. B., Sauer, T. J., & Prueger, J. H. (2011). Carbon dioxide fluxes in corn–soybean rotation in the midwestern U.S.: Inter- and intra-annual variations, and biophysical controls. *Agricultural and Forest Meteorology*, *151*(12), 1831–1842. https://doi.org/10.1016/j.agrformet.2011.07.017

Law, B. E., Falge, E., Gu, L., Baldocchi, D. D., Bakwin, P., Berbigier, P., Davis, K., Dolman, A. J., Falk, M., Fuentes, J. D., Goldstein, A., Granier, A., Grelle, A., Hollinger, D., Janssens, I. A., Jarvis, P., Jensen, N. O., Katul, G., Mahli, Y., … Wofsy, S. (2002). Environmental

controls over carbon dioxide and water vapor exchange of terrestrial vegetation. *Agricultural and Forest Meteorology*, *113*(1–4), 97–120. https://doi.org/10.1016/S0168-1923(02)00104-1

Pingintha, N., Leclerc, M. Y., Beasley, J. P. J., Durden, D., Zhang, G., Senthong, C., & Rowland, D. (2010). Hysteresis response of daytime net ecosystem exchange during drought. *Biogeosciences*, *7*(3), 1159–1170. https://doi.org/10.5194/bg-7-1159-2010

Reverter, B. R., Sánchez-Cañete, E. P., Resco, V., Serrano-Ortiz, P., Oyonarte, C., & Kowalski, A. S. (2010). Analyzing the major drivers of NEE in a Mediterranean alpine shrubland. *Biogeosciences*, *7*(9), 2601–2611. https://doi.org/10.5194/bg-7-2601-2010

Suyker, A. E., & Verma, S. B. (2012). Gross primary production and ecosystem respiration of irrigated and rainfed maize–soybean cropping systems over 8 years. *Agricultural and Forest Meteorology*, *165*, 12–24. https://doi.org/10.1016/j.agrformet.2012.05.021